NTNU
Norwegian University of
Science and Technology

Repair Coatings for Thermally Sprayed Aluminium

Heidi Askestad

NTNU - NORWEGIAN UNIVERSITY
OF SCIENCE AND TECHNOLOGY
DEPARTMENT OF ENGINEERING DESIGN
AND MATERIALS

MASTER THESIS SPRING 2016
FOR
STUD.TECHN. Heidi Askestad

Repair coatings for thermally sprayed aluminium

Reparasjonsbelegg for termisk sprøyta aluminium

Thermally sprayed aluminium (TSA) is a highly resistant coating that is often used in corrosive environments for protection of steel constructions. However, if the TSA is painted a special corrosion mechanism comes in action, the TSA will corrode rapidly and protection of the steel substrate is lost (TSA duplex corrosion). This introduces a problem for repair of damages in the TSA coating, since there will often be limitations on application of new TSA, either due to access problems with the spraying equipment or limitations on hot work (fire hazard). The objective with this thesis is to find coatings that can be used for repair of TSA without triggering the TSA duplex corrosion mechanism. The work will build on the project work performed by the student in 2015.

The thesis will include the following:
- Literature review on relevant topics like, buffering reactions and cathodic protection of TSA.
- Experimental investigation of various coatings by
  - cyclic testing (ISO 20340)
  - crevice corrosion testing simulating the TSA duplex corrosion mechanism
- Characterization of coatings after testing

Formal requirements:

Three weeks after start of the thesis work, an A3 sheet illustrating the work is to be handed in. A template for this presentation is available on the IPM's web site (see https://www.ntnu.edu/web/ipm/master-thesis). This sheet should be updated one week before the master's thesis is submitted.

Risk assessment of experimental activities shall always be performed. Experimental work defined in the problem description shall be planed and risk assessed up-front and within 3 weeks after receiving the problem text. Any specific experimental activities which are not properly covered by the general risk assessment shall be particularly assessed before performing the experimental work. Risk assessments should be signed by the supervisor and copies shall be included in the appendix of the thesis.

The thesis should include the signed problem text, and be written as a research report with summary both in English and Norwegian, conclusion, literature references, table of

contents, etc. During preparation of the text, the candidate should make efforts to create a well arranged and well written report. To ease the evaluation of the thesis, it is important to cross-reference text, tables and figures. For evaluation of the work a thorough discussion of results is appreciated.

The thesis shall be submitted electronically via DAIM, NTNU's system for Digital Archiving and Submission of Master's theses.

The contact person is Ole Øystein Knudsen.

Torgeir Welo
Head of Division

Ole Øystein Knudsen
Professor/Supervisor

NTNU
Norges teknisk-
naturvitenskapelige universitet
Institutt for produktutvikling
og materialer

Abstract

Thermally sprayed aluminium (TSA) is widely used for corrosion protection on offshore installations. Rapid degradation of the TSA has earlier been discovered, if organic coating is applied on top of the TSA. In case of coating damages on the TSA, a duplex corrosion mechanism may occur. Due to access limitations with coating equipment or hot work limitations offshore, application of new TSA may be difficult. Therefore, it is necessary to develop a repair coating for TSA in connection with damage. The repair coating must provide corrosion protection without triggering the duplex corrosion mechanism and shall be applied without removing the intact TSA.

Eight repair coatings were tested on steel coated with TSA to determine the corrosion behavior in marine environment. Four possible protection mechanisms were considered: (1) cathodic polarization, (2) buffering capacity, (3) ability to release an aggressive environment formed under the coating and (4) electrical conductive coatings. The coatings contained anodic elements such as aluminium, zinc or magnesium, except for an inorganic copolymer coating and an MgO pigmented coating. A cyclic coating test was conducted for 20 cycles according to ISO 20340. Highest amount of corrosion creep for the TSA was seen for the Zn epoxy, the inorganic copolymer coating, the high Zn primer and the modified Zn epoxy. An average corrosion creep of approximately 5.1 mm was seen for the Zn epoxy. Due to corrosion products, blistering or cracking of the repair coat were seen for these coatings. The Zn-, MgO-, Mg- and Al-silicate showed promising results without blistering after the same test. The Zn silicate showed an average corrosion creep of approximately 0.6 mm, while the MgO-, Mg- and Al-silicate showed negligible corrosion creep.

Coating resistivity was measured by obtaining several electrochemical impedance spectra (EIS) over a period of time, and the open circuit potential (OCP) was measured. The zinc containing coatings were exposed for 134 days, while the MgO-, Mg-, Al-silicate and the inorganic copolymer coating were exposed for 81 days. All coatings showed an OCP more negative than -800 mV vs. Ag/AgCl, except for the inorganic copolymer coating. This coating had an initial potential of -430 mV vs. Ag/AgCl with decreasing development towards a more negative potential. The coatings that revealed blistering or cracking of the repair coating during the cyclic coating test showed generally higher impedance, compared to the silicate coatings that did not blister. An open coating structure was considered as the most important protection mechanism for a TSA repair coat. The protection mechanisms regarding cathodic polarization, electrical conductive coatings and the buffering effect were assumed less important compared to the open coating structure.

Crevice corrosion tests with different crevice designs were performed in order to have a short-term test for the TSA duplex corrosion mechanism. Further development of the test design is necessary before the mechanism can be investigated by this method.

Sammendrag

Termisk sprøytet aluminium (TSA) brukes ofte i forbindelse med korrosjonsbeskyttelse på offshoreinstallasjoner. Tidligere erfaringer har vist at TSA korroderer raskt i en spaltkorrosjons-mekanisme dersom organiske belegg males over TSA. Påføring av ny TSA ved skade kan være vanskelig grunnet begrenset tilkomst med malingsutstyr eller begrensning i forhold til varmt arbeid. Det er derfor ønskelig å finne ett reparasjonsbelegg for TSA som kan påføres på områder hvor skader har oppstått. Malingen må kunne påføres uten å blåse av intakt TSA, samtidig som at spaltkorrosjonsmekanismen for TSA ikke trigges.

Åtte reparasjonsbelegg ble testet på stål belagt med TSA for å undersøke korrosjonsbeskyttelsen i marint miljø. Fire mulige beskyttelsesmekanismer ble vurdert: (1) katodisk polarisasjon, (2) buffer kapasitet, (3) evnen til å slippe ut aggressivt miljø som dannes under reparasjonsbelegget og (4) elektrisk ledende belegg. Malingene inneholdt anodiske elementer som aluminium, sink eller magnesium, unntatt en uorganisk kopolymer maling og en MgO-pigmentert silikatmaling. En syklisk malingstest med 20 sykler ble gjennomførte i henhold til ISO 20340. Mye korrosjonskryp på TSA-laget ble sett under Zn epoksyen, den uorganiske kopolymer malingen, den modifiserte Zn epoksyen og høy-Zn primeren. Ett gjennomsnittlig korrosjonskryp på TSA-laget på 5.1 mm ble sett under Zn epoksyen. Blærer eller oppsprekking av reparasjonsbelegget grunnet korrosjonsprodukter ble sett på disse malingene. Zn-, MgO-, Mg- og Al-silikaten viste lovende resulter uten blærer etter den sykliske malingstesten. Zn silikaten viste ett gjennomsnittlig korrosjonskryp på 0.6 mm, mens MgO-, Mg- og Al-silikatene viste neglisjerbare verdier.

Beleggenes resistivitet ble målt ved elektrokjemisk impedansspektroskopi (EIS) regelmessig over en lengre periode, og åpen-krets-potensial (OCP) ble målt. De sinkbaserte malingene ble eksponert i 134 dager, mens MgO-, Mg-, Al-silikat og den uorganiske kopolymer malingen ble eksponert i 81 dager. Alle malingene viste ett mer negativt potensial enn -800 mV mot Ag/AgCl. Dette gjaldt ikke for den uorganiske kopolymer malingen. Denne malingen hadde ett startpotensial på -430 mV mot Ag/AgCl, som avtok mot ett mer negativt potensial gjennom testen. Malingene som viste blærer eller oppsprekking av reparasjonsbelegget grunnet korrosjonsprodukter i den sykliske malingstesten viste generelt høyere impedans som funksjon av tid, sammenlignet med silikatmalingene som ikke ga blærer. En åpen malingsstruktur ble ansett som den viktigste beskyttelsesmekanismen for ett malingsbelegg for reparasjon av TSA. Mekanismene relatert til katodisk polarisasjon, buffer kapasitet og elektrisk ledningsevne ble ansett som mindre viktig sammenlignet med malingsstrukturen.

Beleggene ble også forsøkt evaluert i flere spaltkorrosjonstester med ulike spaltdesign. Videre utvikling av spaltdesignet er nødvendig for å kunne undersøke den aktuelle spaltkorrosjons-mekanismen for de ulike reparasjonsbeleggene med denne metoden.

Preface

This Master´s thesis is submitted as the product of *TMM4911-Materials, Master´s Thesis* in fulfillment of the degree Master of Science (MSc) in Materials Science and Engineering. The report is a final report that builds on the project work performed in the course *TMM4511-Materials, Specialization project* during the autumn of 2015.

The work was performed and completed at the Norwegian University of Science and Technology (NTNU) at the Department of Engineering Design and Materials. The project was completed in collaboration with SINTEF, and the aim of the project was to develop a repair coating for thermally sprayed aluminum (TSA).

I would like to specially thank supervisor Ole Øystein Knudsen for all the help and guidance related to the project. I would also like to thank Ann-Karin Kvernbråten, Nils-Inge Nilsen and Christian Torres Rodriguez for all the advice and help related to the laboratory work at the corrosion laboratory at SINTEF. Further, I would like to thank Trygve Lindahl Schanche for assistance in the mechanical laboratories, and Yingda Yu for assistance in the EM-laboratory.

Trondheim, June 8, 2016

Heidi Askestad

Table of Content

Abbreviations

TSA	Thermally sprayed aluminium
EPMA	Electron probe micro analysis
SHE	Standard hydrogen electrode
Ag/AgCl	Silver/silver chloride electrode
TSZ	Thermally sprayed zinc
RH	Relative humidity
DFT	Dry film thickness
EIS	Electrochemical impedance spectra
OCP	Open circuit potential
QQQ	Triple Quadropole
ICP-MS	Inductively coupled plasma mass spectrometry
Rms	Root mean square
EDS	Energy-dispersive spectroscopy
SEM	Scanning electron microscop
XRD	X-ray diffraction

1 Introduction

1.1 Background

Coating systems are the most common protection method against corrosion topside on offshore installations. Coating properties and quality are important parameters to ensure the desired protection level. Thermally sprayed aluminium (TSA) is widely used in corrosive environments for steel constructions. TSA alone provides excellent corrosion protection. Nevertheless, if the TSA is coated with an organic coating a TSA duplex corrosion mechanism is triggered and the TSA may corrode rapidly. This is a current problem in relation to repair of coating damages on TSA. There are often limitations regarding application of new TSA on offshore installations due to fire hazards and limitations with hot work. Access problems with the spraying equipment may also be a problem.

Research regarding coating on TSA has earlier been performed through the project "*Coating systems for long lifetime: Thermally Sprayed Duplex Systems*". This project studied topics such as the actual corrosion mechanism occurring when TSA is painted, in addition to testing of different sealers for thermally sprayed systems. Application parameters related to TSA has also been investigated and different thermally sprayed coatings and the maintenance processes for TSA have been studied [1].

1.2 Objectives

The aim for this MSc project has been to find a repair coating that can be applied on already existing TSA without removing the damaged coating. It is also essential that the TSA corrosion mechanism is not restarted after application. A number of potential repair coatings for TSA were tested and evaluated with respect to performance. The repair coatings were selected based on four potential mechanisms: (1) cathodic polarization, (2) buffering capacity, (3) ability to release an aggressive environment formed under the coating and (4) electric conductivity. Some of the coatings function as a sacrificial anode for the steel, some of the coatings let the electrolyte through due to an open structure and one coating may function as a buffer that neutralizes the pH below the repair coating. A fourth protection mechanism is that electrochemical reactions may be moved to the surface of the repair coating, if the coating is electrical conductive.

The project involves different coating tests and some of the tests were started during the project work carried out the autumn of 2015 [2]. An important requirement to the coating is that it must protect both bare steel and TSA. Different coatings and pigments have been tested to see if some elements improve protection behavior. Silicate coatings containing zinc, aluminium, magnesium or magnesium oxide powder have been tested in addition to zinc rich epoxy coatings, an inorganic copolymer coating and a high zinc primer coating. Both long-term cyclic testing and short-term crevice corrosion tests were performed to determine the desired test method for repair coat evaluation. It is desirable that corrosion of the TSA below the repair coat is reduced, which leads to decreased corrosion rate, rather than triggering the crevice corrosion process.

2 Theory

The basic theory related to TSA and organic coatings, which constitute the main components of the duplex coating system, is presented in this chapter. Further, the corrosion mechanism of coated TSA is discussed together with desired coating properties that may favor protection and avoid further development of the TSA duplex corrosion mechanism. Finally, the corrosion properties for aluminium, zinc and magnesium in a TSA duplex coating system are presented.

2.1 Duplex coating systems

A duplex coating system consists of a metallic coating in combination with an organic coating [3]. Basic information regarding the two coating layers is presented in section 2.1.1 and 2.1.2.

2.1.1 The thermally sprayed aluminium in the duplex system

Thermally sprayed aluminium is a coating based on technically pure aluminium (99.5%) or aluminium alloys containing 5 wt% magnesium [4]. The aluminium/magnesium alloy $AlMg_5$ is an alloy in the 5000 aluminium series, and is often used offshore due to high corrosion resistance in seawater [5].

TSA has a lamellar structure with layers of overlapping particles. The lamellar microstructure is shown in Figure 2.1. Combustion of gases or an electric arc of plasma melts or heats the coating material. A carrier gas (compressed air) accelerates the particles towards the substrate surface. The adhesion of the particles is established parallel to the surface by interlocking of the particles with asperities located on the roughened surface. The lamellar structure is established by further deposition of new particles, which leads to an coating layer [6].
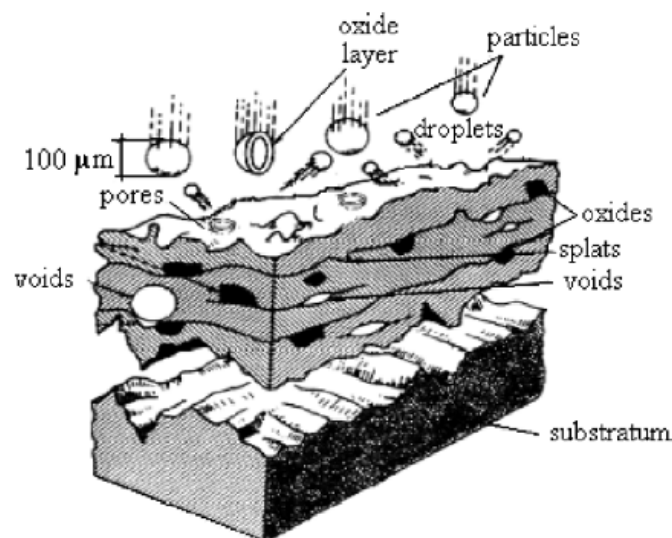

Figure 2.1: Sketch of the lamellar coating layers formed by a thermal spray process [6].

In general, for all thermally sprayed coatings, the adhesion between the coating and the substrate, and the cohesion between the deposited particles are critical for the mechanical performance of the coatings. Blast cleaning of the surface is necessary to obtain sufficient roughness and mechanical anchoring between the flattened particles and the substrate. The coating adhesion is a result of three mechanisms: mechanical interlocking, chemical-metallurgical forces and physical forces [6]. Due to high temperature during application, localized melting and atom diffusion may occur, and solid solution or intermetallic compounds may form. This is referred to as the chemical-metallurgical forces between the particles and the substrate. The physical forces include weak chemical bonding obtained by Van der Waals forces, which give atom attraction within the material. In addition to the mentioned forces, the surface activation and preparation are critical to ensure maximum adhesion. The degree of surface activation depends on the surface cleanliness, degree of surface roughness and substrate preheating obtained before the coating is applied [6].

TSA applied in the Norwegian offshore industry is classified as coating system No. 2A in NORSOK M-501. Cleanliness and roughness of the surface shall respectively be 2 ½ (stated in ISO 8501-1) and Grade Medium G (stated in ISO 8503) [4]. The "G" in "*Grade Medium G*" means that grit abrasives must be used for blast cleaning, not shot abrasives. The roughness of the surface is stated by the grade, in this case medium (50 μm to 85 μm, R_{y5}) [7]. As steel is coated with TSA, the coating will act as a physical barrier between the metal and the surrounding environment. If the coating is damaged (small damages), the aluminium will act as an anode and protect the exposed metal from corroding. The structural steel will act as a cathode, and the salt spray closes the circuit between the anode and the cathode [8].

2.1.2   The organic coating in the duplex system

The organic coating in a duplex system must function as a physical barrier and prevent aggressive elements from the surrounding environment to reach the TSA substrate. If the protective barrier is damaged, the coating must have the capability to constrain the corrosion process. Anticorrosion pigments such as zinc particles or corrosion inhibitors may be added to the organic coating to protect the metal surface if damage occurs. The application and use of the coated metal determine the number of coating layers and the final thickness of the duplex coating system. Each layer offers a specific function, e.g. adhesion between the coating and the TSA substrate, adhesion between the different coating layers, anti-fouling, wear resistance, corrosion inhibition or weathering [9]. ISO 12944 states that epoxy, polyurethane or ethyl silicate may be used as binders in the primer coat, while epoxy, polyurethane or an epoxy combination may be used as binders in the subsequent coat. If the ethyl silicate is used as primer, the subsequent coat is recommended as a tie coat [10]. Polyurethane is not used in the Norwegian oil and gas sector today, due to release of isocyanates when heated [11].

Anodic elements such as magnesium and zinc, which is ranged as less noble compared to aluminium in the galvanic series [12], can be added for cathodic polarization. Zinc rich primers provide good protection of a metal even when the coating is mechanically damaged. The primer initially function as a sacrificial anode. Additional barrier protection is given by the low solubility of zinc corrosion products and the alkaline behavior of zinc. The zinc volume must be 65% or higher to obtain a

dependable percolation path [13]. This is necessary because the sacrificial action of zinc initiates when the metal particles are in continuous contact. The zinc content corresponds to ≥ 90 wt% on dry film. Small and lamellar zinc particles shall provide better protection compared to large and spherical particles [13].

Various sealers have been applied on thermally sprayed coatings during the project *"Coating systems for long lifetime: Thermally Sprayed Duplex Systems"* [1]. Thermally sprayed coatings have a rough surface consisting of crevices and pores, and a sealer may be applied to fill the unevenness. Sufficient penetration of the organic coating is important to avoid pores between the duplex coating layers, which may lead to corrosion initiation. The coating viscosity is important to achieve this [1].

2.2   Corrosion of coated TSA

The actual coating system concerned in this work is a TSA duplex coating, where the TSA has revealed rapid degradation [1]. Since the base layer of TSA has degraded, the corrosion mechanism can be compared to crevice corrosion under the organic coating. This corrosion mechanism occurs in crevices where the opening is sufficiently wide to let fluid penetrate in, but so narrow that the fluid becomes stagnant [14].

The crevice corrosion mechanism can be divided into four steps, where step I-III are referred to as the *incubation period*, while step IV is called the *growth phase*.

I.   The corrosion rate is initially equal inside and outside of the crevice, and the anodic (1) and cathodic reaction (2) occurs on the entire metal surface. Figure 2.2 shows the duplex coating system with the electrochemical reactions occurring at the metal surface and inside the crevice [1].

Anodic reaction:
$$Al\ (s) \rightarrow Al^{3+}(aq) + 3e^- \tag{1}$$
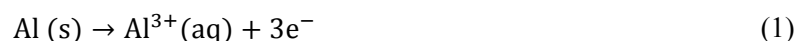
Cathodic reaction:
$$O_2\ (g) + 2H_2O(l) + 4e^- \rightarrow 4OH^-(aq) \tag{2}$$

Figure 2.2: Duplex coating system with the crevice corrosion mechanism occurring under the organic coating [1].

II.   The formation of OH⁻ will stop when oxygen inside the crevice is depleted. The metal dissolution inside the crevice is maintained by the oxygen reduction occurring outside the crevice. The concentration of metal ions inside the crevice increases and the Cl⁻-ions (in

4

chloride containing environments) migrates towards the crevice to achieve charge equilibrium [14]. The migration leads to formation of aluminium 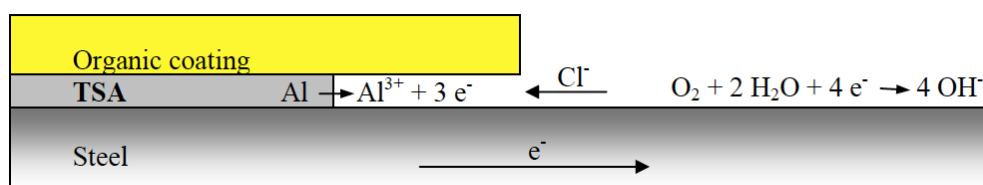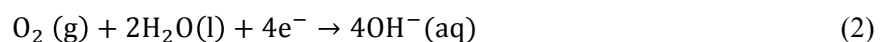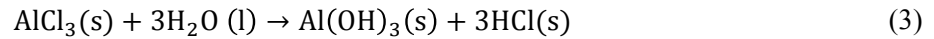chloride (AlCl$_3$) under the organic coating, which is unstable in humid environments. The instability of aluminium chloride leads to formation of hydrochloride acid when reacting with water (3) [1]:

$$AlCl_3 (s) + 3H_2O \ (l) \rightarrow Al(OH)_3 (s) + 3HCl(s) \tag{3}$$

Due to formation of hydrochloride acid, the pH in the crevice will gradually decrease [15]. The reduction leads to active corrosion of the aluminium, since the aluminium oxide is unstable below pH 4, and hydrogen evolution gives an effective cathodic reaction because of acidification of the electrolyte [1].

III. The oxide layer formed on the aluminium is attacked when the pH decreases and the environment inside the crevice becomes acidified. The surface inside the crevice is then activated and the corrosion rate increases [1].

IV. The corrosion rate increases due to the increased amount of Cl$^-$ ions migrated [15], and the cathodic hydrogen evolution (4) occurs because of the pH reduction [1].

$$2H^+(aq) + 2e^- \rightarrow H_2(g) \tag{4}$$

The total corrosion reaction (5) of the TSA below the organic coating is [1]:

$$2Al \ (s) + 6HCl(s) \rightarrow 2AlCl_3 (s) + 3H_2(g) \tag{5}$$
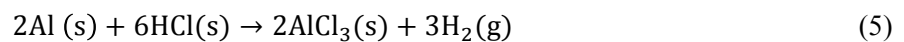
Aluminium chloride is regenerated, which indicates that supply of seawater maintains the reactions [1].

Crevice corrosion is most severe when aluminium is involved and formation of hydrochloric acid takes place, which may lead to rapid degradation and high corrosion rate.

2.3 Desired coating properties for the TSA repair coat

To avoid the TSA duplex corrosion mechanism that occurs when TSA is coated, some coating properties are assumed favorable compared to others. The aim is to develop a coating that can be applied onto surface areas consisting of bare steel, TSA and organic coating, without removing the existing coating system. The repair coating shall therefore be able to provide adhesion to the three surfaces without restarting the crevice corrosion mechanism for TSA. Due to the crevice corrosion mechanism explained in Section 2.2, four different mechanisms are suggested to provide desired corrosion protection: (1) cathodic polarization, (2) buffering capacity, (3) ability to release an aggressive environment formed under the coating and (4) electric conductivity.

Steel can be galvanically protected against corrosion by metals that are ranged as less noble in the galvanic series. Zinc, aluminium and magnesium are all ranged as less noble metals compared to steel (St52) [12], and the coatings shall therefore contain particles of these metals. The Zn-, Al- and Mg-particles will then act as sacrificial elements for the steel if damage occurs. This effect presumes that the particles are in electrically contact with the steel. The particle content should therefore be high, to ensure a continuous path of particles in the coating layer.

The neutralizing effect is chosen for the ability to function as a buffer that neutralizes the pH below the repair coating. The acidic environment formed below the repair coating that leads to the rapid degradation of TSA, as stated in section 2.2, will then be reduced. Metal elements that form alkaline corrosion products may contribute to the buffering mechanism. Aluminium, zinc and magnesium are stable at different pH ranges. This will further be emphasized in section 2.4, 2.5 and 2.6. The formation of alkaline corrosion products will therefore vary between the different repair coatings depending on the anodic element.

The repair coat with reduced barrier effect may lead to increased diffusion of the electrolyte through the topcoat. The acidified environment developed below the topcoat during the crevice corrosion mechanism may then be reduced. Since the instability of aluminium oxide increase with decreasing pH towards 4, it is desirable if the pH below the topcoat is neutralized. The ability to release an aggressive environment formed under the coating will then lead to less acidity and decreased corrosion rate of the TSA. Coatings with open structures are chosen for contribution of this mechanism. If the topcoat is dense, blistering may occur due to corrosion of the TSA. This is the current problem for existing installations where TSA has been coated with an organic coating, and damage to the coating has occurred.

Low ionic resistance is also desirable in order to avoid crevice corrosion below the repair coat. If the ionic resistance is low, the ions will easier diffuse through the coating, rather than be trapped between the TSA layer and the repair coat. Coatings that are electrical conductive may contribute to transfer of the electrochemical reactions to the surface of the repair coating. Low electrical resistance will lead to increased electron conduction. The corrosion reactions will then be moved from the TSA, and the repair coating will hopefully corrode instead of the TSA.

2.4 Corrosion properties of aluminium in a TSA duplex coating

Aluminium is a passive metal that achieves corrosion resistance by an oxide film. An isolating oxide film forms immediately on the metal surface during exposure, which isolates the surface against aggressive environments [15]. The corrosion rate of aluminium outdoor is partly determined by humidity, the pH in rain and the exposure to chloride and SO_2. In situations where SO_2 is present, the oxidizing agents O_3 and H_2O_2 influence the atmospheric corrosion of aluminium [16]. During outdoor exposure of aluminium, a thin film of aluminium oxide (Al_2O_3) initially forms on the surface, which is covered by a thin film of boehmite and bayerite by further exposure [17]. Boehmite and bayerite are oxides formed at different temperatures and processes [18].

The oxide film grows by field-assisted ion diffusion [16]. The field weakens as the film thickness increases, and the growth will eventually stop. Reduction of the passive film occurs through dissolution, and liquid water is necessary for corrosion to occur. The local degradation is caused by the adsorption of chloride on the surface [16]. At high pH-values, aluminium is more affected by general corrosion, rather than pitting corrosion [16], but the corrosion behavior of aluminium and TSA cannot be compared due to different microstructures. Cross section pictures by electron probe micro analysis (EPMA) of a steel coated with TSA and a sealer revealed that TSA was generally degraded, rather than degraded by pitting or localized corrosion [1].

The corrosion rate of aluminium exposed in atmospheric environment varies whether CO_2 is present or not. The corrosion rate is higher for aluminium exposed to CO_2 free air, compared to air with ambient CO_2 levels [16]. The CO_2 level in the atmosphere is estimated to be 350 ppm. This effect is important related to various designs and conditions of exposure, e.g. that the CO_2 level is limited in crevices and below paint films. Blücher et al. suggested that high pH due to cathodic reduction of oxygen could cause rapid corrosion of aluminium exposed to humid CO_2 free air, in the presence of NaCl on the surface. The limited corrosion rate with CO_2 present was explained by the neutralizing effect on the hydroxide formed in the cathodic area [16].

As stated in section 2.2, aluminium chloride is unstable in humid environments below pH 4 [1]. Aluminium chloride is formed in chloride containing environments due to chloride migration towards the crevice. Hydrochloride acid forms after aluminium chloride reacts with water, and the pH of the electrolyte decreases [15]. As seen in Figure 2.3, solubility of the oxide film increases in acidic environment below pH 4 and alkaline environments above pH 9. Aluminium will therefore provide best corrosion protection in neutral environments [15].

Figure 2.3 presents the Pourbaix diagram for pure aluminium. The diagram presents the area for immunity (Al), active corrosion (Al^{3+} and AlO_2^-) and passivation of the metal ($Al_2O_3 \cdot 3H_2O$) relative to pH and potential vs. standard hydrogen electrode (SHE). Between the dashed lines (a) and (b) water stability is present. Water is reduced to hydrogen below (a) and oxidized to form oxygen gas above (b) [19]. The diagram shows that the protective oxide is stabile between approximately pH 4.5 and 9.5 [20]. Note that the diagram uses SHE as reference electrode, not silver/silver chloride (Ag/AgCl) electrode that is applicable for the experiments performed during this project. The potentials are therefore converted to potentials vs. Ag/AgCl, and not SHE as for Figure 2.3. The artificial seawater used for the laboratory work has a pH of approximately 8.2 before exposure. The boundary line between the immune and passive area for aluminium, at pH 8.2, is approximately -2200 mV vs. Ag/AgCl. The corresponding value at pH 4 is approximately -2000 mV vs. Ag/AgCl. The thermodynamic reduction potential for iron at 10^{-5} is approximately -787 mV [21]. This potential corresponds to the passive region at pH 8.2 and the active region at pH 4.
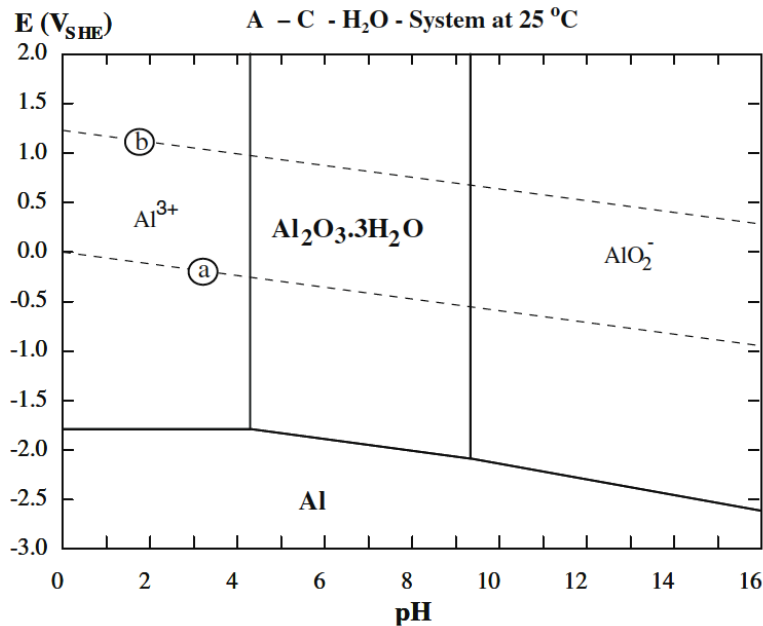
Figure 2.3: Pourbaix diagram of pure Al (Cl⁻ H₂O systems at 25°C) when 0.67 activity of Cl⁻ is present, equivalent to 1 M NaCl [20].

2.5 Corrosion properties of zinc in a TSA duplex coating

Thermally sprayed zinc (TSZ) has been applied on Norwegian road bridges in combination with organic coating since 1965. Some of the bridges are located in coastal areas and the coating thereby represents protection in highly corrosive environments. The overall experience reported for TSZ in combination with organic coating is good [1]. The divergence between TSA and TSZ in combination with organic coating occurs when the chlorides migrate and formation of zinc chloride ($ZnCl_2$) below the organic coating occurs. Zinc chloride is a relatively stable salt in water, and the environment will therefore not be acidified. Hydrochloride acid will not be formed under the organic coating, and the corrosion rate will therefore not accelerate due to lack of cathodic hydrogen evolution [1].

The atmospheric corrosion of zinc increases with the amount of chlorides present in the marine atmosphere. The relationship between corrosion rate and salinity or SO_2 concentration present in the atmosphere is relatively linear [22]. The NaCl-induced zinc corrosion, that may be compared to salt spray, is restrained if ambient CO_2 concentration is present [16]. Humidity and salt spray is likely to be present at the surface in marine environment. NaCl droplets and spreading of the electrolyte form a galvanic element between the droplet center (anodic region) and the droplet edge (cathodic region). The spreading effect of the droplet is influenced by the CO_2 concentration present in humid air. Ambient concentration of CO_2, 350 ppm, gives less spreading effect of the electrolyte compared to <5 ppm CO_2. The pH will also increase towards the periphery of the NaCl droplet [23].

Figure 2.4 presents the Pourbaix diagram for pure zinc. The diagram shows the area for immunity (Zn), active corrosion ($ZnCl^+$ and $HZnO_2^-$/ZnO_2^{2-}) and passivation of the metal (ZnO) relative to pH and potential vs. SHE. The diagram shows that zinc oxide (ZnO) is stable between approximately pH 8.5 and 10.5. The passive pH range is higher and more narrow compared to aluminium, see Figure 2.3.

However, the passive area for ZnO is located at alkaline pH values. The boundary line between the active and passive region at pH 8.2, is approximately -1120 mV vs. Ag/AgCl. Note that the potentials are converted to potentials vs. Ag/AgCl, and not SHE as for Figure 2.4. The conversion is done because an Ag/AgCl reference electrode was used during the experiments.
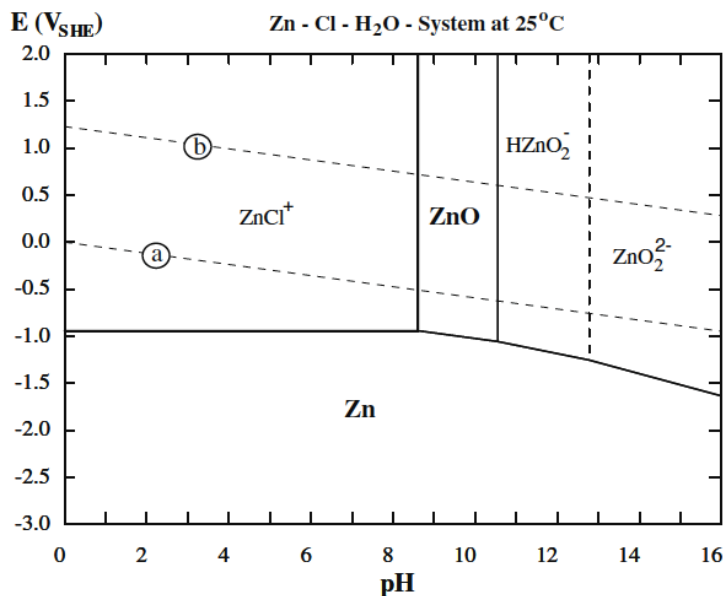
Figure 2.4: Pourbaix diagram of pure Zn (Cl⁻ H₂O systems at 25°C) when 0.67 activity of Cl⁻ is present, equivalent to 1 M NaCl [20].

Corrosion products such as simonkolleite ($Zn_5(OH)_8Cl_2 \cdot (H_2O)$), hydrozincite ($Zn_5(OH)_6(CO_3)_2$) and sodium carbonate ($Na_2CO_3$) are formed at ambient levels of CO_2 at 350 ppm. The sodium carbonate is preferably formed in the secondary spreading area and in the inner edge of the NaCl droplet. At lower values of CO_2, <5 ppm CO_2 and in the case of crevice corrosion, corrosion products such as simonkolleite ($Zn_5(OH)_8Cl_2 \cdot (H_2O)$) and zincite (ZnO) are observed [23]. This emphasized that the corrosion products formed during zinc corrosion is dependent on the environment and design of the structure. Another study of the corrosion products formed in the presence of CO_2 revealed traces of hydroxy carbonate ($Zn_4(CO_3(OH)_6 \cdot (H_2O))$) together with simonkolleite when pH decreased, due to the thermodynamically instability of zincite [24]. The thermodynamically stability of different zinc corrosion products is shown in Figure 2.5. A triple point is present approximately at chloride concentration $10^{-2.3}$ and pH 6.2.

Figure 2.5: Stability diagram in aerated aqueous solution with a zinc ionic species concentration of 0.1 M at 25°C [24].

2.6   Corrosion properties of magnesium in a TSA duplex coating

Similar to aluminium and zinc, magnesium is ranged below steel in the galvanic series, and will act as an sacrificial anode in electrical contact with steel [12]. Earlier studies have stated that the atmospheric corrosion of magnesium alters from exposure in solution with respect to the cathodic process. Water reduction will be the main cathodic reaction during solution exposure, while oxygen reductio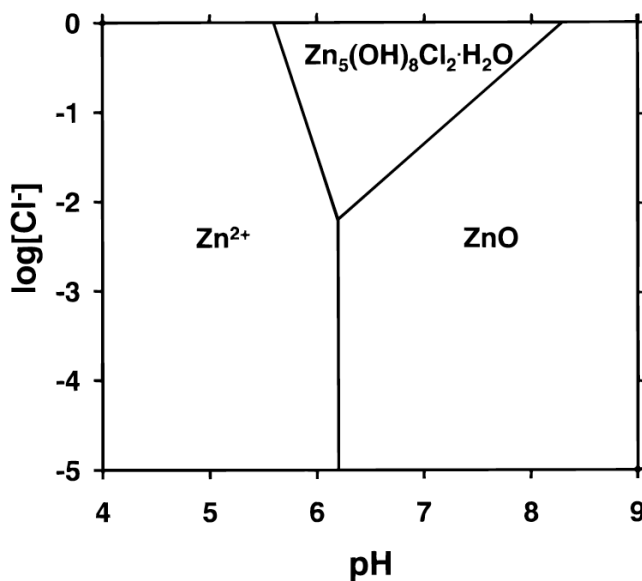n will occur during atmospheric corrosion with a thin layer of electrolyte. The anodic reaction may also be reduced below a thin layer of electrolyte, compared to in a bulk electrolyte. Further, the corrosion rate of magnesium alloys depends on the amount of NaCl present on the samples, and the corrosion rate increase with increasing relative humidity (RH) [25].

The protective oxide film formed during atmospheric exposure appears as a grey film on the surface [26]. Corrosion of magnesium is also dependent on the degree of CO_2 present, similar to aluminium and zinc. Godard et al. reported that the corrosion rate also decreased more rapidly with time when CO_2 was present [27]. Lindström et al. showed that the average corrosion rate of three magnesium alloys exposed in NaCl levels corresponding to marine environments were only 25% compared to when CO_2 was absent [27]. The appearance of the corrosion products altered also with different CO_2 levels. General corrosion with a thick uniform layer of hydrated magnesium hydroxyl carbonate appeared in the presence of CO_2. Pitting attack with brucite ($Mg(OH)_2$) as the dominant corrosion product occurred in the absence of CO_2. Formation of a soluble corrosion product layer containing carbonate with partly protective characteristics was suggested as a factor that reduced the corrosion rate in the presence of CO_2 [27]. Magnesium alloyed with calcium has revealed higher corrosion resistance, compared to alloys without calcium. The calcium may contribute to formation of a protective calcium carbonate layer, which is insoluble and adherent. Long exposure time and high pH, approximately 12, favor formation of the carbonate film. This carbonate film increases the corrosion protection and may be more stable compared to the $Mg(OH)_2$ film [28].

The Pourbaix diagram showing potential-pH for magnesium is presented in Figure 2.6. The diagram presents the area for immunity (Mg), active corrosion (Mg^{2+} and Mg^+) and passivation of the metal ($Mg(OH)_2$) relative to pH and potential vs. SHE [19]. The $Mg(OH)_2$ formation shows that magnesium can resist reasonably strong bases. A thick white precipitated film of $Mg(OH)_2$ form at pH 9, which contributes to relative corrosion protection between pH 8.5 and 11.5. Above pH 11.5 the passive $Mg(OH)_2$ film dominates the electrochemical behavior of Mg [26]. The boundary line between the immune and passive region, at pH 8.2, is approximately -2800 mV vs. Ag/AgCl at 10^{-6}. This potential is clearly more negative compared to aluminium and zinc, see Figure 2.3 and Figure 2.4. Note that the potentials are converted to potentials vs. Ag/AgCl, and not SHE as for Figure 2.4. The conversion is done because an Ag/AgCl reference electrode was used during the experiments.

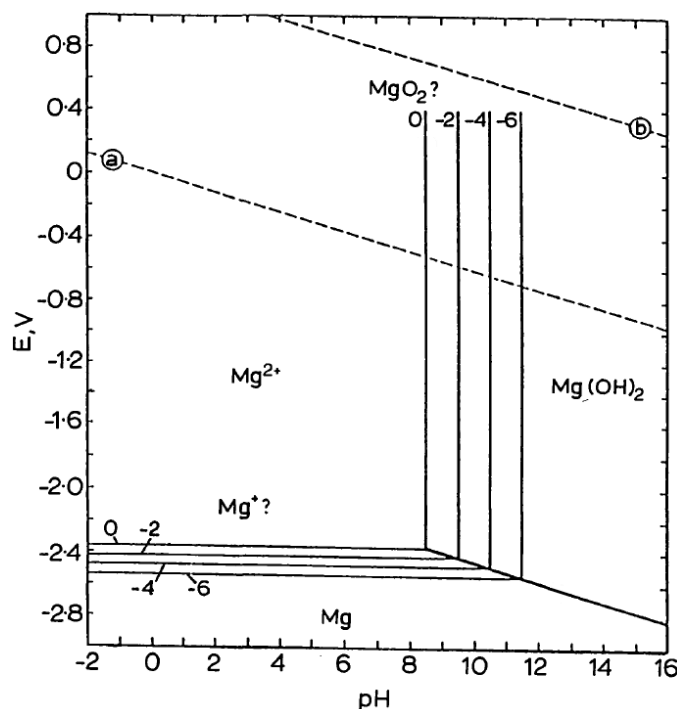Figure 2.6: Pourbaix diagram vs. SHE for magnesium-water system at 25°C showing the phase equilibrium [19].

Earlier studies has revealed brucite ($Mg(OH)_2$) as the outer layer of the corrosion products. As seen in Figure 2.6, brucite is formed at alkaline pH values. OH^- ions are formed during magnesium dissolution, from the cathodic reaction, which leads to increased pH and formation of the magnesium hydroxide layer [29].

3   Experimental Work

Several experiments have been conducted to investigate the corrosion behavior of different repair coatings for TSA. Information regarding the different repair coatings and presentation of the different experiments will be presented in this chapter. Risk assessment of the experimental work is presented in Appendix G.

3.1   Test objects

Steel samples (St52) were grit blasted to Sa 2 ½ before TSA was applied on the steel substrate. Reinertsen AS carried out the surface preparation and the TSA application. The TSA layer had a minimum, maximum and average coating thickness of respectively 190 μm, 270 μm and 230 μm. Various repair coatings, which are presented in Section 3.1.1, were then applied.

3.1.1   Coating specifications

Eight repair coatings were applied as a topcoat with different thicknesses. The high Zn primer, Zn epoxy, modified Zn epoxy and Zn silicate were tested with average dry film thickness (DFT) 50 μm, 100 μm and 150 μm. The MgO silicate, Mg silicate, Al silicate and inorganic copolymer coating were tested with one thickness each. See Table 3.1 for the coating properties of the actual repair coatings.

- The high Zn primer is a single-component coating with a zinc content of 96 wt%. The coating provides excellent UV resistance, according to the producer, and act as anode in relation to corrosion protection. In atmospheric environments, the coating is temperature resistance in the range of -40°C to 120°C, with peaks up to 150°C. In immersed condition the coating is resistant in the pH range of 5.5-9.5, while the range widens to 3.5-12.5 in atmospheric condition.

- The Zn epoxy is a two-component zinc rich primer, which contributes to very good corrosion protection as part of a complete coating system, according to the producer. The coating contain high amount of zinc dust and both components are fluent.

- Modified Zn epoxy is also a two-component zinc rich primer. Hollow glass spheres and an activator are added to activate more zinc. This may increase the protection properties, according to the producer.

- The Zn silicate is a two-component inorganic zinc rich primer. The coating is a moisture-cured inorganic zinc ethyl coating that cures fast and provides excellent corrosion resistant, according to the producer. Relative humidity above 50% is required during the curing process. The coating consists of a mixture of binder and primarily zinc powder. Experimental silicate

coatings were prepared, where the zinc powder was exchanged with Al-, Mg- and MgO-particles. The same binder was used as for the Zn silicate.

- The inorganic copolymer coating is a single-component coating pigmented with MIO (micaceous iron oxide). The coating forms an inert polymer matrix after curing that is able to resist temperatures up to 650°C. The coating is especially developed to prevent corrosion under insulation, and can operate in the service temperature range from -196°C to 650°C, according to the producer.

Table 3.1: Coating specifications for the various repair coatings. Footnotes are given at the next page.

Coating	High Zn primer	Zn epoxy	Zn-, Al-, Mg-, MgO-silicate	Modified Zn epoxy	Inorganic copolymer coating
Labeling	Z	ZE	Z, Al, Mg, MgO	H	V
Type	Single-component	Two-component	Two-component	Two-component	Single-component
Approximately DFT [μm]	50 100 150	50 100 150	Zn: 50, 100, 150 MgO: 100 Mg: 200 Al: 150	50 100 150	150
Solid content (by volume)	58 ± 2%	53 ± 2%	67 ± 2% [1]	65 ± 1%	74± 1%
Induction time [2]	-	30 min (23°C)	-	-	-
Pot life	-	24 hours (23°C)	8 hours	4 hours	-
Dry to touch	15 min (20°C)	10 min (23°C)	15 min (23°C)	10 min (20°C)	45 min (20°C)
Dry to over coat	1 hour (20°C)	1.5 hours (23°C)	4 hours (23°C)	1.5 hours (20°C)	Min: 6 hours (20°C) Max: 7 days (20°C)
Fully cured	2 days (20°C)	5 days (23°C)	4 hours (23°C)	7 days (20°C)	-

[1] MgO silicate was mixed with approximately 17 vol% additional binder compared to Zn-, Mg- and Al-silicate, and the number stated is therefore not applicable for the MgO silicate.

[2] Induction time corresponds to the time when the coating components react to obtain correct viscosity, flow and curing properties according to Undrum, H (email, 26.05.2016).

The coatings were applied with brush directly on the TSA substrate. A wet film thickness gauge was used to estimate the coating thickness before curing. Elcometer Microprocessor Measuring System was used to measure the dry film thickness after curing. The same measuring pattern was performed on each sample. Six measurements were taken along each side of the rectangular sample, while five measurements were taken in a straight line along the center.

An overview of the test samples with lowest, highest and mean dry film thickness is presented in Appendix A. Standard deviation and the total number of measurements conducted for each sample are also included. Five parallels were coated for each repair coating. Parallel X.1-X.3 were tested in the cyclic coating test, parallel X.4 for the electrochemical impedance spectroscopy (EIS) and open circuit potential (OCP) measurements and parallel X.5 for the crevice corrosion tests.

3.2 Electrical resistance

After the repair coatings were applied, the electrical resistance was measured. The rear side of the samples remained uncoated to obtain electrical contact during the measuring. A copper piece was pressed towards the coated side with a screw clamp, and P.A.T. Precision Adhesion Test equipment measured the pressure. A constant pressure of 200 psi was applied and the electrical resistance was measured with a multimeter. One measurement was conducted for each coating thickness. See Figure 3.1 for the test equipment and the setup. The measurements were performed according to MIL-DTL-81706B, Detail Specification: Chemical conversion materials for coating aluminum and aluminum alloys.
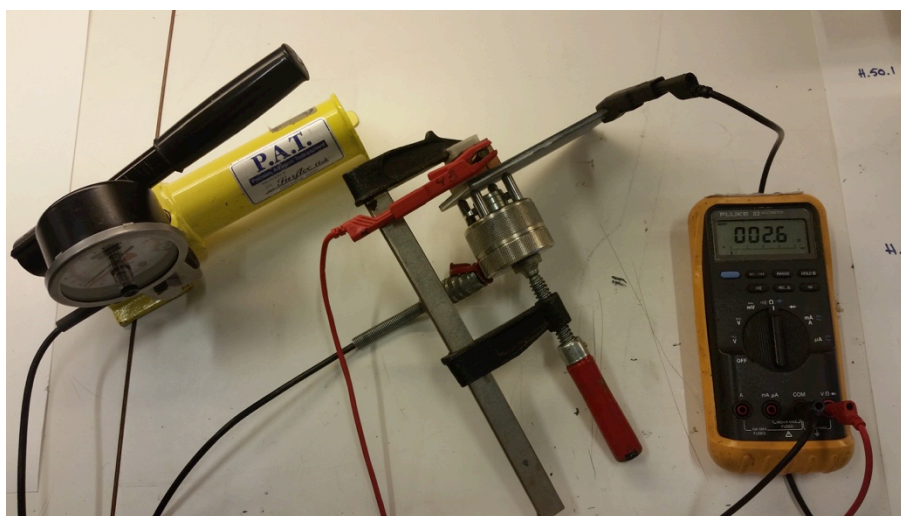

Figure 3.1: Electrical resistance setup with P.A.T Precision Adhesion, multimeter and the copper piece pressed towards the sample.

3.3 Cyclic coating test

A coating test was performed according to ISO 20340 [30] with three different exposures repeated in a defined cycle. The test is an accelerating test for offshore exposure, and the corrosion behavior for the various coatings was evaluated. After the repair coatings presented in Section 3.1.1 were applied, a scribe was machined down to the steel substrate to simulate damage in the coatings. The dimension of the scribe was 50 mm x 2 mm, located 40 mm vertically from the short side of the sample. After the scribe was machined, the rear side was coated with high Zn primer and the edges were coated with modified Zn epoxy. The coating layer on the rear side and edges had to cover the surfaces sufficiently in order to avoid corrosion in these areas. Three parallels were coated for each coating thickness.

The cycle began with automatic alternation every 4th hour between UV light and condensation according to ISO 11507:2007. The UV light held a temperature of 60°C and the condensation a temperature of 50°C. This cycle lasted for 72 hours. The samples were then exposed to constant salt fog for 72 hours at 30°C in a salt fog chamber. Electrolyte consisting of distilled water and 5 wt% NaCl (pH 7) was regularly refilled to ensure constant spray. The salt spray pressure was set to 0.8 bar, while the output was set to approximately 350 cm^3/h. Finally, the samples were exposed in a freezer for 24 hours at -20°C.

After the test was completed, the samples were examined visually and the coating cross sections were investigated in Olympus GX15 Metallurgical Microscope. The samples were machined by Discotom-2, casted in EpoFix resin and grinded to SiC #2400 or #4000 with Struers Rotopol-31 before the light microscope investigations. Element analysis by Triple Quadropol (QQQ) inductively coupled plasma mass spectroscopy (ICP-MS) was carried out by SINTEF, to determine the main elements in the corrosion products. The corrosion products were dissolves in concentrated HCl and HNO$_3$ in an ultrasonic cleanser at 60°C for 2 hours. Elements such as ^{45}Sc, ^{89}Y and ^{115}In were added and all samples were quantified against standards from Inorganic Ventures. Finally, the TSA corrosion creep (M) was calculated (6) based on the average corrosion creep from 11 points (C), 5 mm apart. See Figure 3.2 for the corrosion creep on both sides of the scribe. The width of the scribe (W) was 2 mm.
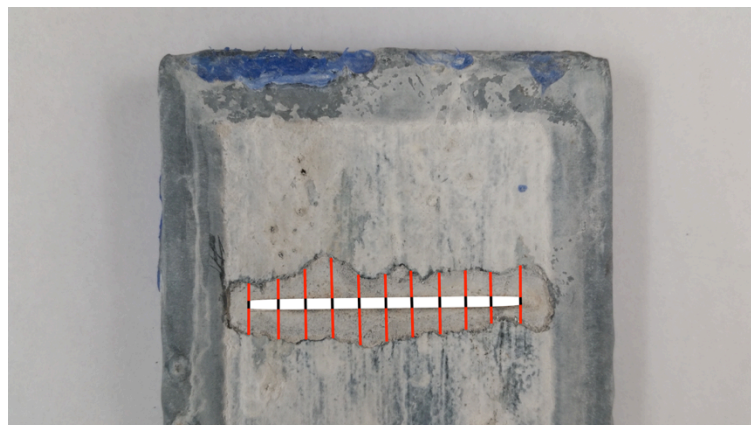
$$M = \frac{C - W}{2} \tag{6}$$

Figure 3.2: Corrosion creep marked in red around the scribe at 11 points, 5 mm apart.

3.4 Electrochemical impedance/Open circuit potential

Electrochemical impedance and open circuit potential were measured during continuous immersion in artificial seawater. Coating structure and adhesion, barrier properties and corrosion protection for the different repair coatings were investigated. Initiation and progression of the corrosion process below the repair coatings were also investigated. A DFT of 100 μm was tested for the zinc containing coatings, while the MgO-, Mg-, Al-silicate and the inorganic copolymer coatings were tested with DFT of respectively 100 μm, 200 μm, 150 μm and 150 μm. The samples were attached to an electrochemical multi-cell, with a circular surface area of 1886 mm^2 exposed for each sample. Six samples were attached to each cell. The rear side and the edges of the samples were not coated.

The samples (working electrode), the Ag/AgCl reference electrode and the platinum counter electrode were connected to a potentiostat. The samples mounted on the same multi-cell shared one reference and one counter electrode. Each sample was connected to a Gamry Instrument, Interface 1000 Potentiostat, during the impedance measurements. The initial and final frequencies were set to 10 x 10^4 Hz and 0.001 Hz. The number of points within one decade of frequency was set to 5. The amplitude of the AC signal was set to 10 root mean square (rms) mV, and a constant potential of -1200 mV vs. Eref was applied during the logging. In addition to the mentioned values, the exposed surface area was set to 1886 mm^2. The test setup for one sample is presented in Figure 3.3.
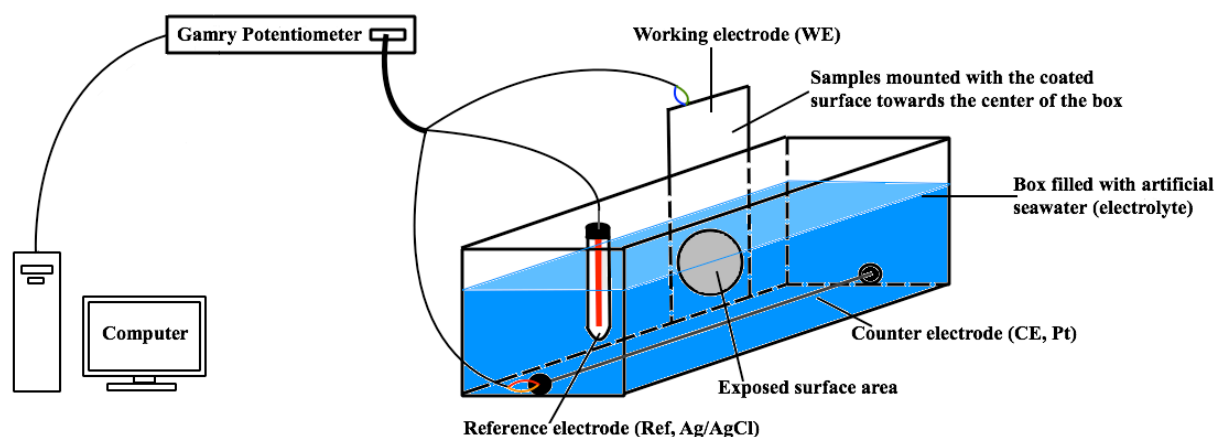
Figure 3.3: Test setup for the electrochemical impedance test with mounted sample (working electrode). A reference electrode is located in the filled multi-cell (to the left) and the counter electrode is connected along the bottom of the multi-cell. The reference, counter and working electrode are connected in a circuit through a Gamry Potentiostat.

OCP vs. Ag/AgCl was manually measured for each sample. The number of measurements decreased with increasing immersion time for the zinc containing coatings. Due to more instability, the MgO-, Mg-, Al-silicate and inorganic copolymer coating were measured every weekday throughout the test.

Cross sections were taken from the samples by Discotom-2, casted in EpoFix resin and grinded to SiC #2400 or #4000 with Struers Rotopol-31 after test completion. Olympus GX15 Metallurgical Microscope was used to investigate the coating cross sections. Energy-dispersive spectroscopy (EDS) analysis by scanning electron microscope (SEM) were carried out on the exposed surface areas to determine the main elements present. SEM parameters are presented in Table 3.2. 12 areas were basis

for the average normalized concentration and the MgO silicate was coated with carbon before the examination due to lack of conductivity. The inorganic copolymer coating was not investigated in SEM due to no active particles, and because the corrosion products were assumed to originate from the TSA.

Table 3.2: SEM parameters used during the EDS analysis.

SEM parameters	
Aperture	60.00 μm
Magnification	500X (495X for the MgO silicate)
Voltage	15.0 kV
Working distance	From 8.4-12.2 mm

3.5 Crevice corrosion test

Two different test setups were investigated to simulate a crevice corrosion situation for the repair coatings. The setups are presented in section 3.5.1 and 3.5.2. These tests were performed as a short-term test to investigate the TSA duplex corrosion mechanism for the various coatings.

3.5.1 Test setup 1

The samples were machined to squares of 30 mm x 30 mm and the repair coatings presented in 3.1.1 were applied on one side. A centered scribe of 20 mm x 2 mm was machined down to the steel on the side with repair coating. A steel wire with shrink sleeve was attached to each sample and silicone sealed the connection. A two-component epoxy coating was applied at the rear side and on the edges of all samples. One sample with TSA without additional repair coating was tested, and the two-component epoxy coating was then applied on both sides (around the scribe) and on the edges. See Figure 3.4 for the sample geometry. The epoxy coating cured for 2 days at 40°C before the samples were continuously immersed in artificial seawater.

Figure 3.4: Sample geometry of the TSA coated with epoxy. Silicone around the steel wire connection was not yet applied, and is therefore not present in the figure.

Figure 3.5 illustrates the test setup for one sample. Each sample (working electrode) was attached to an Ag/AgCl reference electrode and a platinum counter electrode. The electrodes and the samples were connected to a potentiostat, and a potential of -700 mV was applied to initiate corrosion reactions and to simulate the polarization of the TSA by steel in the field. The boundary line between active and immune region for iron at 10^{-5}, at pH 8.2, is located approximately at -787 mV vs. Ag/AgCl [21], and a potential in the active area was chosen. Anodic current to each individual sample was logged as potential drop over a 1 Ω resistor. The samples and the counter electrode were placed in a container filled with artificial seawater, while the reference electrode was placed in a container filled with saturated KCl. A salt bridge connected the two containers. The test was run for 14 days.
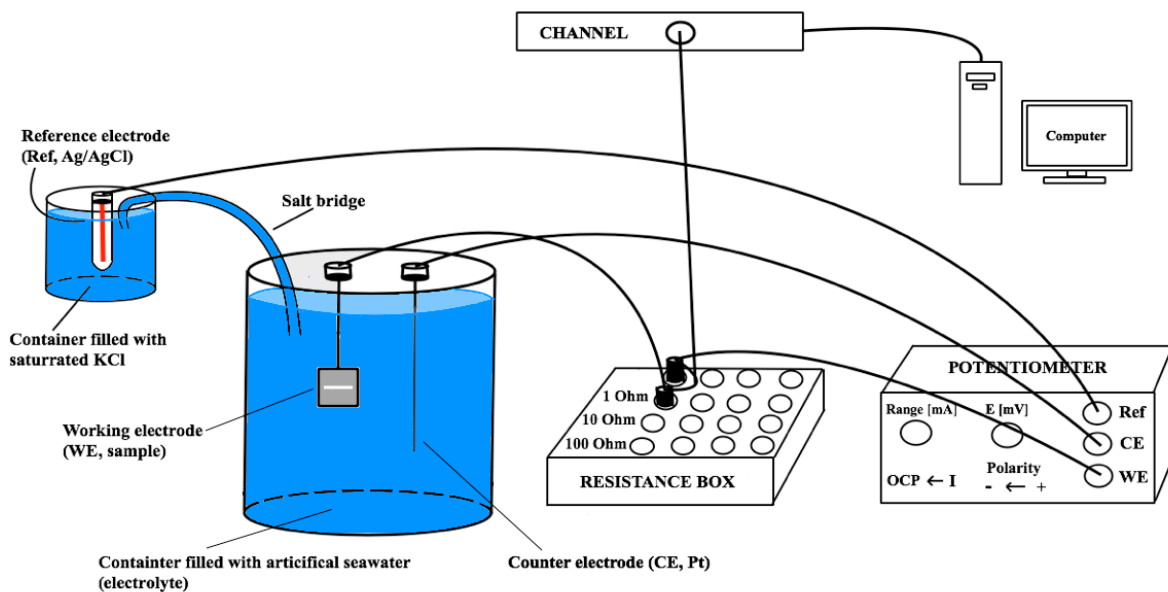
Figure 3.5: Test setup for the crevice corrosion test with sample (working electrode) and counter electrode (Pt) immersed in artificial seawater. The Ag/AgCl electrode (reference electrode) was immersed in a separate container filled with saturated KCl. The three electrodes were connected in a circuit by a potentiometer and a resistance box at 1 Ω.

3.5.2   Test setup 2

The samples were machined to squares of 30 mm x 30 mm, with a centered hole of 7 mm diameter. The repair coatings presented in Section 3.1.1 were applied on one side. A steel wire with shrink sleeve was attached to each sample and silicone sealed the connection. A two-component epoxy coating was applied at the rear side, inside the centered hole and halfway up on the edges starting from the rear side. One sample with TSA without repair coating was also tested and the two-component epoxy coating was applied at both sides, in addition to inside the centered hole and halfway up on the edges starting from the rear side. The epoxy coating cured for 2 days at 40°C. After curing, a crevice former was attached to the repair coating surface. Silicone was applied around the bolt on both sides of the sample to ensure no penetration of electrolyte. See Figure 3.6 for the arrangement of the crevice former. The nut was tightened with 2 Nm. The samples were then continuously immersed in artificial seawater.
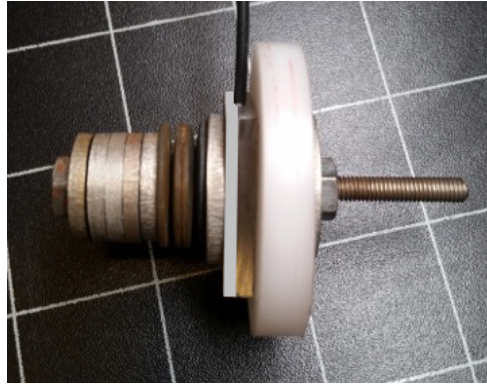
Figure 3.6: Sample attached to a crevice former (white disc) with repair coating towards the crevice former. The epoxy (light grey coating) was applied on the rear side and halfway up on the sides starting from the rear side. Silicone around the steel wire connection was not yet applied, and is therefore not present in the figure.

The test arrangement was equal to the setup shown in Figure 3.5, except for the sample design shown in Figure 3.6 and that a potential of -780 mV was applied. The boundary line between immune and active area for iron at 10^{-5}, at pH 8.2, is located approximately at -787 mV vs. Ag/AgCl [21]. A potential of -780 mV was therefore chosen to avoid corrosion of the steel, and rather initiate corrosion of the TSA or repair coating. Anodic current to each individual sample was logged as potential drop over a 1 Ω resistor. The test was run twice with test periods of respectively 16 days and 30 days.

After exposure of the two test setups, the samples were machined by Discotom-2 and casted in EpoFix resin. Grinding of the samples was conducted to SiC #2400 or #4000 with Struers Rotopol-31. The cross section of the coating layers was then investigated in Olympus GX15 Metallurgical Microscope.

4 Results

Results obtained from the experiments presented in Section 3 will be presented in this chapter. Corrosion of the TSA will be emphasized, since the repair coatings shall provide corrosion protection without triggering the TSA crevice corrosion mechanism.

4.1 Electrical resistance

The electrical resistance was measured for the various repair coatings, see Table 4.1 for an overview of the measured values. One measurement was taken for each coating thickness. Measurements were not conducted for the inorganic copolymer coating due to lack of active pigments. The electrical resistance increased with increasing coating thickness, except for the high Zn primer that showed a constant value.

Table 4.1 Electrical resistance for the different repair coatings relative to coating thickness.

Repair coating	Electrical resistance			
	50 μm	100 μm	150 μm	200 μm
High Zn primer	0.2 Ω	0.2 Ω	0.2 Ω	-
Zn epoxy	0.6 Ω	516 Ω	4200 Ω	-
Modified Zn epoxy	0.2 Ω	0.6 Ω	1.3 Ω	-
Zn silicate	0.3 Ω	1370 Ω	8400 Ω	-
MgO silicate	-	0.2 Ω	-	-
Mg silicate	-	-	-	8.75×10^8 Ω
Al silicate	-	-	OL *	-

* OL = overload condition detected.

4.2 Cyclic coating test

The samples were exposed for 20 cycles according to ISO 20340. The zinc based repair coatings were tested with three different coating thicknesses, respectively 50 μm, 100 μm and 150 μm. The Al-, MgO-, Mg-silicate and the inorganic copolymer coating were tested with one thickness, see Table 3.1. Visual assessment, calculation of average corrosion creep, cross section investigation of the coating layers and element analysis of the corrosion products were performed after the test was completed. An overview of the cycles is presented in Appendix B, in addition to pictures of the samples after 20 cycles of exposure and detailed element analysis of the corrosion products.

4.2.1 Visual assessment after exposure

Table 4.2 presents the visual assessments after exposure. The visual assessment is based on a general evaluation of all three parallels. The cycle when the blistering occurred is stated in the column "*Blistering*". The Zn epoxy showed the highest amount of blistering and the blisters occurred first for this coating. The silicate coatings did not reveal blistering, and the overall impression after exposure was smooth surfaces.

Table 4.2: Visual assessment of the different repair coatings after 20 cycles of exposure.

Repair coating	Visual appearance	Blistering
High Zn primer	• Blistering on DFT 50 μm. • Topcoat cracked near the scribe on DFT 150 μm and 100 μm. Less cracking on DFT 50 μm. • Some small areas where the topcoat had corroded.	Yes *
Zn epoxy	• Blistering and cracking of the topcoat near the scribe on all coating thicknesses. • Large amount of white corrosion products on all samples.	Yes (cycle 4)
Modified Zn epoxy	• Blistering near the scribe on all thicknesses. More blisters on DFT 100 μm and 50 μm, compared to 150 μm. • Topcoat cracked near the scribe on DFT 150 μm. • Less comprehensive blistering compared to the other coatings with blistering. • Large amount of white corrosion products on the entire surface.	Yes (cycle 13)
Zn silicate	• No indication of blistering. • White corrosion products formed on the surfaces.	No
MgO silicate	• No indication of blistering. • The MgO silicate cracked (mud cracking), but white corrosion products sealed the cracks.	No
Mg silicate	• No indication of blistering. • Smooth surfaces, even with a thin layer of white corrosion product on the surfaces.	No
Al silicate	• No indication of blistering. • Some roughness on the surfaces.	No
Inorganic copolymer coating	• Blistering near the scribe. • Some white corrosion products, assumed to be aluminium, filled the scribes.	Yes (cycle 5)

* Due to large amount of white corrosion products covering the surface, it was difficult to state the exact cycle when the blistering occurred. The blistering was discovered after the test was completed.

Only examples of the different types of damage found on the samples are shown in this section. Images of all the samples with blistering are presented in Appendix B, Section B.3. The amount of blistering or cracking of the repair coating near the scribe varied for the different samples. The blistering was concentrated around the scribe, as for the high Zn primer DFT 150 μm in Figure 4.1. The blistering is marked with red circles.

Figure 4.1: Blistering near the scribe on the high Zn primer DFT 50 μm. The picture is taken after 20 cycles of exposure.

Blistering on the Zn epoxy DFT 150 μm was seen after 4 cycles of exposure. Some blisters transformed to cracks of the repair coating after further exposure. This occurred due to increased amount of corrosion products from the TSA formed below the repair coating. The cracks were concentrated around the scribe and are shown in Figure 4.2.

Figure 4.2: Blistering and cracking of the topcoat near the scribe on the Zn epoxy DFT 150 μm. The picture is taken after 20 cycles of exposure.

The inorganic copolymer coating was tested with a coating thickness of 150 μm and showed blistering after 5 cycles of exposure. The blistering occurred around the scribe, and the amount of blistering increased with increasing exposure time. No cracks in the repair coating were seen even though the first blister occurred only after 5 cycles, and a total exposure of 20 cycles was performed. Figure 4.3 presents the sample after 5 cycles (a) and 20 cycles (b) of exposure.

| (a) After 5 cycles | (b) After 20 cycles |
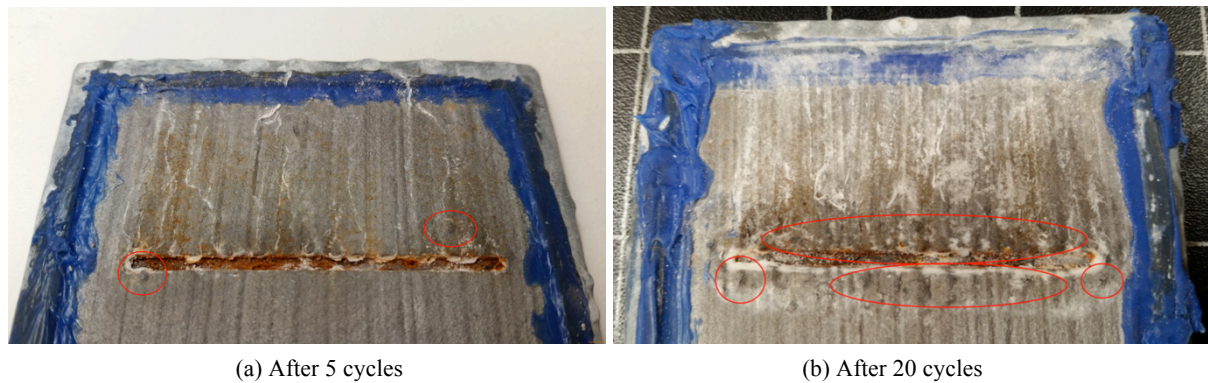
Figure 4.3: Blistering near the scribe on the inorganic copolymer coating after 5 cycles (a) and 20 cycles (b) of exposure.

4.2.2 Corrosion creep on TSA

The average corrosion creep for the samples is shown in Figure 4.4. Two parallels were evaluated per sample and the average value of 22 measurements (11 measurement for each parallel) is shown in this section. The equation used for calculation is shown in Section 3.3. The standard deviation for each sample is also marked in Figure 4.4.

Highest amount of corrosion creep on the TSA was seen for the Zn epoxy (ZE), followed by the inorganic copolymer coating (V), the high Zn primer (Z) and the modified Zn epoxy (H). The silicate coatings revealed very low degree of corrosion creep, except for the Zn silicate (ZS) with approximately corrosion creep of 0.6 mm. Complete overview of the measurements taken is presented in Appendix B, Section B.4. The numbers stated after the labeling indicates the average DFT.
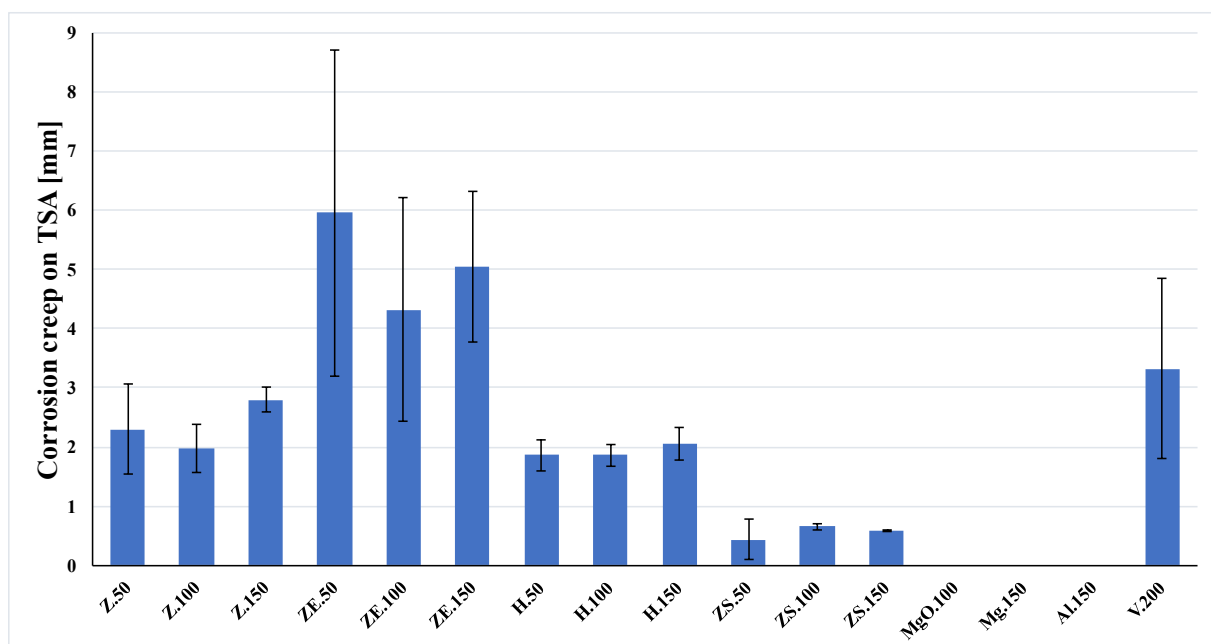
Figure 4.4: Average corrosion creep on TSA for each sample with standard deviations included in the graph. The following labeling is used for the various repair coatings (starting from the left): high Zn primer (Z), Zn epoxy (ZE), modified Zn epoxy (H), Zn silicate (ZS), MgO silicate (MgO), Mg silicate (Mg), Al silicate (Al) and the inorganic copolymer coating (V).

4.2.3 Corrosion morphology under the repair coatings

Light microscope images of the cross sections are presented from Figure 4.5 to Figure 4.21. All images contain a steel substrate coated with TSA and a topcoat of the current repair coat. The samples were machined vertically through the scribe, and both sides of the scribe were evaluated. In case of small differences, only one side is presented. The Zn silicate DFT 150 μm are presented on both sides of the scribe due to different amount of TSA corrosion. The numbers stated in the parentheses below the images indicate the orientation related to the crevice opening. Note that the order of the numbers varies between the different coatings. The DFT of each sample is stated in the images.

High Zn primer

Figure 4.5 shows that both the repair coating and the TSA had corroded approximately 3.6 mm into the crevice. Total reduction of the TSA can be seen in image (1) and (2), and partly in image (3). Some of the dark areas on the TSA layer are air bobbles present in the epoxy resin. In image (4), some zinc particles is seen in the repair coating.

(1)   (2)   (3)

(4)   (5)
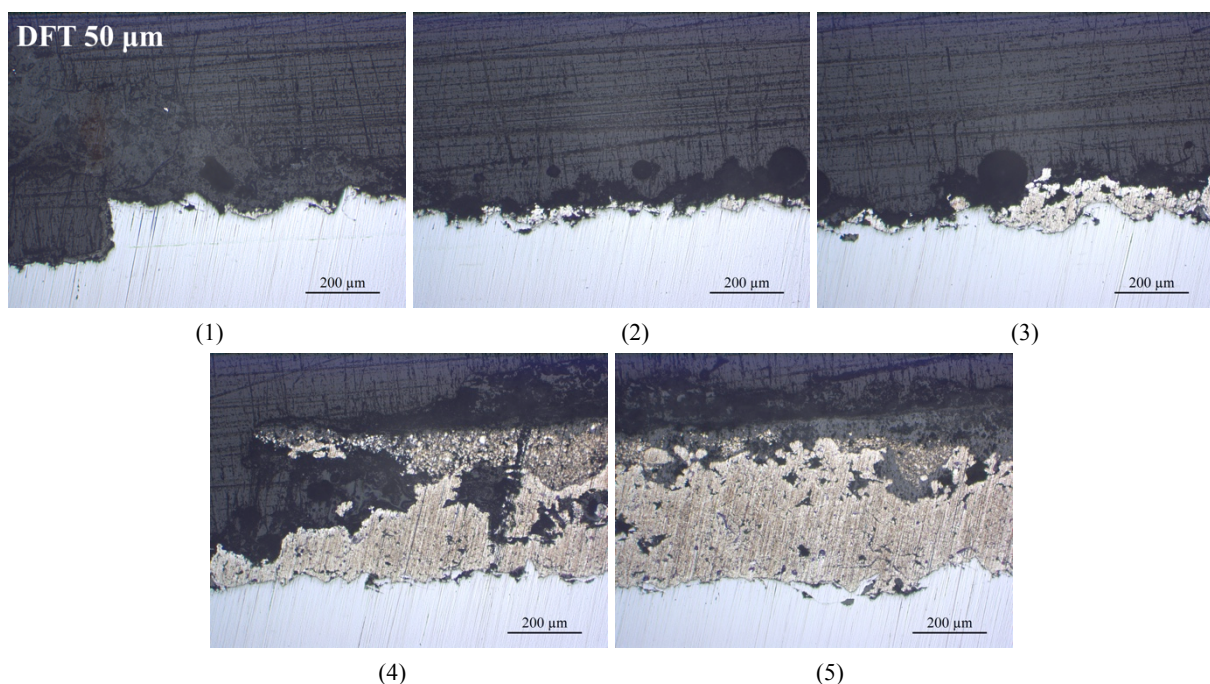
Figure 4.5: Light microscope images of the high Zn primer DFT 50 μm at the crevice opening (1) and further into the crevice (5). Combined corrosion creep and flaking had occurred approximately 3.6 mm into the crevice.

Figure 4.6 reveals both continuous TSA corrosion approximately 1.4 mm into the crevice and some reduction of the repair coating. However, the reduction of the zinc is greatest at the crevice opening. Some combined corrosion of both the TSA and the high Zn primer can be seen in images (3) from 1.5 mm to 2.3 mm for the DFT 100 μm. Continuous corrosion of the TSA can be seen approximately 2.2 mm into the crevice in Figure 4.7 for the DFT 150 μm.

(3)　　　　　　　　　　　(2)　　　　　　　　　　　(1)

Figure 4.6: Light microscope images of the high Zn primer DFT 100 μm at the crevice opening (1) and further into the crevice (3). Corrosion creep of approximately 1.4 mm had occurred from the crevice opening.

(3)　　　　　　　　　　　(2)　　　　　　　　　　　(1)

Figure 4.7: Light microscope images of the high Zn primer DFT 150 μm at the crevice opening (1) and further into the crevice (3). Corrosion creep of approximately 2.2 mm had occurred into the crevice.

Zn epoxy

Figure 4.8 reveals high amount of continuous TSA corrosion approximately 6.1 mm into the crevice, in addition to reduction of the zinc particles.

(3)　　　　　　　　　　　(2)　　　　　　　　　　　(1)

(6)　　　　　　　　　　　(5)　　　　　　　　　　　(4)

Figure 4.8: Light microscope images of the Zn epoxy DFT 50 μm at the crevice opening (1) and further into the crevice (6). Corrosion creep of approximately 6.1 mm had occurred into the crevice.

Corrosion products from the TSA had clearly cracked the repair coating on the DFT 100 μm and 150 μm, see Table 4.2. See Figure 4.9 and Figure 4.10 for the corrosion morphology. Continuous corrosion creep was seen respectively 7.8 mm and 7.5 mm into the crevice. The cracking appeared as lifting of the repair coating in the images.

(3)   (2)   (1)

(5)   (4)

Figure 4.9: Light microscope images of the Zn epoxy DFT 100 μm at the crevice opening (1) and further into the crevice (5). Corrosion creep of approximately 7.8 mm had occurred into the crevice.

(3)   (2)   (1)

(5)   (4)
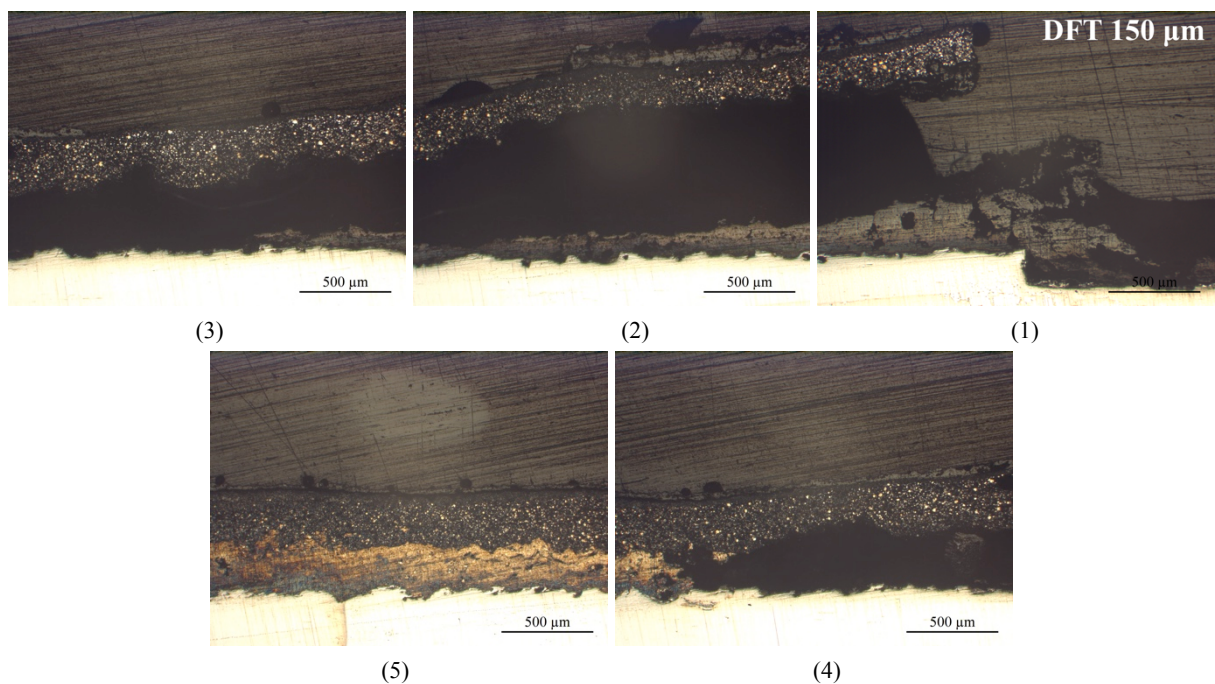
Figure 4.10: Light microscope images of the Zn epoxy DFT 150 μm at the crevice opening (1) and further into the crevice (5). Corrosion creep of approximately 7.5 mm had occurred into the crevice.

Modified Zn epoxy

Continuous corrosion of the TSA can be seen for approximately 2.2 mm in Figure 4.11, for 2.3 mm in Figure 4.12 and for 2.0 mm in Figure 4.12. Some intact zinc particles can be seen in the repair coatings for all coating thicknesses, in addition to the glass spheres. Smallest amount of TSA corrosion can be seen for the DFT 150 μm.

(1) (2) (3)
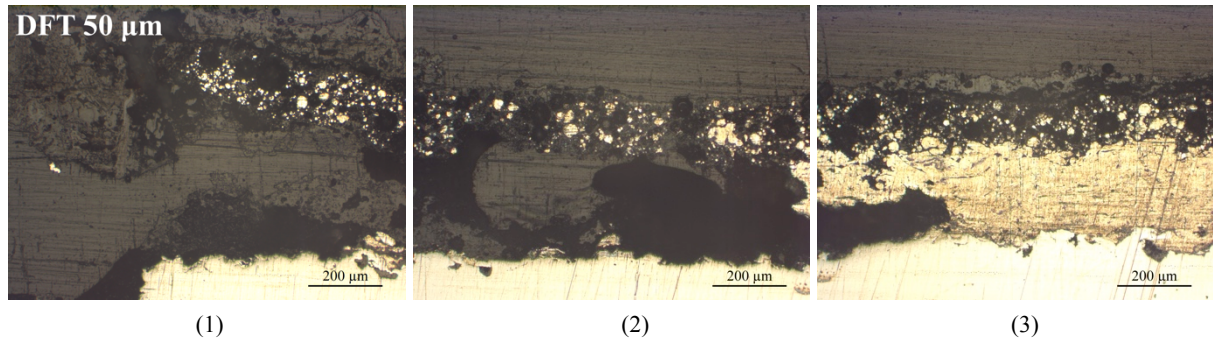
Figure 4.11: Light microscope images of the modified Zn epoxy DFT 50 μm at the crevice opening (1) and further into the crevice (3). Corrosion creep of approximately 2.2 mm had occurred into the crevice.

(1) (2) (3)
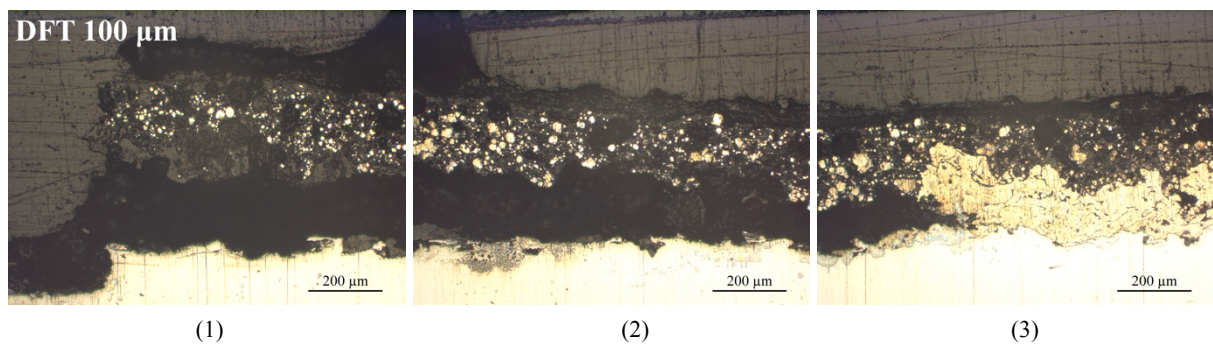
Figure 4.12: Light microscope images of the modified Zn epoxy DFT 100 μm at the crevice opening (1) and further into the crevice (3). Corrosion creep of approximately 2.3 mm had occurred into the crevice.
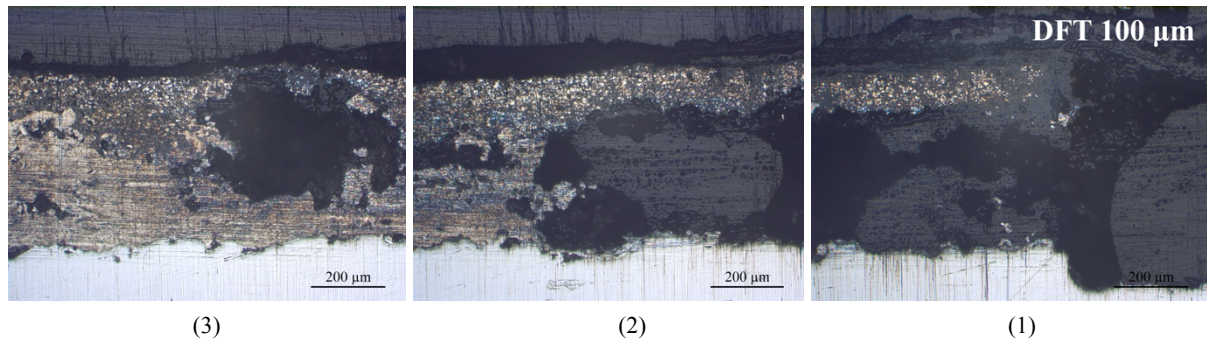

(1) (2) (3)
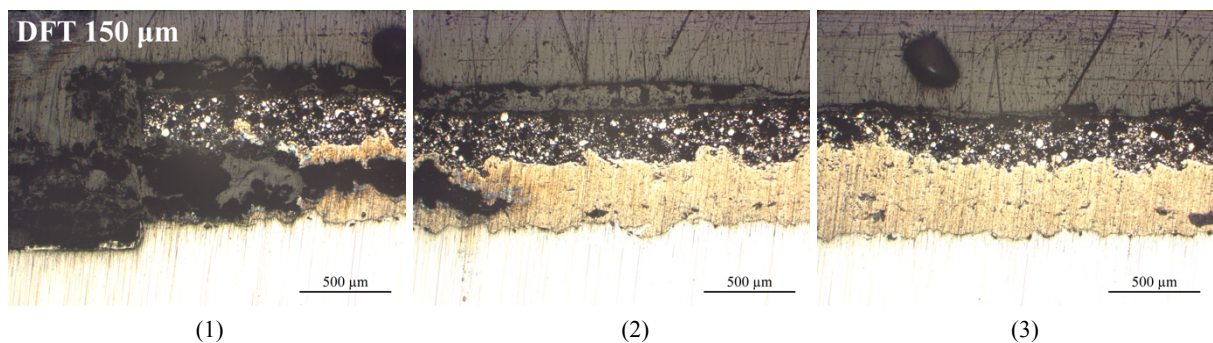
Figure 4.13: Light microscope images of the modified Zn epoxy DFT 150 μm at the crevice opening (1) and further into the crevice (3). Corrosion creep of approximately 2.0 mm had occurred into the crevice.

Zn silicate
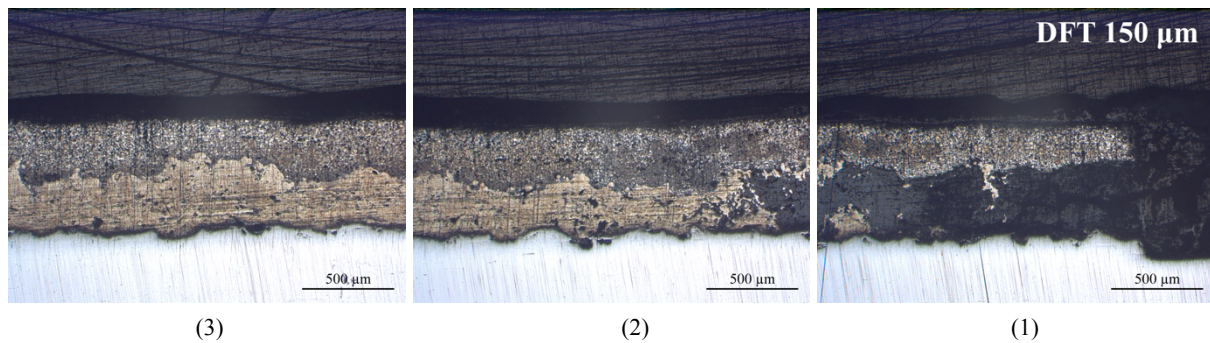
TSA corrosion can be seen at the crevice opening for DFT 50 µm in Figure 4.14 and 100 µm in Figure 4.15. Figure 4.16 presents DFT 150 µm (1) with only sporadic TSA corrosion. Figure 4.17 presents continuous corrosion of the TSA approximately 2.6 mm into the crevice for DFT 150 µm (2). Small amount of reduced zinc particles can be seen for DFT 50 µm and 150 µm. Highest amount of reduced zinc particles was seen for the DFT 100 µm and side 2 of the DFT 150 µm.

| (1) | (2) | (3) |
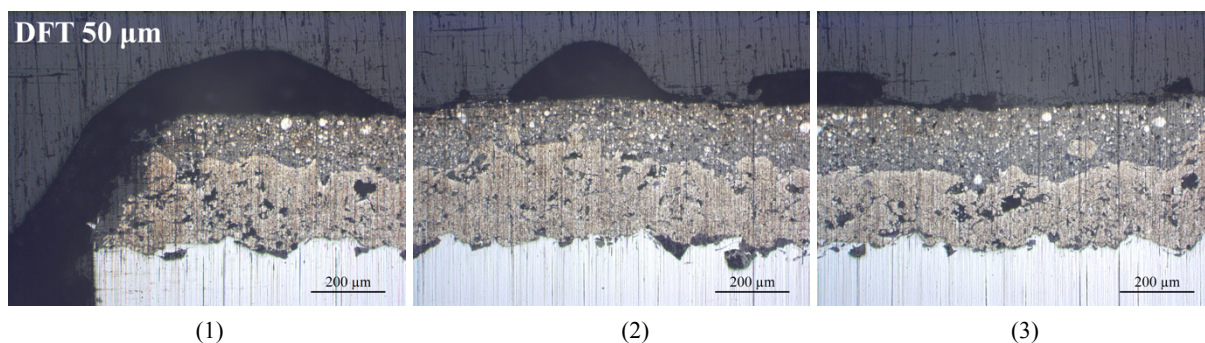
Figure 4.14: Light microscope images of the Zn silicate DFT 50 µm at the crevice opening (1) and further into the crevice (3). The TSA had only corroded at the crevice opening, in addition to some sporadic corrosion further into the crevice. Machining of the samples may have led to reduction at the crevice opening.

| (3) | (2) | (1) |
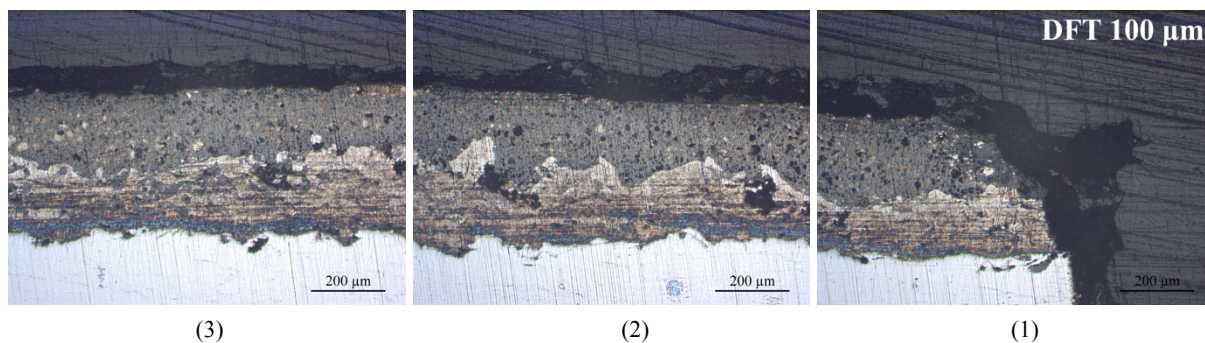
Figure 4.15: Light microscope images of the Zn silicate DFT 100 µm at the crevice opening (1) and further into the crevice (3). The TSA had only corroded at the crevice opening, in addition to some sporadic corrosion further into the crevice. Machining of the samples may have caused reduction at the crevice opening.

| (3) | (2) | (1) |
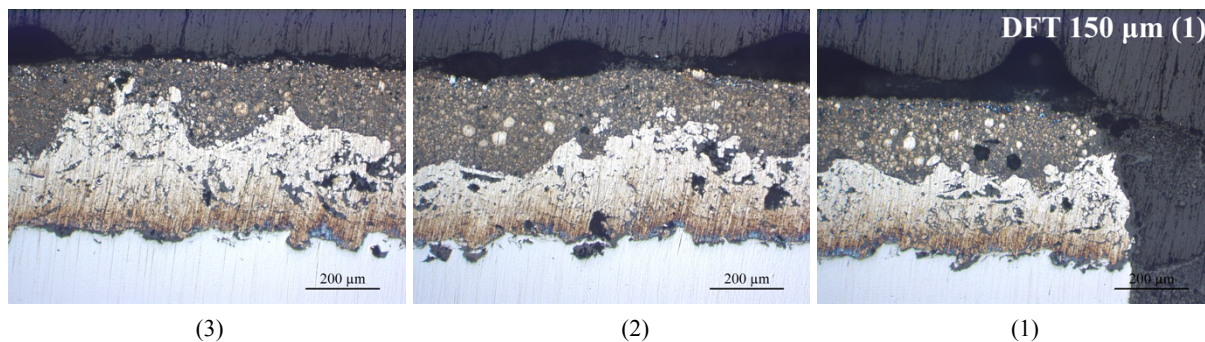
Figure 4.16: Light microscope images of the Zn silicate DFT 150 µm at the crevice opening (1) and further into the crevice (3). The dark areas may either be corrosion or voids from the coating application, or a combination of both.
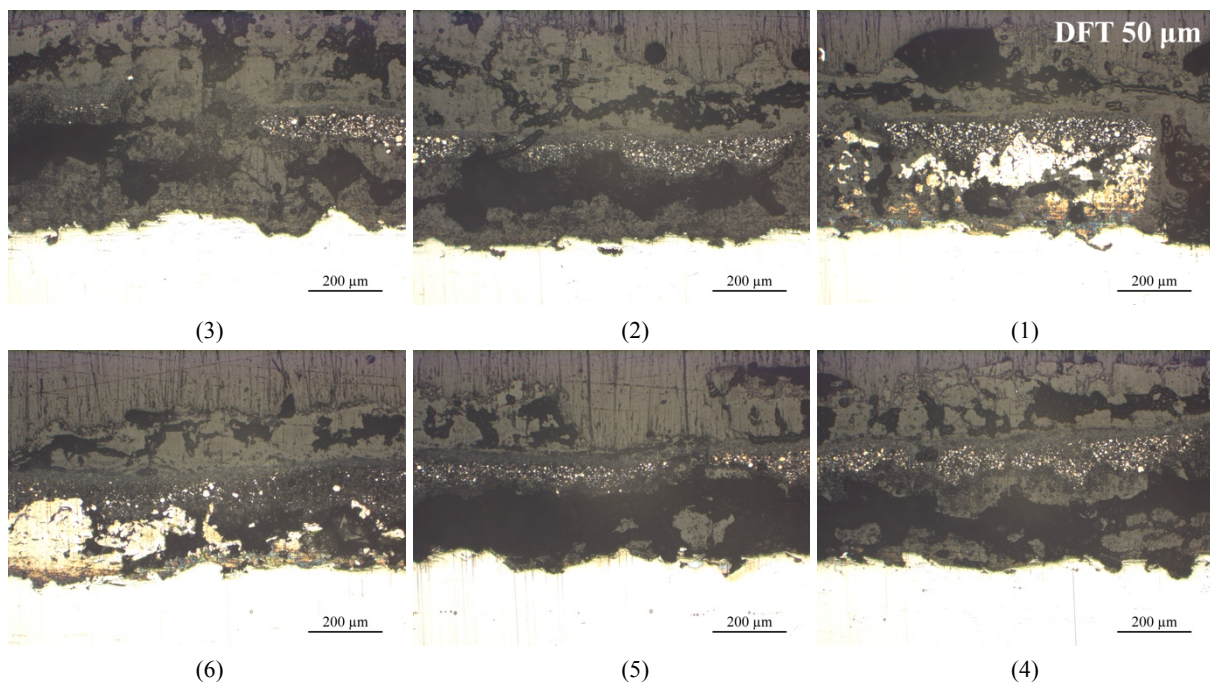
(1)　　　　　　　　　　(2)　　　　　　　　　　(3)
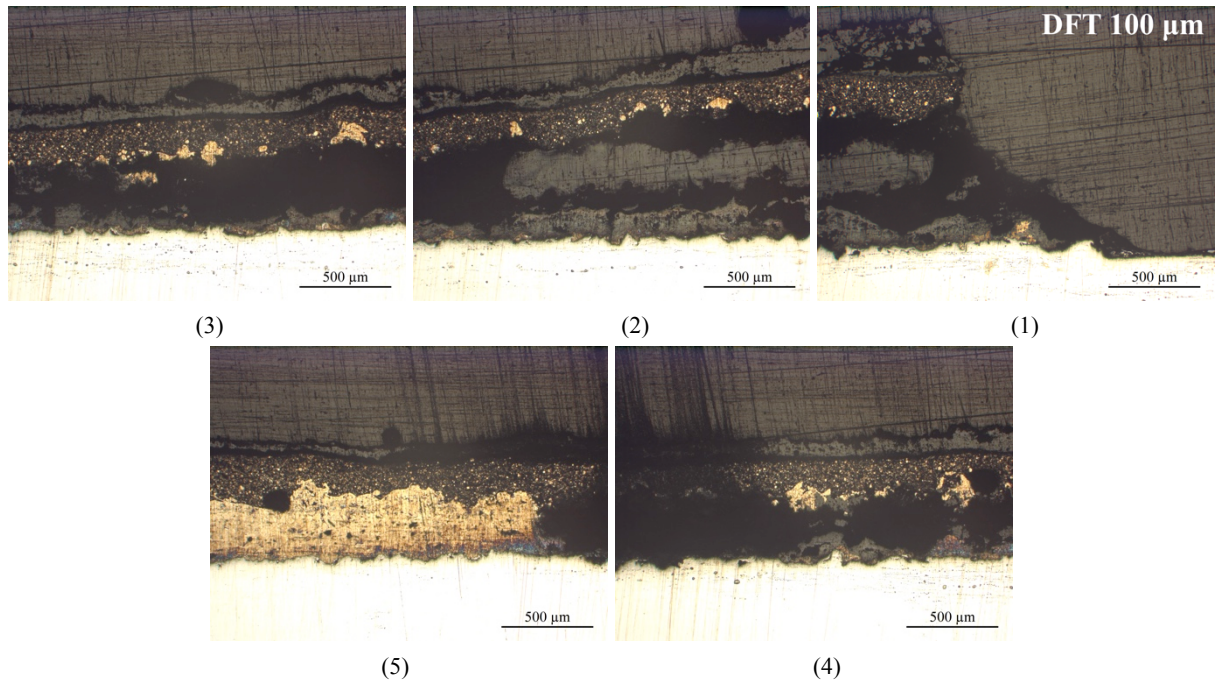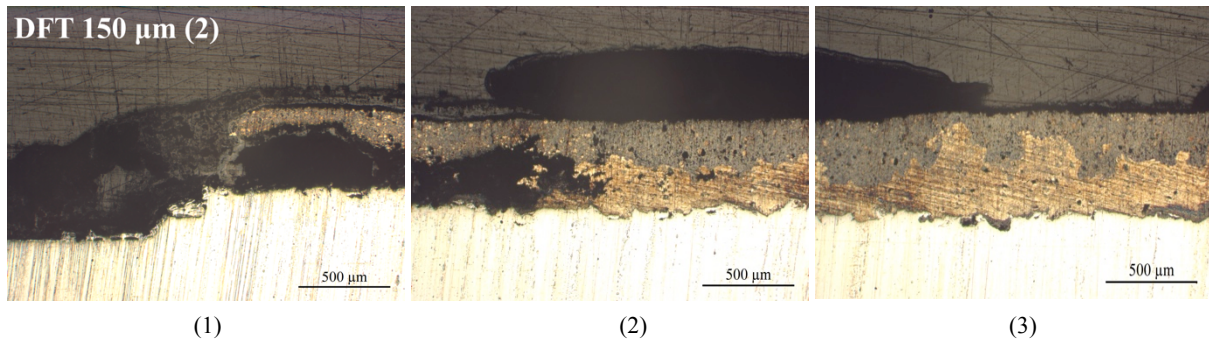
Figure 4.17: Light microscope images of the Zn silicate DFT 150 μm at the crevice opening (1) and further into the crevice (3). Corrosion creep of approximately 2.6 mm had occurred into the crevice.

Small amount of TSA corrosion was seen for both MgO- and Mg-silicate in Figure 4.18 and Figure 4.19.

MgO silicate

(1)　　　　　　　　　　(2)　　　　　　　　　　(3)
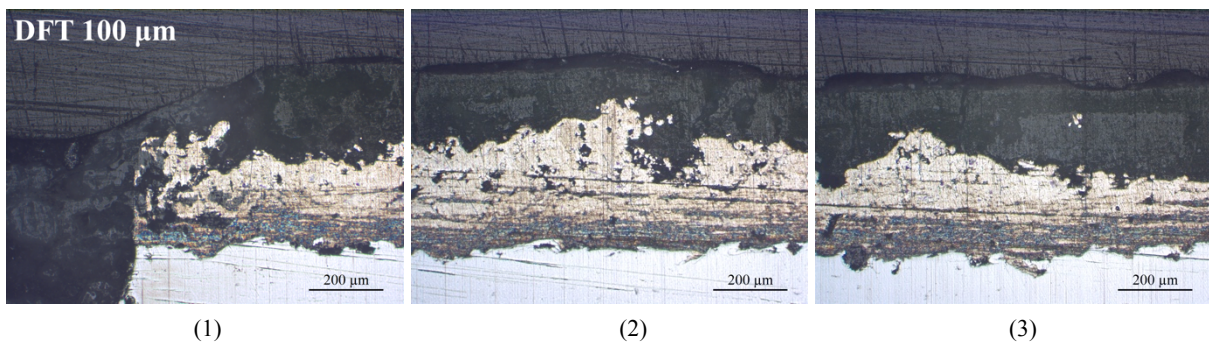
Figure 4.18: Light microscope images of the MgO silicate DFT 100 μm at the crevice opening (1) and further into the crevice (3). The TSA layer had only corroded at the crevice opening, and the dark areas further into the crevice may either be corrosion or voids from the coating application, or a combination of both.

Mg silicate

(1)　　　　　　　　　　(2)　　　　　　　　　　(3)
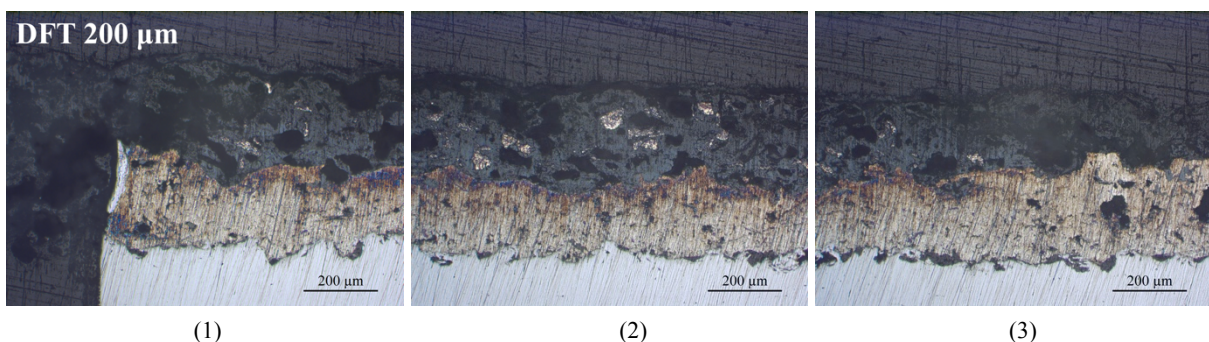
Figure 4.19: Light microscope images of the Mg silicate DFT 200 μm at the crevice opening (1) and further into the crevice (3). No TSA corrosion was seen at the crevice opening and the dark areas may either be corrosion or voids from the coating application, or a combination of both.

Al silicate

Sporadic corrosion of both the TSA and Al silicate can be seen in Figure 4.20. No continuous corrosion appeared, and the amount of intact aluminium particles was high.
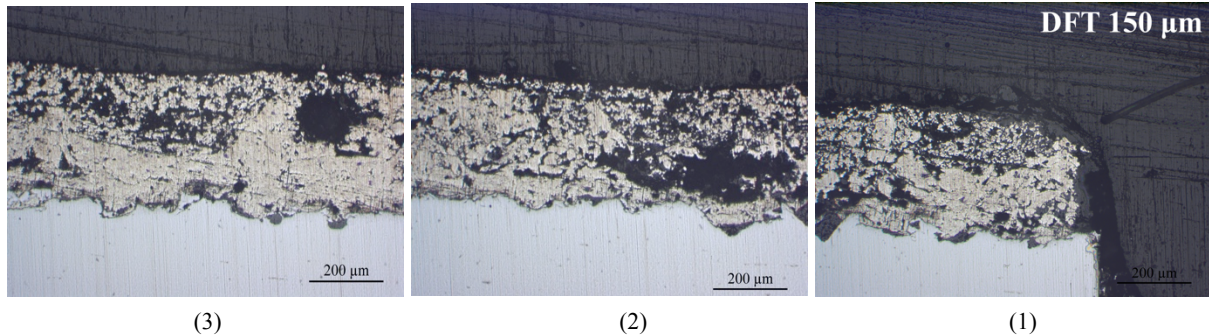
Figure 4.20: Light microscope images of the Al silicate DFT 150 μm at the crevice opening (1) and further into the crevice (3). The TSA had only corroded sporadically. Machining of the samples may have reduced the TSA at the crevice opening.

Inorganic copolymer coating

High amount of TSA corrosion was seen, and corrosion products caused cracking of the repair coat. The TSA corroded approximately 4.8 mm into the crevice. Active particles are not present in the repair coating.
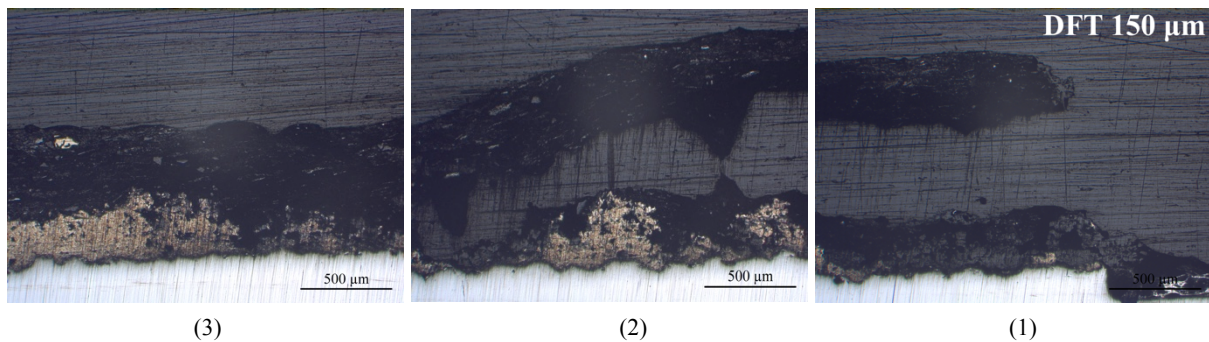
Figure 4.21: Light microscope images of the inorganic copolymer coating DFT of 150 μm at the crevice opening (1) and further into the crevice (3). Corrosion creep of approximately 4.8 mm had occurred into the crevice.

4.2.4 Element analysis of the corrosion products

SINTEF examined the corrosion products formed on the surfaces with Agilent 8800 Triple Quadropole ICP-MS (ICP-QQQ). In the case of little corrosion products at the surface, corrosion products were collected from the entire surface. The products were collected from the surface area around the scribe if the amount of corrosion products was high. The analysis was not used as a quantitative analysis, but as a method to determine the Al-, Zn- and Mg-content in the corrosion products. The results are given in Table 4.3, while a complete presentation of the results from SINTEF is presented in Appendix B, Section B.5. See Table 3.1 for the labeling used for the various repair coatings.

Table 4.3: Amount of Zn, Al or Mg in the corrosion products formed on the surfaces after 20 cycles of exposure.

Sample	Zn	Al	Mg
Z.50.3	31.0 %	69.0 %	-
Z.100.1	21.0 %	79.0 %	-
Z.150.2	32.2 %	67.8 %	-
ZE.50.2	26.7 %	73.3 %	-
ZE.100.1	23.0 %	77.0 %	-
ZE.150.1	24.6 %	75.4 %	-
H.50.3	36.7 %	63.3 %	-
H.100.1	12.8 %	87.2 %	-
H.150.2	38.1 %	61.9 %	-
ZS.50.1	64.9 %	35.1 %	-
ZS.100.2	73.4 %	26.6 %	-
ZS.150.3	34.6 %	65.4 %	-
MgO.100.2	-	65.2 %	34.8 %
Mg.200.3	-	48.5 %	51.5 %
Al.150.3	-	100 %	-
V.150.1	-	100 %	-

4.3 Electrochemical impedance

The zinc containing repair coatings were attached to one multi-cell, while MgO-, Mg-, Al-silicate and the inorganic copolymer coating were attached to another multi-cell. This was due to different start dates. The high Zn primer, Zn epoxy, Zn silicate and the modified Zn epoxy were immersed in artificial seawater for 134 days. MgO-, Mg-, Al-silicate and the inorganic copolymer coating were immersed for 81 days. Pictures of the samples after exposure and cross sectional images of the coating layers are presented in Appendix D.

Several spectra were obtained for each repair coating. Spectra were recorded more frequently at the beginning of the test period. The electrochemical impedance at 0.001 Hz is presented in Figure 4.22 for the different repair coatings. This frequency was chosen due to lowest value and most similar conditions as to the DC. The resistance against ion diffusion through the coating is therefore measured best at this frequency. The silicate coatings (Zn-, MgO-, Mg- and Al-silicate) showed increasing impedance at 0.001 Hz with increasing exposure time. High Zn primer showed the same tendency. The Zn epoxy, the modified Zn epoxy and the inorganic copolymer coating showed decreasing impedance at 0.001 Hz with increasing exposure time. The highest impedance was shown for the inorganic copolymer coating, followed by the high Zn primer, Zn epoxy and the modified Zn epoxy. The silicate coatings showed lower impedance, and the Zn silicate revealed the lowest impedance. Impedance values from each specter with Bode plots are presented in Appendix D, Section D.2.
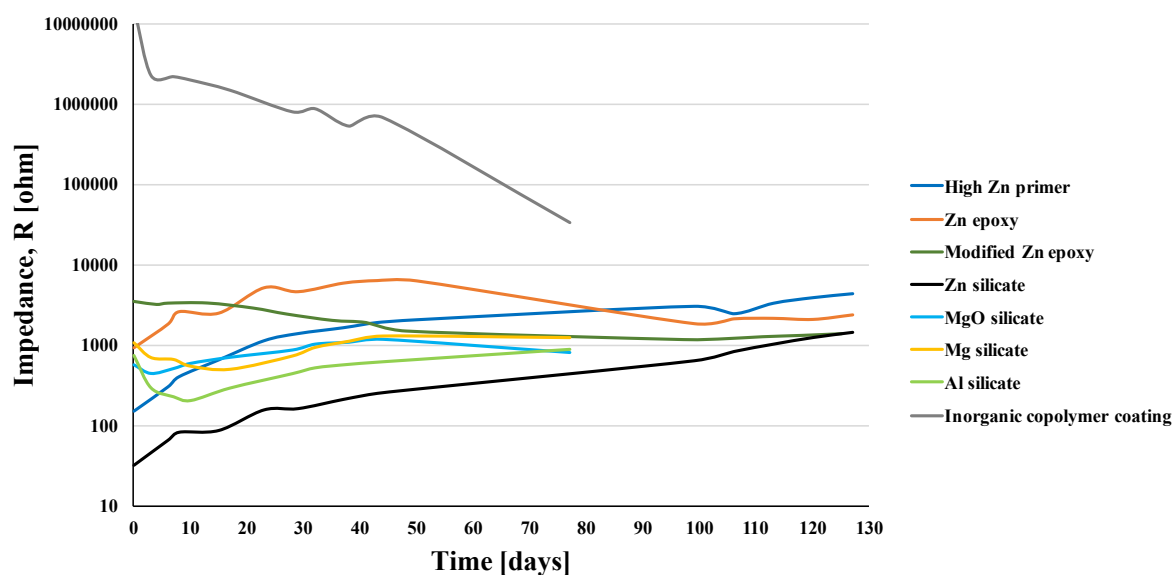
Figure 4.22: Electrochemical impedance at 0.001 Hz (y-axis) plotted against exposure time (x-axis).

Development of the pH during the test period is presented in Figure 4.23. The pH of the electrolyte in the multi-cell holding the zinc containing coatings decreased from 8.24 to 8.00, while the pH values decreased from 8.34 to 8.27 for the MgO-, Mg-, Al-silicate and the inorganic copolymer coating mulit-cell. Exact pH values are presented in Appendix D, Section D.3.
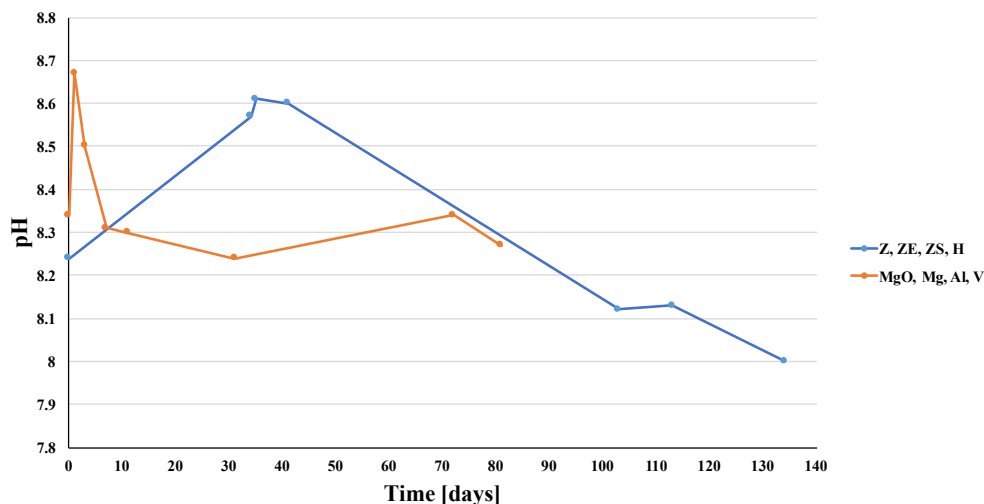
Figure 4.23: Development of pH (y-axis) plotted against the number of days from test initiation (x-axis).

4.3.1   Diffusion properties of the repair coatings

The EIS measured the resistance of ion diffusion through the coatings. No damages were introduced to the coating layers, and the cross sections of the various coatings are shown from Figure 4.24 to Figure 4.31. The light microscope images revealed sufficient ion diffusion through the repair coating to avoid severe TSA corrosion. No indication of cracks can be seen in the repair coatings.

High Zn primer
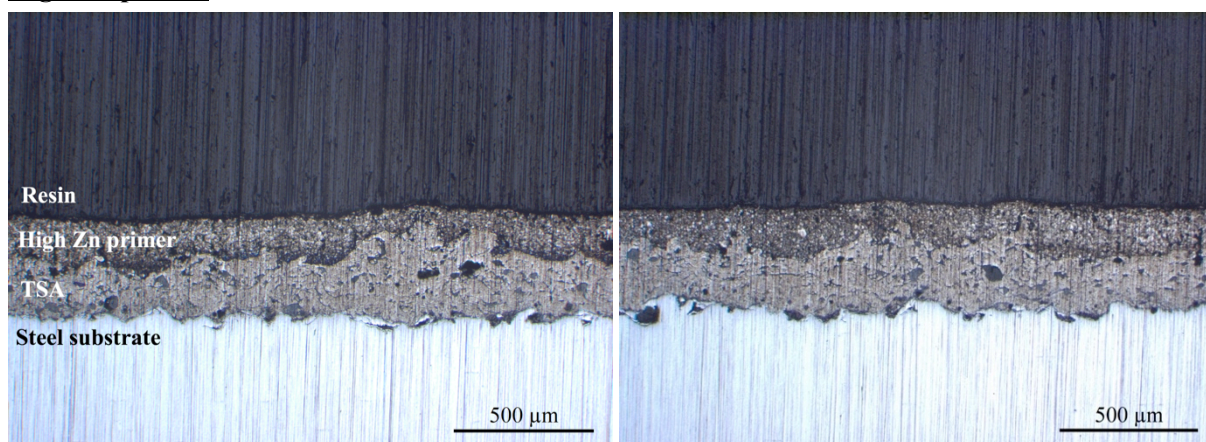
Figure 4.24: Light microscope images of the high Zn primer from the exposed surface areas. No extensive corrosion of the TSA occurred. Some smaller dark areas can be seen in the TSA, which may either be corrosion or voids from the coating application process.

Zn epoxy
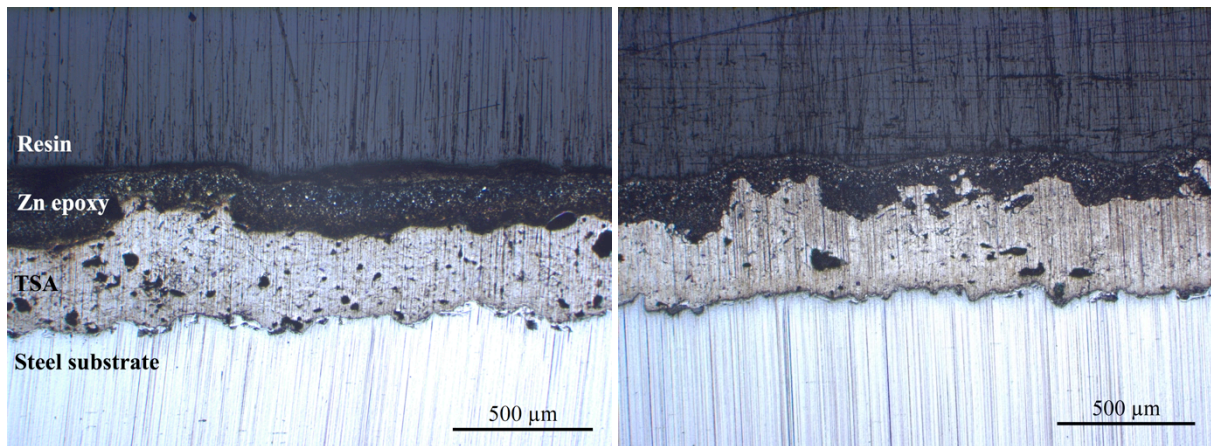
Figure 4.25: Light microscope images of the Zn epoxy from the exposed surface areas. Some dark areas can be seen in the TSA, which may either be corrosion or voids from the coating application process. Some lager dark areas may be corroded TSA.

Modified Zn epoxy
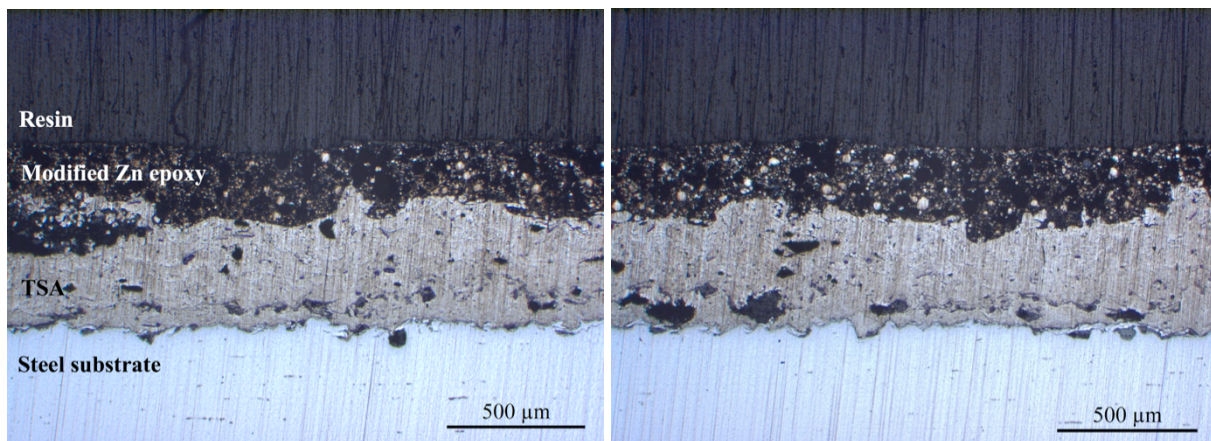
Figure 4.26: Light microscope images of the modified Zn epoxy from the exposed surface areas. Some dark areas can be seen in the TSA, which may either be corrosion or voids from the coating application process. Some larger dark areas may be corroded TSA.

Zn silicate
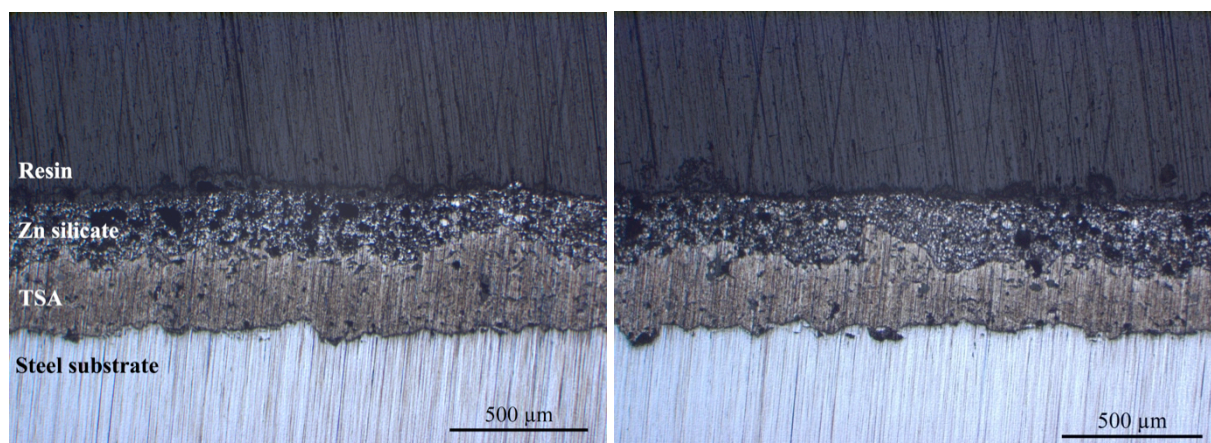
Figure 4.27: Light microscope images of the Zn silicate from the exposed surface areas. No extensive corrosion of the TSA occurred, and the TSA appeared relative unaffected.

MgO silicate
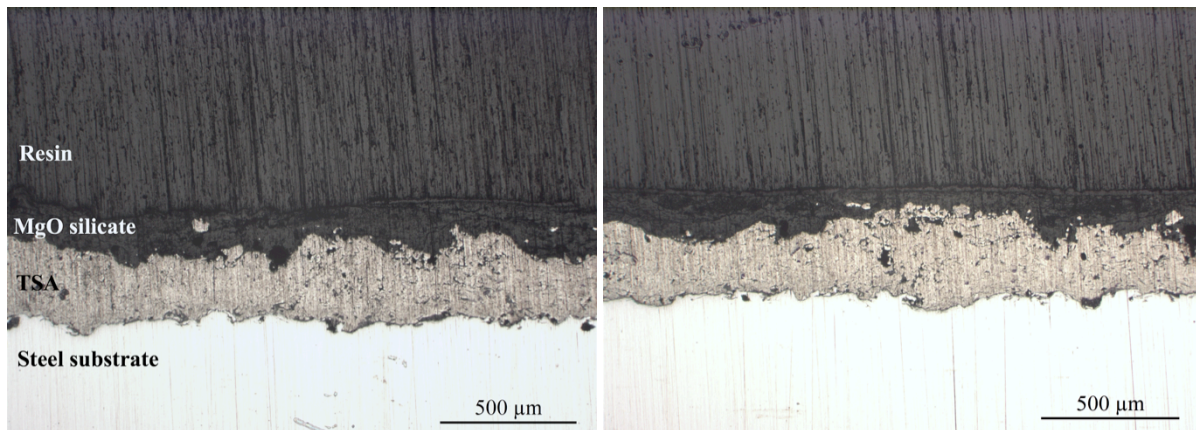
Figure 4.28: Light microscope images of the MgO silicate from the exposed surface areas. Some dark areas can be seen in the TSA, which may either be corrosion or voids from the coating application process. A thin layer can be seen on top of the repair coating.

Mg silicate
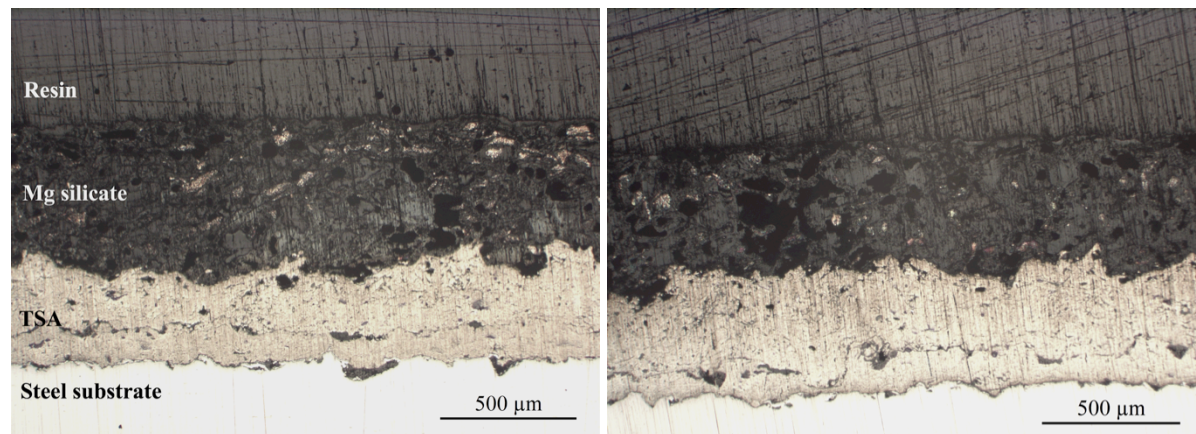
Figure 4.29: Light microscope images of the Mg silicate from the exposed surface areas. Some dark areas can be seen in the TSA, which may either be corrosion or voids from the coating application process. A thin layer can be seen on top of the repair coating.

Al silicate
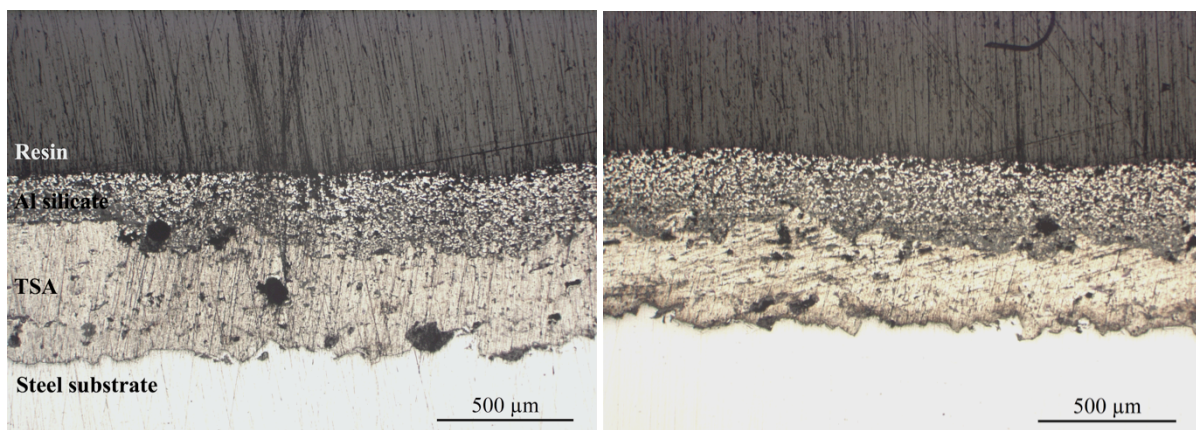
Figure 4.30: Light microscope images of the Al silicate from the exposed surface areas. Some concentrated dark areas can be seen in the TSA and the Al silicate, which may either by corrosion or voids from the coating application.

Inorganic copolymer coating
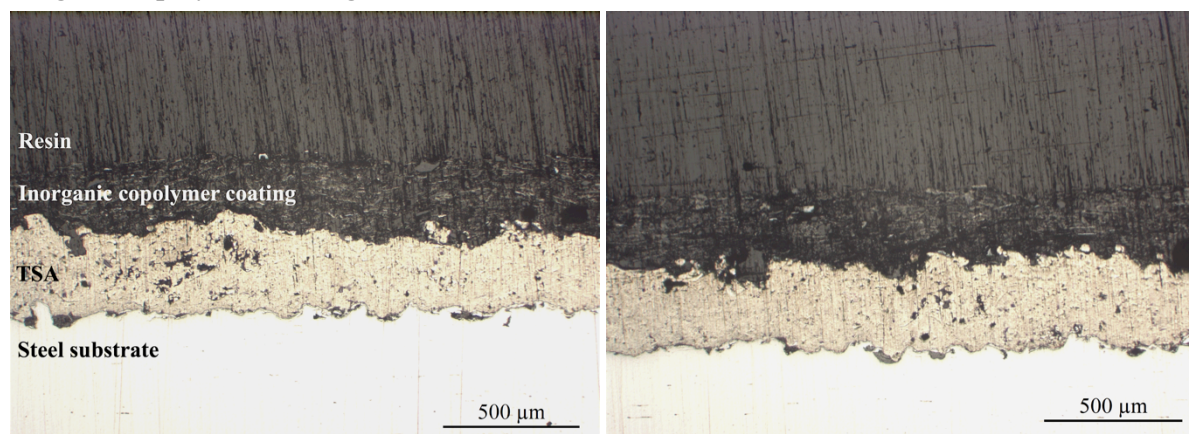
Figure 4.31: Light microscope images of the inorganic copolymer coating from the exposed surface areas. Some concentrated dark areas could be seen in the TSA layer, which may be corrosion or voids.

4.3.2 Element analysis of the exposed surface areas

The exposed surface areas were investigated in SEM, where the corrosion products were analyzed by EDS. 12 areas were scanned on each sample and the average normalized concentrations are presented in Table 4.4. The artificial seawater contained elements such as Cl, Mg, Ca, Na and K. These are included in "*Other*". This is also applicable for Si, derived from the silicate. See Appendix C for the artificial seawater composition.

Magnesium is presented as a separate element instead of in "*Other*" for the MgO- and Mg-silicate coatings. Calcium is also presented as a separate element for these two coatings due to high concentrations compared to other elements. Oxygen is included for all coatings because the corrosion products contained oxides. A percentage values is presented for aluminium (from the TSA) and the anodic element from the repair coating, to see the relation between these elements on the surfaces. The inorganic copolymer coating was not investigated since the coating did not contain active pigments, and the white corrosion products on the surface were assumed to be aluminium from the TSA. A complete overview of all elements from the 12 areas, in addition to SEM images taken of the scanned areas can be seen in Appendix D, Section D.4.

Table 4.4: EDS analysis with average normalized concentration, standard deviation and percentage amount of the central elements from the 12 scanned areas.

Repair coating	Element	Average normalized concentration [wt %]	Standard deviation	Percentage [%]
High Zn primer	Zn	51.7	6.7	85
	Al	9.2	2.1	15
	O	28.4	3.2	-
	Other $_{Cl, Mg}$	10.7	2.0	-
Zn epoxy	Zn	65.7	12.0	95
	Al	3.8	3.1	5
	O	24.1	7.4	-
	Other $_{Cl, Mg, Ca}$	6.4	4.1	-
Modified Zn epoxy	Zn	33.6	4.4	67
	Al	16.2	3.4	33
	O	37.7	2.9	-
	Other $_{Cl, Mg}$	12.6	5.1	-
Zn silicate	Zn	58.2	8.8	94
	Al	3.8	1.3	6
	O	28.3	5.3	-
	Other $_{Si, Cl, Na}$	9.7	4.7	-
MgO silicate	Mg	13.1	4.2	71
	Al	5.4	3.0	29
	O	47.9	2.0	-
	Ca	26.7	9.2	-
	Other $_{Si, Cl, Na}$	6.8	4.5	-
Mg silicate	Mg	2.1	0.9	64
	Al	1.2	0.5	36
	O	50.4	1.8	-
	Ca	42.3	2.2	-
	Other $_{Si, Cl, Na}$	4.1	1.5	-
Al silicate	Al	30.6	12.7	100
	O	36.4	5.2	-
	Other $_{Si, Mg, K, Cl, Na}$	33.0	7.8	-

The thermodynamically instability of various zinc corrosion products relative to different pH and chloride values are shown in Figure 2.5 in Section 2.5. The logarithmic chloride concentration for the artificial seawater is calculated (7) to be able to determine the corrosion product in Figure 2.5. The zinc containing coatings were attached to the same multi-cell and the pH of the artificial seawater decreased towards 8. See Figure 4.23 for the pH development. Composition of the artificial seawater used during exposure is presented in Appendix C. The chloride concentration was 0.55952 moles Cl/l.

$$\log 0.5595 \frac{mole\ Cl}{liter} = -0.25 \tag{7}$$

With a pH of approximately 8 and a logarithmic chloride concentration of -0.25, the actual corrosion product should be ZnO according to equation (7) and Figure 2.5.

4.4   Open circuit potential

The same reference electrode was used both for the OCP measurements and the electrochemical impedance test, i.e. an Ag/AgCl electrode. Figure 4.32 presents the OCP as function of immersion times. The zinc containing repair coatings were exposed for 134 days, while MgO-, Mg-, Al-silicate and the inorganic copolymer coating were exposed for 81 days. The different exposure times were due to different start dates. The exact OCP values measured are presented in Appendix E.
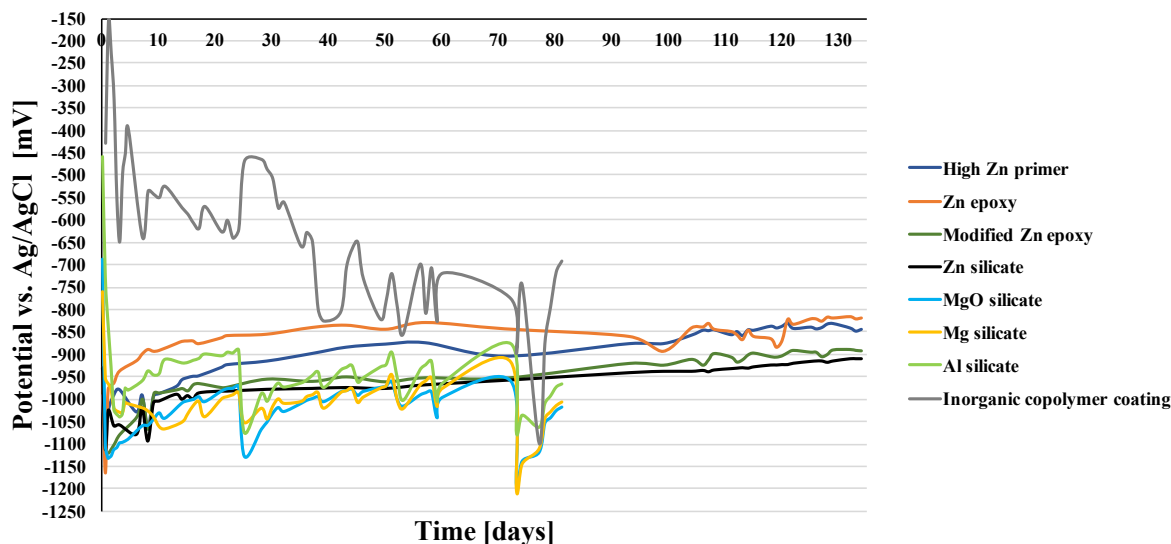
Figure 4.32: OCP for the different repair coatings with potential vs. Ag/AgCl (y-axis) plotted against the number of days from test initation (x-axis).

4.5 Crevice corrosion test

Two different design setups were tested and the results are presented in section 4.5.1 and 4.5.2. Images of the samples after exposure, pH development and anodic current curves are presented for both setups, in addition to an overview of the corrosion degradation.

4.5.1 Test setup 1

The test was carried out for 14 days and Figure 4.33 presents the samples after exposure. Blisters were seen on the Zn epoxy (ZE), the modified Zn epoxy (H) and the inorganic copolymer coating (V).
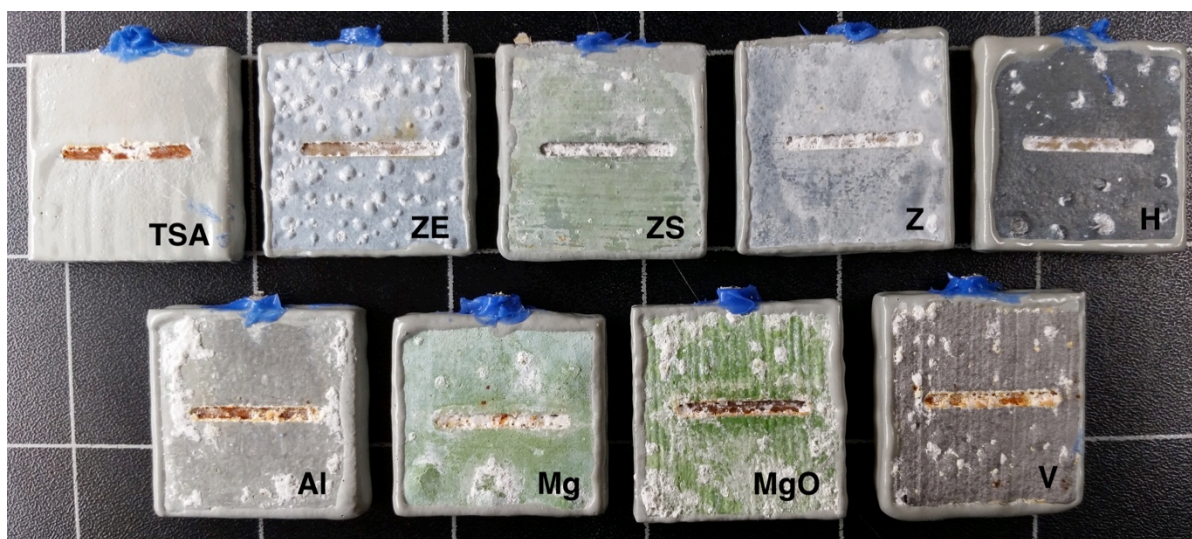
Figure 4.33: Visual appearance of the samples after 14 days of exposure. The order of the repair coatings on the upper row is: TSA coated with epoxy (TSA), Zn epoxy (ZE), Zn silicate (ZS), high Zn primer (Z) and modified Zn epoxy (H). The order on the lower row is: Al silicate (Al), Mg silicate (Mg), MgO silicate (MgO) and the inorganic copolymer coating (V).

The pH development for both containers is shown in Figure 4.34. The pH of the electrolyte in the MgO-, Mg-, Al-silicate and the inorganic copolymer coating container decreased from 8.31 to 4.51 due to increased concentration of Al in the electrolyte. The corresponding value for the high Zn primer, Zn epoxy, Zn silicate and the modified Zn silicate was 8.31 to 4.60. Both containers revealed the same trend with relatively gentle decrease initially, a steeper decrease at the middle of the test period and no significant change at the end. Exact pH values are presented in Appendix F, Section F.1.
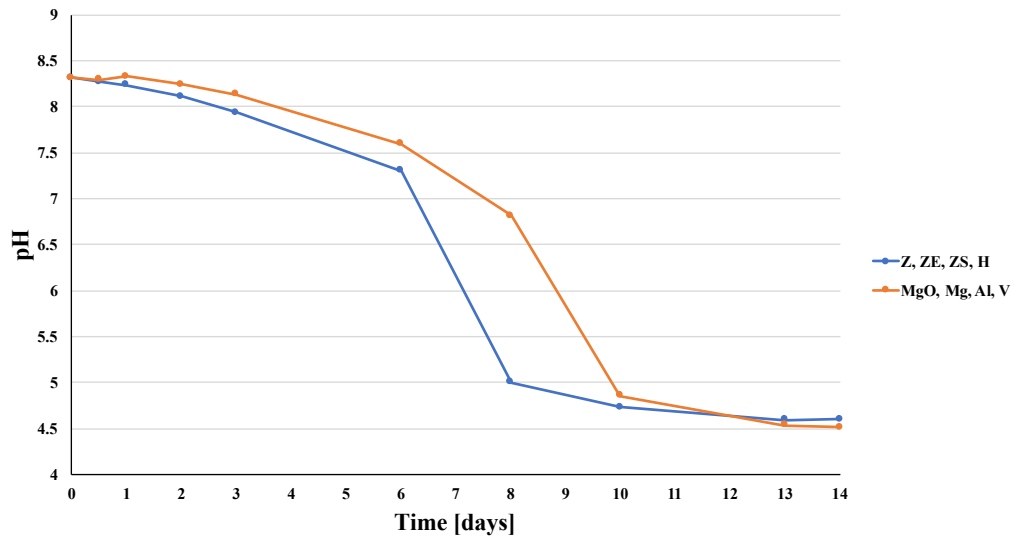
Figure 4.34: Development of the pH. The blue line represents the high Zn primer, Zn epoxy, Zn silicate and the modified Zn epoxy, while the orange line represents the MgO-, Mg-, Al-silicate and the inorganic copolymer coating.

See Figure 4.35 for the anodic current measured during the test period. The Zn-, MgO-silicate and the high Zn primer revealed a steep increase early before the current decreased after some days. Mg silicate and Zn epoxy showed the same tendency of increase early, while the current stabilized instead of decreasing further. A high current peak was also seen for the Zn epoxy early. The anodic current for Al silicate increased steadily before a decreased was seen. The steady increase could also be seen for the TSA coated with epoxy, the inorganic copolymer coating and the modified Zn epoxy, without a decrease towards the end.
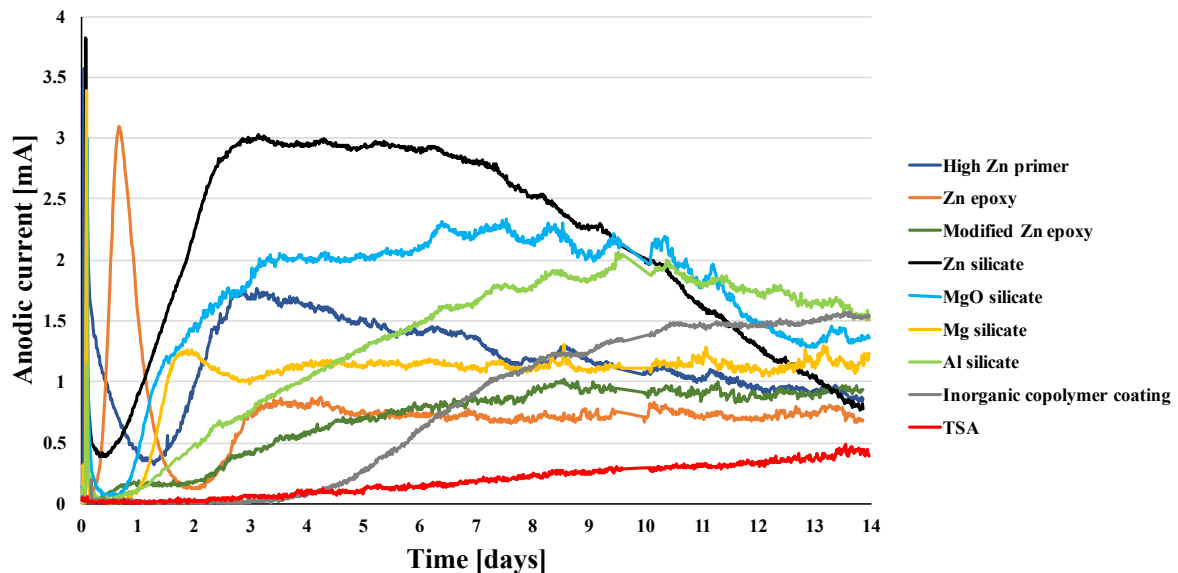
Figure 4.35: Anodic current for the repair coatings for test setup 1 with anodic current (y-axis) plotted against time (x-axis).

Table 4.5 presents the amount of TSA corrosion and the repair coat reduction after exposure. Corrosion of the TSA is emphasized. The numbers stated for the continuous TSA corrosion are approximate values and based on the light microscope images in Appendix F, Section F.1. The "*Blistering*" evaluations are based on Figure 4.33. Lowest degree of TSA corrosion was seen on the Al silicate, followed by the modified Zn epoxy and the TSA coated with epoxy. The inorganic copolymer coating, the epoxy applied on the TSA and the MgO silicate did not contain active particles, and the column "*Amount of corroded metal particles*" was therefore not estimated for these coatings. The results presented in Table 4.5 will be compared to the results obtained from the cyclic coating test, in Section 5.6.

Table 4.5: Degree of both TSA corrosion and reduction of the repair coating for crevice corrosion test setup 1.

Sample	Blistering	Continuous TSA corrosion from crevice opening [mm]	Amount of corroded metal particles
High Zn primer	No	12.3	Low
Zn epoxy	Yes	14 *	Medium
Modified Zn epoxy	Yes	3	Low
Zn silicate	No	Totally reduced	Flaked off
MgO silicate	No	14 *	-
Mg silicate	No	14 *	High
Al silicate	No	1.3	Medium
Inorganic copolymer coating	Yes	2.5	-
TSA coated with epoxy	No	3.8	-

* Continuous TSA corrosion along the entire crevice.

4.5.2 Test setup 2

Test setup 2 was tested twice, with test periods of 16 days and 30 days. The 30 days test was conducted to have a parallel to the 16 days exposure. Only the test conducted for 16 days will be emphasized in this section, due to similar tendency of anodic current, pH development and corrosion of the TSA. However, the corrosion after 30 days was more severe due to longer exposure time. Test results obtained after 30 days are presented in Appendix F, Section F.2. All repair coatings were exposed in the same container. The samples tested for 16 days are presented in Figure 4.36. No blistering was seen after exposure.
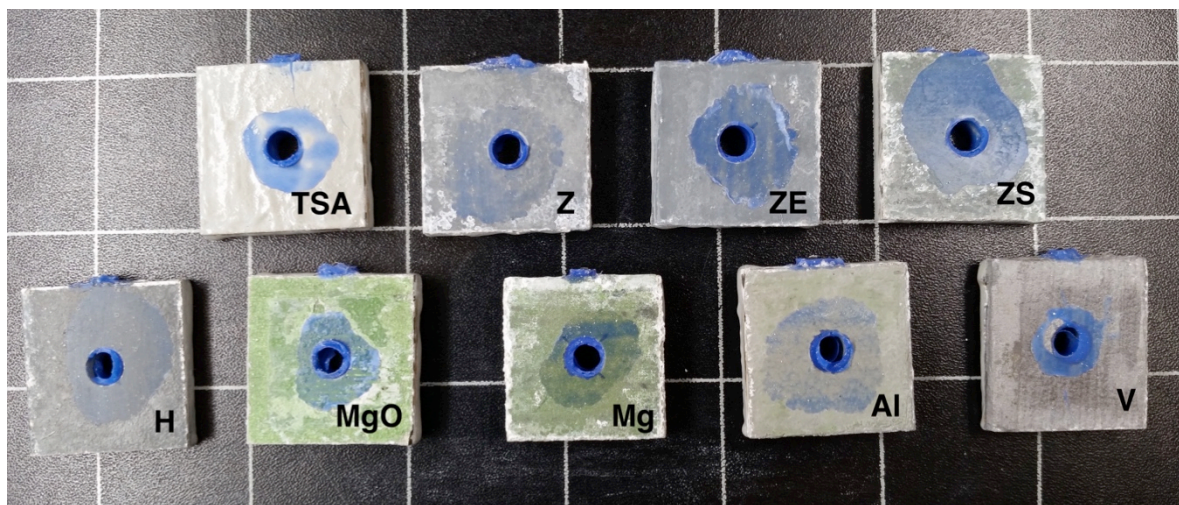
Figure 4.36: Visual appearance of the samples after 16 days of exposure. The order of the repair coatings on the upper row is: TSA coated with epoxy (TSA), high Zn primer (Z), Zn epoxy (ZE) and Zn silicate (ZS). The order on the lower row is: modified Zn epoxy (H), MgO silicate (MgO), Mg silicate (Mg), Al silicate (Al) and the inorganic copolymer coating (V).

The pH development is presented in Figure 4.37. A general pH decrease from 8.19 to 7.07 was seen during the test period. Exact pH values are presented in Appendix F, Section F.2.
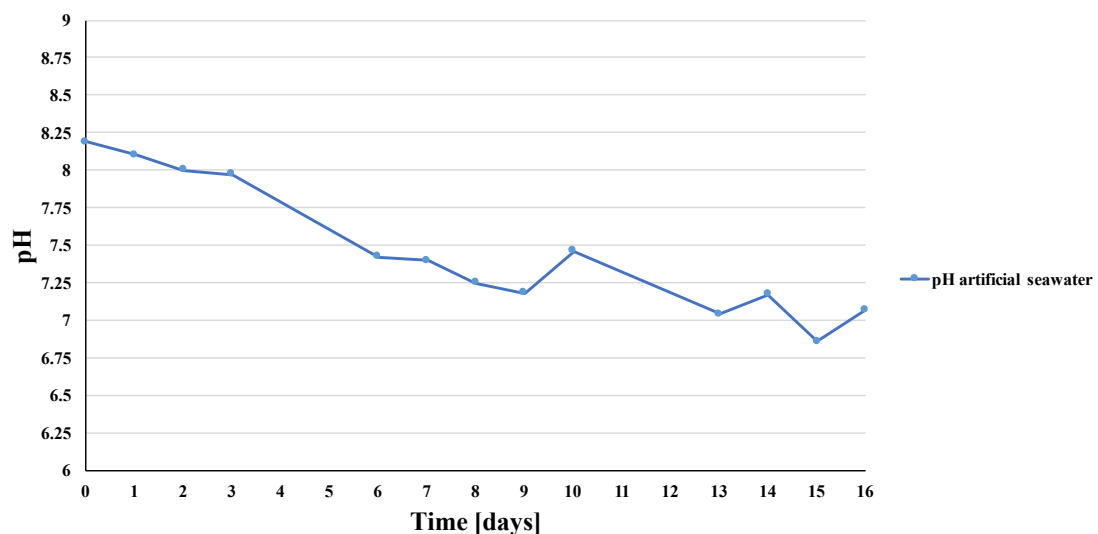
Figure 4.37: Development of the pH for the test run for 16 days.

See Figure 4.38 for the anodic current measured during the test period. The Zn-, MgO- and Al-silicate showed a current increase before a decrease towards the end of the test. The Mg silicate showed the same trend with initial increase, but the decrease was gentler towards the end of the test. The high Zn primer and the Zn epoxy revealed both a current increase and decrease, before an increase towards the end of the test. The anodic current for the modified Zn epoxy, the TSA coated with epoxy and the inorganic copolymer coating showed a steady increase from the test initiation.
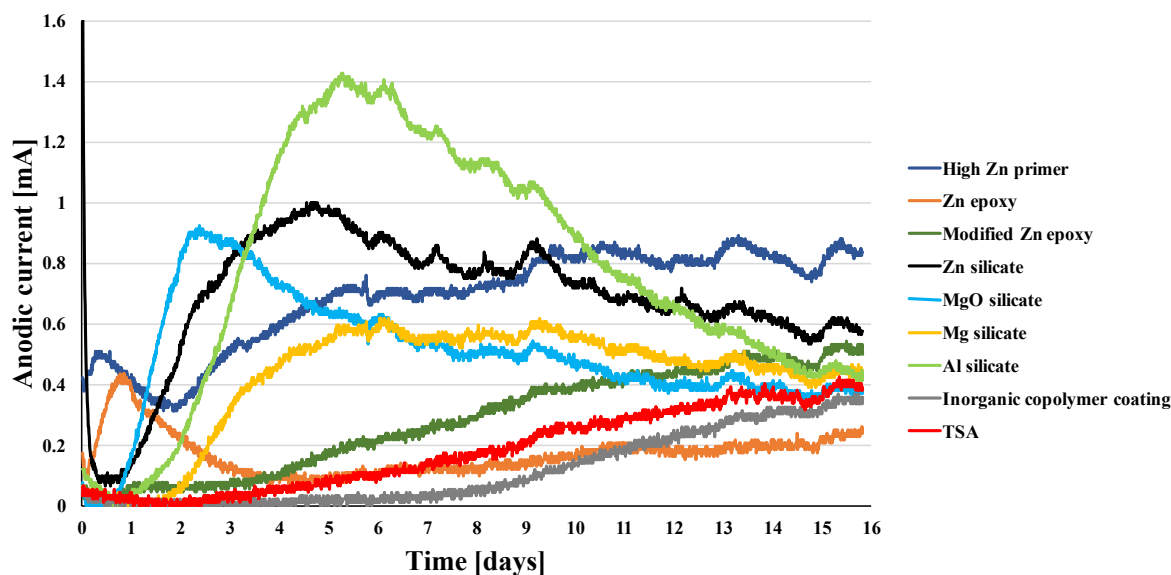
Figure 4.38: Anodic current for the repair coatings for the test setup run for 16 days with anodic current (y-axis) plotted against time (x-axis).

Table 4.6 presents the degree of corrosion for both TSA and the repair coating. Corrosion of the TSA is emphasized. The TSA corrosion was estimated from light microscope images presented in Appendix F, Section F.2. The "*Blistering*" evaluations are based on Figure 4.36. Highest degree of TSA corrosion was observed for the silicate coatings and the modified Zn epoxy. The high Zn primer, Zn epoxy and the inorganic copolymer coating showed TSA corrosion just at the crevice opening. A corroded field was also seen between the coating layers for the Zn epoxy. The inorganic copolymer coating, the epoxy applied on TSA and the MgO silicate did not contain active particles and the column "*Amount of corroded metal particles*" was therefore not estimated for these coatings. The results in Table 4.6 will be compared to the results obtained from the cyclic coating test, in Section 5.6.

Table 4.6: Degree of both TSA corrosion and reduction of the repair coating for crevice corrosion test setup 2 run for 16 days.

Sample	Blistering	Continuous TSA corrosion from crevice opening [mm]	Amount of corroded metal particles
High Zn primer	No	0.5	Low
Zn epoxy	No	0.4	Medium
Modified Zn epoxy	No	2.7	Medium
Zn silicate	No	4.4	Low *
MgO silicate	No	2.2	- *
Mg silicate	No	3.1	High
Al silicate	No	3.4	Low *
Inorganic copolymer coating	No	0.2	-
TSA coated with epoxy	No	1.3	-

* Totally removed/reduced at the crevice opening.

5 Discussion

The results obtained in Section 4 will be discussed, in addition to the experience gained during the coating application. An individual section for each experiment will first be presented before a section related to the desired coating properties is presented relative to the different repair coatings and the contributing protection mechanisms.

5.1 Coating application

All samples were coated manually with brush. A wet film thickness gauge was used to measure the coating thickness before curing, and some variations in the dry film thickness were found. However, this is normal. The unevenness of the surfaces did also depend on the coating viscosity. Lowest viscosity was seen for the silicate coatings, while the modified Zn epoxy showed highest viscosity. The sample edges were therefore covered with modified Zn epoxy to achieve sufficient thickness around the edges. The viscosity of the silicate coatings varied slightly depending on the amount of metal particles mixed with binder. The same volume fraction of binder and metal powder were used for the Zn-, Mg- and Al-silicate. Approximately 17 vol% additional binder was added to the MgO silicate, to be able to apply the coating onto the TSA substrate. By adding the same amount of binder to the MgO powder as for the Zn-, Mg- and Al-silicate, the coating viscosity increased so that coating application onto the substrate became impossible.

Some cracking (mud cracking) was seen after curing. This was applicable for the MgO silicate and partly for the Zn silicate. The MgO silicate coating cracked if the coating either was applied too thick, or in two separate layers where the upper layer flaked off after curing. The MgO silicate was therefore tested with an average dry film thickness of 100 μm. The Zn silicate showed the same cracking if too thick coating layers were applied. Coating thicknesses above 100 μm was therefore obtained by applying two layers.

5.2 Electrical resistance

The electrical resistance measured in the different repair coatings are presented in Section 4.1. The electrical resistance increased with increasing coating thickness, except for the high Zn primer with a constant value for all thicknesses. The electron path through the coating layer may explain the increasing electrical resistance with increasing thicknesses. In order to provide corrosion protection as a sacrificial coating, electrical contact between the metallic particles is required. This is the case for the coatings containing Zn-, Al- or Mg-particles. The contact points between the particles have higher resistance compared to the particle itself. As the coating thickness increases, the electrons have to cross more particle contact points, and the electrical resistance will therefore increase.

The Zn silicate had lower resistance than the Al- and Mg-silicates. The Al silicate showed overload during the measuring. The silicate coatings are two-component coatings consisting of a binder mixed

with metal particles. Uneven particle distribution in the coatings may contribute to the high resistance. Magnesium oxide is none conductive, and the electrical resistance value of 0.2 Ω was therefore unexpected. Aluminium oxide is a good insulator [15], which may contribute to higher resistance for the Al silicate. An aluminium oxide forms immediately after exposure, and it was therefore assumed that the oxide was present during the measuring. The Zn silicate showed increasing resistance values with increasing coating thickness. Zinc oxide is a semiconductor [31], and would contribute to lower resistance. Zinc oxide may also have formed around the particles, e.g. during the production process. The high Zn primer revealed a constant resistance of 0.2 Ω for all thicknesses. This tendency diverged from the other coatings with increasing resistance with increasing coating thickness. The high Zn primer contained 96 wt% zinc and the high amount of zinc particles may explain the constant value. Transportation of current through the coating layer may be easier due to the high amount of particles in electrical contact, which lead to constant values independent of the thickness.

5.3 Cyclic coating test

The samples were exposed for 20 cycles according to ISO 20340. This test was performed to evaluate the coating behaviors over a period of time. The samples were visually examined, and the average corrosion creep, corrosion morphology under the repair coat and the corrosion products were analyzed. The results are presented in Section 4.2.

Blistering on the surface and cracks of the repair coating were associated with TSA corrosion. This has earlier been reported during the study "*Coating systems for long lifetime: Thermally Sprayed Duplex Systems*" [1]. This study reported cracks of the organic coating due to corrosion products from the TSA, and blisters were therefore formed. During the cyclic coating test, the Zn epoxy, the modified Zn epoxy and the inorganic copolymer coating blistered after respectively 4, 13 and 5 cycles of exposure. Due to the high amount of white corrosion products covering the entire surface on the high Zn primer samples, the blistering was first observed after the test was completed. All three coating thicknesses of the Zn epoxy showed blistering, in addition to extensive cracks around the scribe on the DFT 150 μm. See Figure 4.2 for both the blistering and cracking on the 150 μm sample. As mentioned, cracks are associated with TSA corrosion, something that also was revealed based on the average corrosion creep. The modified Zn epoxy did also show blistering on all coating thicknesses, but not so severe as for the Zn epoxy samples. The inorganic copolymer coating was only tested with one coating thickness, but all three parallels revealed blistering. All blistering occurred near or in affiliation to the machined scribe that simulated damage in the coating layers. None of the silicate coatings revealed visible blistering after 20 cycles of exposure.

The average corrosion creep was measured for all samples after exposure. Two parallels were used as basis for each coating thickness. The corrosion creep at 11 points was measured for each scribe, 5 mm apart, and the average value was calculated. See Figure 3.2 for the measuring method and Figure 4.4 for the average corrosion creep calculated for the various samples. As can be seen in Figure 4.4, highest corrosion creep was seen for the Zn epoxy, followed by the inorganic copolymer coating, high Zn primer and the modified Zn epoxy. ISO 20340 states that the corrosion creep after qualification

testing shall be less than 3.0 mm for coating systems with Zn-rich primers and less than 8.0 mm for coating systems with primers other than Zn [30]. The cyclic coating test is defined as exposure for a total of 25 cycles, and the cyclic coating test performed during the MSc project were conducted for 20 cycles. The requirements regarding the corrosion creep will there only be a estimate, and note definite, since the test did not complete 25 cycles of exposure. All repair coatings, except the Zn epoxy, fulfilled the requirements regarding the amount of corrosion creep. The Zn epoxy revealed an average corrosion creep of 5.9 mm (DFT 50 μm), 4.3 mm (DFT 100 μm) and 5.0 mm (DFT 150 μm). All these values exceed the requirement of a corrosion creep less than 3.0 mm for zinc-rich primers.

The high Zn primer, the modified Zn epoxy and the inorganic copolymer revealed average corrosion creep of approximately 2.4 mm, 1.9 mm and 3.3 mm. These values are average values for all coating thicknesses. The requirement of 3.0 mm and 8.0 mm for the corrosion creep is therefore fulfilled for theses coatings. Note that the results are reported after 20 cycles of exposure, and it is difficult to state if the requirements had been fulfilled after 25 cycles of exposure. Even though the high Zn primer, the modified Zn epoxy and the inorganic copolymer coating showed corrosion creep less than the requirements, these coatings revealed higher corrosion creep than the silicate coatings. The Zn silicate revealed higher corrosion creep, compared to the MgO-, Mg- and the Al-silicate. The Zn silicate showed an average corrosion creep of approximately 0.6 mm for all coating thicknesses, while the MgO-, Mg-, Al-silicate showed negligible values. This shows that the silicate coatings fulfilled the creep requirements, and will also most likely fulfill the requirements after 25 cycles of exposure. Blistering seen during the visual assessment did therefore show a correlation with the highest corrosion creep. All the coatings that showed visual blisters, i.e. the Zn epoxy, high Zn primer, the modified Zn epoxy and the inorganic copolymer coating, did also reveal the highest average corrosion creep.

Cross sections were prepared vertically through the scribe after the test was terminated. The samples were machined vertically at two different points, so that four cross sections were compared for each coating thickness. If the differences between the cross sections were small, one example was presented. This was not applicable for the Zn silicate DFT 150 μm. The coatings that revealed blistering and the highest corrosion creep had most continuous TSA corrosion in the light microscope images. The images are presented in Section 4.2.3 and were taken to evaluate the corrosion morphology under the repair coatings. The repair coatings with blisters and highest corrosion creep showed also tendency to cracking of the repair coat near the scribe, due to increased amount of aluminium corrosion products below the repair coating. Cracks around the scribe were seen for these coatings during the visual assessment.

The coatings with high amount of corrosion creep are dense coatings, compared to the silicate coatings. The coatings that revealed highest corrosion creeps are epoxy coatings, a high Zn primer and an inorganic coating without active pigments. Dense coatings lead to less ion diffusion through the coating layer, compared to a more open structure where the ion diffusion increases. The resistance against ion transfer through the coating is therefore limited. Less diffusion may lead to increased amount of TSA corrosion because the environment under the repair coating becomes acidified. The crevice corrosion mechanism that occur on coated TSA is presented in Section 2.2. The high corrosion

creep for the high Zn primer was most unexpected, since the coating is not classified as an epoxy coating. The electrical resistance showed constant value for all the coating thicknesses. However, the impedance values presented in Section 4.3 revealed relative similar values for the high Zn primer and the Zn epoxy. The high Zn primer showed even higher impedance values compared to the modified Zn epoxy. This shows that the high Zn primer is a relative dense coating, which may have contributed to blistering. Lowest corrosion creep, of the coatings that showed blistering, was seen for the modified Zn epoxy. This may also be linked to the impedance, because the modified Zn epoxy revealed lowest impedance of the coatings that blistered. The inorganic copolymer coating did also reveal high impedance. The coatings that revealed highest corrosion creep showed also the highest impedance due to dense structures. This shows that dense coating structures are unfavorable for a TSA repair coat.

The Zn epoxy, high Zn primer and the modified Zn epoxy showed blisters after the cyclic coating test. These coatings are dense, contain anodic particles (Zn) and were electrical conductive. Zinc form oxide (ZnO) at alkaline pH values. This is shown in the Pourbaix diagram for pure zinc in Section 2.5. Since alkaline corrosion products forms, this may have led to neutralization of the pH below the repair coating. The aspect regarding electrical conductivity could also have contributed to transfer of the electrochemical reactions to the surface of the repair coating. However, these two effects were assumed limited due to blistering and high amount of TSA corrosion. The protection mechanisms related to cathodic polarization, electrical conductivity and buffering effect was therefore assumed not dominant enough to avoid blistering when a dense coating was present.

Some of the silicate coatings contained anodic elements that form alkaline corrosion products, such as magnesium and partly zinc, while other contained aluminium that form corrosion products at lower pH. The Pourbaix diagrams for aluminum is shown in Section 2.4, zinc in Section 2.5 and magnesium in Section 2.6. The Al silicate showed similar results as the Mg silicate and Zn silicate without blisters, even though magnesium and zinc form corrosion products at more alkaline pH values. All silicate coatings showed promising results without blistering, and the protection mechanism regarding the neutralizing effect was assumed to be less dominant than the open structure mechanism. The MgO silicate is assumed to be none conductive due to none conductive oxide, even though an electrical resistance of 0.2 Ω was measured. The MgO silicate revealed similar results without blisters such as the Mg silicate that is electrical conductive. The amount of conductive particles decrease with increasing exposure time due to oxidizing, but still some intact particles was assumed to be present for the Mg silicate. This shows that open structured repair coatings may provide good corrosion protection both as conductive and none conductive, and that alkaline corrosion products are not decisive to avoid blistering.

Corrosion products formed on the surfaces were examined by ICP-QQQ to evaluate the main element present in the products. The results are presented as percentage in Section 4.2.4, while the report from SINTEF are presented in Appendix B, Section B.5. Magnesium, aluminium and zinc were chosen for the analysis, since these elements were present in some of the repair coatings. This is stated in Section 2.3. The amount of aluminium corrosion products varied for the different repair coatings. The coatings with blisters and highest corrosion creep had higher amount of aluminium from the TSA compared to the anodic element in the corrosion products. This showed that blisters can be associated with high

amount of TSA corrosion and the aluminium corrosion products. The corrosion product formed on the inorganic copolymer coating was white and assumed to be aluminium from the TSA, since the coating did not contain active particles. Only zinc containing coatings, in addition to the inorganic copolymer coating, revealed blisters. For the coatings without blisters, no trend regarding the main element present in the corrosion products was seen. Some of the coatings without blisters showed higher amount of aluminium from the TSA compared to the anodic element, while some showed higher amount of the anodic element. In the case of Al silicate, it was difficult to determine whether the aluminium originated from the TSA or the repair coating.

The ICP-QQQ analysis was not able to dissolve all the corrosion products, and some precipitates were seen, especially for the silicate coatings. The precipitate was green for the Zn-, MgO- and Mg silicates, which may indicate that some of the binder was collected together with the corrosion products. Green pigments are added to the binder used for the silicate coatings. Cations such as Zn^{2+}, Mg^{2+} and Al^{3+} were dissolved by this method. Other possible components that do not dissolve in HCl or HNO_3 are not reported due to lack of charging. However, the method was not used as a quantitative analysis to determine all elements present in the corrosion products. The most important elements were aluminium, zinc and magnesium to be able to determine in which degree aluminium from the TSA layer was present.

5.4   Electrochemical impedance

The electrochemical impedance was measured in order to evaluate the ion diffusion for the various coatings, and the results will be compared to the results obtained during the cyclic coating test. The electrochemical impedance at frequency 0.001 Hz is plotted against immersion time in Section 4.3. All silicate coatings and the high Zn primer revealed increasing impedance at 0.001 Hz with increasing immersion time. The Zn epoxy, the modified Zn epoxy and the inorganic copolymer coating showed decreasing impedance at 0.001 Hz with increasing immersion time. Epoxy coatings diverge from silicate coatings relative to structure and density. The inorganic copolymer coating showed even higher impedance than the epoxy coatings. The silicate coatings showed generally lower impedance compared to the other repair coatings due to a more open structure. Low density did therefore reveal lower impedance, compared to higher impedance for more compact coatings. Low impedance is favorable in order to avoid TSA corrosion due to increased ion diffusion through the coating layer. The acidified environment below the repair coating is then avoided. The silicate coatings with lowest impedance showed promising results in the cyclic coating test.

The impedance increased with exposure time for the silicate coatings due to corrosion of the metal particles, and increased amount of oxides sealing the coatings. Initially, the amount of metal particles was high, but as the exposure time increased the particles corroded and transformed to oxides. This was not applicable for the MgO silicate, where oxides already were formed. As the exposure time increased, the coating structure appeared more open, due to less intact metal particles. This was also seen for the high Zn primer. The particles in the epoxy coatings are more protected and the coating structure appear more compact, compared to the silicate coatings. This may be the reason why the impedance generally was higher for the epoxy coatings. As the immersion time increased, the amount

of corroded particles increased and the structure appeared more open. This led to decreasing impedance.

No damage was introduced to the samples, as for the cyclic coating test. However, some correlation between the impedance and the type of repair coatings that revealed blistering during the cyclic coating test was seen. The coatings that revealed highest impedance, showed blistering and highest corrosion creep during the cyclic coating test. This was applicable for the Zn epoxy, the high Zn primer, the modified Zn epoxy and the inorganic copolymer coating. The silicate coatings did not reveal blistering, but these showed lower impedance and a more open structure. This proves that an open coating structure is important for a TSA repair coating to provide corrosion protection. With a dense coating layer, the ion diffusion decrease, which again leads to increased TSA corrosion.

The light microscope images presented in Section 4.3.1 revealed intact repair coatings, without cracks. The density of the different repair coatings varies due to different coating type, as explained before. However, all coatings showed sufficient diffusion properties in order to avoid acidification and pH decrease below the repair coatings. This was the case when no damage was introduced to the samples, and the artificial seawater gradually reduced the repair coatings. Some sporadic TSA corrosion was seen, but not enough to affect the corrosion behavior. The crevice corrosion mechanism presented in Section 2.2 with rapid degradation of the TSA due to acidification and pH decrease, was therefore not seen below the repair coatings when no damage was introduced.

EDS analysis were performed on the corrosion products formed on the surfaces. The results are based on the average values from 12 scanned areas. All coatings revealed higher amount of the anodic element, Al, Zn or Mg, compared to aluminium from the TSA. Calcium was also dominant for the MgO- and Mg-silicate. A thin film can be seen on the MgO silicate in Figure 4.28 and the Mg silicate in Figure 4.29. Both figures are presented in Section 4.3.1. The artificial seawater contained calcium, which may have contributed to a calcium carbonate film on the surfaces. As mentioned in Section 2.6, a protective calcium carbonate film may form on magnesium alloyed with calcium. The coatings did not contain calcium, but due to exposure in electrolyte containing this element this may have formed on the surfaces. The film forms at high pH values, while the pH in the electrolyte did not exceed 8.67 during the test period. See Figure 4.23 for the pH development during the test period. This may indicate that the pH on the coating surface was higher than in the electrolyte. The MgO silicate was chosen as a possible repair coating due to the neutralizing effect. Corrosion products of magnesium are formed at alkaline pH values. This is shown in the Pourbaix diagram for magnesium in Section 2.6. The MgO- and Mg-silicate did also reveal promising results after the cyclic coating test, and the buffering effect may therefore have contributed to good corrosion behavior, in addition to the open coating structure.

Based on the pH development towards 8.00 and the chloride concentration in the electrolyte, the type of corrosion product could be estimated for the zinc according to Figure 2.5. This is only an estimate, and further testing for either X-ray diffraction (XRD) analysis or by EPMA analysis should be carried out to find the exact corrosion products. This was not conducted during the Msc project due to lack of time. The ICP-QQQ analysis performed after the cyclic coating test revealed more aluminium in the

corrosion products compared to anodic elements, for the samples with blisters and high amount of corrosion creep. EDS analysis introduce some uncertainties to the element analysis. No blisters were seen during the exposure for the electrochemical impedance measuring. The trend with more aluminium for the samples with blisters was therefore not seen for the EDS analysis. The corrosion products formed on the surface was not collected, as for the ICP-QQQ analysis performed after the cyclic coating test. Due to this, the results from the EDS analysis and the ICP-QQQ analysis cannot be directly compared.

5.5   Open circuit potential

The OCP measurements vs. Ag/AgCl are presented in Section 4.4 with exposure time plotted against potential. The repair coatings, except for the inorganic copolymer coating, showed partly similar tendency of potential development. The development may be divided into three stages. This was not applicable for the inorganic copolymer coating due to different behavior compared to the other coatings. The first stage was characterized with a rapid drop in potential to a minimum value where the steel polarized. The minimum value corresponded to a potential where the zinc, aluminium or magnesium started to dissolve on the surface. When the minimum potential was reached, the potential increased towards a more positive potential. This increase corresponded to the second stage where formation of oxides on the surfaces occurred. The change in potential during stage two appeared gentler compared to the first stage. The third stage consisted of a slow potential increase, which corresponded to stable growth of corrosion products on the surfaces.

All the zinc containing coatings had a potential more negative than -800 mV during the test, which indicates that the steel was protected. A potential more negative than approximately -787 mV vs. Ag/AgCl is located in the immune area for iron in the Pourbaix diagram [21]. The instability of the curves representing the zinc containing coatings may be explained by increased number of measurements after approximately 100 days. Increased instability was seen for the MgO-, Mg- and Al-silicates and the inorganic copolymer coating. Every time the electrochemical impedance was measured, the multi-cells were moved due to restricted space near the Gamry Potentiostats. Movement of the equipment may therefore partly explain the rapid potential drops for these coatings since the corrosion products on the surface were affected. The MgO-, Mg- and Al-silicate revealed a potential more negative than -850 mV during the test period. This potential corresponds to the immune area for iron [21]. A potential of respectively -800 mV and -850 mV vs. Ag/AgCl at a pH of approximately 8 corresponds to the passive region for aluminium and the active area for respectively zinc and magnesium. This is shown in the Pourbaix diagrams for aluminium, zinc and magnesium in Figure 2.3, Figure 2.4 and Figure 2.5. The MgO silicate showed generally the lowest OCP of all the repair coatings. The TSA layer below the MgO silicate may have influenced the potential measurements, so that the potential of aluminium was measured instead of the MgO potential.

OCP for the inorganic copolymer coating decreased steadily towards a more negative potential during the test period. The potential curve presented was admittedly not smooth. Each time a measurement was taken the potential started at a relative negative value before it increased towards a more positive value. The stabilized values are presented in Section 4.4 and Appendix E. The reason for the overall

decrease in potential may be explained by a gradual reduction of the coating. The barrier effect was therefore reduced with increasing exposure time. A clear drop in potential to approximately -1100 mV vs. Ag/AgCl was seen after 77 days. The electrochemical impedance did also decrease with increasing immersion time for the inorganic copolymer coating. The barrier effect was reduced and the coating became more open as the exposure time increased. However, blisters and high corrosion creep of the TSA was seen during the cyclic coating test even though the barrier effect was reduced with increasing exposure time. Combination between no active elements and high density of the coating structure did therefore appear unfavorable for a TSA repair coating.

The pH development revealed a pH decrease for the multi-cell holding the zinc containing coatings. The lowest pH measured for the MgO-, Mg-, Al- and the inorganic copolymer coating was 8.34. The lowest value for the zinc containing coatings was 8.00. The small pH change may indicate that the aluminium ion concentration was small. No damage was introduced and all repair coatings were intact according to the images presented in Section 4.3.1. Since all repair coatings were intact with no severe TSA corrosion, the ionic resistance was assumed to be low enough so that ions diffused instead of being trapped below the repair coating.

5.6   Crevice corrosion test

The crevice corrosion tests were performed in order to have a short-term test compared to the cyclic coating test, and still test the corrosion behavior of the various repair coatings. This was not so successful. Two different test setups were tested during the MSc project. The differences between the setups were related to the crevice design and how the crevice corrosion mechanism was tested. The results for both setups are presented in Section 4.5.

Test setup 1 is presented in Section 3.5.1, while the results are presented in Section 4.5.1. A potential of -700 mV was applied and the test was conducted for 14 days. This potential corresponds to the active region for iron, aluminium, zinc and magnesium, and was chosen to initiate corrosion reactions for all elements. Figure 4.33 revealed high amount of blistering on some of the repair coatings, not only around the machined scribe. Corrosion reactions were initiated, but most likely on the entire surface of the repair coating and not in the crevice at the machined scribe. Due to ion diffusion through the repair coatings, TSA corrosion occurred on the entire surface and not only at the crevice opening. This was not desirable in order to test the TSA crevice corrosion mechanism. Highest amount of blistering was seen on the Zn epoxy, the modified Zn epoxy and the inorganic copolymer coating. These three coatings did also show blistering in the cyclic coating test.

The samples were divided into two containers during the test period and the same pH development was seen for both containers, see Figure 4.34. After respectively 7 and 9 days of exposure, the pH dropped before the values stabilized between pH 4.50 and 4.60. Aluminium oxide formed during corrosion of coated TSA appears unstable below pH 4, as stated in Section 2.2. Aluminium was exposed both from the TSA at the crevice openings, and the freely exposed Al silicate surface. Based on pH decrease, it was assumed that active corrosion of the aluminium had occurred. The test was finished after 14 days because the anodic current showed either decreasing or stabilizing values. The

anodic current curves for all the repair coatings are shown in Figure 4.35. It was then assumed that the main corrosion processes had occurred, and that further corrosion would not lead to change in results.

The continuous TSA corrosion from the crevice opening and the amount of corroded metal particles were evaluated based on cross sectional light microscope images. A summary is given in Table 4.5 and the light microscope images are presented in Appendix F, Section F.1. Highest amount of continuous TSA corrosion was seen for the high Zn primer, the Zn epoxy and all the silicate coatings, except for the Al silicate. Lowest continuous TSA corrosion was seen for the modified Zn epoxy, the Al silicate, the inorganic copolymer coating and the TSA coated with epoxy. During machining of the samples before resin casting, large parts of the Zn silicate layer flaked off. High amount of TSA corrosion was therefore assumed for the Zn silicate, since the topcoat flaked off. The results regarding high TSA corrosion for the silicate coatings differ from the results obtained during the cyclic coating test. The light microscope images in Appendix F revealed high amount of TSA corrosion for these coatings.

Earlier experiences [1] have revealed high amount of blistering and continuous corrosion of the TSA for Zn epoxy. No sample with TSA coated with epoxy was exposed in the cyclic coating test, and the result for this sample can only be compared to earlier experiences. All the silicate coatings showed promising results after the cyclic coating test. This was not the case for crevice corrosion test setup 1. Only the Al silicate showed low degree of TSA corrosion, while the other silicate coatings showed continuous corrosion along the entire crevice. The electrochemical impedance measurements revealed a relative open structure for the silicate coatings that contributed to ion diffusion. Blistering was not seen on the silicate coatings in Figure 4.33. This means that the high amount of TSA corrosion most likely was caused by high ion diffusion, and due to low degree of ion trapping, blistering was avoided. Blisters were not seen for the silicate coatings during the cyclic coating test, which shows correlation to the crevice corrosion test 1. However, low average corrosion creep was seen for the silicate coatings after the cyclic coating test, while the crevice corrosion test revealed high amount of continuous TSA corrosion. Note that the measuring method regarding the TSA corrosion differed between the cyclic coating test and the crevice corrosion test. The average corrosion creep was measured around the entire scribe after the cyclic coating test, while the continuous TSA corrosion was estimated based on cross sectional images represented one spot at the scribe after the crevice corrosion test. The samples were not continuously immersed in artificial seawater during the cyclic coating test, while this was the case for the crevice corrosion test. Since the samples had continuously access to chloride containing electrolyte, this may have caused increased corrosion for the silicate coatings during the crevice corrosion test compared to the cyclic coating test.

The TSA coated with epoxy was also expected to corrode more than the results revealed, since epoxy is a barrier coat with high density that contributes to ion trapping. No blisters were seen for this samples and relative low degree of TSA corrosion, compared to the silicate coatings. However, due to dense coating structure ions was not able to diffuse through the epoxy, as was the case for the silicate coatings. The inorganic copolymer coating showed blisters and high TSA corrosion creep after the cyclic coating test. The electrochemical impedance did also reveal high impedance and a dense coating structure for this coating. Higher degree of TSA corrosion was therefore expected during the

crevice corrosion test. The same case was concluded for the modified Zn epoxy. Based on the results obtained and comparison to the cyclic coating test and earlier experiences, it was therefore decided that test setup 1 could not be used as a short-term crevice corrosion test. High amount of blistering on the freely exposed surface area, not only concentrated around the scribe, was also taken into account when the design was considered not fully optimized. During the cyclic coating test, the blisters were mostly concentrated around the machined scribe.

Test setup 2 presented in Section 3.5.2 was run twice, respectively for 16 and 30 days. Only the test run for 16 days is presented in Section 4.5.2 due to similar trends of pH development, anodic current and corrosion degradation. However, the corrosion was more severe on the samples exposed for 30 days, but the tendency was consistent. A potential of -780 mV was applied. This potential was chosen in order to initiate corrosion reactions on the aluminium from the TSA, or the aluminium, magnesium or zinc from the repair coatings. The steel was then located in the immune region [21]. The pH decreased initially from 8.19 to 7.07. The decrease in pH was smaller and more gradual compared to test setup 1. No Al silicate surface was freely exposed in the electrolyte and the TSA was only exposed on the lateral sides of the samples. It was therefore assumed that the amount of aluminium ions was smaller in the electrolyte for test setup 2, compared to test setup 1. This caused smaller pH reduction. A potential of -700 mV was applied during test setup 1, while a potential of -780 mV was applied during test setup 2. More corrosion was therefore initiated during test setup 1 due to more positive potential, and less pH decrease was seen during test setup 2. The tests were completed when the anodic current showed decreasing or stabilizing values as explained for test setup 1. The pH development and anodic current are presented in Figure 4.37 and Figure 4.38.

Test setup 2 did neither test the TSA crevice corrosion mechanism, as for test setup 1. A summary of the evaluations is presented in Table 4.6. The light microscope images that the evaluations were based on are presented in Appendix F, Section F.2. It was expected that the Zn epoxy, the TSA coated with epoxy and the inorganic copolymer coating should have considerably more TSA corrosion than just at the crevice opening. These assumptions were based on earlier experiences and the results obtained after the cyclic coating test. In previous studies, severe corrosion has been seen on TSA coated with epoxymastic [1]. Zn epoxy revealed highest corrosion creep and considerable amount of blisters after the cyclic coating test compared to the other coatings. The inorganic copolymer coating did also reveal high amount of corrosion creep and blisters after the cyclic coating test. No significant corrosion of the TSA was seen for these coatings after testing test setup 2. All the silicate coatings showed either general, continuous or sporadic TSA corrosion. The silicate coatings revealed more TSA corrosion than the Zn epoxy, the TSA coated with epoxy and the inorganic copolymer coating.

The results obtained by crevice corrosion setup 2 differ from earlier results [1] and from the cyclic coating test. The silicate coatings showed promising results after the cyclic coating test with almost no TSA corrosion. During test setup 2, extensive TSA corrosion was seen for these coatings, especially the Al- and Mg-silicate. The mentioned aspects may therefore indicate that the setup must be further developed to be able to test the TSA crevice corrosion mechanism. The crevice former covered the entire surface, and ions were therefore not able to diffuse through the repair coating layer. The ion diffusion that caused high TSA corrosion on the silicate coatings during crevice corrosion test setup 1

was not present in test setup 2. The mechanism with ion trapping below dense coating layers was also avoided. The coatings with highest impedance due to denser structures revealed lowest degree of TSA corrosion after test setup 2. This result differs from the results obtained in the cyclic coating test.

Another crevice corrosion test was performed for the zinc containing coatings during the project work performed in 2015 [2]. This test setup consisted of a crevice former, corresponding to the crevice former used in test setup 2, but with a different size. The crevice former did not cover the entire surface where the repair coatings were applied. The test setup was therefore a combination of test setup 1 with freely exposed surface area, and test setup 2 with a crevice former covering the surface. The desired crevice corrosion mechanism for the TSA was neither tested by this test setup. This was figured out on the basis of average corrosion current calculations. The calculations emphasized that the main corrosion reactions occurred outside on the freely exposed surface area, and not under the crevice former [2]. The calculations were based on light microscope images of the coating cross sections.

Since none of the crevice corrosion setups were considered optimal in relation to the TSA crevice corrosion mechanism, the results obtained after the cyclic coating test is considered as the main results. The silicate coatings showed promising results during the cyclic coating test, while the Zn epoxy showed highest TSA corrosion creep. This was not seen during the crevice corrosion tests. The high Zn primer, the modified Zn epoxy and the inorganic copolymer coating did also reveal higher corrosion creep during the cyclic coating test, compared to the silicate coatings. During the crevice corrosion tests the silicate coatings showed generally more TSA corrosion, compared to the repair coatings that revealed blisters after the cyclic coating test. This shows that the long-term coating test showed more reliable results and more similar results as earlier studies, compared to the short-term crevice corrosion test that must be further developed.

5.7   Repair coatings for TSA – desired properties

Desired coating properties for the repair coat are discussed in Section 2.3. The cyclic coating test was performed to test the corrosion behavior in a long-term test. The crevice corrosion test was performed to have an alternative short-term test. As discussed in Section 5.6, the desirable TSA crevice corrosion mechanism was not tested, and should be further developed. The results obtained by the cyclic coating test will therefore be emphasized. Visual assessment, calculations of the average corrosion creep and corrosion morphology was evaluated after the cyclic coating test was finished. The differences between the various coatings were significant. Blistering and cracking of the topcoat has earlier been associated with TSA corrosion, and this was supported by average corrosion creep calculations and light microscope images.

The silicate coatings showed promising results without blisters and low corrosion creep after 20 cycles of exposure in the cyclic coating test. The corrosion morphology did also revealed low degree of TSA corrosion for these coatings. The Zn silicate showed highest corrosion creep of the silicate coatings, but the corrosion creep requirement stated in ISO 20340 was still fulfilled. The Al-, Mg- and MgO-silicate showed negligible corrosion creep. The electrochemical impedance measurements showed

lower impedance for these coatings compared to the coatings with blisters. This showed that an open coating structure contributed to less blisters because the environment below the repair coating was not acidified. Aggressive environment was therefore not formed, and the mechanism contributed to good corrosion behavior for the silicate coatings as a TSA repair coat. All the silicate coatings, except the MgO silicate, was electrical conductive, and the Zn-, Mg- and Al-silicate contained anodic elements. Some of the silicate coatings contained alkaline elements, such as magnesium and zinc, which may have contributed to neutralization of the environment below the repair coating. Nevertheless, the Al silicate and aluminium forms corrosion products at a lower pH, compared to magnesium and zinc, and still showed similar results without blisters. The MgO silicate, which contains oxides that are none conductive, showed also promising results like the conductive silicate coatings. The protection mechanisms regarding electrical conductivity and buffering capacity were therefore not assumed to be the most important mechanisms. Common for all the silicate coatings were an open structure. This protection mechanism was therefore considered as the most contributing factor to provide good protection behavior as a TSA repair coat.

Zn epoxy revealed highest amount of blistering of the repair coatings during the cyclic coating test. Blisters were also seen on the high Zn primer, the modified Zn epoxy and the inorganic copolymer coating. These coatings did also reveal higher corrosion creep compared to the silicate coatings. The coatings that revealed blisters during the cyclic coating test showed higher electrochemical impedance compared to the silicate coatings that had a more open structure. Due to denser coating structures, the barrier effect may have led to decreased diffusion of the electrolyte. This may further have developed an acidic environment below the repair coating, which caused blistering. This shows that the coating structure is important to avoid development of blisters. A dense coating structure is therefore unfavorable for a repair coating because it may lead to TSA corrosion. The Zn epoxy, the high Zn primer and the modified Zn epoxy contained zinc particles, which are both anodic and electrical conductive. However, the amount of active zinc particles decreased with increasing exposure time since the zinc oxidized to zinc oxide. The transfer of electrochemical reactions to the surface was most likely reduced with increasing exposure time. Even with high zinc content and low electrical resistance, blistering occurred on the high Zn primer. The inorganic copolymer coating did not contain active elements and had a dense structure. This coating revealed blisters, and a combination of dense coating structure and absence of active elements is therefore unfavorable for the repair coating.

Based on the results obtained during the MSc project, an open coating structure has proven to be an important property for a TSA repair coat. Aggressive environment has been released, instead of being formed below the repair coating. This is applicable for the silicate coatings. Coatings with denser structures and anodic elements, such as Zn epoxy, high Zn primer and the modified Zn epoxy, revealed blistering after the cyclic coating test. These coatings were also electrical conductive. This shows that even with cathodic protection and electrical conductivity, the mechanism regarding the coating structure was more dominate. None of the silicate coatings showed blisters after the cyclic coating test. Al silicate showed similar results as the silicate containing anodic elements that form alkaline elements. The MgO silicate that contain none conductive oxides did also show similar results as the conductive silicate coating. Based on this, the protection mechanism regarding the coating structure is considered the most important for the tested repair coatings.

6 Conclusion

The aim for the MSc project has been to find a repair coating for TSA in connnection to coating damages. The coating must provide corrosion protection without triggering the TSA duplex corrosion mechanism, and shall be applied without removing the intact TSA. Eight different repair coatings were tested. These results were obtained:

- The silicate coatings, i.e. Zn-, MgO-, Mg- and Al-silicate, showed best corrosion behavior as a TSA repair coat without blistering after the cyclic coating test. The Zn silicate showed highest corrosion creep, of the silicate coatings, with an average corrosion creep of approximately 0.6 mm. The MgO-, Mg- and Al-silicate revealed negligible corrosion creep.

- The Zn epoxy showed highest amount of blistering and the most severe TSA corrosion creep after the cyclic coating test. The coating showed an average corrosion creep of approximately 5.1 mm. The high Zn primer, the modified Zn epoxy and the inorganic copolymer coating did also reveal blistering during the same test, but not as severe as the Zn epoxy.

- An open coating structure proved to be the most important coating property for the tested TSA repair coatings. Aggressive environment below the repair coating was then released.

- The mechanisms regarding cathodic polarization, electrical conductive coatings and the neutralizing effect are considered less important compared to the mechanism regarding an open coating structure.

- The crevice corrosion tests were performed in order to have a short-term test for the TSA crevice corrosion mechanism. This was not successful, and further development of the test setups must be performed in order to evaluate the corrosion behavior for various TSA repair coatings.

7   Recommendations for Further Work

Several experiments were performed during the MSc project. Some further work may be performed to fully be able to characterize the corrosion behavior for the various repair coatings. The proposals in this section were not performed during the MSc project due to lack of time.

- Further development of the design regarding the short-term crevice corrosion test should be carried out to be able to actually test the TSA crevice corrosion mechanism for the various repair coatings. Steel samples coated with TSA and the repair coatings may be fully coated with epoxy, except for the entire lateral sides. Figure 7.1 shows the lateral side of the sample with freely exposed TSA and repair coating. No steel or freely exposed surface on top of the samples will then be exposed, except for the cross sectional coating layers. Other potentials than -700 mV and -780 mV vs. Ag/AgCl should be applied.

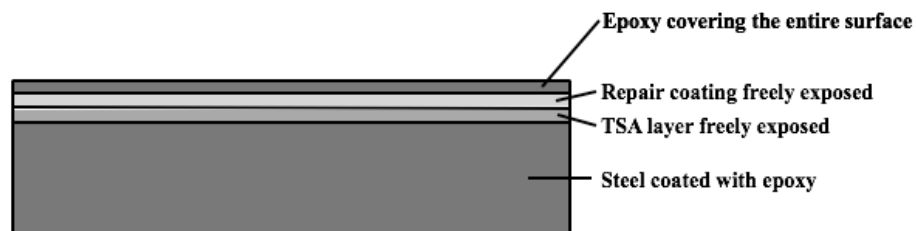Figure 7.1: Proposal for further work regarding the crevice corrosion design.

- The corrosion products formed on the sample surfaces during the cyclic coating test may be further analyzed by other test methods then the ICP-QQQ. Then, it may be possible to analyze and decide exact corrosion products formed on the surfaces, not only the main elements present. These methods may be either XRD or EPMA analysis.

8 Bibliography

1. Knudsen, O.Ø., *Coating systems for long lifetime: Thermally Sprayed Duplex Systems.* Report no. SINTEF A14189, 2010, SINTEF: Trondheim.

2. Askestad, H., *Painted TSA - Coating repair (internal report).* 2015, Department of Engineering Design and Materials: Norwegian University of Science and Technology (NTNU).

3. Grundmeier, G., Schmidt, W., Stratman, M., *Corrosion protection by organic coatings: electrochemical mechanism and novel methods of investigation.* Electrochimica Acta, 2000. **45**(15-16): p. 2515-2533.

4. NORSOK, *NORSOK M-501: Surface preparation and protective coating.* Edition 6, February 2012.

5. Nisancioglu, K., *Corrosion behaviour and protection of copper and aluminium alloys in seawater.* 50, ed. E.F.o. Corrosion. 2007: Woodhead Publishing.

6. Paredes, R.S.C., Amico, S.C., d´Oliveira, A.S.C.M., *The effect of roughnes and pre-heating of the substrate on the morphology of aluminium coatings deposited by thermal spraying.* Surface & Coatings Technology, 2006. **200**(9): p. 3049-3055.

7. ISO, *ISO 8503-1: Preparation of steel substrates before application of paints and related products-Surface roughness characteristics of blast-cleaned steel substrates-Part 1: Specifications and definitions for ISO surface profile comparators for the assessment of abrasive blast-cleaned surfaces.* Edition 2, 2012.

8. Glogović, Z., Alar, V., Kožuh, Z., Stojanović, I., Kralj, S., *Corrosion properties of thermal sprayed aluminium (TSA) coatings deposited by powder flame spraying.* Materials Science & Engineering Technology, 2011. **42**(3): p. 224-228.

9. Montemor, M.F., *Functional and smart coatings for corrosion protection: A review of recent advances.* Surface & Coatings Technology, 2014. **258**: p. 17-37.

10. ISO, *ISO 12944-5: Paints and varnishes-Corrosion protection of steel structures by protective paint systems -Part 5: Protective paint systems.* Edition 2, 2007.

11. Dalene, M., Skapring, G., Spanne, M., Willers, S., *Present knowledge regarding exposure and possible health effects of "hot work" in coated metal parts offshore* 2007, Institutet För Kemisk Analys Norden AB: Sweden.

12. Bardal, E., Drugli, J.M., Gartland, P.O, *The behaviour of corrosion-resistant steels in seawater: A review.* Corrosion Science, 1993. **35**(1-4): p. 257-267.

13. Shreepathi, S., Priyansh, B, Mallik, B.P, *Electrochemical impedance spectroscopy investigations of epoxy zinc rich coatings: Role of Zn content on corrosion protection mechanism.* Electrochimica Acta, 2010. **55**(18): p. 5129-5134.

14. Cho, K., Abdulsalam, M.I., Pickering, H.W., *The Effect of Electrolyte Properties on the Mechanism of Crevice Corrosion in Pure Iron.* Journal of The Electrochemical Society, 1998. **145**(6): p. 1862-1869.

15. Reboul, M.C., Baroux, B., *Metallurgical aspects of corrosion resistance of aluminium alloys.* Materials and Corrosion, 2011. **62**(3): p. 215-233.

16. Blücher, D.B., Lindström, R., Svensson, J-E., Johansson, L-G., *The Effect of CO2 on the NaCl-Induced Atmospheric Corrosion of Aluminum.* The Electrochemical Society, 2001. **148**(4): p. 127-131.

17. Graedel, T.E., *Corrosion Mechanisms for Aluminum Exposed to the Atmosphere.* The Electrochemical Society, 1989. **136**(4): p. 204-212.

18. Rodriguez, R.M.H.P., Paredes, R.S.C., Wido, S.H., Calixto, A., *Comparison of aluminum coatings deposited by flame spray and by electric arc spray.* Surface & Coatings Technology, 2007. **202**(1): p. 172-179.

19. Makar, G.L., Kruger, J., *Corrosion of magnesium.* International Materials Reviews, 1993. **38**(3): p. 138-153.

20. Alfantazi, A.M., Ahmed, T.M., Tromans, D., *Corrosion behavior of copper alloys in chloride media.* Materials & Design, 2009. **30**(7): p. 2425-2430.

21. Barnum, D.W., *Potential-pH diagrams.* Chemical Eduction, 1982. **59**(10): p. 809-812.

22. Fuente, D., Castaño, J.G., Morcilloa, M., *Long-term atmospheric corrosion of zinc.* Corrosion Science, 2007. **49**(3): p. 1420-1436.

23. Chen, Z.Y., Persson, D., Leygraf, C., *Initial NaCl-particle induced atmospheric corrosion of zinc-Effect of CO2 and SO2.* Corrosion Science, 2008. **50**(1): p. 111-123.

24. Lindström, R., Svensson, J-E., Johansson, L-G., *The Atmospheric Corrosion of Zinc in the Presence of NaCl-The Influence of Carbon Dioxide and Temperature.* The Electrochemical Society, 2000. **147**(5): p. 1751-1757.

25. Jönsson, M., Persson, D., Leygraf, C., *Atmospheric corrosion of field-exposed magnesium alloy AZ91D.* Corrosion Science, 2008. **50**(5): p. 1406-1413.

26. Ghali, E., Dietzel, W., Kainer, K-U., *General and Localized Corrosion of Magnesium Alloys: A Critical Review.* Materials Engineering and Performance, 2004. **13**(1): p. 7-23.

27. Lindström, R., Svensson, J-E., Johansson, L-G., *The Influence of Carbon Dioxide on the Atmospheric Corrosion of Some Magnesium Alloys in the Presence of NaCl.* The Electrochemical Society, 2002. **149**(4): p. 103-107.

28. Mandal, M., Moon, A.P., Deo, G., Mendis, C.L., Mondal, K., *Corrosion behavior of Mg-2.4Zn alloy micro-alloyed with Ag and Ca.* Corrosion Science, 2014. **78**: p. 172-182.

29. Feliu Jr., S., Maffiotte, C., Samaniego, A., Galván, J.C., Barranco, V., *Effect of naturally formed oxide films and other variables in the early stages of Mg-alloy corrosion in NaCl solution.* Electrochimica Acta, 2011. **56**(12): p. 4554-4565.

30. ISO, *ISO 20340: Paints and varnishes-Performance requirements for protective paint systems for offshore and related structures*. Edition 2, 2009.

31. Smith, J., Akbari-Sharbaf, A., Ward, M.J., Murphy, M.W., Fanchini, G., Sham, T.K., *Luminescence properties of defects in nanocrystalline ZnO.* Applied Physics, 2013. **113**: p. 093104-1-093104-6.

32. Aylward, G., Findlay, T., *SI Chemical Data*. Vol. 6th edition. 2008: John Wiley& Sons Australia.

Appendix A　　Dry Film Thickness

Lowest, highest and mean DFT, in addition to standard deviation and number of measurements per sample are presented in Table A.1 to Table A.5. The same measurement pattern with 17 measuring points was used for all samples. Parallel X.1-X.3 were tested in the cyclic coating test, parallel X.4 for the electrochemical impedance and OCP measurements and parallel X.5 for the crevice corrosion tests.

Table A.1: Overview of the dry film thickness for the parallels coated with high Zn primer.

Sample	Material	Metallic coating	Repair coating	Lowest DFT [μm]	Highest DFT [μm]	Mean DFT [μm]	St. dev.	Number of measurements
Z.50.1	St 52	TSA	High Zn primer	20	109	71	23	17
Z.50.2				33	98	64	17	17
Z.50.3				49	95	74	15	17
Z.100.1	St 52	TSA	High Zn primer	52	132	88	22	17
Z.100.2				92	156	116	18	17
Z.100.3				88	190	122	27	17
Z.100.4				50	109	76	18	17
Z.150.1	St 52	TSA	High Zn primer	121	196	156	20	17
Z.150.2				72	175	121	27	17
Z.150.3				148	206	182	16	17
Z.150.5				121	176	149	19	17

Table A.2: Overview of the dry film thickness for the parallels coated with Zn epoxy.

Sample	Material	Metallic coating	Repair coating	Lowest DFT [μm]	Highest DFT [μm]	Mean DFT [μm]	St. dev.	Number of measurements
ZE.50.1	St 52	TSA	Zn epoxy	40	82	59	13	17
ZE.50.2				31	109	70	25	17
ZE.50.3				26	68	45	13	17
ZE.100.1	St 52	TSA	Zn epoxy	52	124	90	20	17
ZE.100.2				61	159	98	24	17
ZE.100.3				53	102	78	12	17
ZE.100.4				21	123	76	24	17
ZE.150.1	St 52	TSA	Zn epoxy	129	245	171	34	17
ZE.150.2				140	201	163	20	17
ZE.150.3				122	211	162	27	17
ZE.150.5				78	191	111	24	17

Table A.3: Overview of the dry film thickness for the parallels coated with modified Zn epoxy.

Sample	Material	Metallic coating	Repair coating	Lowest DFT [μm]	Highest DFT [μm]	Mean DFT [μm]	St. dev.	Number of measurements
H.50.1	St 52	TSA	Modified Zn epoxy	40	117	62	17	17
H.50.2				49	111	76	19	17
H.50.3				49	116	78	19	17
H.100.1	St 52	TSA	Modified Zn epoxy	56	174	101	26	17
H.100.2				69	149	101	24	17
H.100.3				54	143	92	22	17
H.100.4				51	181	100	32	17
H.150.1	St 52	TSA	Modified Zn epoxy	101	235	166	36	17
H.150.2				105	301	194	64	17
H.150.3				136	258	198	36	17
H.150.5				97	187	140	26	17

Table A.4: Overview of the dry film thickness for the parallels coated with Zn silicate.

Sample	Material	Metallic coating	Repair coating	Lowest DFT [μm]	Highest DFT [μm]	Mean DFT [μm]	St. dev.	Number of measurements
ZS.50.1	St 52	TSA	Zn silicate	29	87	58	18	17
ZS.50.2				24	107	57	19	17
ZS.50.3				23	100	63	22	17
ZS.100.1	St 52	TSA	Zn silicate	73	158	108	26	17
ZS.100.2				91	147	118	19	17
ZS.100.3				70	182	105	31	17
ZS.100.4				81	215	136	36	17
ZS.150.1	St 52	TSA	Zn silicate	123	152	137	10	17
ZS.150.2				127	207	168	20	17
ZS.150.3				120	214	170	27	17
ZS.150.5				130	188	150	14	17

Table A.5: Overview of the dry film thickness for the parallels coated with MgO-, Mg-, Al-silicate and the inorganic copolymer coating.

Sample	Material	Metallic coating	Repair coating	Lowest DFT [μm]	Highest DFT [μm]	Mean DFT [μm]	St. dev.	Number of measurements
MgO.100.1			MgO Silicate	64	190	106	29	17
MgO.100.2				65	161	109	25	17
MgO.100.3	St 52	TSA		81	156	119	25	17
MgO.100.4				69	143	104	23	17
MgO.100.5				50	158	97	31	17
Mg.200.1			Mg silicate	119	305	198	54	17
Mg.200.2				139	290	243	49	17
Mg.200.3	St 52	TSA		154	281	225	45	17
Mg.200.4				190	281	240	25	17
Mg.200.5				121	288	218	56	17
Al.150.1			Al silicate	75	187	115	32	17
Al.150.2				110	181	156	21	17
Al.150.3	St 52	TSA		108	216	156	30	17
Al.150.4				124	239	180	33	17
Al.150.5				153	204	184	14	17
V.150.1			Inorganic copolymer coating	97	279	175	52	17
V.150.2				124	237	175	38	17
V.150.3	St 52	TSA		118	212	165	31	17
V.150.4				69	290	183	59	17
V.150.5				117	222	157	30	17

Appendix B   Cyclic Coating Test

B.1   Cycles

The time from test initiation for each cycle is presented in Table B.1. The samples coated with the different repair coatings were inserted at different dates. The zinc containing repair coatings were initiated first, while the MgO-, Mg-, Al-silicate and the inorganic copolymer coating were inserted after 3 cycles. A delay of 3 cycles was therefore introduced for the zinc containing coatings after cycle 8 to abreast.

Table B.1: Overview of the cycles, the type of exposure, exposure time and total time from test initiation.

Cycle		Exposure	Exposure time [days]	Time from test initiation [days]	
1		UV/condensation	3	0	
		Salt fog	3	3	
		Freezer	1	6	
2		UV/condensation	3	7	
		Salt fog	3	10	
		Freezer	1	13	
3		UV/condensation	3	14	
		Salt fog	3	17	
		Freezer	1	20	
4	1	UV/condensation	3	21	0
		Salt fog	3	24	3
		Freezer	1	27	6
5	2	UV/condensation	3	28	7
		Salt fog	3	31	10
		Freezer	1	34	13
6	3	UV/condensation	3	35	14
		Salt fog	3	38	17
		Freezer	1	41	20
7	4	UV/condensation	3	42	21
		Salt fog	3	45	24
		Freezer	1	48	27
8	5	UV/condensation	3	49	28
		Salt fog	3	52	31
		Freezer	1	55	34
	6	UV/condensation	3		35
		Salt fog	3		38
		Freezer	1		41
	7	UV/condensation	3		42
		Salt fog	3		45
		Freezer	1		48
	8	UV/condensation	3		49
		Salt fog	3		52
		Freezer	1		55
9		UV/condensation	3	56	
		Salt fog	3	59	
		Freezer	1	62	

	UV/condensation	3	63
10	Salt fog	3	66
	Freezer	1	69
	UV/condensation	3	70
11	Salt fog	3	73
	Freezer	1	76
	UV/condensation	3	77
12	Salt fog	3	80
	Freezer	1	83
	UV/condensation	3	84
13	Salt fog	3	87
	Freezer	1	90
	UV/condensation	3	91
14	Salt fog	3	94
	Freezer	1	97
	UV/condensation	3	98
15	Salt fog	3	101
	Freezer	1	104
	UV/condensation	3	105
16	Salt fog	3	108
	Freezer	1	111
	UV/condensation	3	112
17	Salt fog	3	115
	Freezer	1	118
	UV/condensation	3	119
18	Salt fog	3	122
	Freezer	1	125
	UV/condensation	3	126
19	Salt fog	3	129
	Freezer	1	132
	UV/condensation	3	133
20	Salt fog	3	136
	Freezer	1	139

B.2   Visual appearance after 20 cycles

Pictures of the samples after 20 cycles of exposure are presented from Figure B.1 to Figure B.16. Three parallels are presented per coating thickness.
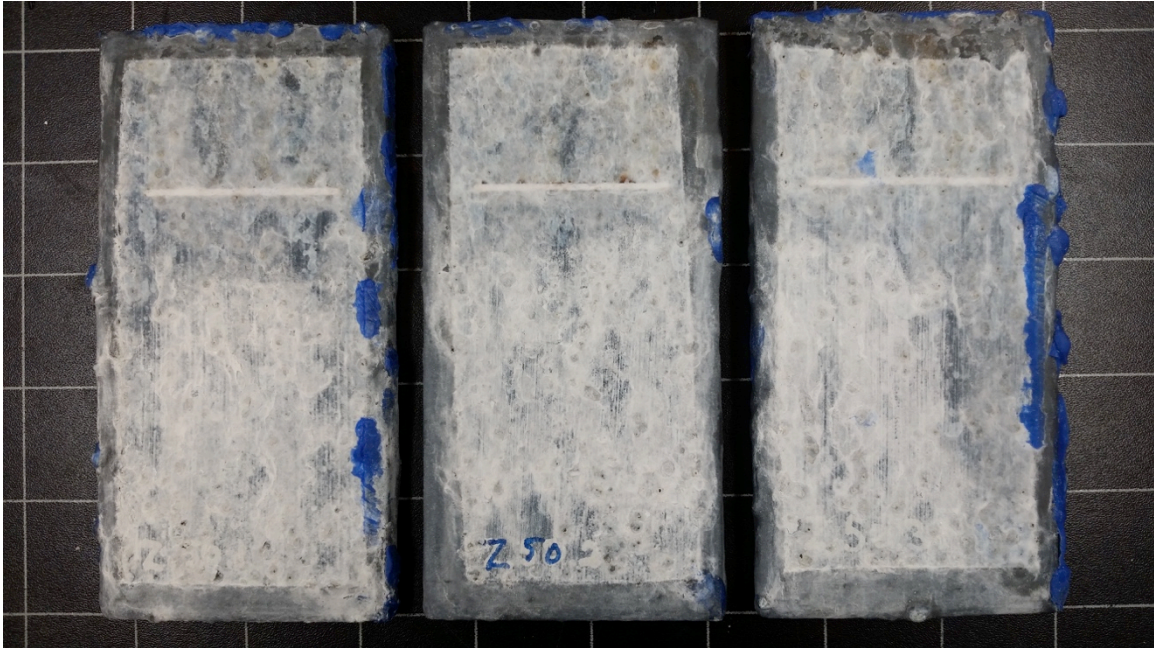
High Zn primer

DFT 50 μm

Figure B.1: Visual appearance of the high Zn primer with DFT 50 μm after 20 cycles of exposure.

DFT 100 μm
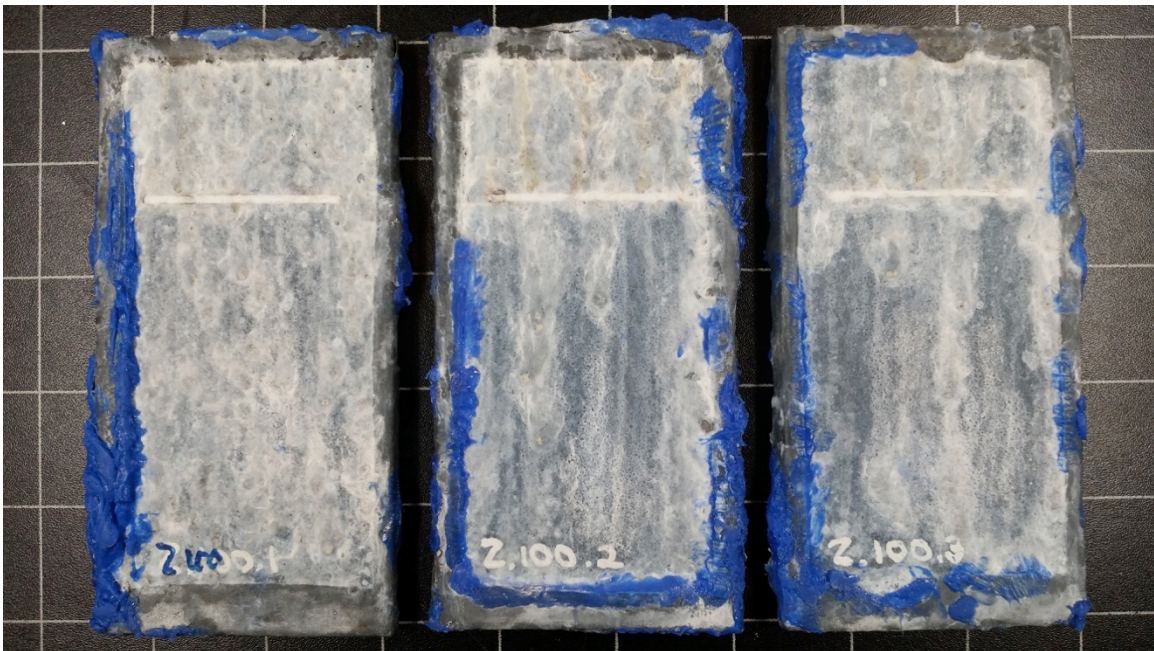

Figure B.2: Visual appearance of the high Zn primer with DFT 100 μm after 20 cycles of exposure.
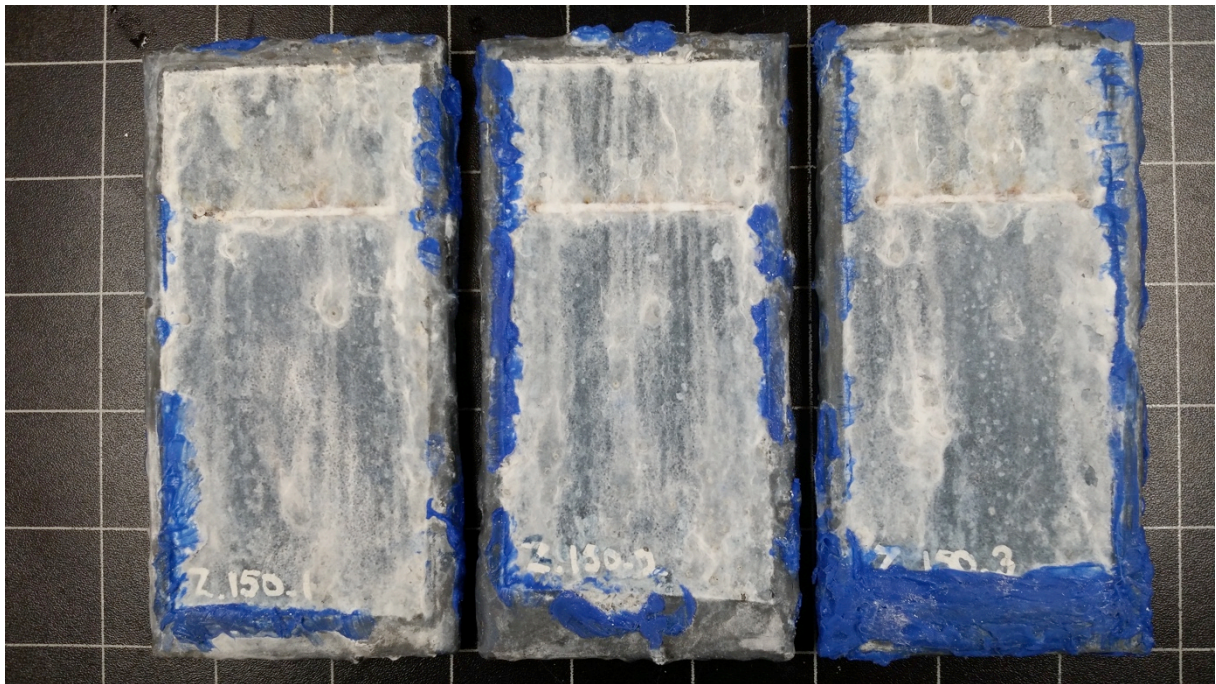
DFT 150 μm

Figure B.3: Visual appearance of the high Zn primer with DFT 150 μm after 20 cycles of exposure.

<u>Zn epoxy</u>

DFT 50 μm

Figure B.4: Visual appearance of the Zn epoxy with DFT 50 μm after 20 cycles of exposure.

DFT 100 μm

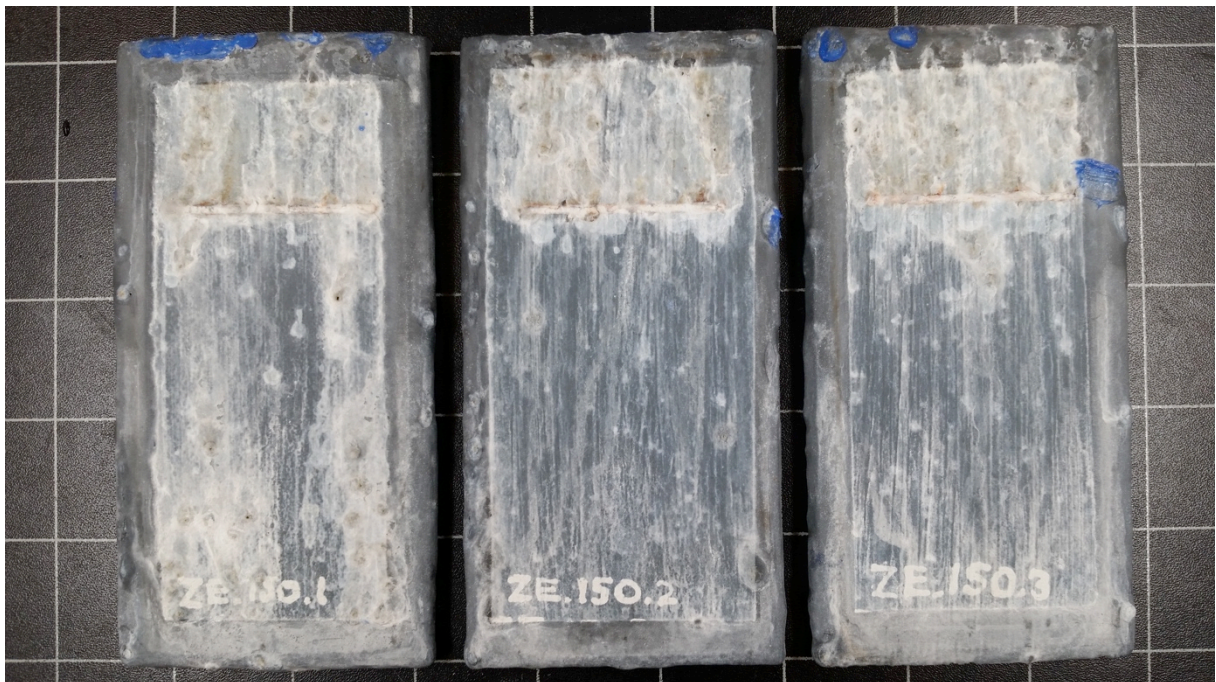Figure B.5: Visual appearance of the Zn epoxy with DFT 100 μm after 20 cycles of exposure.

DFT 150 μm

Figure B.6: Visual appearance of the Zn epoxy with DFT 150 μm after 20 cycles of exposure.
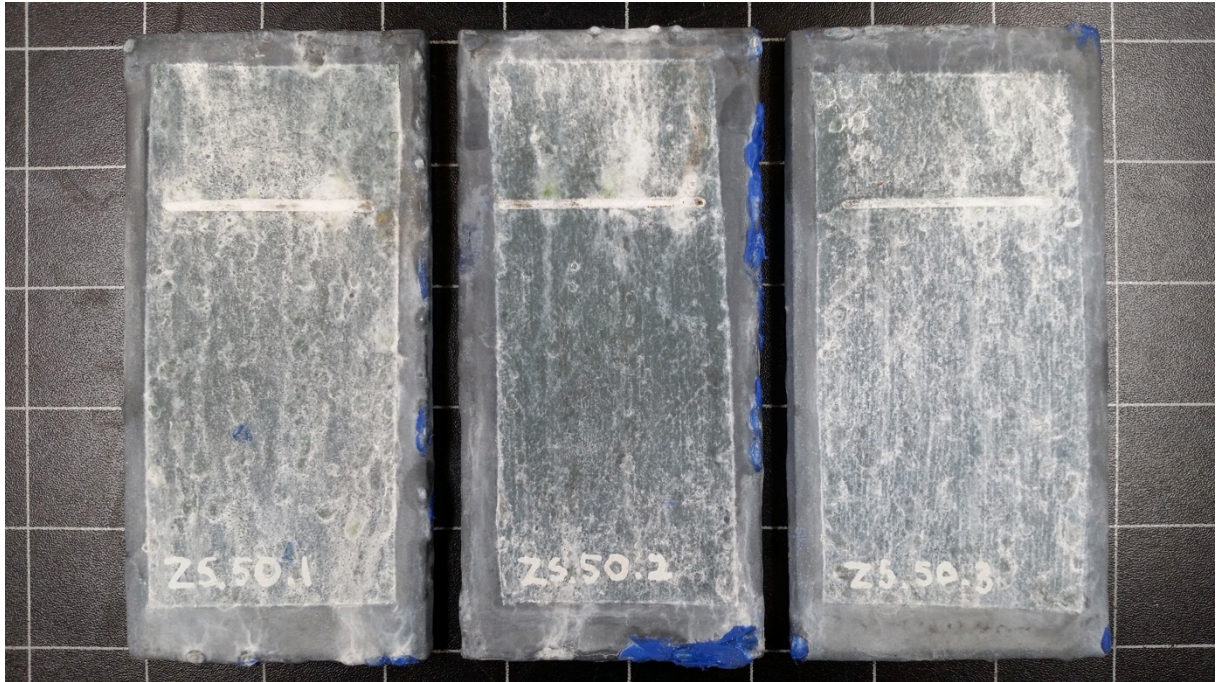
Zn silicate

DFT 50 μm

Figure B.7: Visual appearance of the Zn silicate with DFT 50 μm after 20 cycles of exposure.
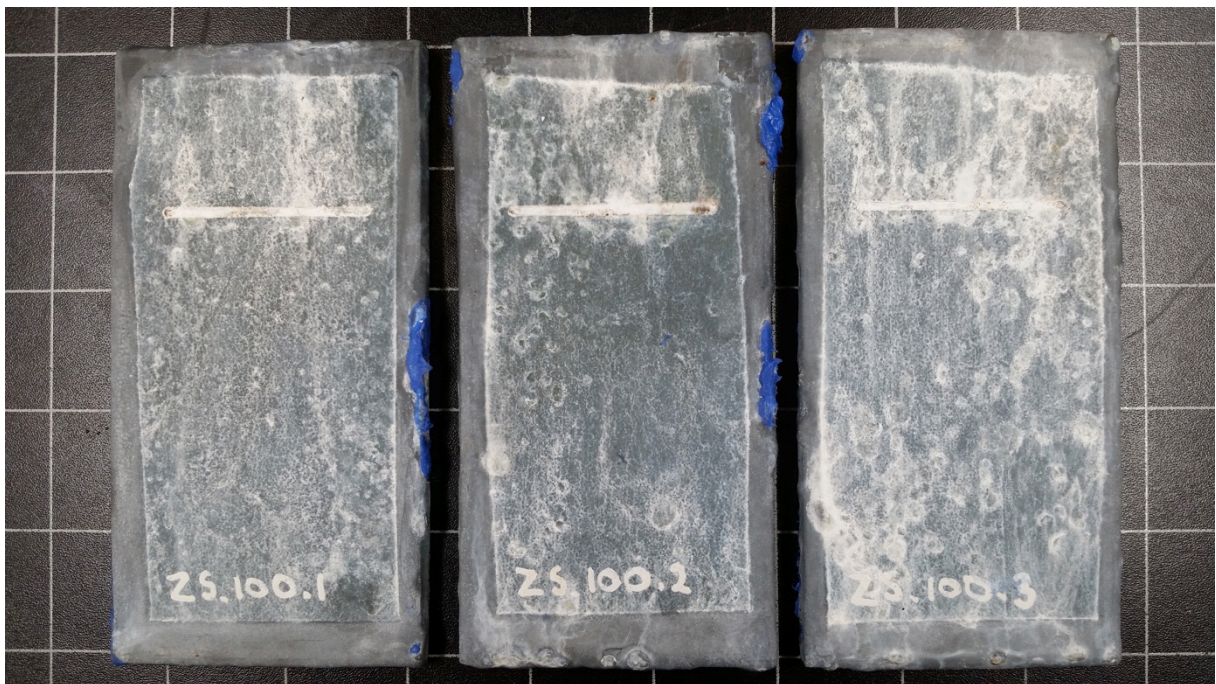
DFT 100 μm

Figure B.8: Visual appearance of the Zn silicate with DFT 100 μm after 20 cycles of exposure.
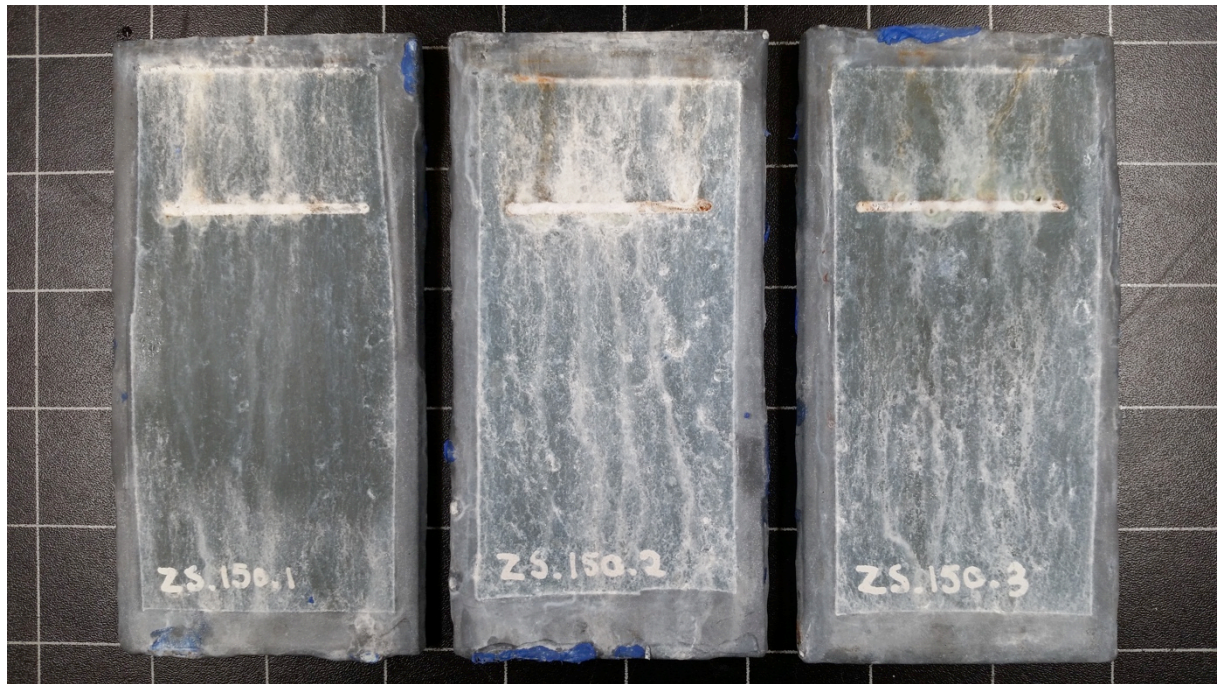
DFT 150 µm

Figure B.9: Visual appearance of the Zn silicate with DFT 150 µm after 20 cycles of exposure.

<u>Modified Zn epoxy</u>

DFT 50 µm
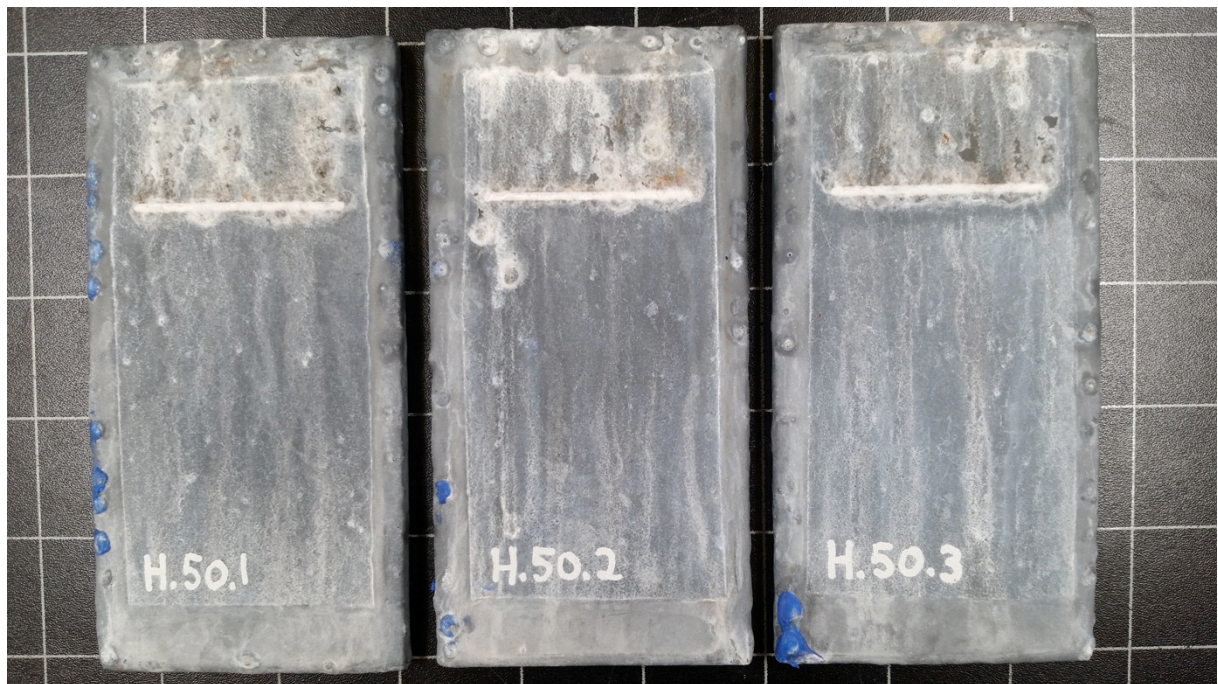
Figure B.10: Visual appearance of the modified Zn epoxy with DFT 50 µm after 20 cycles of exposure.

DFT 100 µm

Figure B.11: Visual appearance of the modified Zn epoxy with DFT 100 µm after 20 cycles of exposure.
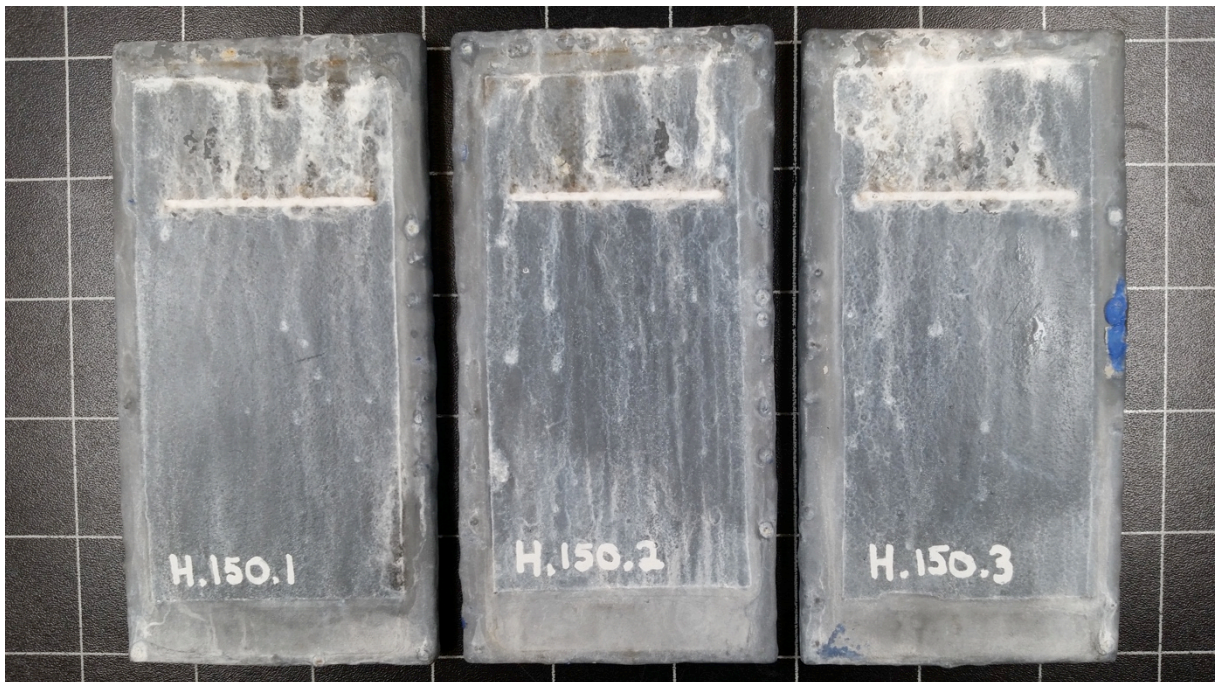
DFT 150 µm

Figure B.12: Visual appearance of the modified Zn epoxy with DFT 150 µm after 20 cycles of exposure.

MgO silicate

DFT 100 μm
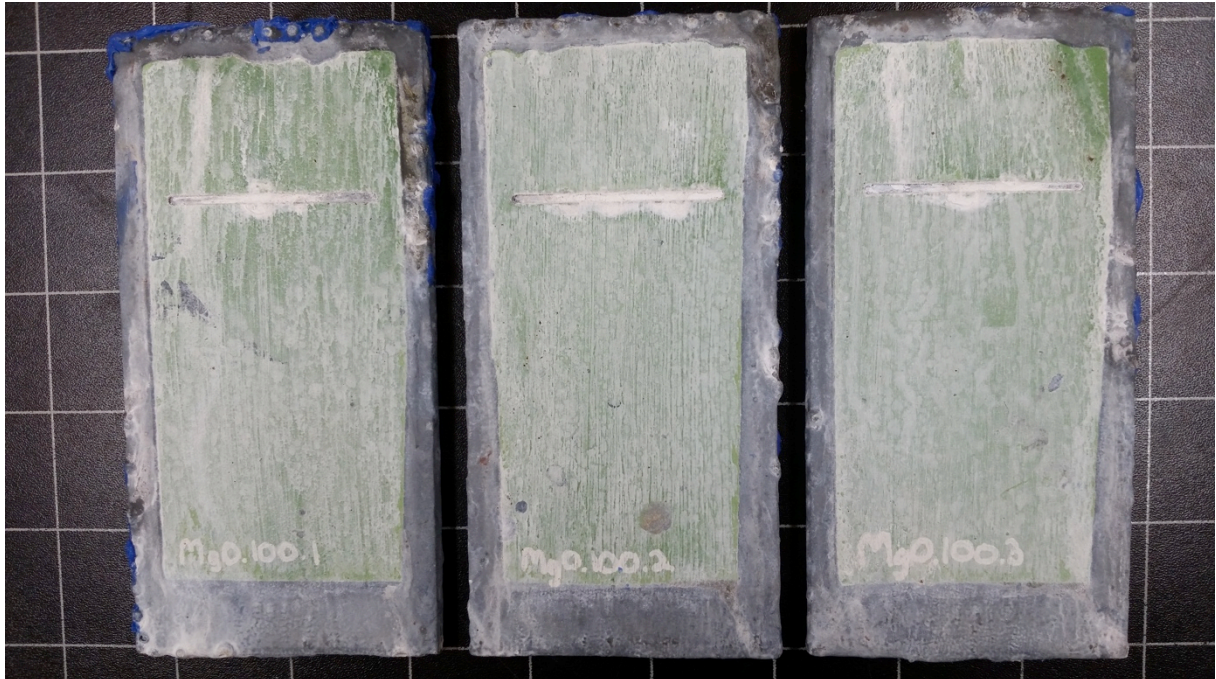
Figure B.13: Visual appearance of the MgO silicate with DFT 100 μm after 20 cycles of exposure.

Mg silicate

DFT 200 μm

Figure B.14: Visual appearance of the Mg silicate with DFT 200 μm after 20 cycles of exposure.

Al silicate

DFT 150 µm

Figure B.15: Visual appearance of the Al silicate with DFT 150 µm after 20 cycles of exposure.

Inorganic copolymer coating

DFT 150 µm
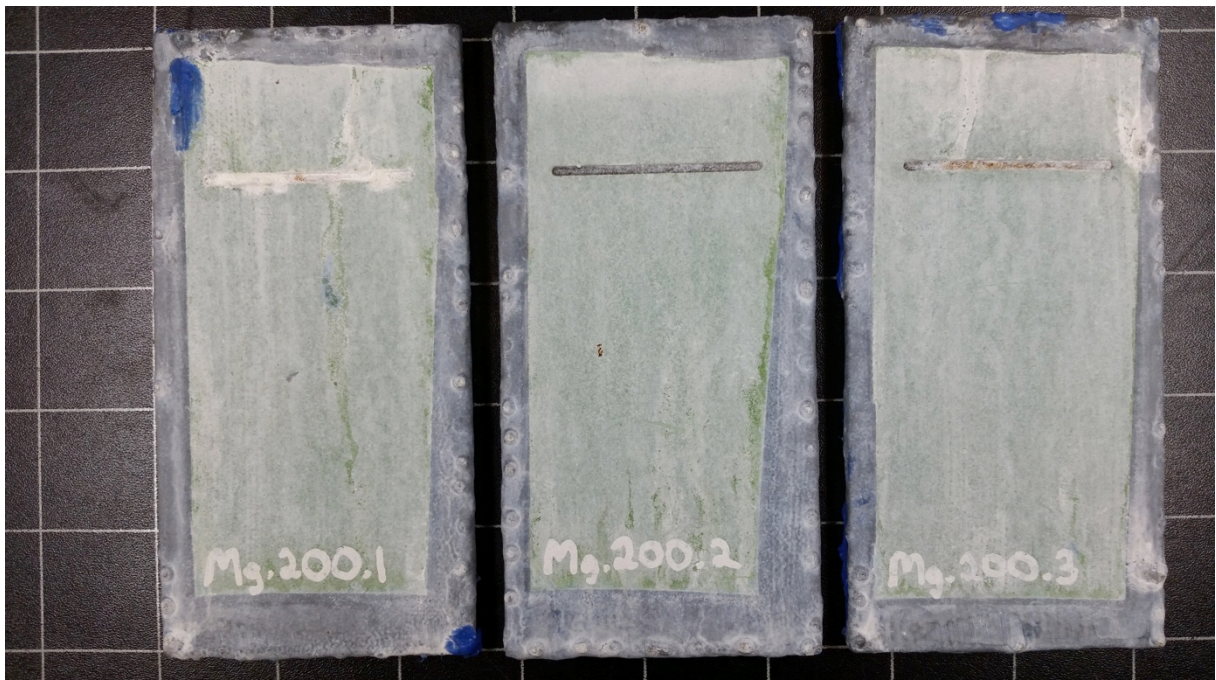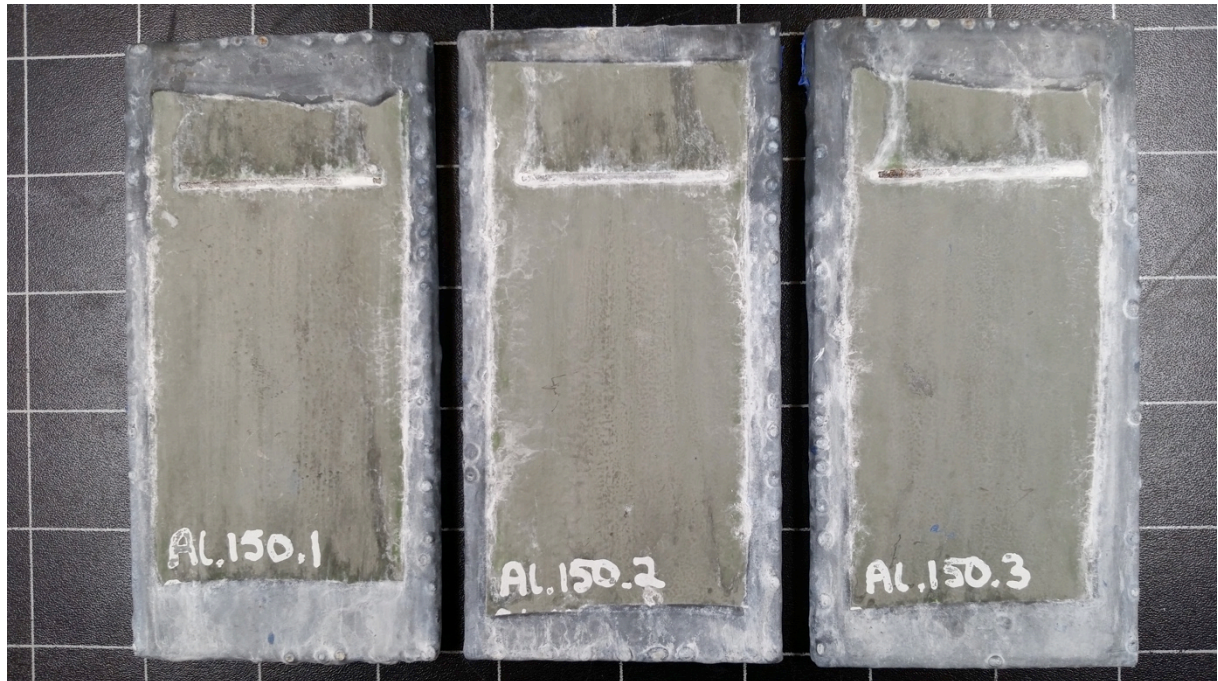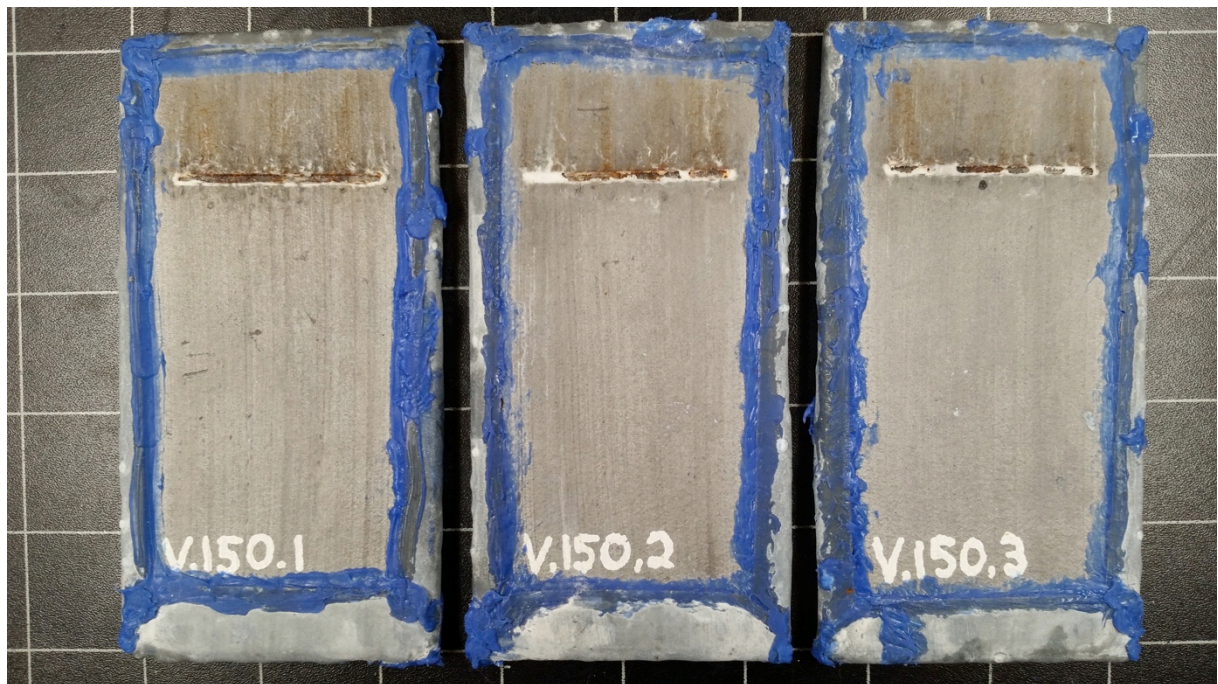

Figure B.16: Visual appearance of the inorganic copolymer coating with DFT 150 µm after 20 cycles of exposure.

B.3 Blistering and cracks after 20 cycles of exposure

The inorganic copolymer coating is only shown in Section 4.2.1. Figure B.17 presents the blistering and cracking of the high Zn primer for DFT 50 μm (a), DFT 100 μm (b) and DFT 150 μm (c). The DFT 50 μm are also shown in Section 4.2.1. Highest amount of visual blistering was seen on the DFT 50 μm, while DFT 100 μm and 150 μm showed both blistering and cracking of the repair coating. The pictures present the samples after 20 cycles of exposure and the blistering was concentrated around the scribe. The blistering and the cracking of the topcoat are marked with red circles.

(a) DFT 50 μm   (b) DFT 100 μm

(c) DFT 150 μm
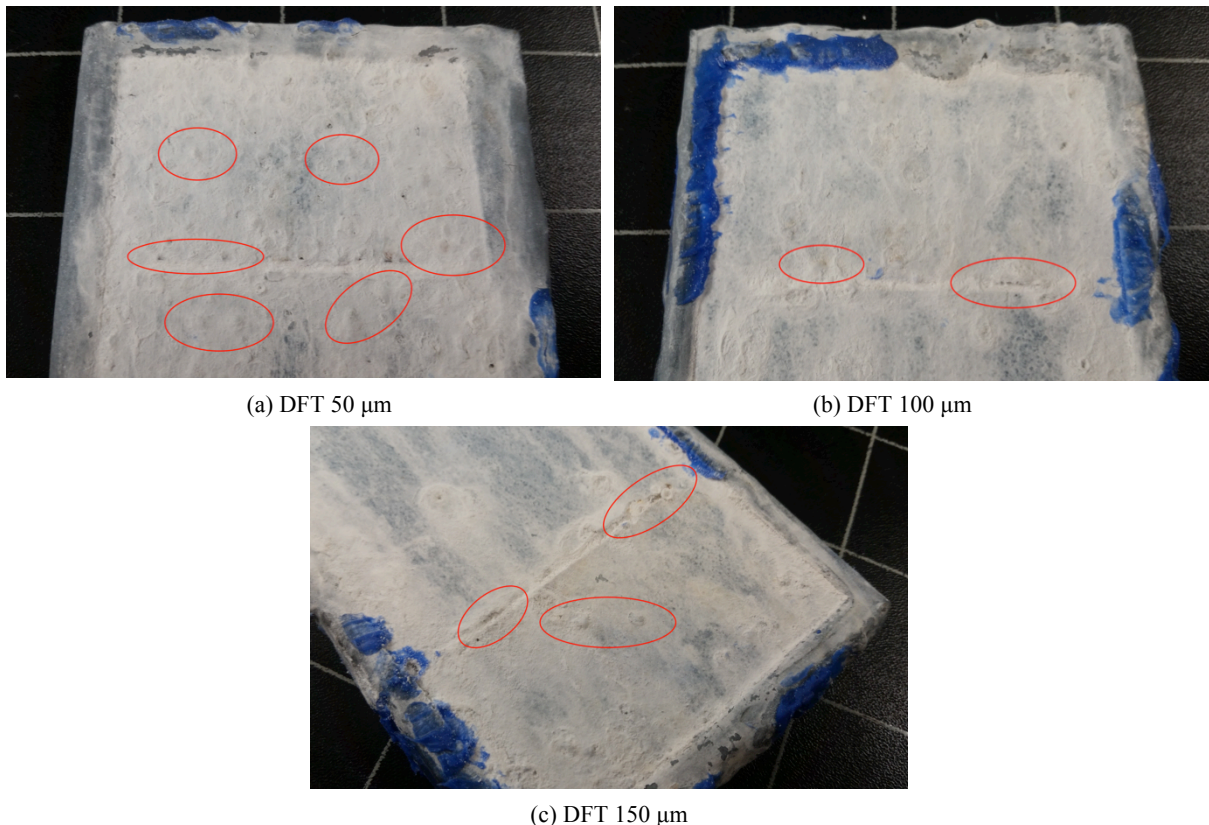
Figure B.17: Blistering near the scribe on the high Zn primer DFT 50 μm (a), in addition to blistering and cracking of the topcoat on DFT 100 μm (b) and DFT 150 μm (c). The pictures are taken after 20 cycles of exposure.

Blistering on the Zn epoxy DFT 150 μm was seen after 4 cycles of exposure. The 100 μm and 50 μm samples revealed blistering after 5 and 6 cycles respectively. The blistering on the Zn epoxy DFT 50 μm (a), DFT 100 μm (b) and DFT 150 μm (c) are presented in Figure B.18. The DFT 150 μm are also shown in Section 4.2.1.

Blistering on the modified Zn epoxy DFT 150 μm occurred after 13 cycles of exposure. See Figure B.19 for blistering on the DFT 50 μm (a), DFT 100 μm (b) and 150 μm (c). The blistering on the DFT 100 μm and 50 μm was first discovered after the test was terminated. The modified Zn epoxy had less comprehensive blistering tendency compared to the other repair coatings that showed blistering.

(a) DFT 50 μm

(b) DFT 100 μm

(c) DFT 150 μm
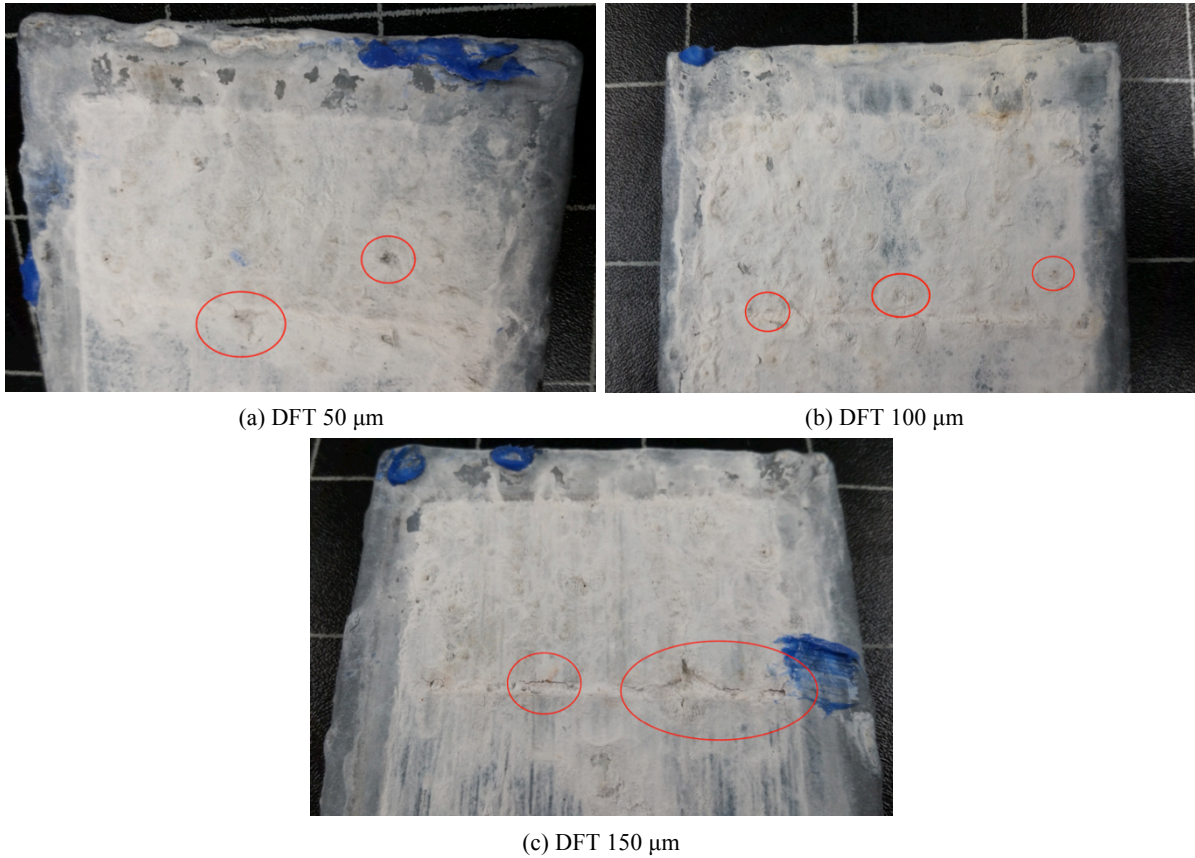
Figure B.18: Blistering and cracking of the topcoat near the scribe on the Zn epoxy DFT 50 μm (a), DFT 100 μm (b) and DFT 150 μm (c). The pictures are taken after 20 cycles of exposure.

(a) DFT 50 μm

(b) DFT 100 μm

(c) DFT 150 μm
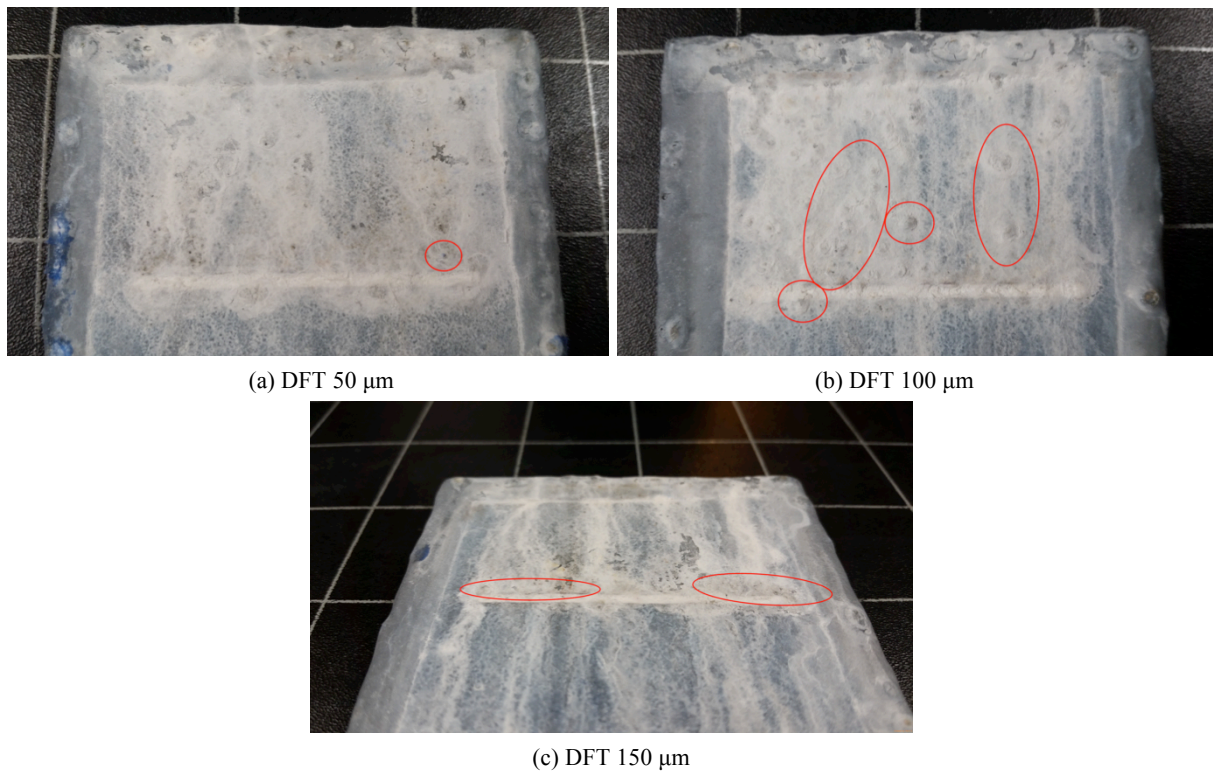
Figure B.19: Blistering near the scribe on the modified Zn epoxy DFT 50 μm (a) and DFT 100 μm (b), in addition to both blistering and cracking of the topcoat on DFT 150 μm (c). The pictures are taken after 20 cycles of exposure.

B.4   Corrosion creep on TSA

The corrosion creep measured for each sample is presented in Table B.2. Two parallels were evaluated per sample and the values represent "C-W" in equation (6) presented in Section 3.3. The values are not divided on 2.

Table B.2: Measured corrosion creep for each samples at 11 different spots.

| Sample/ Parallel		Corrosion creep on TSA [mm]										
		1	2	3	4	5	6	7	8	9	10	11
Z.50	1	3.8	5.2	4.4	5.6	6.4	3.7	5.2	4.8	6.2	13.6	3.5
	2	0.8	2.3	5.9	3.1	4.0	3.8	2.0	6.0	5.0	3.3	2.6
Z.100	1	1.6	2.2	2.2	3.6	2.2	4.0	6.7	3.2	6.5	3.3	1.5
	2	1.9	3.8	4.5	7.3	5.2	5.7	6.2	6.2	4.3	3.9	1.6
Z.150	1	3.0	3.0	5.0	5.1	7.7	4.8	4.1	5.6	8.3	5.8	6.0
	2	0.5	5.4	7.4	7.4	7.5	8.3	5.9	7.8	9.9	3.2	1.1
ZE.50	1	13.4	16.8	10.4	9.3	21.6	18.6	19.1	18.0	10.8	18.4	17.5
	2	4.6	4.3	10.4	11.8	11.5	10.0	6.6	10.7	4.8	5.9	7.4
ZE.100	1	5.5	9.3	3.2	5.8	3.8	6.0	5.0	10.5	4.8	6.8	4.8
	2	5.3	8.5	13.9	15.5	8.4	12.7	11.6	17.8	14.9	10.5	5.5
ZE.150	1	7.4	6.6	6.0	7.9	6.8	10.3	9.7	11.4	10.8	8.3	5.8
	2	21.8	13.5	11.0	10.7	8.8	11.4	11.7	11.8	13.2	9.7	7.9
H.50	1	2.5	4.2	5.5	4.3	4.3	4.9	3.5	3.5	3.8	4.8	3.6
	2	3.6	2.8	2.8	3.0	3.4	3.8	3.2	2.6	3.5	4.5	3.8
H.100	1	3.6	2.5	3.9	4.7	5.0	3.7	5.0	4.4	2.8	4.1	4.3
	2	2.9	0.9	4.9	4.5	3.6	4.1	2.9	4.5	3.9	4.9	1.0
H.150	1	2.4	3.6	5.0	5.9	4.6	3.4	4.2	3.0	4.2	2.7	1.7
	2	2.2	3.3	4.6	4.1	7.6	8.0	2.8	4.6	3.9	3.9	4.4
ZS.50	1	1.5	1.8	2.5	2.8	1.5	3.0	2.0	-	-	-	-
	2	0.9	-	0.4	1.9	-	-	-	1.1	-	-	-
ZS.100	1	-	2.3	-	3.5	4.3	-	-	-	-	3.6	-
	2	-	-	4.4	-	3.2	1.3	-	1.2	3.0	2.0	-
ZS.150	1	-	2.3	-	2.5	1.8	2.8	1.5	2.3	-	-	-
	2	-	-	-	-	1.7	1.7	3.0	1.8	2.1	2.7	-
MgO.100	1	-	-	-	-	-	-	-	-	-	-	-
	2	-	-	-	-	-	-	-	-	-	-	-
Mg.150	1	-	-	-	-	-	-	-	-	-	-	-
	2	-	-	-	-	-	-	-	-	-	-	-
Al.150	1	-	-	-	-	-	-	-	-	-	-	-
	2	-	-	-	-	-	-	-	-	-	-	-
V.200	1	3.6	4.2	3.2	3.8	4.5	4.5	3.5	7.0	5.6	4.7	4.9
	2	6.4	8.2	9.6	10.2	11.1	11.1	9.0	9.8	8.9	7.2	5.4

B.5 Element analysis of the corrosion products

SINTEF analyzed the corrosion products formed on the surfaces with Agilent 8800 Triple Quadropole ICP-MS (ICP-QQQ). The results are presented in Table B.3. The term *"μg/mg"* means microgram Mg, Al or Zn per milligram corrosion products, and *"RSD (%)"* means relative standard deviation presented in percentage.

Table B.3: Overview of the Mg-, Al- and Zn-content in the corrosion products formed on the samples.

Sample	Mg		Al		Zn	
	μg/mg	RSD (%)	μg/mg	RSD (%)	μg/mg	RSD (%)
Z.50.3	0.0	9.4	245.6	2.2	110.6	1.1
Z.100.1	0.3	13.5	255.8	2.6	67.9	0.5
Z.150.2	0.3	22.2	233.8	2.6	111.0	2.0
ZE.50.2	1.4	5.3	257.6	3.6	94.0	2.9
ZE.100.1	0.8	1.3	261.5	0.7	77.9	0.5
ZE.150.1	0.7	0.1	261.4	3.3	85.3	1.4
H.50.3	3.4	3.0	225.7	2.7	130.8	1.1
H.100.1	1.3	5.2	280.5	2.9	41.3	1.3
H.150.2	2.8	3.0	228.2	1.7	140.6	0.9
ZS.50.1 [1]	0.9	3.7	157.2	1.7	290.6	0.6
ZS.100.2 [1]	1.0	4.0	124.4	1.5	342.7	2.0
ZS.150.3 [1]	0.2	11.0	216.9	2.3	114.5	1.3
MgO.100.2 [1]	101.2	2.0	189.3	2.3	2.7	2.3
Mg.200.3 [1]	112.0	2.8	105.3	2.8	72.3	1.2
Al.150.3 [2]	2.5	5.3	279.2	2.6	23.5	1.1
V.150.1 [3]	3.9	5.5	214.8	1.5	7.2	3.6

[1] Green precipitates, oxides and/or silicates

[2] Precipitates, oxides and/or silicates

[3] Dark precipitates, (iron) oxides and/or silicates

Appendix C   Composition Artificial Seawater

The artificial seawater was used for the electrochemical impedance measurements, the OCP measurements and the crevice corrosion tests. The composition of the water is presented in Table C.2 and the molar mass of the metals is given in Table C.1. Complete dissolution of all salts is assumed for the calculations.

Table C.1: Molar mass for the different elements present in the artificial seawater [32].

Element	Molar mass [g/mole]
Cl	35.45
Na	22.99
Mg	24.31
Ca	40.08
K	39.10
Sr	87.62
H	1.008

Table C.2: Composition artificial seawater.

Species containing Cl	Molar mass [g/mole]	Concentration		
		[g/L]	[Mole/L]	[Mole Cl/L]
NaCl	58.44	24.53	0.4197	0.4197
$MgCl_2$	95.21	5.2	0.0546	0.1092
$CaCl_2$	110.98	1.16	0.0105	0.0209
KCl	74.55	0.695	0.0093	0.0093
$SrCl_2$	158.52	0.025	0.0002	0.0003
Total concentration of chloride				0.5595

Appendix D   Electrochemical Impedance

D.1   Samples after exposure

Figure D.1 and Figure D.2 present the samples after exposure. The amount of corrosion products formed on the exposed surface diverges between the different repair coatings. The number stated on each sample after the labeling, i.e. 100, 150 or 200, represents the average dry film thickness of the coatings.
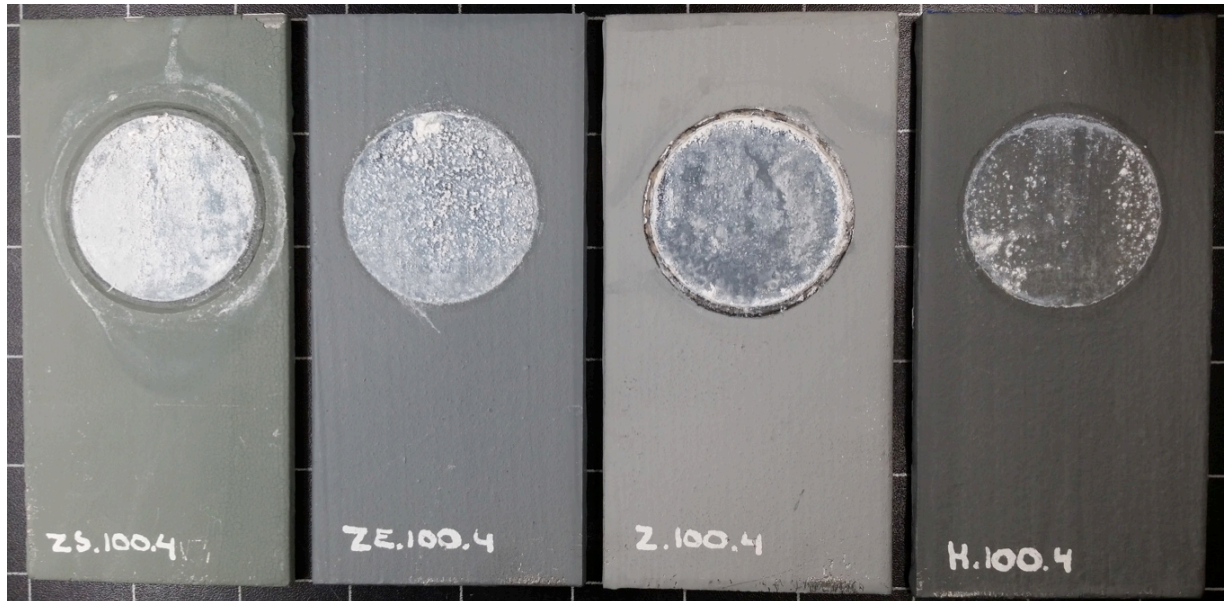
Figure D.1: Samples coated with respectively Zn silicate (ZS), Zn epoxy (ZE), high Zn primer (Z) and modified Zn epoxy (H). The exposed surface area is where the white corrosion products are present.
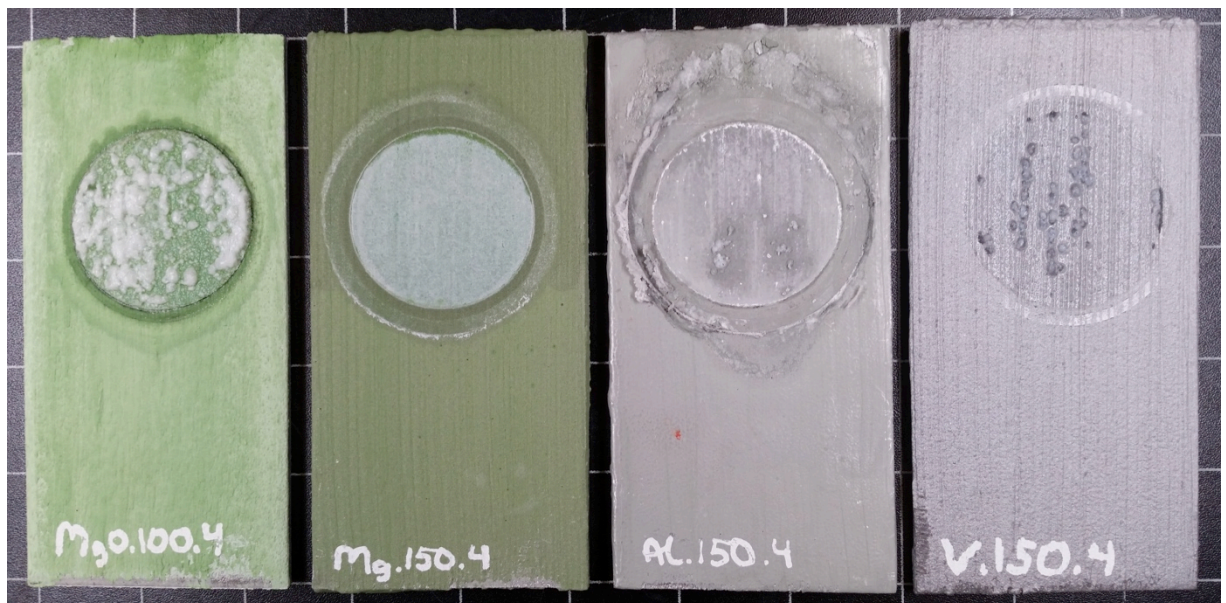
Figure D.2: Samples coated with respectively MgO silicate (MgO), Mg silicate (Mg), Al silicate (Al) and the inorganic copolymer coating (V). The exposed surface area is where the white corrosion products are present. The number 150 stated on the Mg silicate should be changed to 200.

D.2 Electrochemical impedance spectra

The electrochemical impedance values for the different repair coatings at each specter are stated in Table D.1 to Table D.8. Accompanying Bode plots with frequency plotted against electrochemical impedance are presented from Figure D.3 to Figure D.10. The number stated in the parentheses for each specter indicates the number of days from test initiation.

High Zn primer

Table D.1: Electrochemical impedance values for the high Zn primer relative to the frequency.

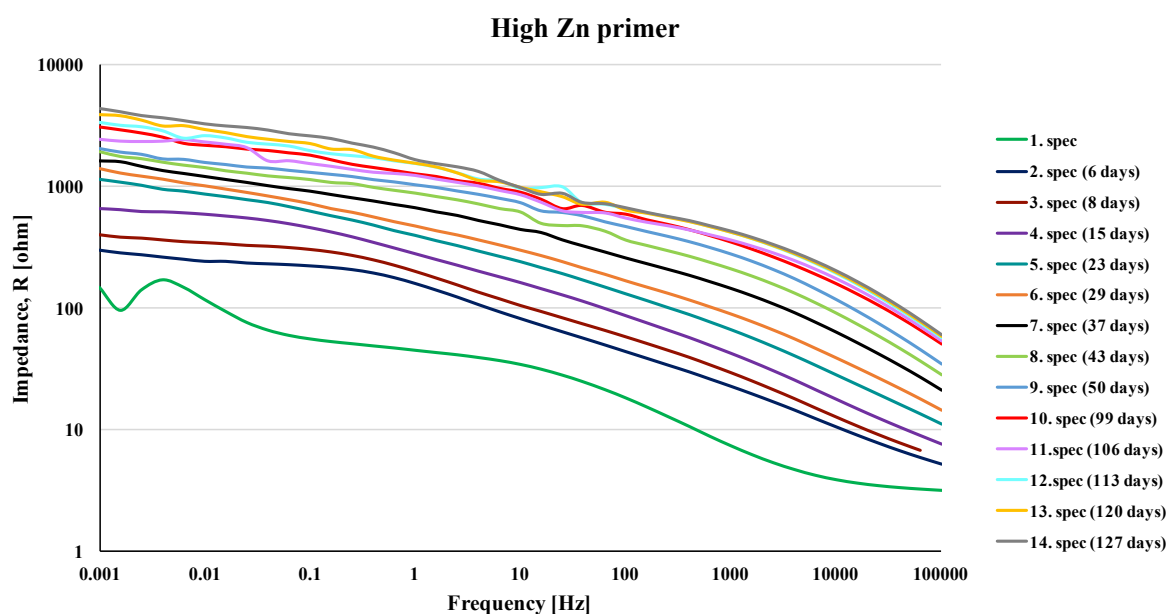| Electrochemical impedance [Ω]	Frequency [Hz]								
	100000	10000	1000	100	10	1	0.1	0.01	0.001
1. spec	3.2	3.9	7.3	18.3	34.6	45.2	56.1	118.3	149.4
2. spec (6 days)	5.3	10.7	23.0	44.4	82.6	160.1	223.1	243.1	300.1
3. spec (8 days)	-	12.8	29.7	58.6	105.9	202.0	305.7	347.6	403.6
4. spec (15 days)	7.6	17.7	42.3	86.3	161.4	278.4	456.1	587.4	653.7
5. spec (23 days)	11.2	28.4	66.6	131.0	240.1	394.4	622.7	859.1	1134.5
6. spec (29 days)	14.5	38.8	89.0	166.9	297.6	470.3	717.4	1004.6	1392.5
7. spec (37 days)	21.3	63.9	146.7	261.7	449.3	678.4	928.5	1227.0	1648.3
8. spec (43 days)	28.3	90.5	208.9	360.4	612.3	874.6	1129.2	1416.5	1914.4
9. spec (50 days)	35.0	118.4	280.8	473.2	743.4	1043.1	1320.1	1592.5	2073.1
10. spec (99 days)	51.7	160.2	350.8	592.8	895.4	1265.3	1796.6	2162.3	3051.5
11. spec (106 days)	53.5	174.0	363.2	551.7	859.5	1240.7	1552.1	2342.3	2465.1
12. spec (113 days)	56.4	190.8	416.4	650.3	954.5	1531.6	1951.6	2591.5	3334.8
13. spec (120 days)	59.0	197.7	422.7	643.7	990.1	1560.9	2265.5	2954.0	3914.0
14. spec (127 days)	61.3	204.5	432.9	673.7	986.4	1669.6	2614.5	3283.0	4387.0

Figure D.3: Electrochemical impedance (y-axis) plotted against frequency (x-axis) for the high Zn primer. 14 spectra were taken, and the numbers stated in the parentheses indicate the number of days from test initiation.

Zn epoxy

Table D.2: Electrochemical impedance values for the Zn epoxy relative to the frequency.

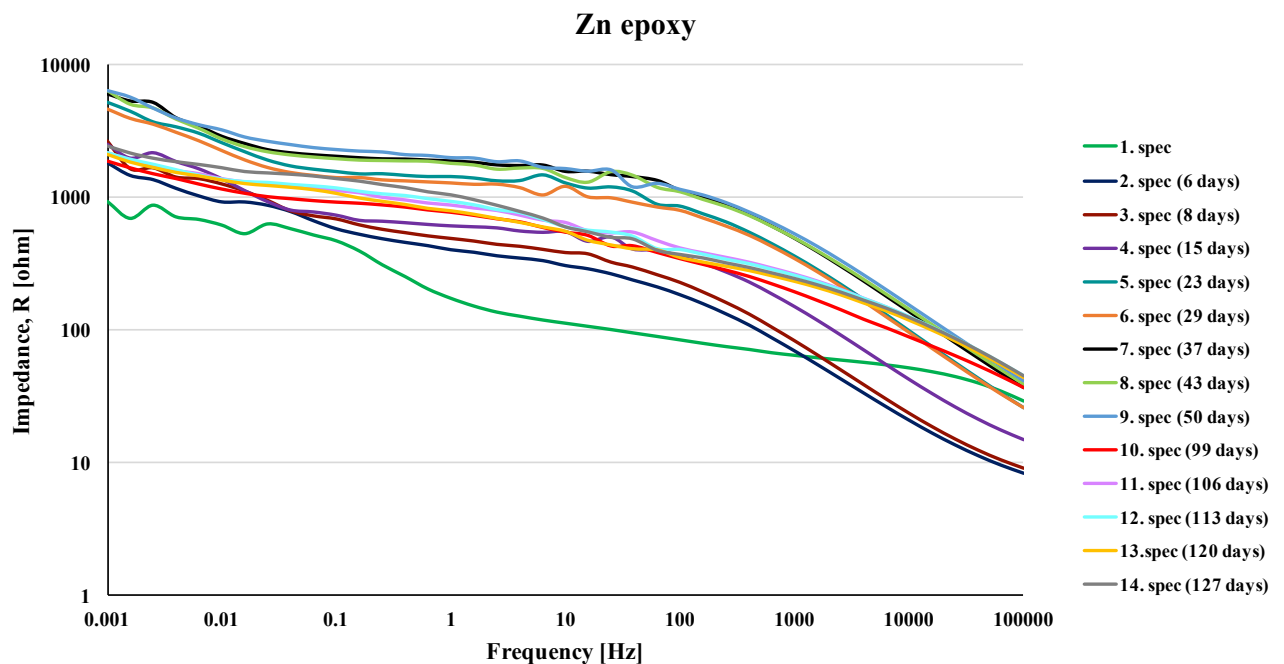| Electrochemical impedance [Ω]	Frequency [Hz]								
	100000	10000	1000	100	10	1	0.1	0.01	0.001
1. spec	29.4	52.3	65.1	85.1	113.7	175.1	474.9	624.5	944.0
2. spec (6 days)	8.3	20.9	70.0	186.2	309.4	407.5	586.0	936.8	1852.7
3. spec (8 days)	9.1	23.5	82.7	228.0	382.5	488.7	684.9	1257.0	2652.9
4. spec (15 days)	15.2	43.0	152.1	364.7	559.0	618.1	743.2	1396.4	2545.1
5. spec (23 days)	26.3	99.9	364.5	868.8	1299.1	1451.4	1582.0	2609.0	5259.3
6. spec (29 days)	26.2	96.9	349.5	808.4	1227.3	1301.3	1427.1	2282.2	4697.5
7. spec (37 days)	36.5	136.4	487.7	1122.5	1561.5	1871.5	2029.9	2872.0	6001.8
8. spec (43 days)	39.2	144.0	496.9	1112.3	1423.7	1822.3	1975.1	2784.5	6455.8
9. spec (50 days)	42.0	156.0	535.2	1156.9	1657.7	2002.3	2302.8	3236.9	6396.5
10. spec (99 days)	36.6	88.2	193.4	344.9	546.6	772.6	921.0	1156.5	1882.6
11. spec (106 days)	44.5	126.1	265.2	417.1	647.3	874.8	1123.1	1378.4	2161.0
12. spec (113 days)	45.8	127.6	261.6	409.4	607.0	942.3	1189.1	1384.6	2192.9
13. spec (120 days)	44.1	119.1	234.3	354.8	558.7	797.5	1078.6	1359.7	2126.0
14. spec (127 days)	45.8	125.5	245.7	372.3	598.9	1041.3	1377.6	1661.7	2421.0

Figure D.4: Electrochemical impedance (y-axis) plotted against frequency (x-axis) for the Zn epoxy. 14 spectra were taken, and the numbers stated in the parentheses indicate the number of days from test initiation.

Modified Zn epoxy

Table D.3: Electrochemical impedance values for the modified Zn epoxy relative to the frequency.

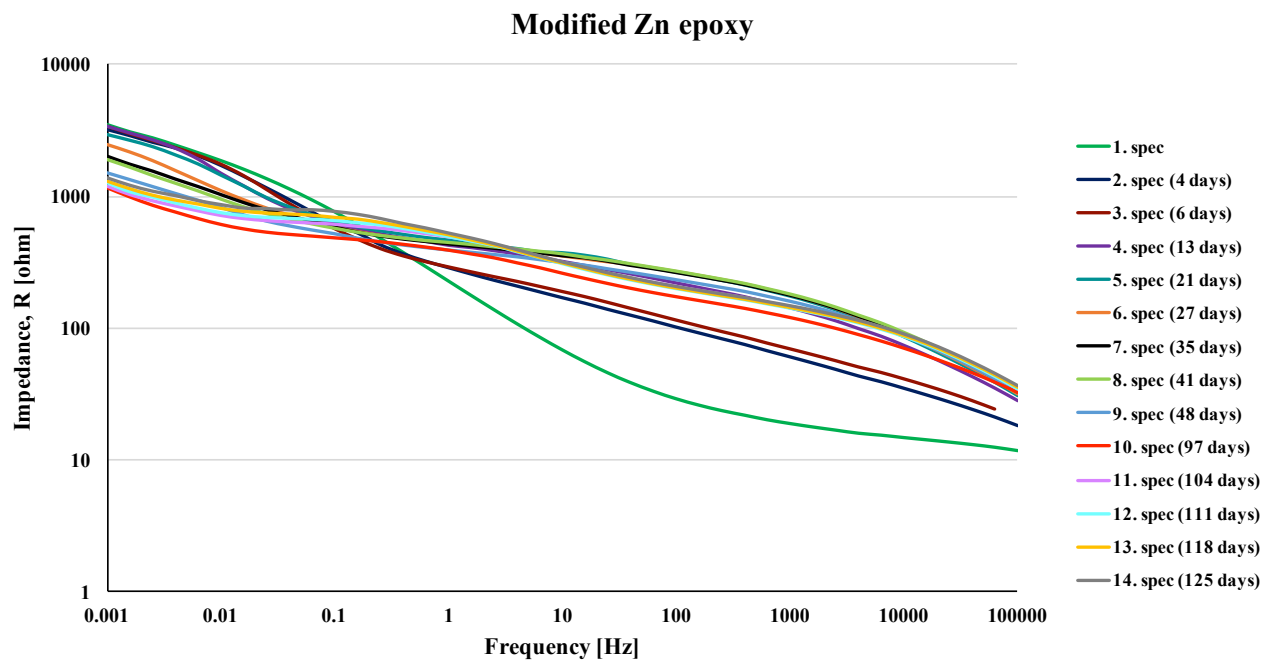| Electrochemical impedance [Ω]	Frequency [Hz]								
	100000	10000	1000	100	10	1	0.1	0.01	0.001
1. spec	11.6	14.6	18.7	28.8	67.9	226.8	761.5	1871.7	3521.7
2. spec (4 days)	18.2	35.0	60.7	102.1	170.8	288.5	619.5	1723.9	3226.2
3. spec (6 days)	-	41.3	69.6	114.9	188.8	289.7	563.1	1731.0	3352.0
4. spec (13 days)	27.9	73.2	141.1	218.1	317.5	421.0	614.5	1479.5	3362.8
5. spec (21 days)	30.9	86.2	174.8	265.5	372.1	463.7	642.4	1435.5	2909.8
6. spec (27 days)	31.8	88.8	178.7	268.1	351.4	437.6	578.7	1095.8	2441.0
7. spec (35 days)	33.0	91.6	179.6	266.9	358.0	439.9	590.3	1040.4	2034.8
8. spec (41 days)	33.6	93.0	182.0	271.8	367.8	448.7	574.1	956.1	1909.4
9. spec (48 days)	32.7	86.8	159.8	232.4	313.3	389.6	517.1	818.4	1494.3
10. spec (97 days)	32.3	70.1	120.0	172.9	260.8	390.6	484.6	613.3	1165.8
11. spec (104 days)	34.3	87.3	145.4	205.8	315.1	490.9	611.5	713.6	1191.7
12. spec (111 days)	34.7	86.7	142.1	199.9	308.9	495.5	655.6	751.5	1266.4
13. spec (118 days)	35.9	88.7	144.9	203.5	315.1	516.2	699.1	818.3	1317.0
14. spec (125 days)	36.6	90.4	148.0	207.4	318.4	527.0	768.6	866.2	1383.4

Figure D.5: Electrochemical impedance (y-axis) plotted against frequency (x-axis) for the modified Zn epoxy. 14 spectra were taken, and the numbers stated in the parentheses indicate the number of days from test initiation.

Zn silicate

Table D.4: Electrochemical impedance values for the Zn silicate relative to the frequency.

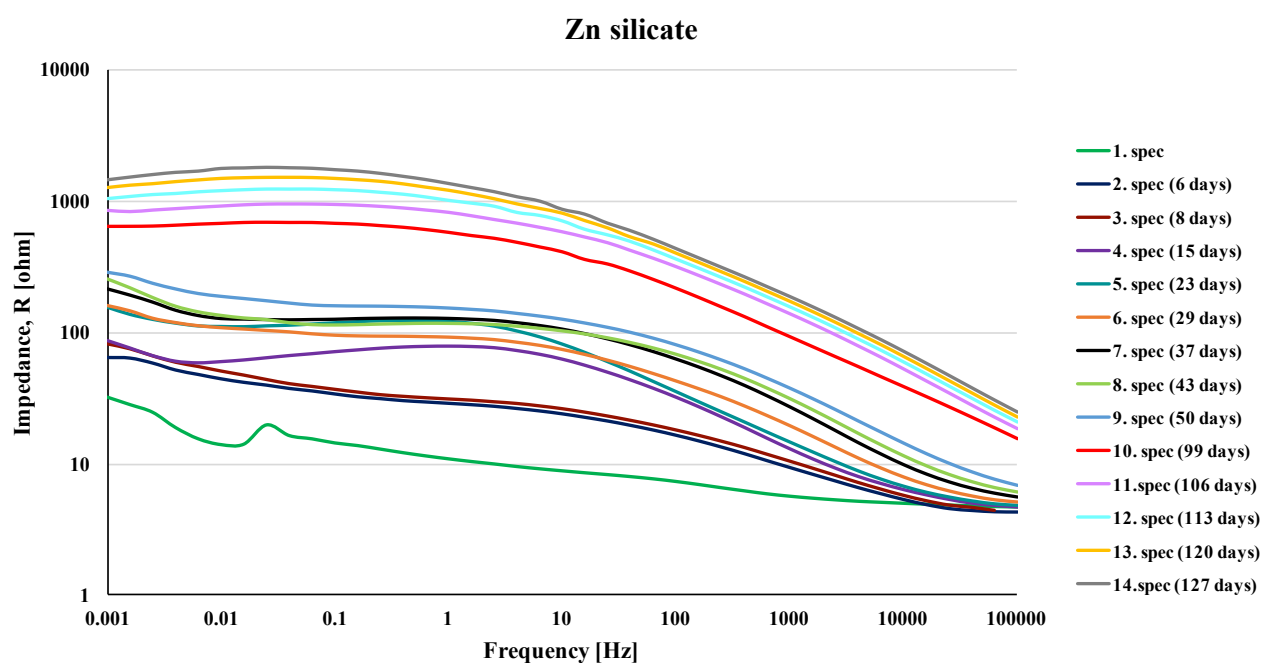| Electrochemical impedance [Ω]	Frequency [Hz]								
	100000	10000	1000	100	10	1	0.1	0.01	0.001
1. spec	4.7	5.0	5.7	7.3	8.8	10.9	14.3	13.9	31.7
2. spec (6 days)	4.3	5.4	9.4	16.6	24.2	19.1	34.3	44.7	65.0
3. spec (8 days)	-	5.7	10.4	18.1	26.2	31.1	36.9	50.9	82.1
4. spec (15 days)	4.7	6.3	12.9	31.9	62.3	78.2	71.0	59.6	86.4
5. spec (23 days)	4.8	6.7	14.6	35.4	81.6	121.7	118.8	111.3	156.2
6. spec (29 days)	5.1	7.8	19.4	42.8	74.6	92.7	95.9	109.5	161.9
7. spec (37 days)	5.6	9.8	27.0	62.1	104.6	126.2	124.3	125.9	211.1
8. spec (43 days)	6.0	11.3	30.8	67.1	101.1	115.3	112.1	132.6	251.3
9. spec (50 days)	6.8	14.2	37.2	79.6	124.6	151.7	157.8	186.2	284.3
10. spec (99 days)	15.7	38.9	93.2	217.7	411.5	578.5	677.3	676.8	642.3
11. spec (106 days)	18.7	52.7	138.1	314.0	576.0	808.6	927.8	902.1	837.0
12. spec (113 days)	20.5	58.7	154.7	358.4	700.5	1004.9	1211.2	1191.1	1035.3
13. spec (120 days)	22.4	64.8	170.6	396.8	800.1	1195.5	1470.7	1471.0	1253.1
14. spec (127 days)	24.6	71.3	186.8	4344	866.3	1364.4	1738.6	1776.3	1454.9

Figure D.6: Electrochemical impedance (y-axis) plotted against frequency (x-axis) for the Zn silicate. 14 spectra were taken, and the numbers stated in the parentheses indicate the number of days from test initiation.

MgO silicate

Table D.5: Electrochemical impedance values for the MgO silicate relative to the frequency.

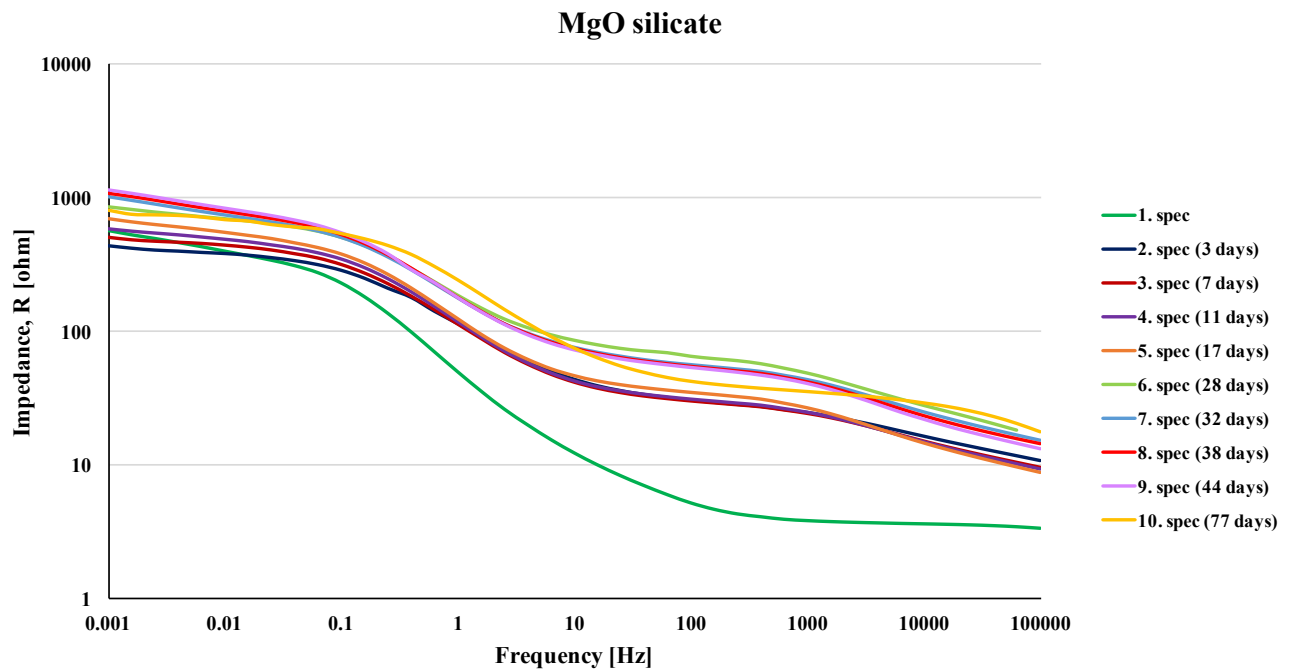| Electrochemical impedance [Ω]	Frequency [Hz]								
	100000	10000	1000	100	10	1	0.1	0.01	0.001
1. spec	3.4	3.6	3.8	5.2	12.3	49.8	228.9	396.5	565.7
2. spec (3 days)	10.8	16.4	24.8	30.7	44.0	115.1	289.1	386.7	442.4
3. spec (7 days)	9.8	15.4	24.7	30.6	42.3	114.6	318.5	444.5	508.5
4. spec (11 days)	9.3	14.9	24.8	31.1	42.6	118.5	349.2	491.4	588.7
5. spec (17 days)	9.0	14.9	27.2	35.5	47.2	125.7	381.1	553.3	699.7
6. spec (28 days)	16.4	28.1	49.0	65.5	86.3	187.6	508.2	700.7	860.3
7. spec (32 days)	15.6	25.4	44.2	57.1	76.8	179.2	504.8	742.8	1015.8
8. spec (38 days)	14.6	23.5	42.1	54.9	74.9	180.1	527.9	788.2	1072.6
9. spec (44 days)	13.2	22.0	40.9	53.9	73.2	180.9	554.8	849.0	1165.0
10. spec (77 days)	17.9	29.4	35.7	42.6	75.3	242.7	536.4	681.4	801.2

Figure D.7: Electrochemical impedance (y-axis) plotted against frequency (x-axis) for the MgO silicate. 10 spectra were taken, and the numbers stated in the parentheses indicate the number of days from test initiation.

Mg silicate

Table D.6: Electrochemical impedance values for the Mg silicate relative to the frequency.

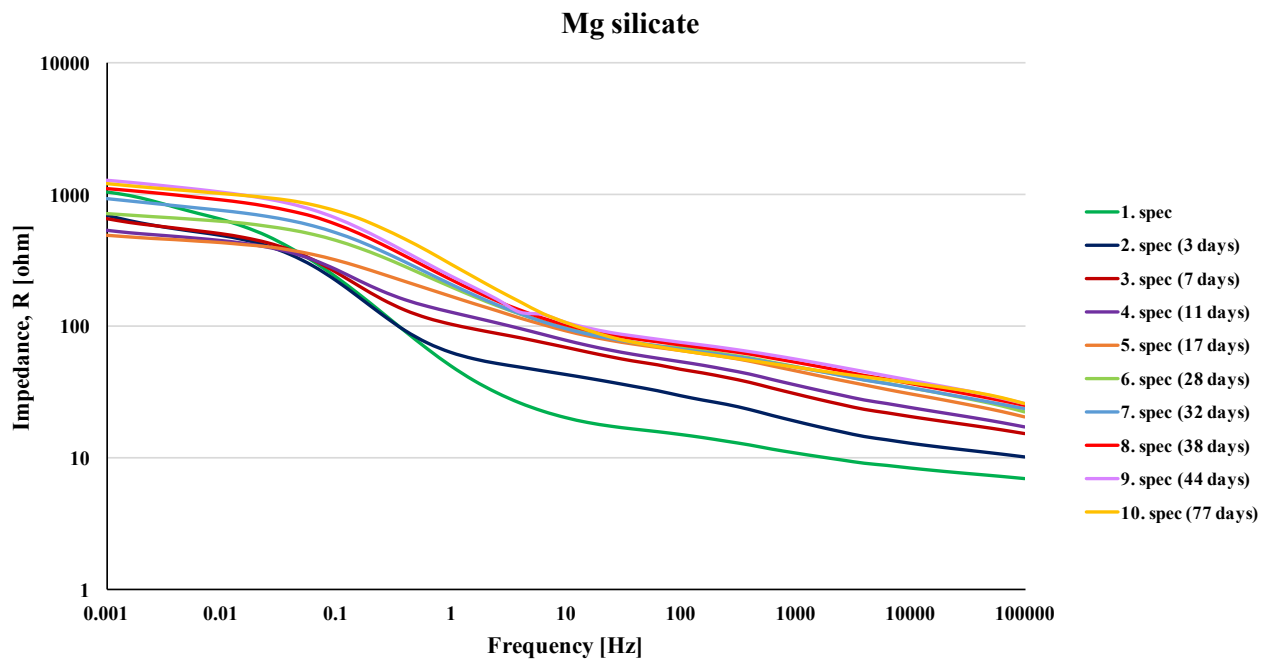| Electrochemical impedance [Ω]	Frequency [Hz]								
	100000	10000	1000	100	10	1	0.1	0.01	0.001
1. spec	7.0	8.4	10.9	15.1	20.3	50.4	238.8	655.5	1058.5
2. spec (3 days)	10.4	13.2	19.3	30.1	43.5	63.9	222.7	487.2	691.7
3. spec (7 days)	15.2	20.5	30.6	46.9	69.0	103.3	256.1	502.0	654.0
4. spec (11 days)	17.3	24.4	36.2	54.3	79.1	129.1	272.1	450.5	539.5
5. spec (17 days)	20.5	30.7	46.0	65.7	92.8	169.7	319.6	433.8	493.3
6. spec (28 days)	22.8	34.8	50.4	70.0	99.0	202.6	453.4	632.6	723.6
7. spec (32 days)	23.7	34.2	49.1	66.9	96.0	208.3	510.0	753.2	925.8
8. spec (38 days)	25.5	37.3	54.0	73.0	103.6	227.8	595.0	908.5	1105.5
9. spec (44 days)	25.9	39.1	56.5	75.8	107.4	241.8	664.0	1044.4	1284.8
10. spec (77 days)	26.3	37.9	49.8	66.7	108.9	301.4	763.2	1032.2	1226.8

Figure D.8: Electrochemical impedance (y-axis) plotted against frequency (x-axis) for the Mg silicate. 10 spectra were taken, and the numbers stated in the parentheses indicate the number of days from test initiation.

Al silicate

Table D.7: Electrochemical impedance values for the Al silicate relative to the frequency.

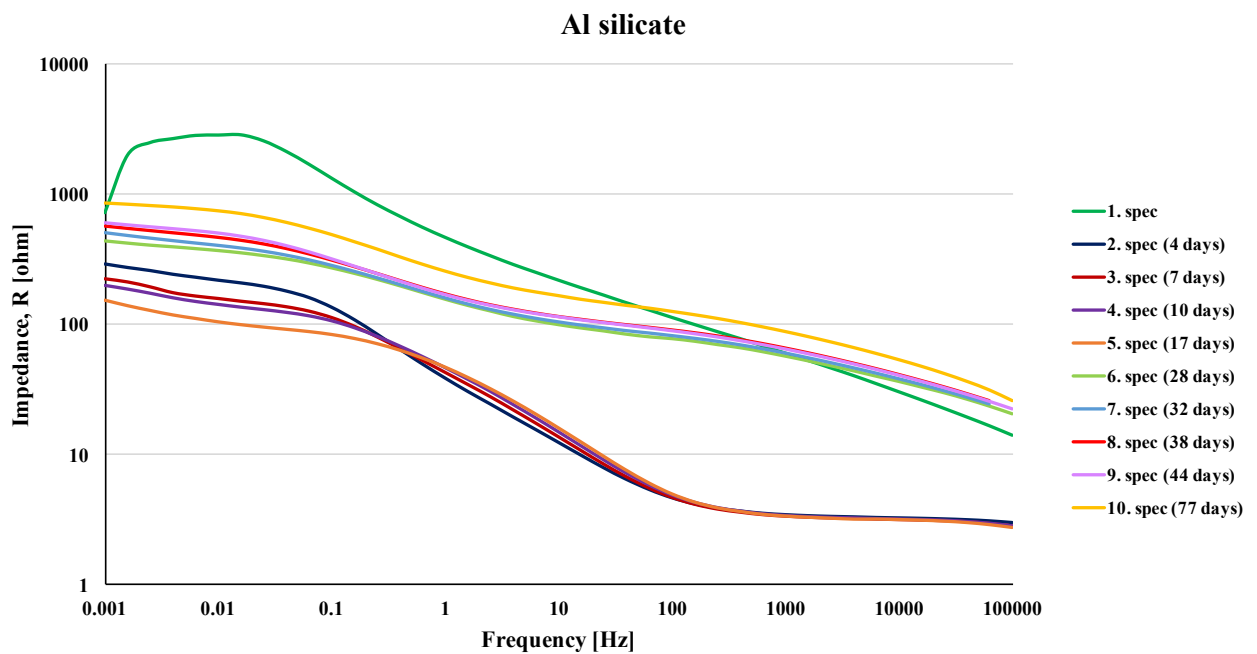| Electrochemical impedance [Ω]	Frequency [Hz]								
	100000	10000	1000	100	10	1	0.1	0.01	0.001
1. spec	14.3	30.9	61.1	114.9	221.8	472.8	1340.4	2877.2	730.6
2. spec (4 days)	3.0	3.3	3.4	4.6	12.4	38.6	134.8	217.6	290.2
3. spec (7 days)	2.9	3.2	3.4	4.8	13.8	43.1	113.3	158.6	224.6
4. spec (10 days)	2.8	3.2	3.4	4.9	15.0	46.8	107.3	143.6	201.4
5. spec (17 days)	18.7	30.8	47.3	63.8	82.8	121.3	156.4	211.1	288.4
6. spec (28 days)	20.7	36.6	57.1	77.8	99.5	155.8	270.2	366.9	434.9
7. spec (32 days)	-	38.0	60.1	82.1	104.8	160.8	286.5	409.0	513.1
8. spec (38 days)	-	41.8	66.6	91.5	115.9	172.6	312.0	465.0	567.2
9. spec (44 days)	22.4	40.7	64.8	89.7	115.0	170.6	321.4	508.8	610.7
10. spec (77 days)	26.0	53.8	88.8	127.1	168.1	259.9	496.8	758.0	870.7

Figure D.9: Electrochemical impedance (y-axis) plotted against frequency (x-axis) for the Al silicate. 10 spectra were taken, and the numbers stated in the parentheses indicate the number of days from test initiation.

Inorganic copolymer coating

Table D.8: Electrochemical impedance values for the inorganic copolymer coating relative to the frequency.

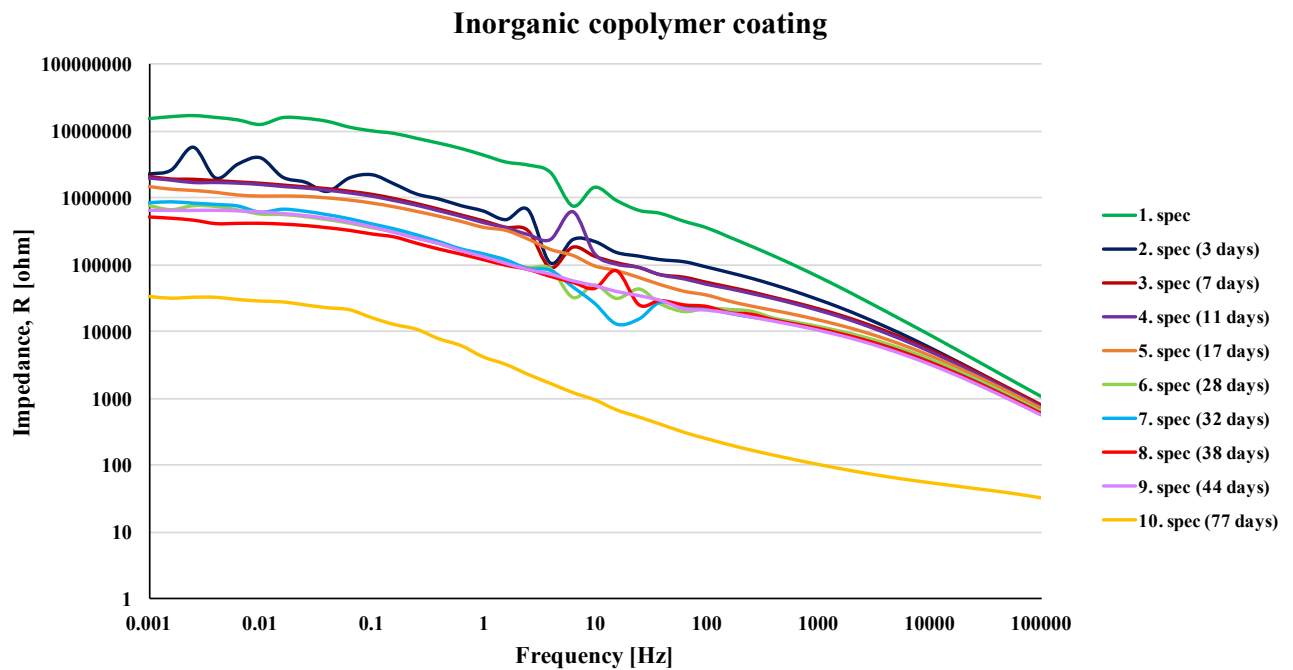| Electrochemical impedance [Ω]	Frequency [Hz]								
	100000	10000	1000	100	10	1	0.1	0.01	0.001
1. spec	1.1E+03	8.9E+03	6.7E+04	3.6E+05	1.4E+06	4.4E+06	1.0E+07	1.3E+07	1.5E+07
2. spec (3 days)	7.7E+02	5.8E+03	3.0E+04	9.2E+04	2.2E+05	6.3E+05	2.2E+06	3.9E+06	2.2E+06
3. spec (7 days)	8.1E+02	5.5E+03	2.2E+04	5.6E+04	1.4E+05	4.6E+05	1.2E+06	1.7E+06	2.1E+06
4. spec (11 days)	7.8E+02	5.2E+03	2.1E+04	5.1E+04	1.5E+05	4.2E+05	1.0E+06	1.6E+06	1.9E+06
5. spec (17 days)	7.3E+02	4.4E+03	1.5E+04	3.5E+04	9.5E+04	3.6E+05	8.2E+05	1.0E+06	1.5E+06
6. spec (28 days)	6.2E+02	3.8E+03	1.2E+04	2.2E+04	5.0E+04	1.3E+05	3.6E+05	5.8E+05	7.9E+05
7. spec (32 days)	6.2E+02	3.6E+03	1.1E+04	2.3E+04	2.7E+04	1.5E+05	4.1E+05	6.2E+05	8.6E+05
8. spec (38 days)	6.0E+02	3.5E+03	1.1E+04	2.4E+04	4.5E+04	1.2E+05	2.9E+05	4.2E+05	5.2E+05
9. spec (44 days)	5.8E+02	3.3E+03	1.1E+04	2.1E+04	5.0E+04	1.3E+05	3.7E+05	6.3E+05	6.7E+05
10. spec (77 days)	3.3E+01	5.5E+01	1.0E+02	2.5E+02	9.5E+02	4.1E+03	1.6E+04	2.8E+04	3.3E+04

Figure D.10: Electrochemical impedance (y-axis) plotted against frequency (x-axis) for the inorganic copolymer coating silicate. 10 spectra were taken, and the numbers stated in the parentheses indicate the number of days from test initiation.

D.3 Development of pH during the exposure

The pH values measured for each container during the test period are presented in Table D.9 and Table D.10. The zinc containing coatings were attached to one multi-cell, while the MgO-, Mg-, Al-silicate and the inorganic copolymer were attached to another multi-cell.

Table D.9: Measured pH values for the multi-cell holding the zinc containing coatings.

Time from test initiation [days]	pH
0	8.24
34	8.57
35	8.61
41	8.60
103	8.12
113	8.13
134	8.00

Table D.10: Measured pH values for the multi-cell holding the MgO-, Mg-, Al-silicate and the inorganic copolymer coating.

Time from test initiation [days]	pH
0	8.34
1	8.67
3	8.50
7	8.31
11	8.30
31	8.24
72	8.34

D.4 EDS analysis of the exposed surface area

Normalized concentrations of the different elements are given from Table D.11 to Table D.17. Corresponding SEM images of the scanned areas are shown from Figure D.11 to Figure D.38.

High Zn primer

Table D.11: EDS results for the high Zn primer with normalized concentration, average normalized concentration and standard deviation of each element at each area.

Element	Normalized concentration [wt %]												Average	STD
	157	161	169	170	171	172	174	175	176	177	178	179		
Zn	65.3	50.2	48.6	52.8	50.5	40.7	43.2	55.5	50.0	51.5	60.8	51.9	51.7	6.7
Al	5.1	8.7	10.7	10.0	10.7	12.4	11.3	9.2	9.4	8.5	5.9	8.5	9.2	2.1
O	23.2	28.9	29.2	26.8	28.3	34.2	32.6	24.4	29.1	30.4	25.4	28.5	28.4	3.2
Mg	6.4	11.8	11.2	9.8	10.0	12.2	12.5	10.5	11.2	9.2	7.8	11.1	10.3	1.8
Cl	0.1	0.4	0.4	0.6	0.4	0.5	0.4	0.4	0.3	0.5	0.1	0.2	0.4	0.2
Total	100.0	100.0	100.0	100.0	100.0	100.0	100.0	100.0	100.0	100.0	100.0	100.0	100.0	-
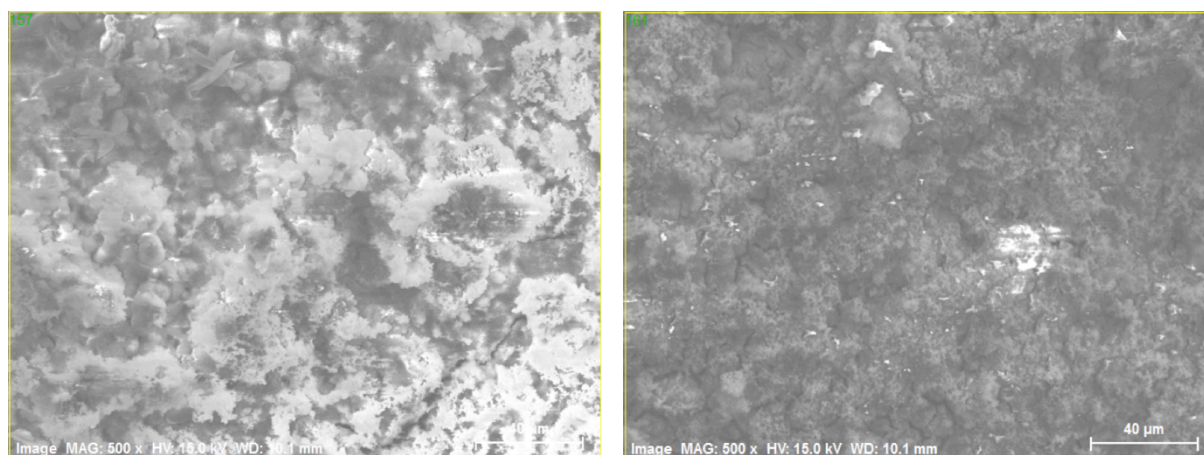
Figure D.11: SEM images of the scanned areas 157 (left image) and 161 (right image). Magnification (500X), accelerating voltage (15.0 kV) and working distance (10.1 mm) are given in each image.
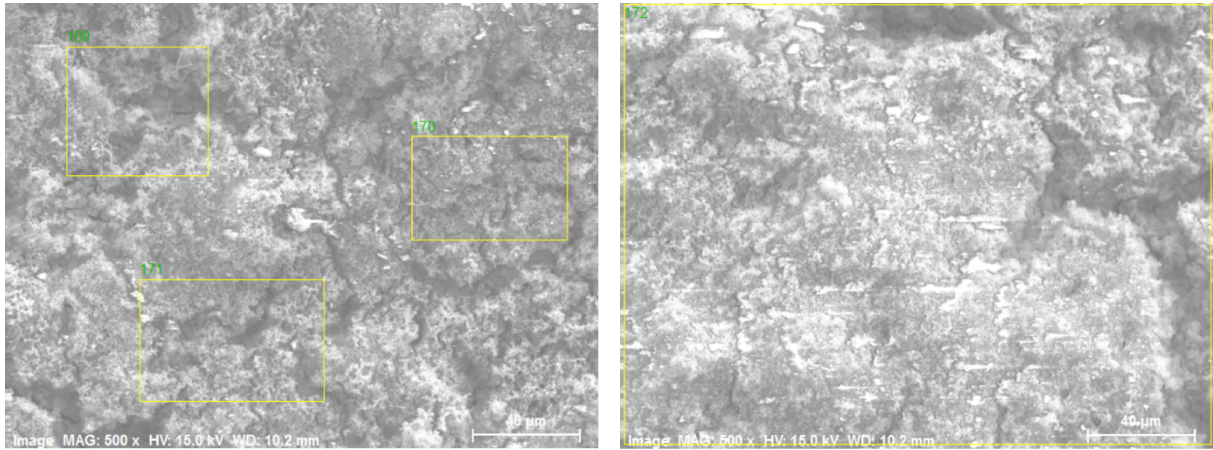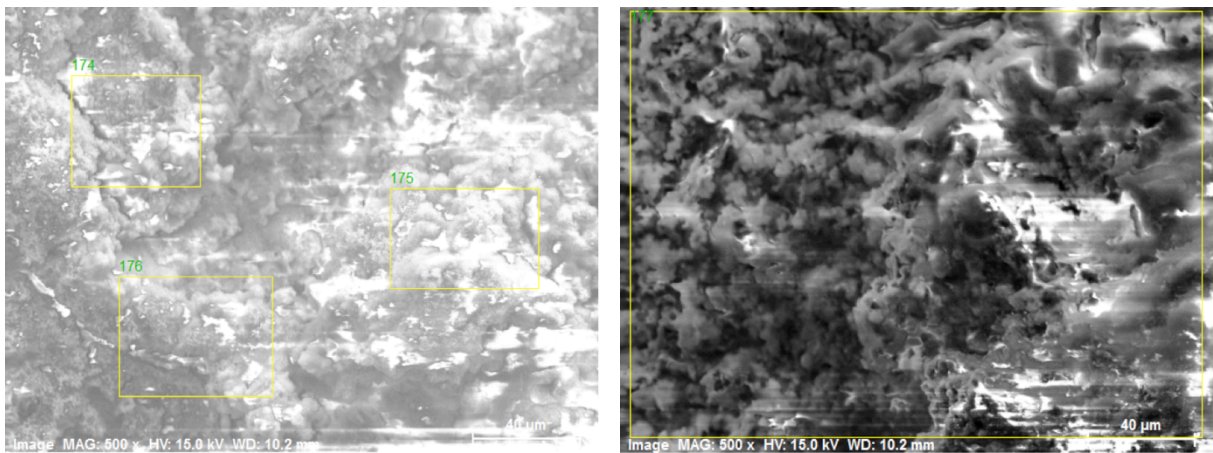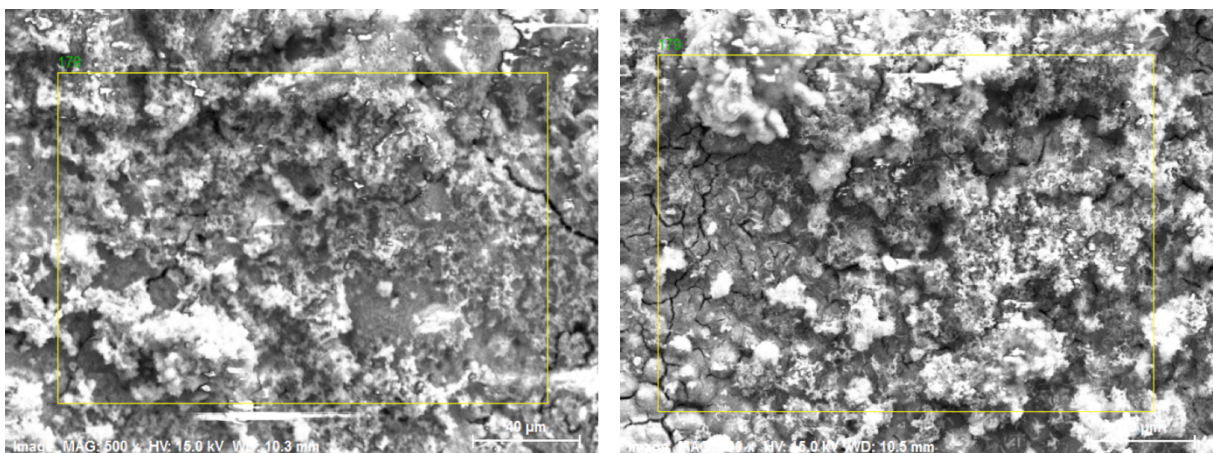
Figure D.12: SEM images of the scanned areas 169, 170 and 171 (left image) and 172 (right image). Magnification (500X), accelerating voltage (15.0 kV) and working distance (10.2 mm) are given in each image.

Figure D.13: SEM images of the scanned areas 174, 175 and 176 (left image) and 177 (right image). Magnification (500X), accelerating voltage (15.0 kV) and working distance (10.2 mm) are given in each image.

Figure D.14: SEM images of the scanned areas 178 (left image) and 179 (right image). Magnification (500X), accelerating voltage (15.0 kV) and working distance (10.3 mm and 10.5 mm) are given in each image.

Zn epoxy

Table D.12: EDS results for the Zn epoxy with normalized concentration, average normalized concentration and standard deviation of each element at each area.

| Element	Normalized concentration [wt %]												Average	STD
	246	253	259	260	261	262	265	275	276	277	278	279		
Zn	39.0	51.5	69.6	85.2	66.1	66.7	76.9	58.2	69.0	64.0	68.8	73.9	65.7	12.0
Al	11.6	8.4	2.5	1.4	2.5	3.6	1.8	3.7	3.0	3.0	2.5	1.7	3.8	3.1
O	35.5	32.6	17.5	9.3	25.0	23.5	16.5	31.5	23.7	28.2	24.9	20.9	24.1	7.4
Mg	11.6	5.9	5.5	3.2	5.7	5.8	3.9	4.2	4.1	4.4	3.5	3.1	5.1	2.3
Cl	2.4	1.6	1.1	0.2	0.8	0.4	0.2	0.7	0.3	0.5	0.3	0.3	0.7	0.7
Ca	0.0	0.0	3.9	0.7	0.0	0.0	0.7	1.7	0.0	0.0	0.0	0.0	0.6	1.2
Total	100.0	100.0	100.0	100.0	100.0	100.0	100.0	100.0	100.0	100.0	100.0	100.0	100.0	-
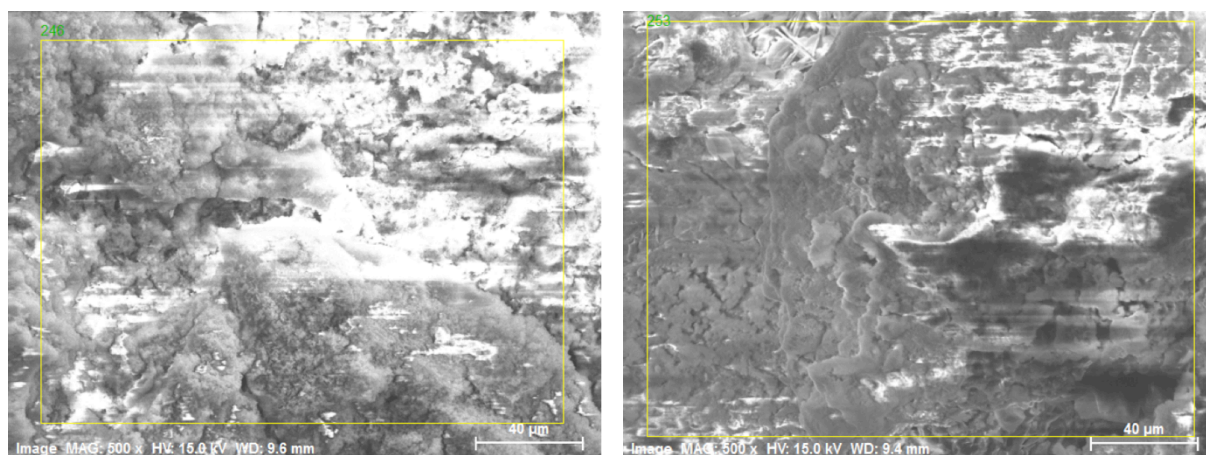
Figure D.15: SEM images of the scanned areas 246 (left image) and 253 (right image). Magnification (500X), accelerating voltage (15.0 kV) and working distance (9.6 mm and 9.4 mm) are given in each image.
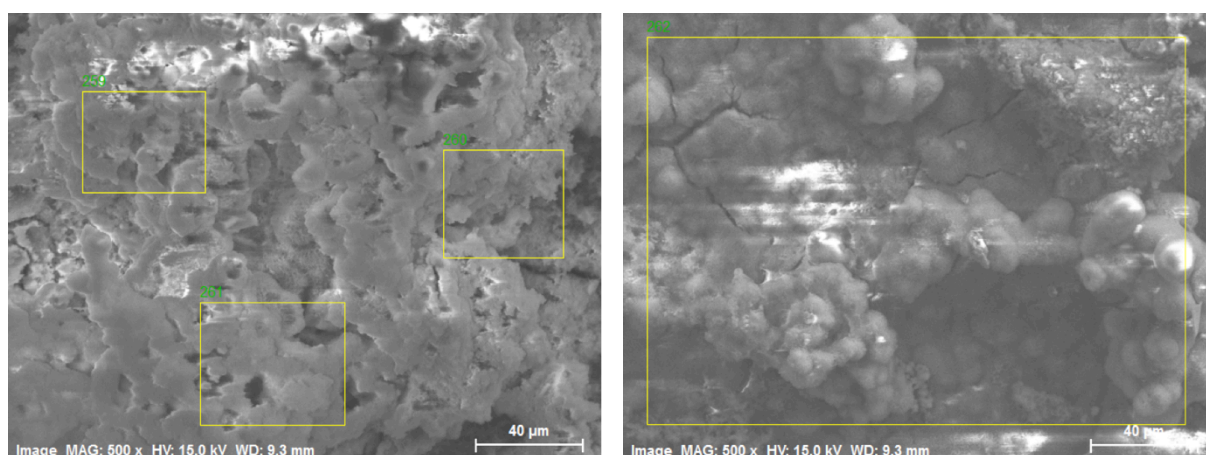

Figure D.16: SEM images of the scanned areas 259, 260 and 261 (left image) and 262 (right image). Magnification (500X), accelerating voltage (15.0 kV) and working distance (9.3 mm) are given in each image.
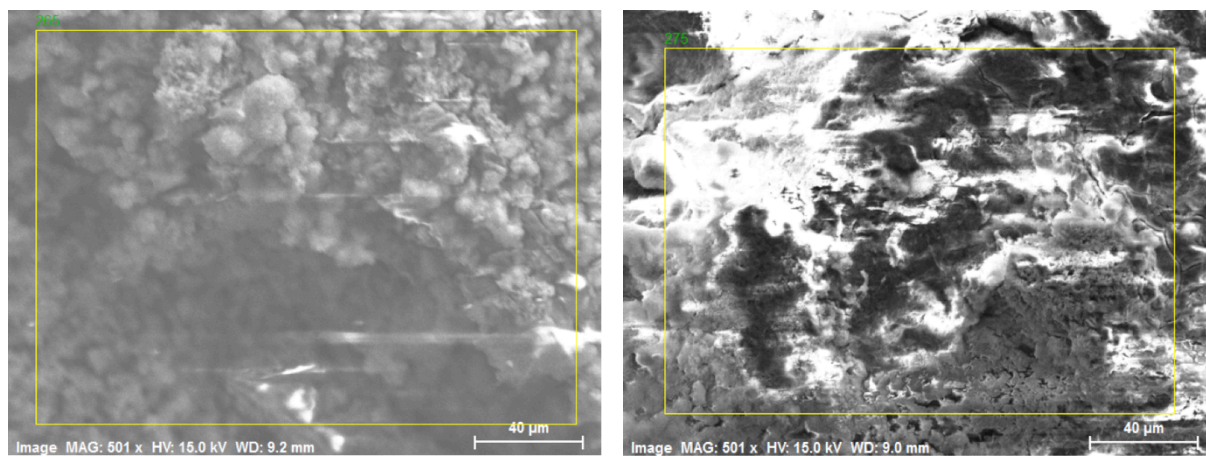
Figure D.17: SEM images of the scanned areas 265 (left image) and 275 (right image). Magnification (500X), accelerating voltage (15.0 kV) and working distance (9.2 mm and 9.0 mm) are given in each image.
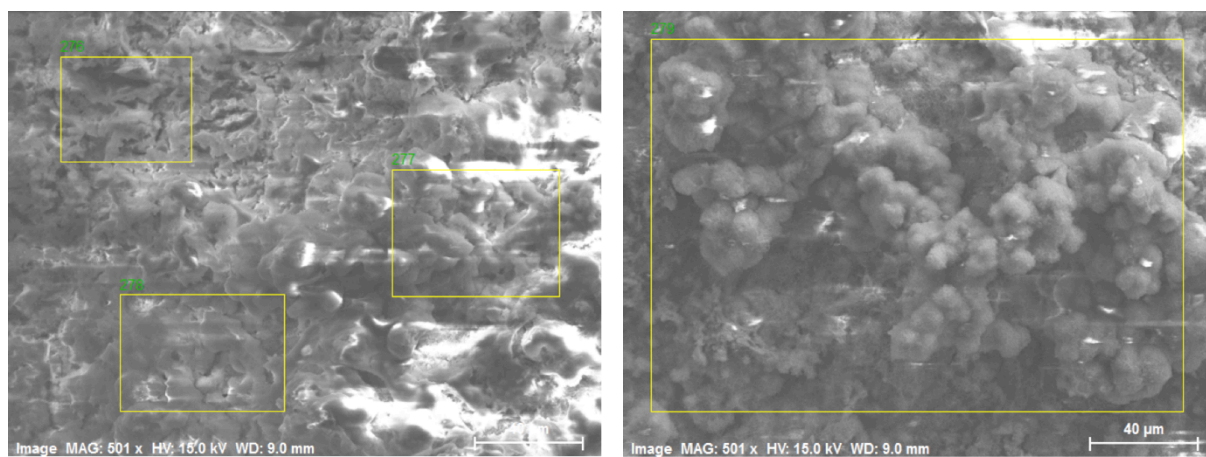

Figure D.18: SEM images of the scanned areas 276, 277 and 278 (left image) and 279 (right image). Magnification (500X), accelerating voltage (15.0 kV) and working distance (9.0 mm) are given in each image.

Modified Zn epoxy

Table D.13: EDS results for the modified Zn epoxy with normalized concentration, average normalized concentration and standard deviation of each element at each area.

| Element	Normalized concentration [wt %]												Average	STD
	213	214	215	216	221	231	232	233	234	235	236	237		
Zn	38.2	28.4	37.2	43.4	34.9	28.6	29.4	33.3	32.4	30.9	32.3	34.3	33.6	4.4
Al	18.3	23.6	20.3	13.3	18.7	14.9	15.9	14.5	14.7	14.9	12.1	13.1	16.2	3.4
O	34.1	38.9	32.7	35.5	37.7	43.7	39.3	35.8	37.6	38.3	39.2	39.3	37.7	2.9
Mg	5.0	4.3	3.8	5.6	5.9	8.6	8.5	13.1	9.9	12.7	13.3	11.1	8.5	3.5
Cl	4.4	4.9	6.0	2.3	2.9	4.3	7.0	3.3	5.4	3.2	3.2	2.2	4.1	1.5
Total	100.0	100.0	100.0	100.0	100.0	100.0	100.0	100.0	100.0	100.0	100.0	100.0	100.0	-
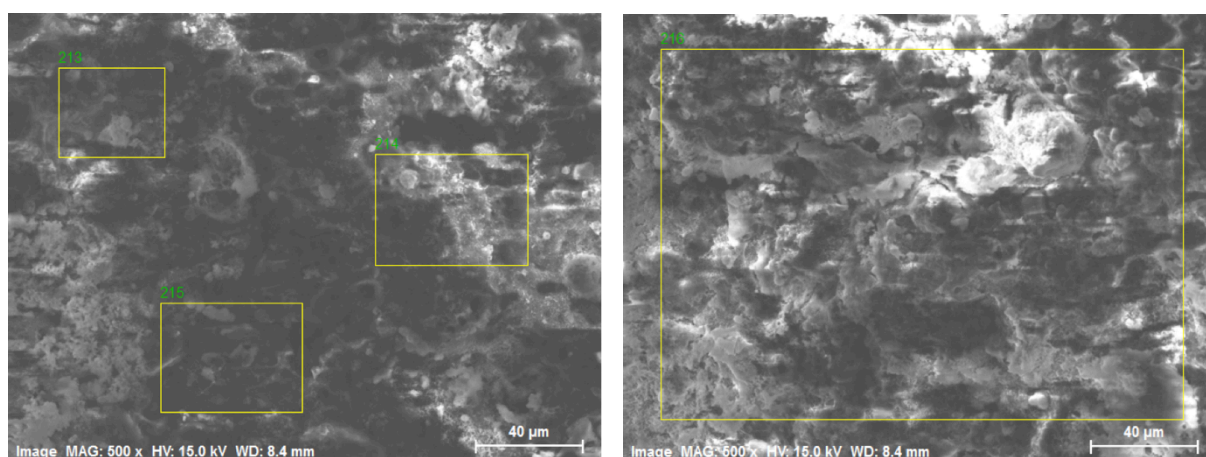
Figure D.19: SEM images of the scanned areas 213, 214 and 215 (left image) and 216 (right image). Magnification (500X), accelerating voltage (15.0 kV) and working distance (8.4 mm) are given in each image.
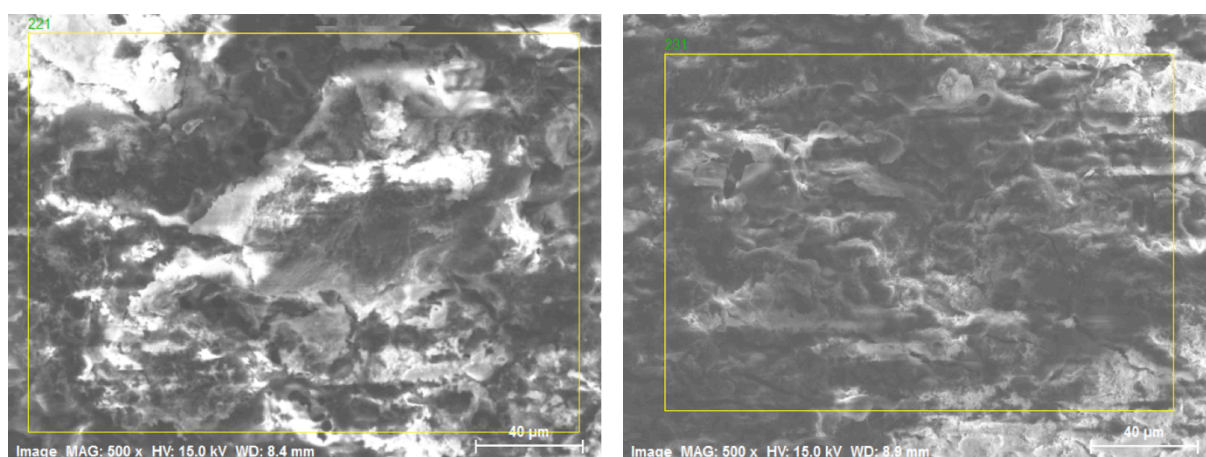

Figure D.20: SEM images of the scanned areas 221 (left image) and 231 (right image). Magnification (500X), accelerating voltage (15.0 kV) and working distance (8.4 mm and 8.9 mm) are given in each image.
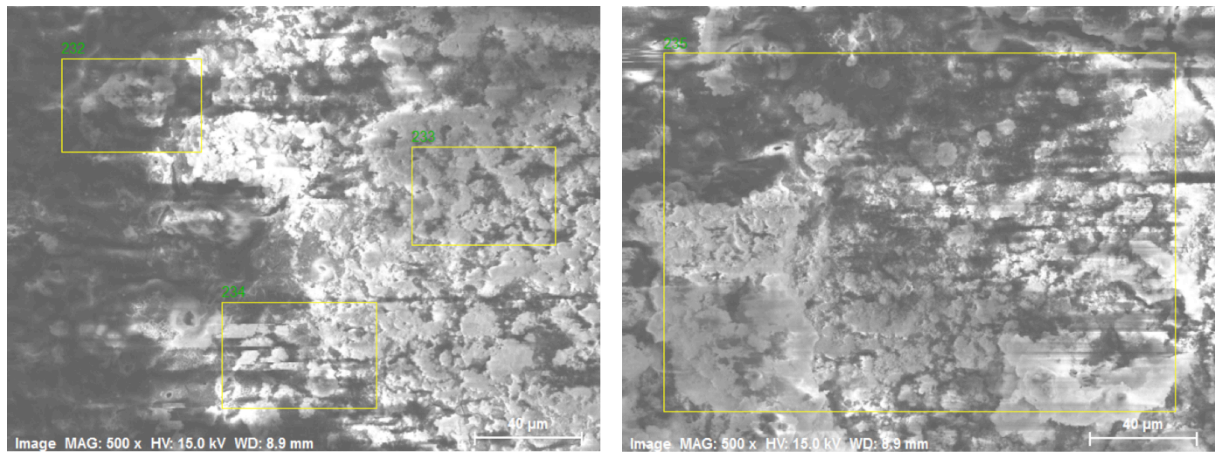
Figure D.21: SEM images of the scanned areas 232, 233 and 234 (left image) and 235 (right image). Magnification (500X), accelerating voltage (15.0 kV) and working distance (8.9 mm) are given in each image.
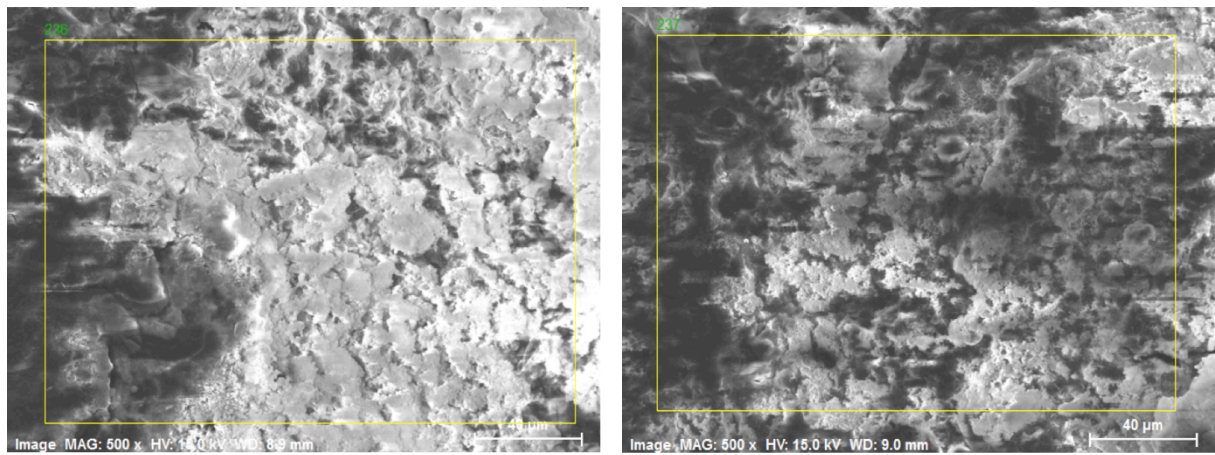

Figure D.22: SEM images of the scanned areas 236 (left image) and 237 (right image). Magnification (500X), accelerating voltage (15.0 kV) and working distance (8.9 mm and 9.0 mm) are given in each image.

Zn silicate

Table D.14: EDS results for the Zn silicate with normalized concentration, average normalized concentration and standard deviation of each element at each area.

| Element	Normalized concentration [wt %]													
	185	193	194	195	197	202	206	207	208	209	210	211	Average	STD
Zn	46.5	57.6	62.9	62.6	44.0	54.9	70.8	53.8	55.8	57.8	74.7	57.2	58.2	8.8
Al	3.6	3.1	2.4	2.5	7.0	4.1	3.1	4.7	3.7	4.1	2.2	4.7	3.8	1.3
O	30.6	29.6	27.0	26.5	35.1	30.1	18.4	33.8	33.2	30.2	18.8	26.5	28.3	5.3
Mg	12.5	6.5	5.0	5.0	11.1	8.2	6.5	4.9	3.6	4.3	1.8	8.9	6.5	3.1
Cl	3.0	2.0	1.7	1.8	2.1	1.9	0.8	2.0	2.2	2.2	1.5	2.1	1.9	0.5
Si	2.6	1.2	1.1	1.0	0.8	0.7	0.2	0.8	0.7	1.0	0.1	0.4	0.9	0.6
Ca	1.2	0.0	0.0	0.6	0.0	0.0	0.2	0.0	0.8	0.4	0.9	0.3	0.4	0.4
Total	100.0	100.0	100.0	100.0	100.0	100.0	100.0	100.0	100.0	100.0	100.0	100.0	100.0	-
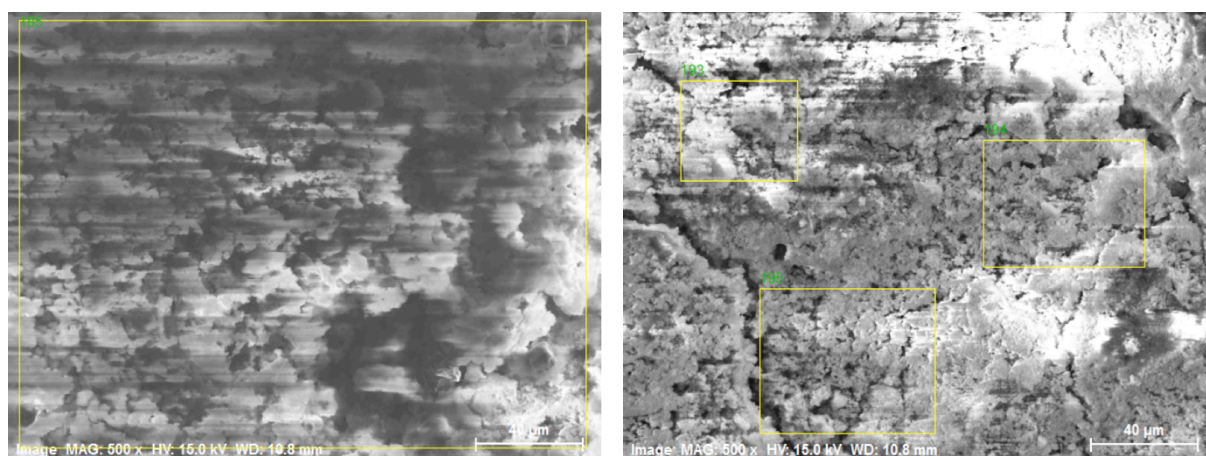
Figure D.23: SEM images of the scanned surface 185 (left image) and 193, 194 and 195 (right image). Magnification (500X), accelerating voltage (15.0 kV) and working distance (10.8 mm) are given in each image.
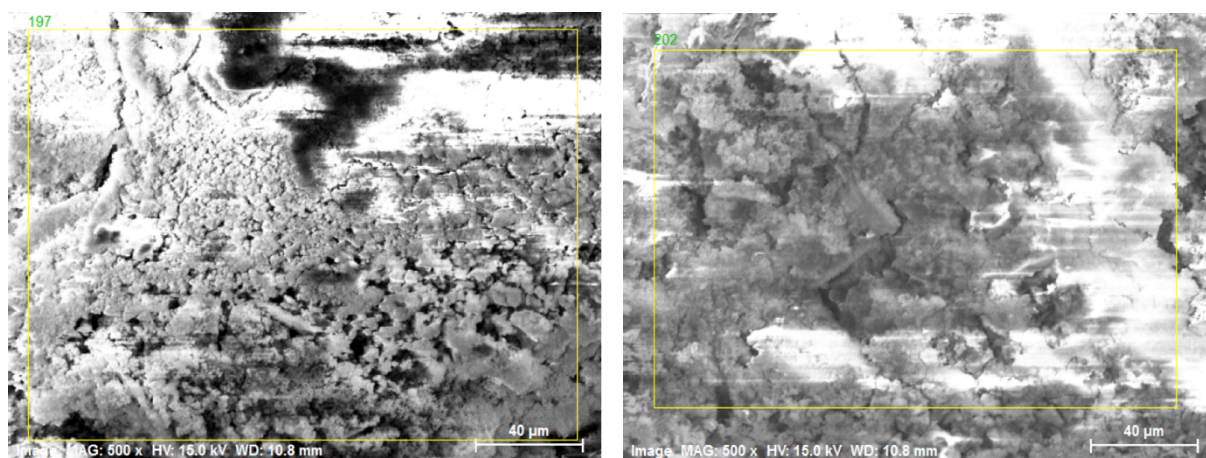

Figure D.24: SEM images of the scanned areas 197 (left image) and 202 (right image). Magnification (500X), accelerating voltage (15.0 kV) and working distance (10.8 mm) are given in each image.
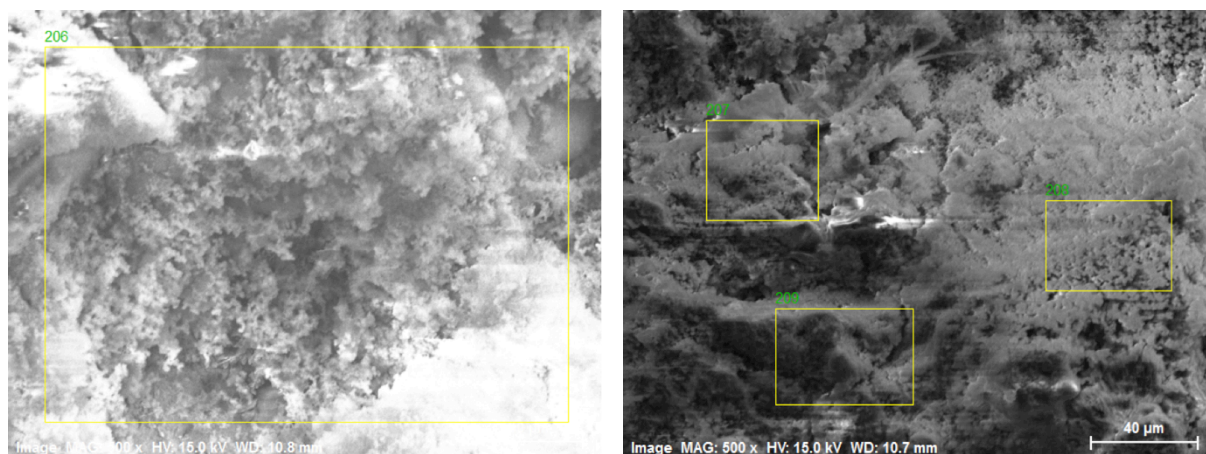
Figure D.25: SEM images of the scanned areas 206 (left image) and 207, 208 and 209 (right image). Magnification (500X), accelerating voltage (15.0 kV) and working distance (10.8 mm and 10.7 mm) are given in each image.
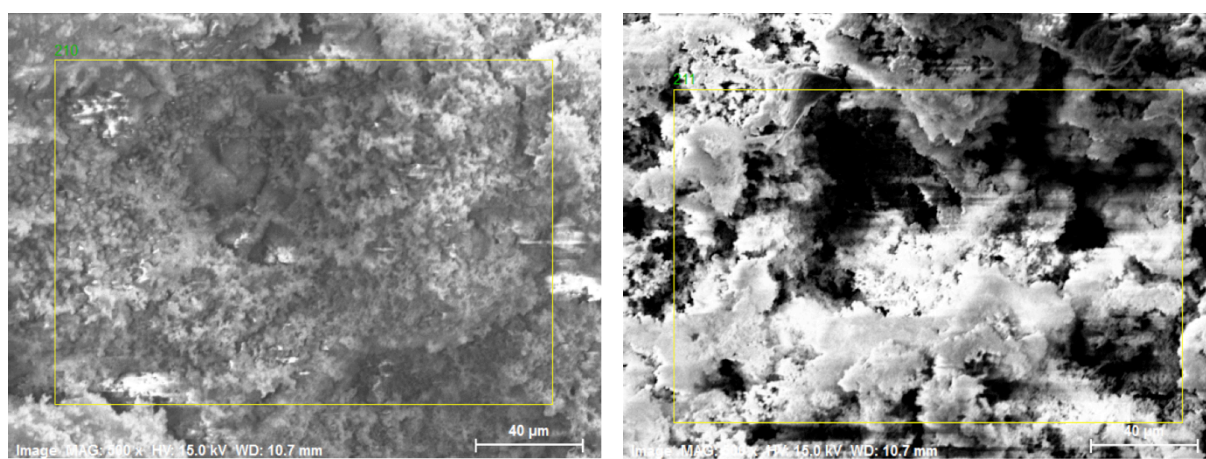

Figure D.26: SEM images of the scanned areas 210 (left image) and 211 (right image). Magnification (500X), accelerating voltage (15.0 kV) and working distance (10.7 mm) are given in each image.

MgO silicate

Table D.15: EDS results for the MgO silicate with normalized concentration, average normalized concentration and standard deviation of each element at each area.

| Element	Normalized concentration [wt %]												Average	STD
	368	369	370	372	373	374	375	376	377	378	379	380		
Mg	8.2	7.4	9.4	8.9	11.6	16.5	17.2	12.8	14.2	19.2	19.1	12.9	13.1	4.2
Al	2.4	1.7	2.5	2.4	4.4	5.4	10.1	9.3	7.5	7.5	8.5	3.5	5.4	3.0
O	47.1	50.5	48.9	48.4	47.7	46.8	47.1	52.4	48.9	45.0	46.1	46.4	47.9	2.0
Ca	38.8	37.0	35.1	35.7	31.5	22.8	13.4	19.0	18.6	19.7	16.7	32.3	26.7	9.2
Si	1.1	1.2	1.1	1.3	1.5	2.8	7.6	2.9	8.3	1.5	1.7	2.2	2.8	2.5
Cl	1.2	1.0	1.7	1.8	2.2	3.8	2.8	1.7	1.3	4.8	5.3	1.8	2.4	1.4
Na	1.2	1.2	1.4	1.4	1.1	2.0	1.9	2.0	1.1	2.4	2.6	1.0	1.6	0.5
Total	100.0	100.0	100.0	100.0	100.0	100.0	100.0	100.0	100.0	100.0	100.0	100.0	100.0	-
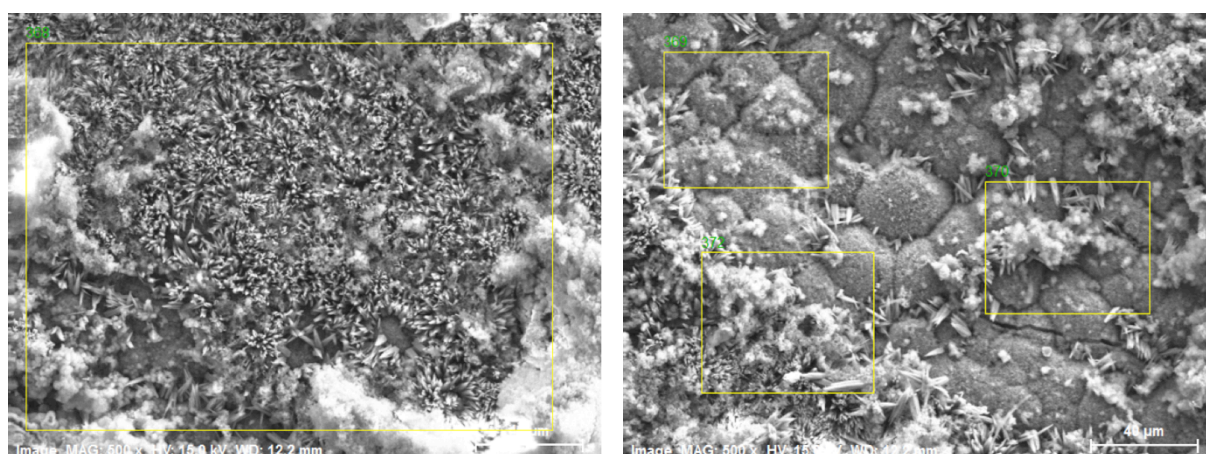
Figure D.27: SEM images of the scanned areas 368 (left image) and 369, 370 and 371 (right image). Magnification (500X), accelerating voltage (15.0 kV) and working distance (12.2 mm) are given in each image.
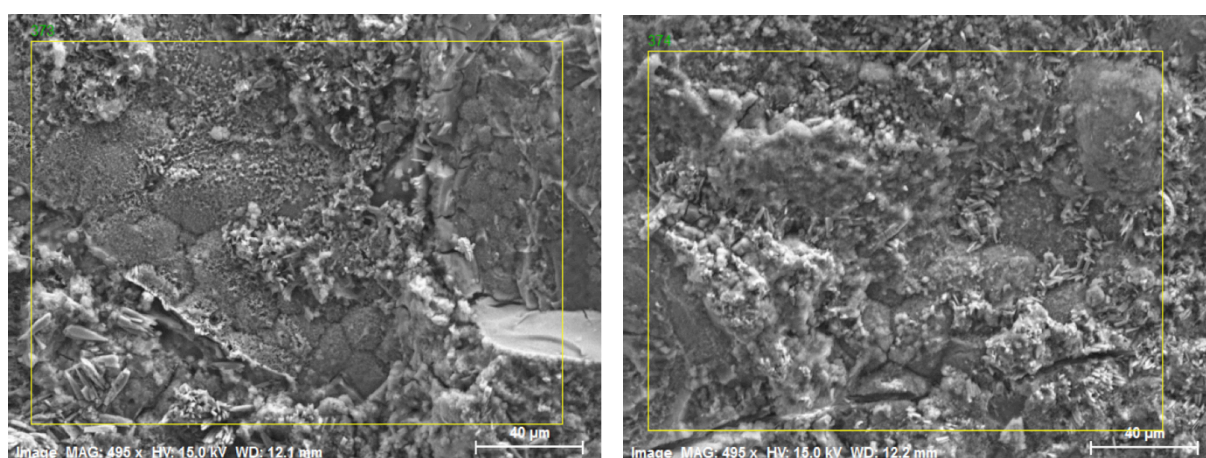

Figure D.28: SEM images of the scanned areas 373 (left image) and 374 (right image). Magnification (495X), accelerating voltage (15.0 kV) and working distance (12.1 mm and 12.2 mm) are given in each image.
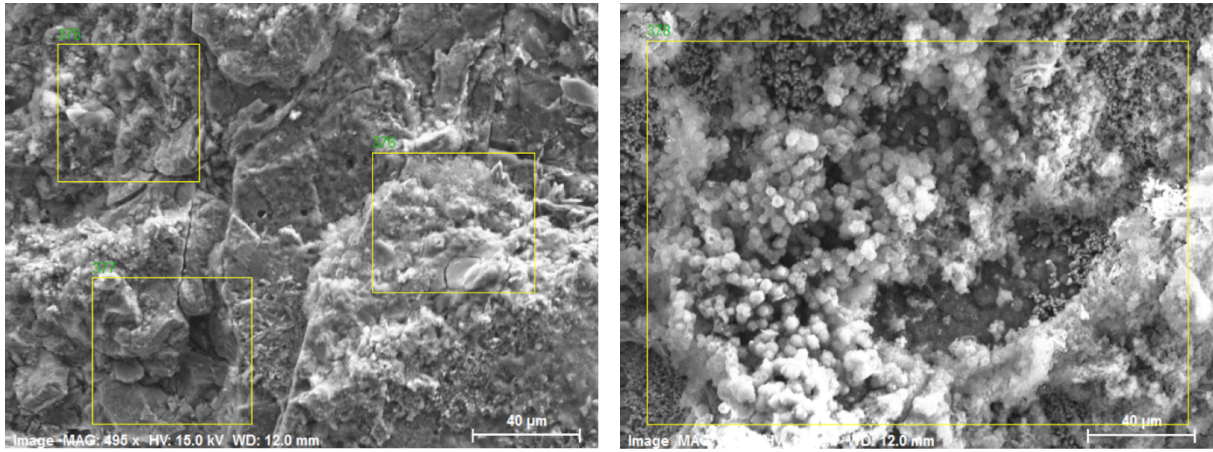
Figure D.29: SEM images of the scanned areas 375, 376 and 377 (left image) and 378 (right image). Magnification (495X), accelerating voltage (15.0 kV) and working distance (12.0 mm) are given in each image.
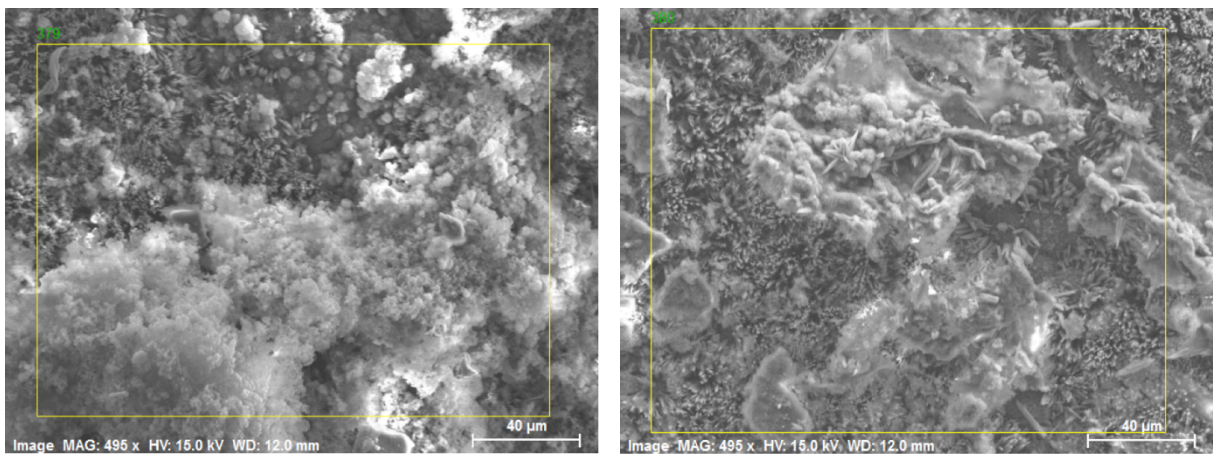

Figure D.30: SEM images of the scanned areas 379 (left image) and 389 (right image). Magnification (495X), accelerating voltage (15.0 kV) and working distance (12.0 mm) are given in each image.

Mg silicate

Table D.16: EDS results for the Mg silicate with normalized concentration, average normalized concentration and standard deviation of each element at each are.

| Element	Normalized concentration [wt %]												Average	STD
	308	309	310	311	312	313	314	315	316	317	319	321		
Mg	2.6	3.1	2.4	3.9	1.5	1.9	1.3	1.1	0.7	2.1	2.8	1.7	2.1	0.9
Al	1.3	1.2	2.3	1.3	0.7	1.3	0.6	1.5	0.6	0.7	1.7	0.8	1.2	0.5
O	51.2	50.3	48.2	46.1	49.8	51.5	49.4	51.9	50.8	51.7	51.7	51.9	50.4	1.8
Ca	40.2	40.6	40.9	43.3	45.0	41.4	46.1	41.5	45.4	42.2	38.8	42.4	42.3	2.2
Si	2.3	2.4	4.6	3.3	1.6	2.3	1.3	2.7	1.4	1.6	2.8	1.4	2.3	1.0
Na	1.3	1.3	1.1	1.1	0.9	1.2	0.9	1.1	0.8	1.1	1.3	1.1	1.1	0.2
Cl	1.0	1.2	0.6	1.1	0.5	0.5	0.4	0.2	0.3	0.6	0.9	0.7	0.7	0.3
Total	100.0	100.0	100.0	100.0	100.0	100.0	100.0	100.0	100.0	100.0	100.0	100.0	100.0	-
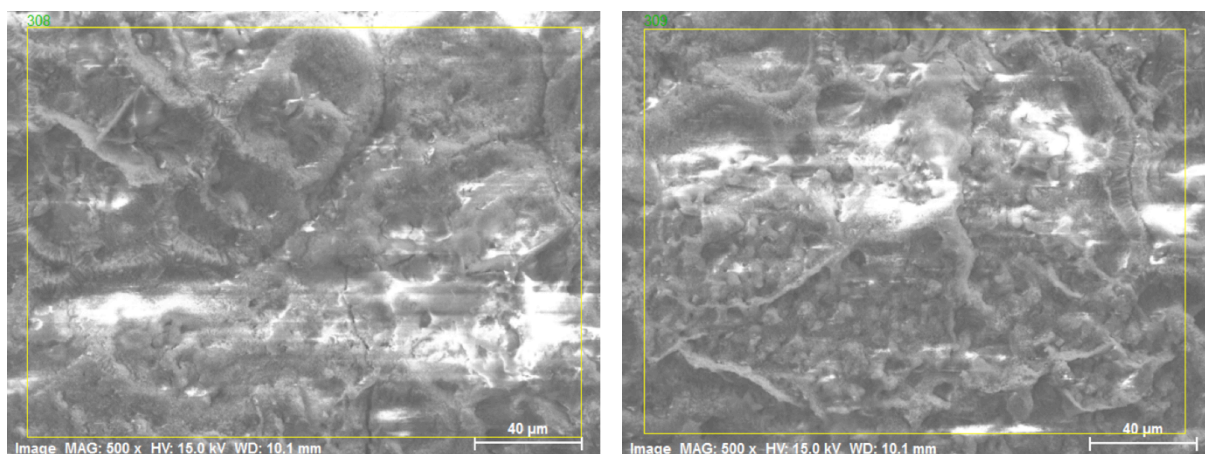
Figure D.31: SEM images of the scanned areas 308 (left image) and 309 (right image). Magnification (500X), accelerating voltage (15.0 kV) and working distance (10.1 mm) are given in each image.
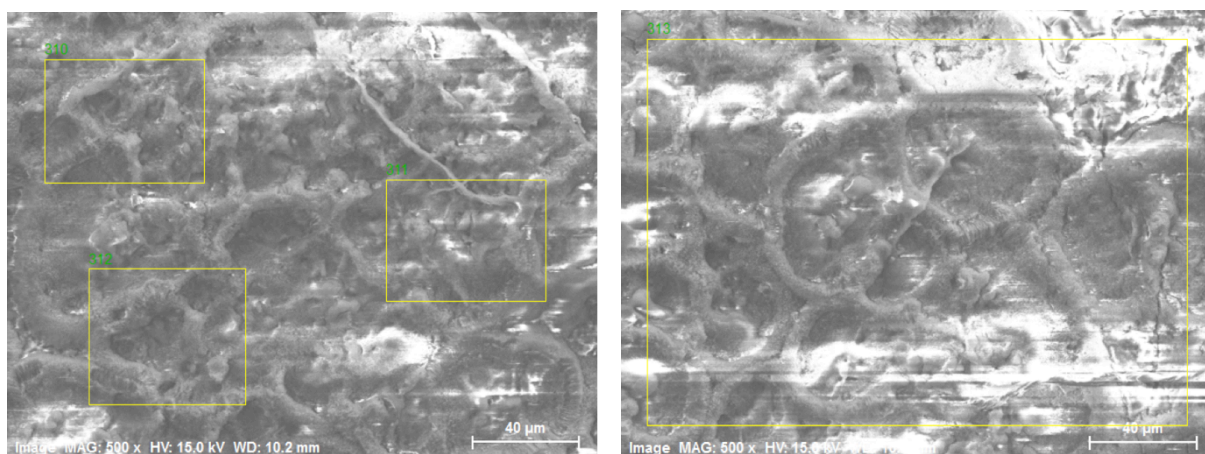

Figure D.32: SEM images of the scanned areas 310, 311 and 312 (left image) and 313 (right image). Magnification (500X), accelerating voltage (15.0 kV) and working distance (10.2 mm) are given in each image.
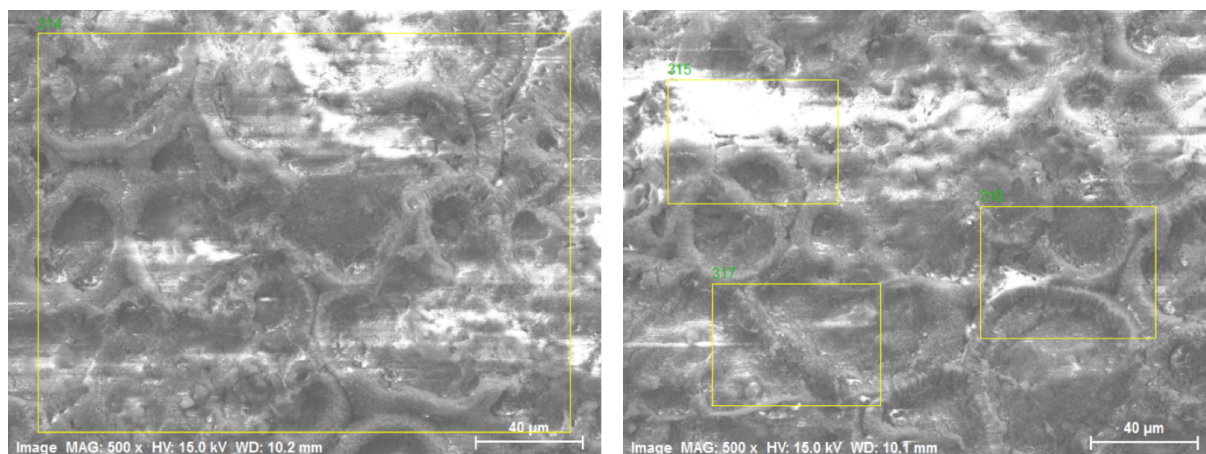
Figure D.33: SEM images of the scanned areas 314 (left image) and 315, 316 and 317 (right image). Magnification (500X), accelerating voltage (15.0 kV) and working distance (10.2 mm and 10.1 mm) are given in each image.
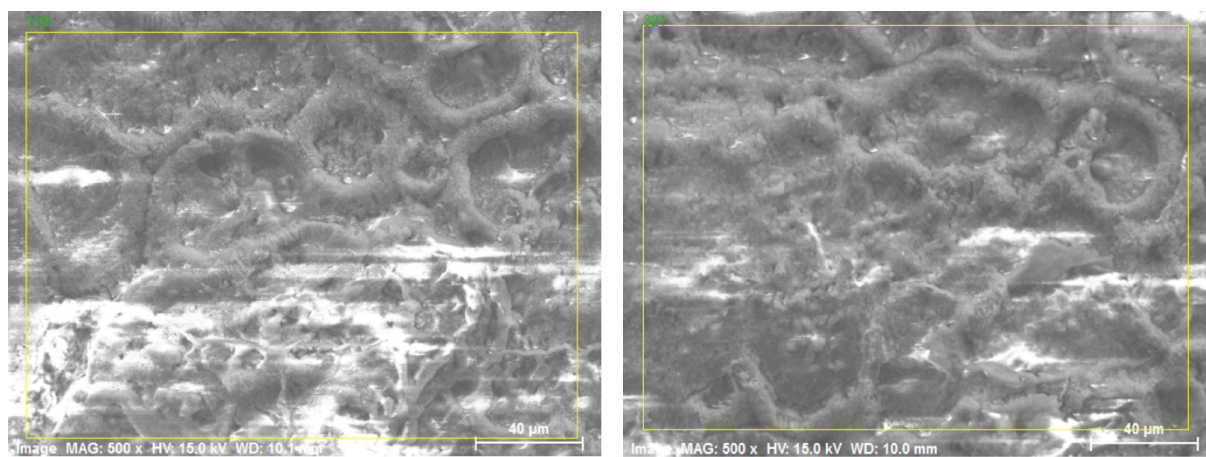

Figure D.34: SEM images of the scanned areas 319 (left image) and 321 (right image). Magnification (500X), accelerating voltage (15.0 kV) and working distance (10.1 mm and 10.0 mm) are given in each image.

Al silicate

Table D.17: EDS results for the Al silicate with normalized concentration, average normalized concentration and standard deviation of each element at each area.

| Element	Normalized concentration [wt %]												Average	STD
	335	336	337	338	339	340	341	342	343	360	361	363		
Al	26.12	22.49	26.11	25.40	27.56	44.26	22.73	23.38	20.35	56.18	52.18	20.32	30.6	12.7
O	37.87	40.07	37.53	38.52	37.58	31.17	39.58	38.94	40.27	25.42	27.85	41.54	36.4	5.2
Si	23.90	24.14	24.12	23.85	22.77	16.90	24.07	24.61	25.67	13.53	14.49	24.61	21.9	4.3
Mg	8.08	8.44	7.91	7.81	7.65	4.68	8.99	8.71	9.23	2.79	3.19	9.37	7.2	2.3
Na	2.31	3.02	2.59	2.72	2.69	1.53	3.05	2.86	3.08	1.02	1.20	3.03	2.4	0.8
K	1.16	1.03	1.14	1.01	1.02	1.05	0.78	0.95	0.81	1.06	1.10	0.68	1.0	0.2
Cl	0.55	0.81	0.61	0.69	0.73	0.41	0.81	0.54	0.58	0.00	0.00	0.45	0.5	0.3
Total	100.0	100.0	100.0	100.0	100.0	100.0	100.0	100.0	100.0	100.0	100.0	100.0	100.0	-
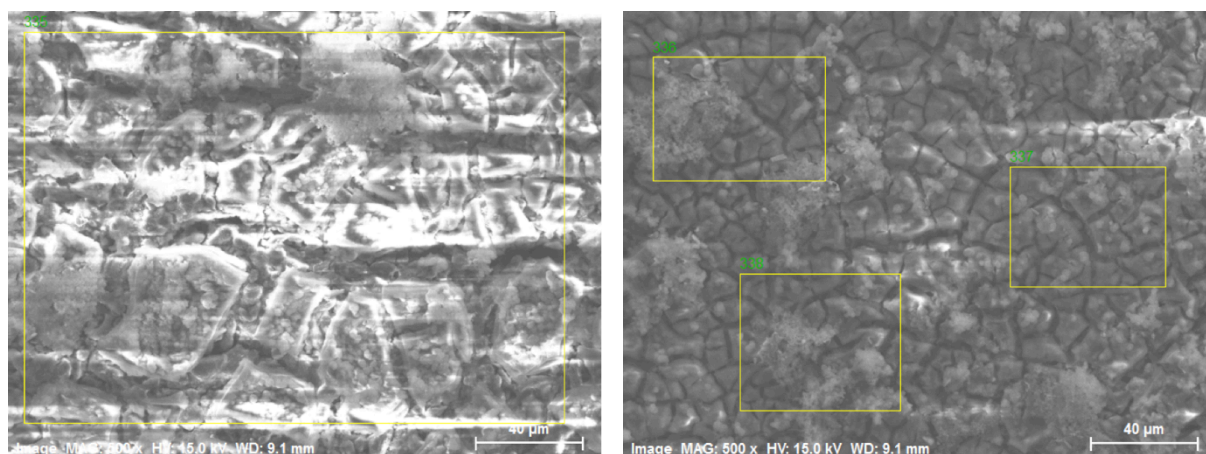
Figure D.35: SEM images of the scanned areas 335 (left image) and 336, 337 and 338 (right image). Magnification (500X), accelerating voltage (15.0 kV) and working distance (9.1 mm) are given in each image.
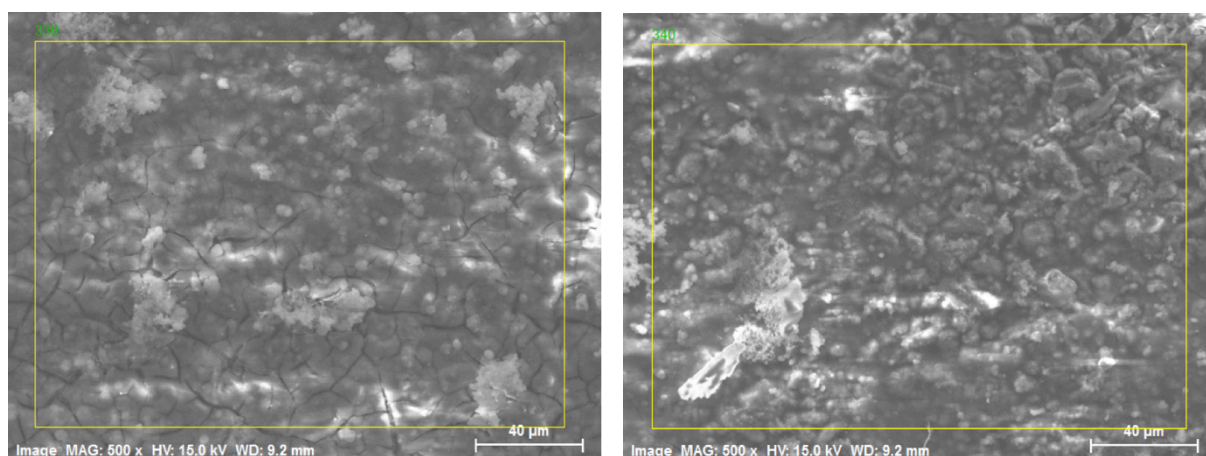

Figure D.36: SEM images of the scanned areas 339 (left image) and 340 (right image). Magnification (500X), accelerating voltage (15.0 kV) and working distance (9.2 mm) are given in each image.
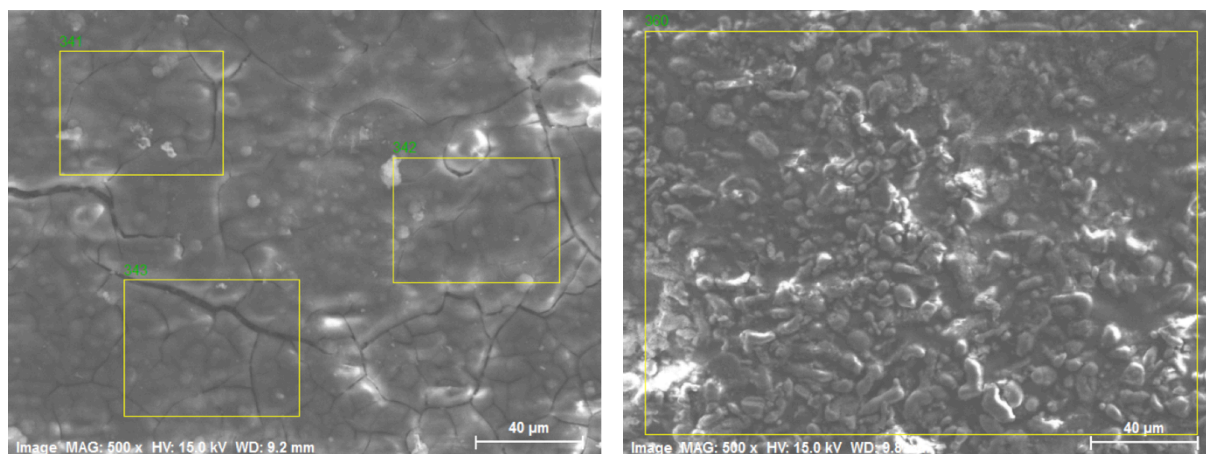
Figure D.37: SEM images of the scanned areas 341, 342 and 343 (left image) and 360 (right image). Magnification (500X), accelerating voltage (15.0 kV) and working distance (9.2 mm) are given in each image.
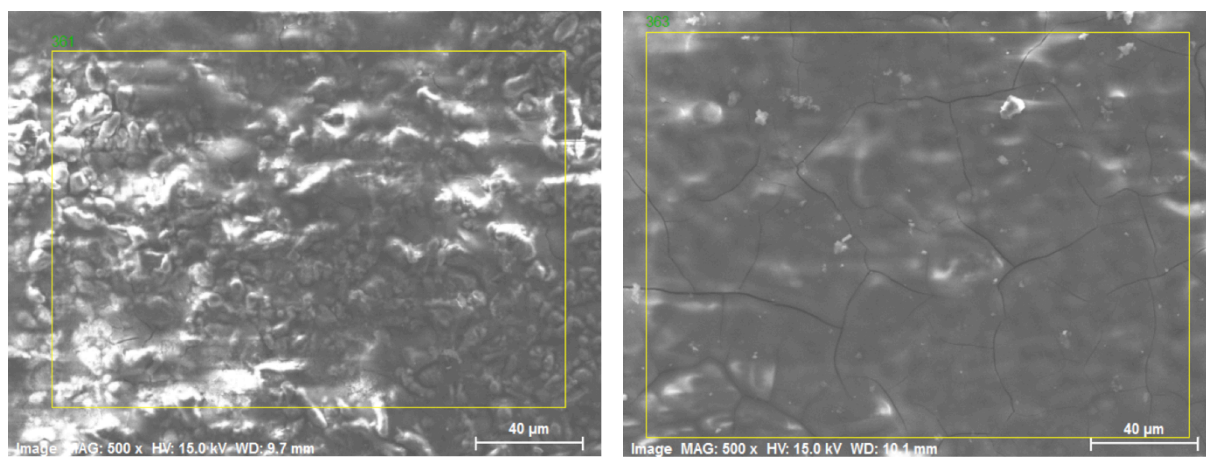

Figure D.38: SEM images of the scanned areas 361 (left image) and 363 (right image). Magnification (500X), accelerating voltage (15.0 kV) and working distance (9.7 mm and 10.1 mm) are given in each image.

Appendix E   Open Circuit Potential

The OCP values measured for the samples are presented in Table E.1 and Table E.2. The values are presented in two tables due to different test multi-cells. The zinc containing coatings were attached to one multi-cell, while the MgO-, Mg-, Al-silicate and inorganic copolymer coating were attached to another multi-cell.

Table E.1: Overview of the OCP for the high Zn primer, Zn epoxy, Zn silicate and the modified Zn epoxy.

Time from test initiation [days]	OCP vs. Ag/AgCl [mV]			
	High Zn primer	Zn epoxy	Zn silicate	Modified Zn epoxy
0	-991	-931	-931	-841
0.5	-1128	-1164	-1112	*
1	-1028	-979	-1026	-1121
2	-990	-965	-1060	-1101
3	-978	-938	-1058	-1079
6	-1028	-915	-1079	-1040
7	-990	-900	-1020	-1001
8	-1065	-890	-1094	-1068
9	-993	-894	-1009	-988
10	-987	-892	-1005	-987
13	-971	-877	-990	-980
14	-956	-872	-1001	-977
15	-951	-871	-993	-982
16	-948	-871	-1001	-968
17	-947	-877	-987	-966
21	-928	-864	-983	-975
22	-922	-859	-983	-974
29	-914	-856	-979	-956
37	-897	-841	-977	-961
43	-883	-836	-975	-951
50	-876	-845	-977	-962
57	-873	-830	-969	-953
71	-903	-844	-959	-954
93	-875	-861	-942	-921
99	-875	-894	-939	-925
104	-856	-842	-939	-912
106	-845	-840	-937	-925
107	-846	-832	-940	-913
108	-844	-845	-936	-899
111	-855	-850	-933	-907

112	-848	-857	-932	-918
113	-857	-868	-931	-913
114	-844	-847	-932	-902
115	-845	-861	-929	-898
118	-836	-866	-925	-906
119	-840	-885	-925	-907
120	-836	-870	-924	-904
121	-829	-823	-924	-897
122	-841	-834	-921	-892
125	-838	-822	-917	-896
126	-842	-822	-916	-896
127	-839	-827	-916	-906
128	-831	-818	-919	-901
129	-830	-820	-916	-891
132	-840	-817	-911	-890
133	-847	-822	-911	-892
134	-843	-820	-911	-893

* Unstable value presented for the second measurement, and is therefore not included.

Table E.2: Overview of the OCP for the MgO-, Mg-, Al-silicate and the inorganic copolymer coating.

Time from test initiation [days]	OCP vs. Ag/AgCl [mV]			
	MgO silicate	Mg silicate	Al silicate	Inorganic copolymer coating
0	-686	-760	-458	*
0.5	-1102	-952	-728	-430
1	-1132	-965	-836	-160
2	-1127	-978	-927	-230
2.5	-1112	-1019	-1024	-333
3	-1108	-1026	-1035	-556
3.5	-1097	-1029	-1041	-650
4	-1096	-1031	-1034	-498
4.5	-1093	-1007	-976	-452
5	-1089	-1010	-981	-397
7	-1059	-1019	-960	-640
8	-1058	-1026	-938	-537
9	-1044	-1039	-947	-544
10	-1030	-1061	-944	-551
11	-1042	-1066	-912	-526
14	-1008	-1051	-920	-574
15	-1003	-1033	-919	-588
16	-1000	-1014	-914	-608
17	-994	-1005	-910	-620
18	-1005	-1039	-900	-571
21	-981	-999	-904	-628
22	-976	-994	-896	-602
23	-975	-990	-898	-642
24	-971	-985	-891	-622
25	-1127	-1052	-1076	-470
28	-1067	-1020	-989	-466
29	-1051	-1044	-1006	-488
30	-1031	-1016	-981	-509
31	-1018	-999	-965	-575
32	-1027	-1009	-974	-562
35	-1009	-1005	-965	-660
36	-1002	-994	-958	-629
37	-998	-990	-948	-650
38	-994	-985	-940	-800
39	-1005	-1020	-975	-827
42	-983	-985	-936	-806
43	-980	-981	-930	-707
44	-977	-976	-926	-666

45	-991	-1007	-963	-651
46	-982	-995	-953	-733
49	-973	-975	-929	-823
50	-970	-970	-924	-782
51	-960	-945	-896	-721
52	-1001	-1003	-955	-798
53	-1015	-1021	-1004	-856
56	-990	-968	-935	-700
57	-985	-959	-924	-810
58	-983	-952	-916	-708
59	-1041	-1016	-1006	-828
60	-995	-975	-965	-720
72	-959	-917	-877	-777
73	-1193	-1204	-1077	-899
74	-1138	-1144	-1037	-746
77	-1118	-1110	-1064	-1100
78	-1053	-1043	-1011	-878
79	-1041	-1028	-994	-796
80	-1025	-1014	-974	-718
81	-1017	-1006	-967	-693

* Unstable value presented for the first measurement, and is therefore not included.

Appendix F   Crevice Corrosion Test

F.1   Test setup 1

The repair coatings were immersed in two different containers due to restricted space. The zinc containing coatings and the TSA sample coated with epoxy were immersed in one container (container 1), while MgO-, Mg-, Al-silicate and the inorganic copolymer coating in another container (container 2). The pH values measured during the test period are presented in Table F.1

Table F.1: Measured pH for the crevice corrosion test setup 1 for both containers.

Time from test initiation [days]	pH	
	Container 1 (Z, ZE, ZS, H, TSA)	Container 2 (MgO, Mg, Al, V)
0	8.31	8.31
0.5	8.27	8.29
1	8.23	8.33
2	8.11	8.24
3	7.93	8.13
6	7.30	7.59
8	5.00	6.81
10	4.73	4.85
13	4.59	4.53
14	4.60	4.51

Light microscope images, presented from Figure F.1 to Figure F.9, revealed the amount of TSA corrosion and corrosion creep into the crevice. All cross section images contain a steel substrate coated with TSA and the current repair coat. Lowest degree of TSA corrosion was seen on the modified Zn epoxy, Al silicate and the TSA coated with epoxy. The numbers stated in the parentheses indicate the orientation related to the crevice opening. Note that the order of the numbers varies.

High Zn primer
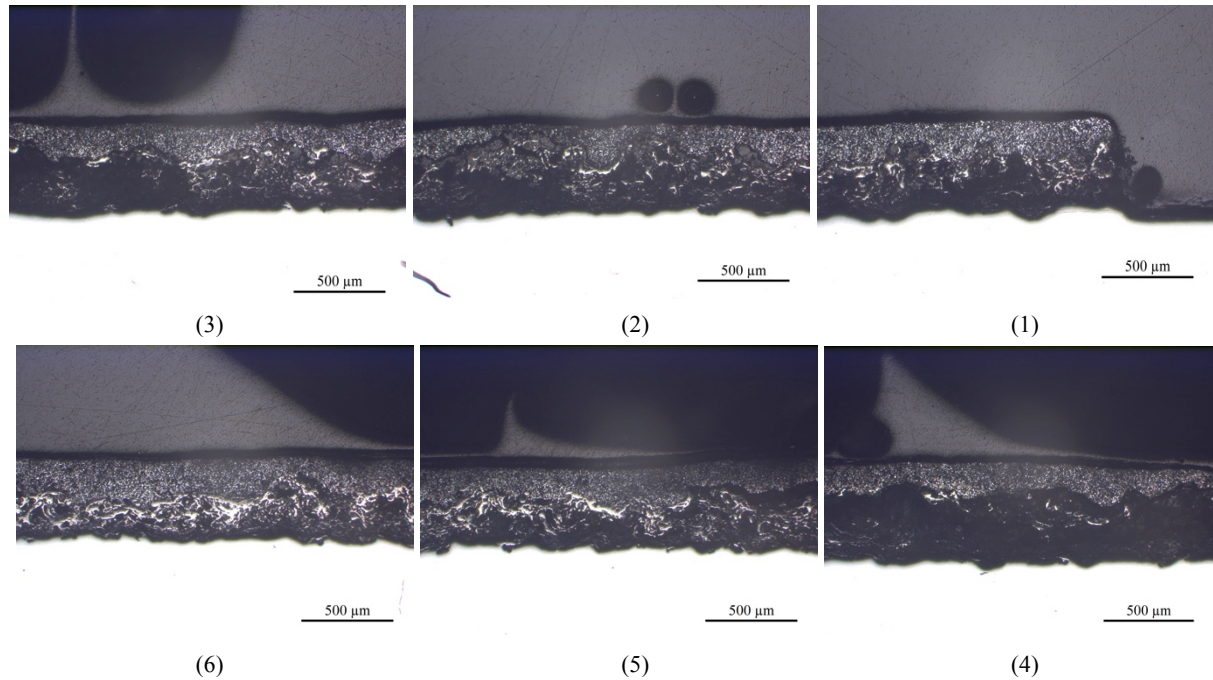
Figure F.1: Light microscope images of the high Zn primer at the crevice opening (1) and further into the crevice (6). Corrosion creep can be seen approximately 12.3 mm into the crevice, in addition to some corrosion of the high Zn primer.
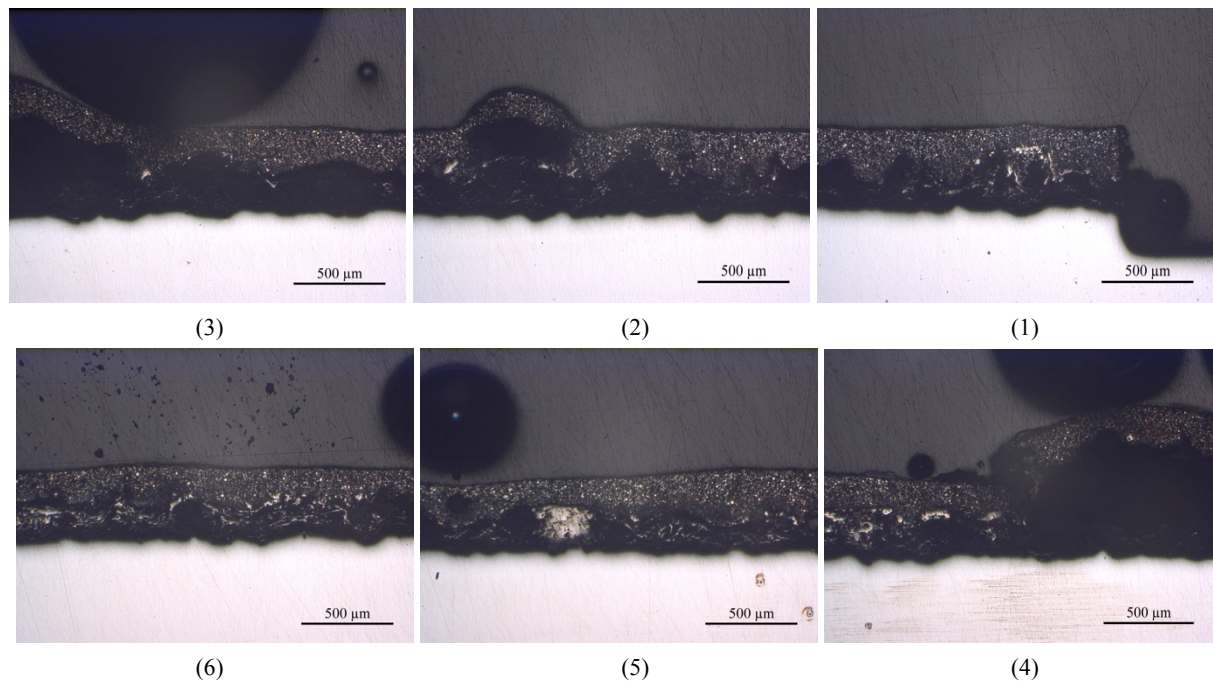
Zn epoxy

Figure F.2: Light microscope images of the Zn epoxy at the crevice opening (1) and further into the crevice (6). Corrosion creep for the TSA can be seen in the entire crevice, in addition to blistering. The Zn epoxy was also reduced.

Modified Zn epoxy

(1)   (2)   (3)
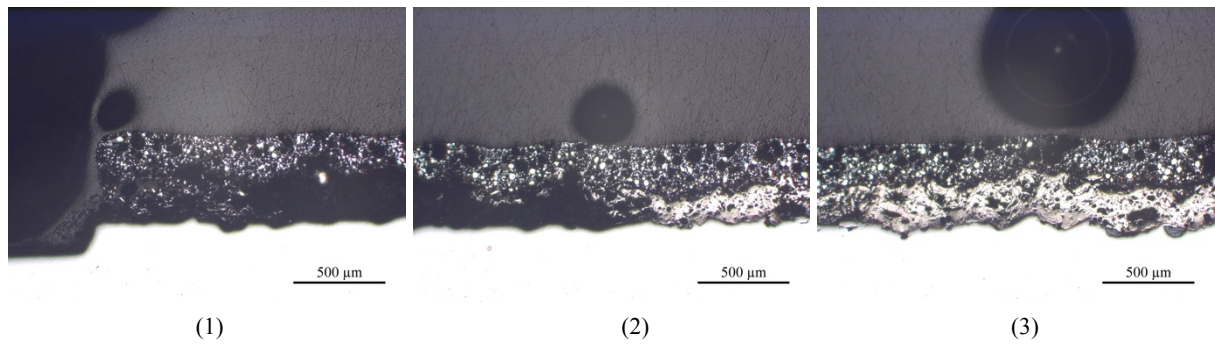
Figure F.3: Light microscope images of the modified Zn epoxy at the crevice opening (1) and further into the crevice (3). Corrosion creep of the TSA can be seen approximately 3 mm into the crevice, in addition to sporadic TSA corrosion. Intact zinc particles can be seen in the modified Zn epoxy.
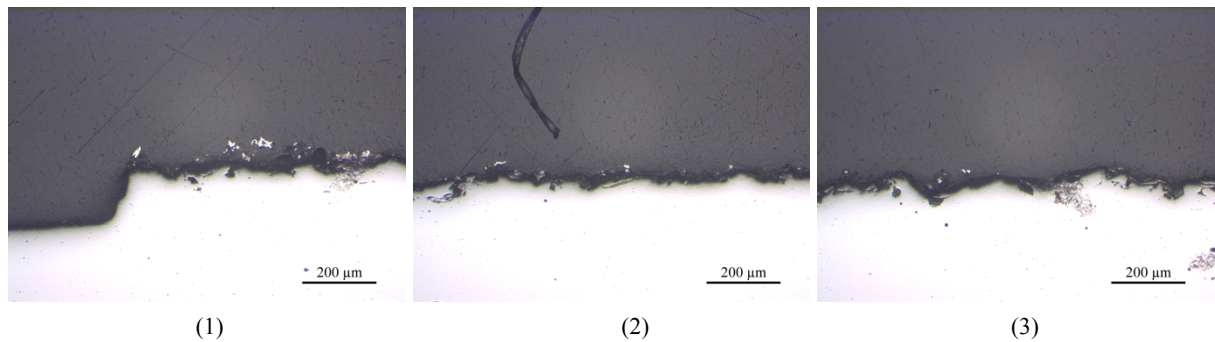
Zn silicate

(1)   (2)   (3)

Figure F.4: Light microscope images of the Zn silicate at the crevice opening (1) and further into the crevice (3). During the machining of the sample, the Zn silicate layer flaked off. The TSA layer was totally reduced where the repair coating had flaked off.

MgO silicate

(3)   (2)   (1)
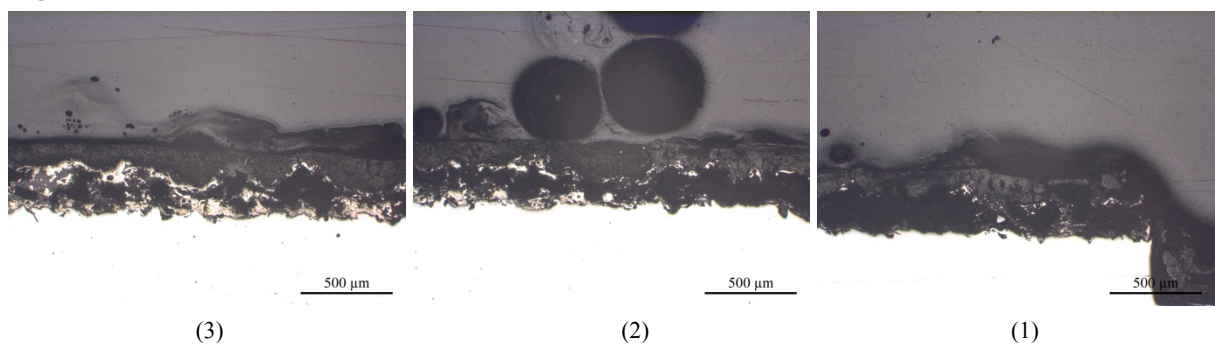
Figure F.5: Light microscope images of the MgO silicate at the crevice opening (1) and further into the crevice (3). High amount of corrosion for both coating layers can be seen, in addition to corrosion creep and sporadic corrosion of the TSA.
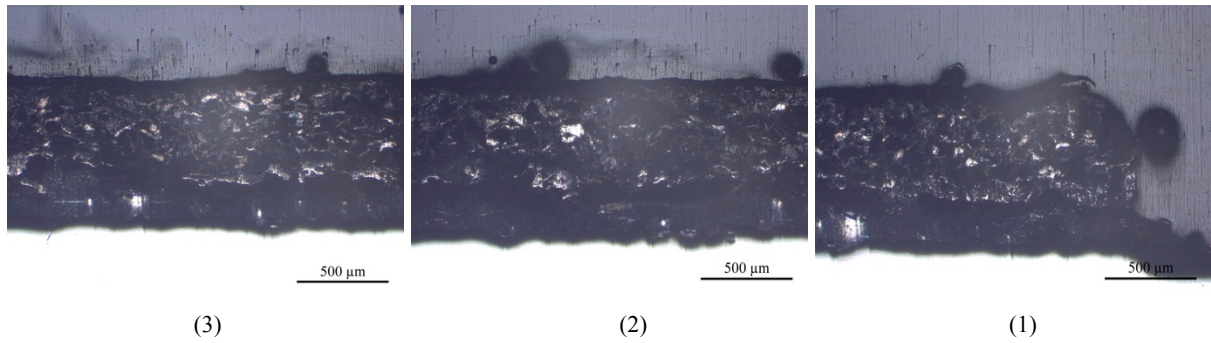
Mg silicate

(3)	(2)	(1)

Figure F.6: Light microscope images of the Mg silicate at the crevice opening (1) and further into the crevice (3). High amount of corrosion for both coating layers can be seen, in addition to corrosion creep of the TSA in the entire crevice.
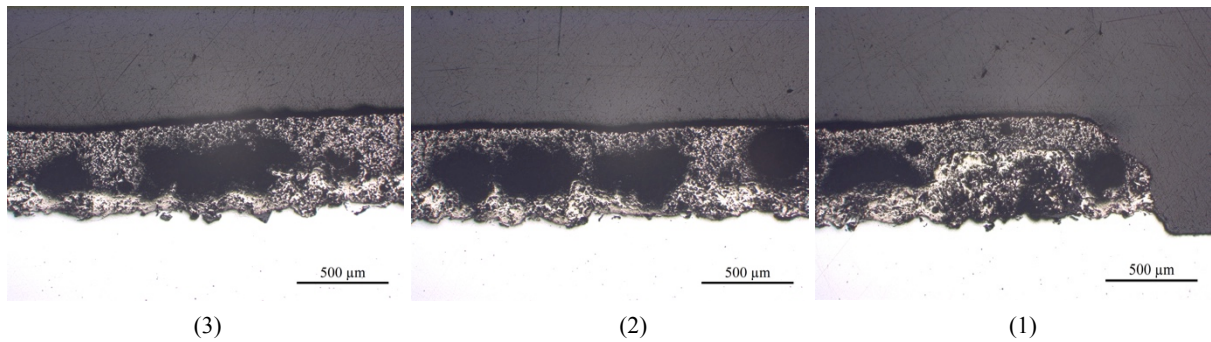
Al silicate

(3)	(2)	(1)

Figure F.7: Light microscope images of the Al silicate at the crevice opening (1) and further into the crevice (3). The TSA was only sporadically corroded, while the Zn silicate corroded in clusters.

Inorganic copolymer coating

(3)	(2)	(1)
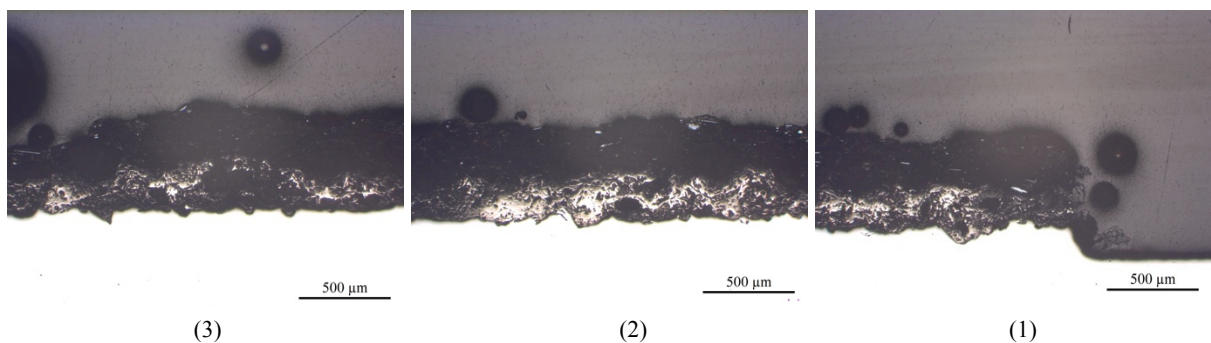
Figure F.8: Light microscope images of the inorganic copolymer coating at the crevice opening (1) and further into the crevice (3). The amount of TSA corrosion was high, like for the inorganic copolymer coating.
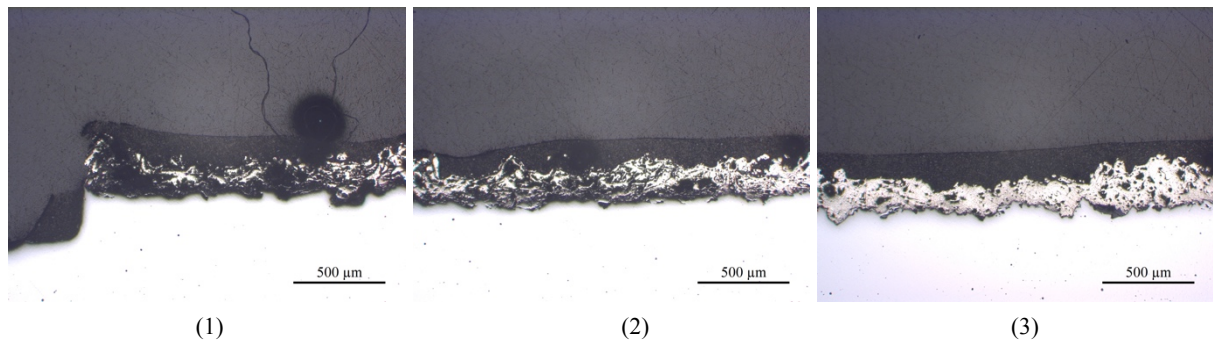
TSA coated with epoxy

(1)   (2)   (3)

Figure F.9: Light microscope images of the TSA coated with epoxy at the crevice opening (1) and further into the crevice (3). Continuously corrosion of the TSA can be seen approximately 3.8 mm into the crevice, while dark areas of either corrosion or voids can be seen further into the crevice.

F.2 Test setup 2

Test setup 2 was run twice, with test periods of respectively 16 days and 30 days. All samples were exposed in the same container. The pH values measured for test setup 2 (16 days) are presented in Table F.2.

Table F.2: Measured pH for the crevice corrosion test setup 2 run for 16 days.

Time from test initiation [days]	pH
0	8.19
1	8.10
2	8.00
3	7.97
6	7.42
7	7.40
8	7.25
9	7.18
10	7.46
13	7.04
14	7.17
15	6.86
16	7.07

Light microscope images of the cross sections are presented from Figure F.10 to Figure F.18. All images contain a steel substrate coated with TSA and a topcoat of the current repair coating. The numbers stated in the parentheses below the images indicate the orientation related to the crevice opening. Note that the order of the numbers varies between the different coatings. The amount of TSA corrosion and repair coat reduction are explained in the figure text.

High Zn primer

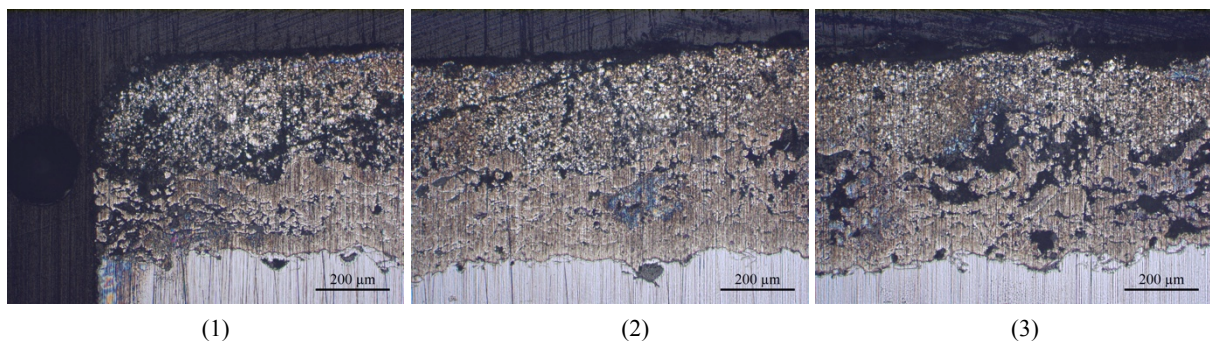(1)   (2)   (3)

Figure F.10: Light microscope images of the high Zn primer at the crevice opening (1) and further into the crevice (3). The TSA had only corroded at the crevice opening, in addition to sporadically further into the crevice. High amount of intact zinc particles can be seen.
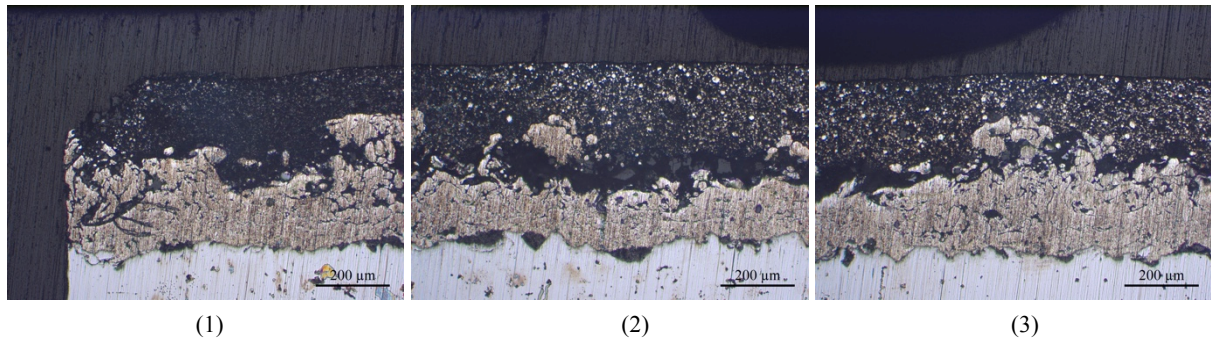
Zn epoxy

| (1) | (2) | (3) |

Figure F.11: Light microscope images of the Zn epoxy at the crevice opening (1) and further into the crevice (3). The TSA had only corroded at the crevice opening, and some corrosion between the two coating layers can be seen. Highest amount of zinc corrosion occurred at the crevice opening.
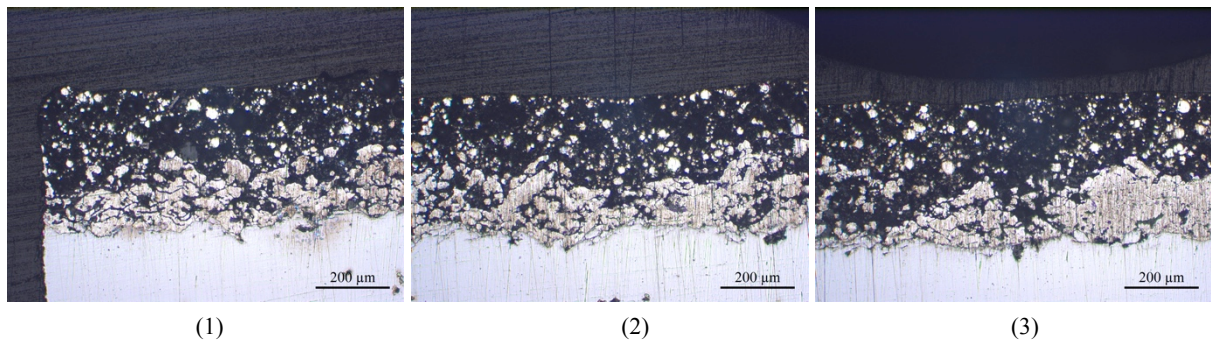
Modified Zn epoxy

| (1) | (2) | (3) |

Figure F.12: Light microscope images of the modified Zn epoxy at the crevice opening (1) and further into the crevice (3). General corrosion of both the TSA and the modified Zn epoxy had occurred.
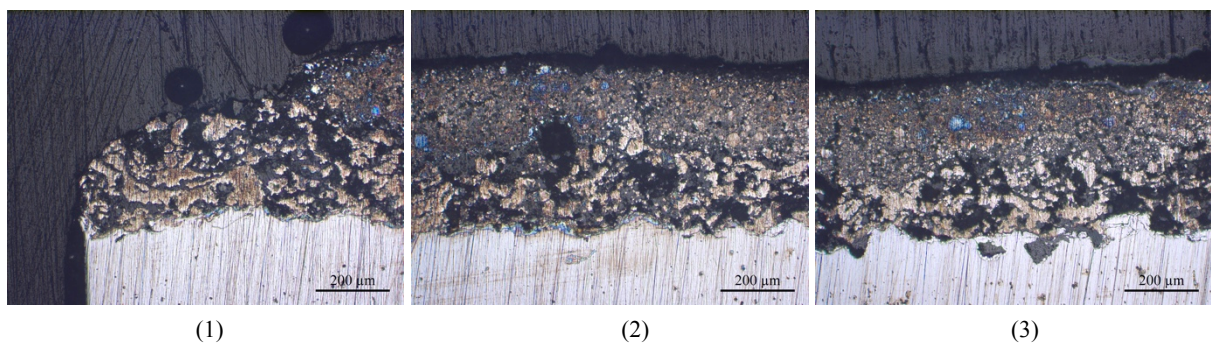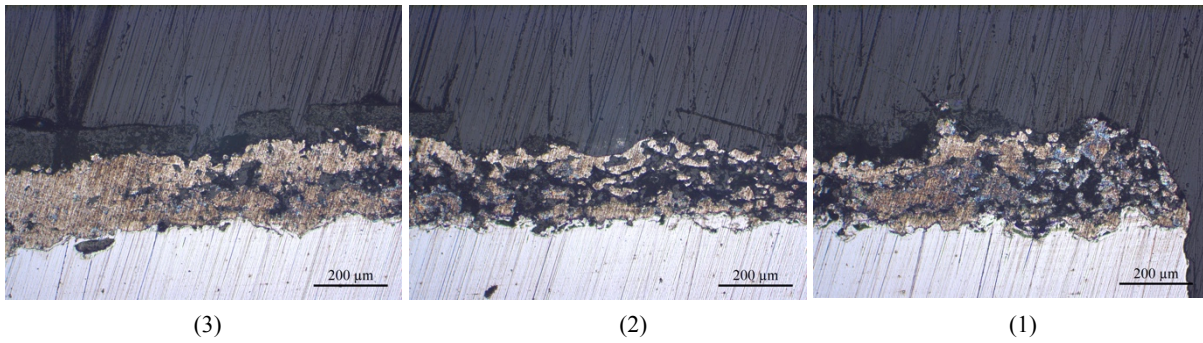
Zn silicate

| (1) | (2) | (3) |

Figure F.13: Light microscope images of the Zn silicate at the crevice opening (1) and further into the crevice (3). General corrosion of the TSA had occurred, and total reduction of the Zn silicate could be seen at the crevice opening.

MgO silicate

(3)   (2)   (1)

Figure F.14: Light microscope images of the MgO silicate at the crevice opening (1) and further into the crevice (3). General corrosion of the TSA had occurred approximately 3 mm into the crevice, in addition to high degree of MgO silicate reduction.

Mg silicate

(1)   (2)   (3)
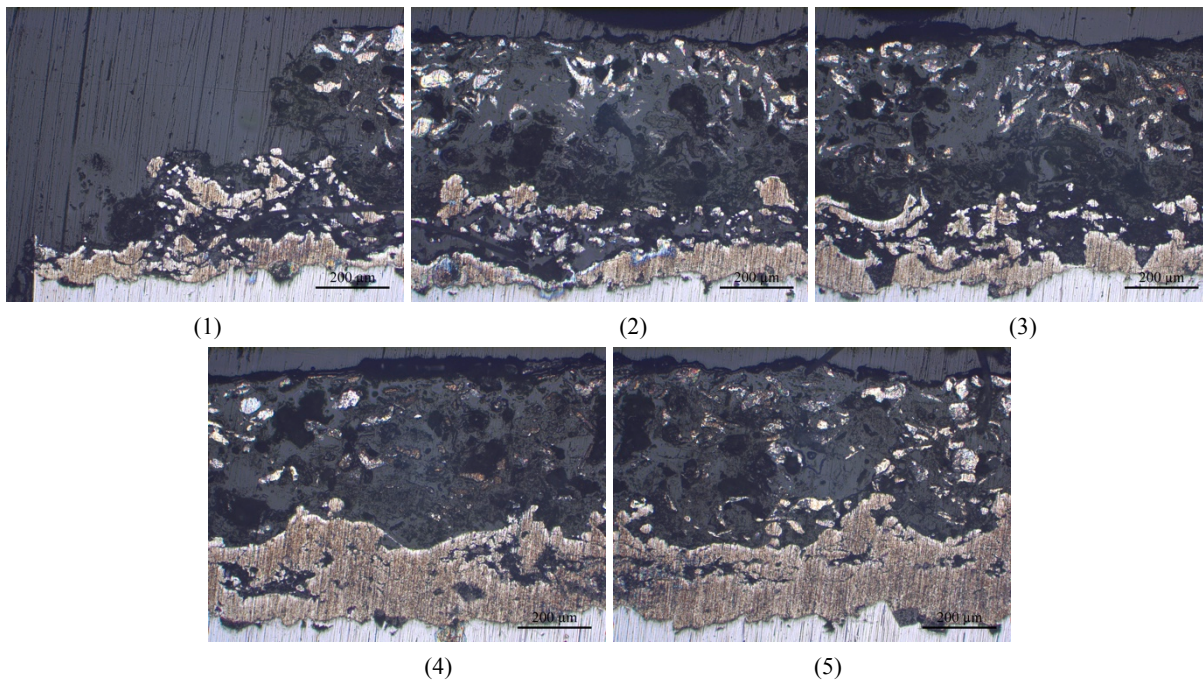
(4)   (5)

Figure F.15: Light microscope images of the Mg silicate at the crevice opening (1) and further into the crevice (5). Continuous corrosion of the TSA had occurred from the crevice opening, in addition to high degree of Mg silicate reduction. Machining may have caused the reduction of the Mg silicate at the crevice opening.
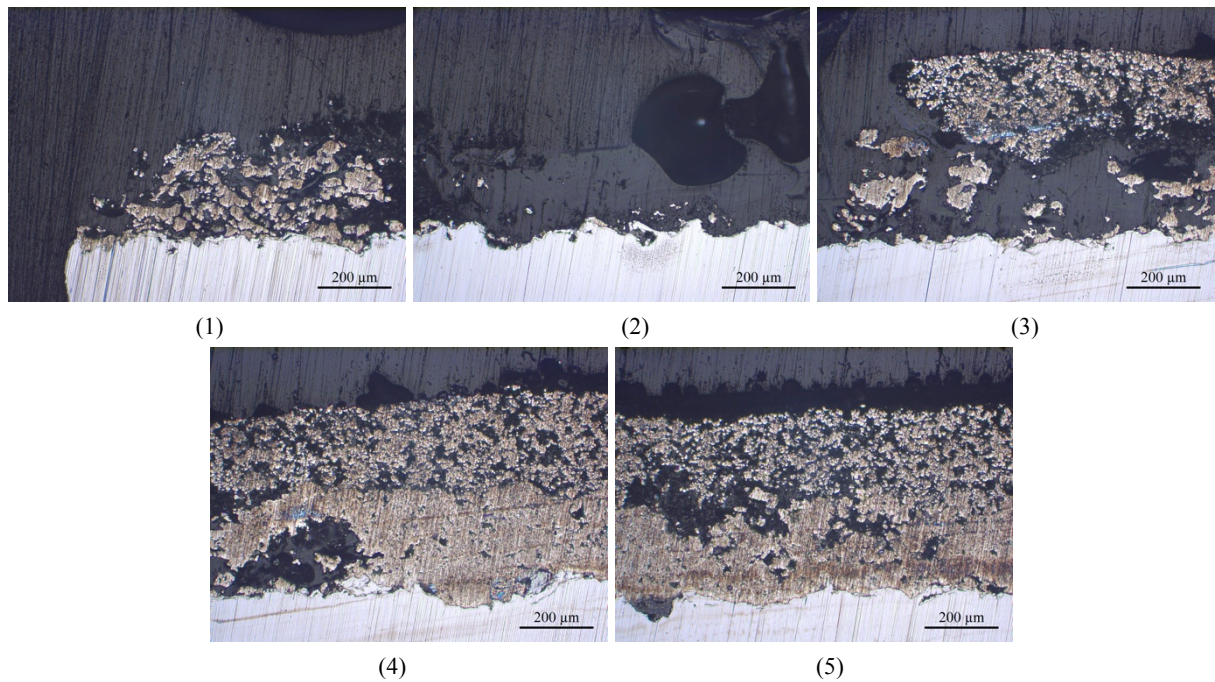
114

Al silicate

(1) (2) (3)

(4) (5)

Figure F.16: Light microscope images of the Al silicate at the crevice opening (1) and further into the crevice (5). High degree of TSA corrosion had occurred approximately 2.5 mm into the crevice, in addition to general corrosion of the Al silicate.
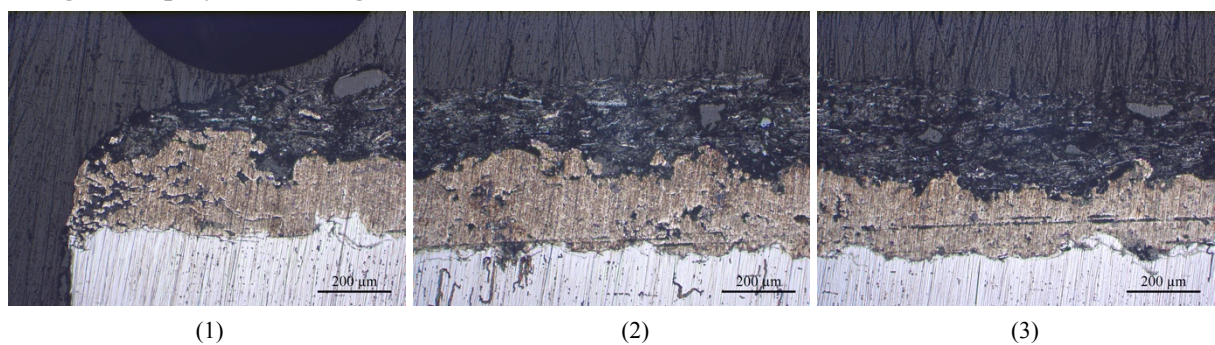
Inorganic copolymer coating

(1) (2) (3)

Figure F.17: Light microscope images of the inorganic copolymer coating at the crevice opening (1) and further into the crevice (3). The TSA had only corroded at the crevice opening, and appeared intact further into the crevice.
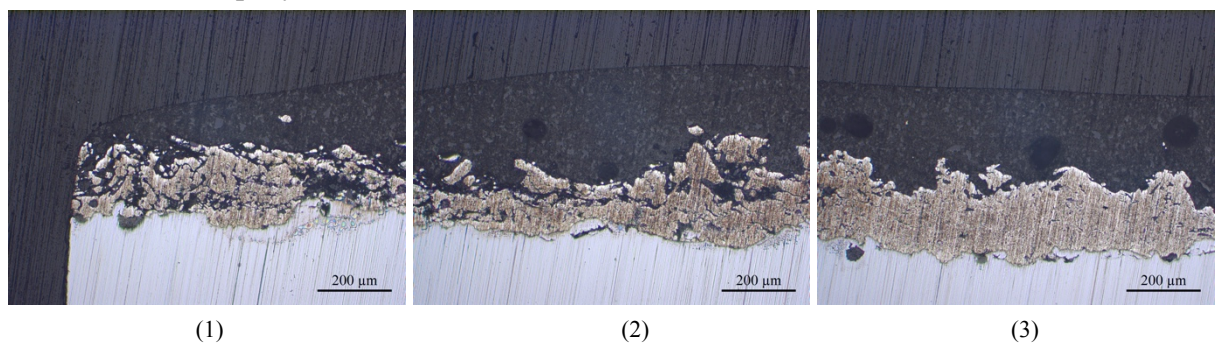
TSA coated with epoxy

(1) (2) (3)

Figure F.18: Light microscope images of the TSA coated with epoxy at the crevice opening (1) and further into the crevice (3). The TSA had corroded sporadically approximately 2 mm into the crevice, while the TSA was intact further into the crevice.

Figure F.19 presents the samples after 30 days of exposure. The pH values measured during the test period is presented in Table F.3, in addition to pH development presented in Figure F.20. Furthermore, the anodic current is presented in Figure F.21, and the coating cross sections are presented from Figure F.22 to Figure F.30. The amount of TSA corrosion and repair coat reduction are explained in the figure text.
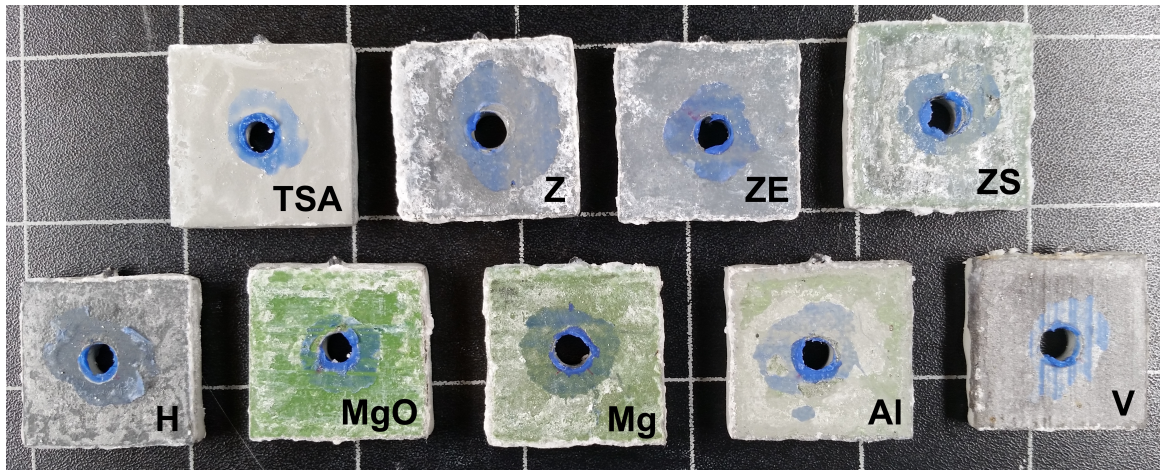

Figure F.19: Visual appearance of the samples after 30 days of exposure. The order of the repair coatings on the upper row is: TSA coated with epoxy (TSA), high Zn primer (Z), Zn epoxy (ZE) and Zn silicate (ZS). The order on the lower row is: modified Zn epoxy (H), MgO silicate (MgO), Mg silicate (Mg), Al silicate (Al) and the inorganic copolymer coating (V).

Table F.3: Measured pH for the crevice corrosion test setup 2 run for 30 days.

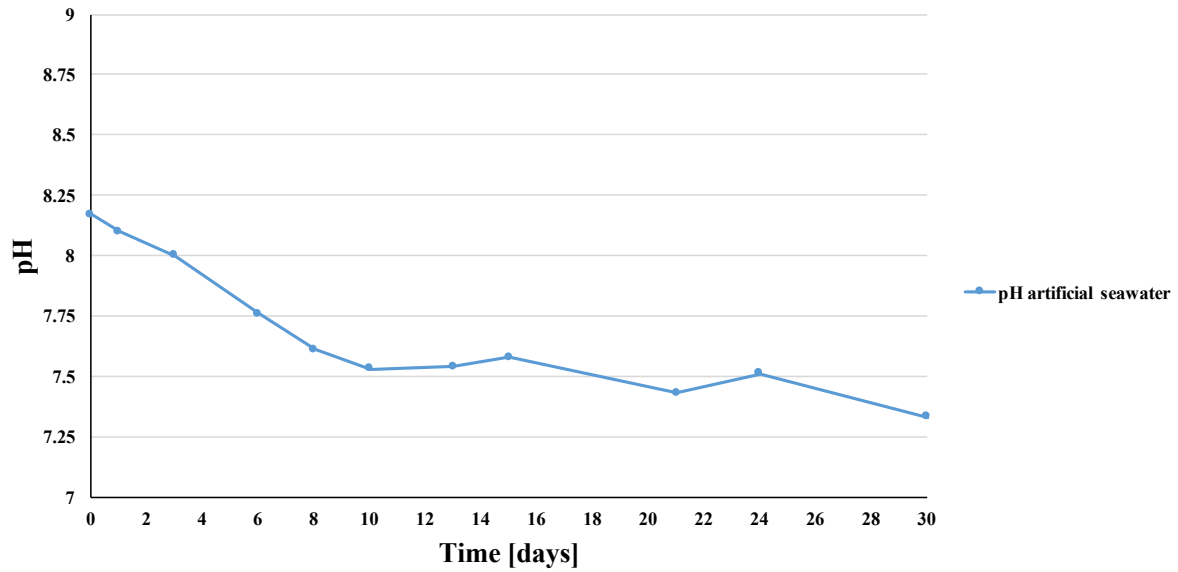| Time from test initiation [days]	pH
0	8.17
1	8.10
3	8.00
6	7.76
8	7.61
10	7.53
13	7.54
15	7.58
21	7.43
24	7.51
30	7.33

Figure F.20: Development of the pH during the test run for 30 days.

Overall, the anodic current was lower for the test that ran for 30 days, compared to the 16 days exposure, but the trend was consistent. The TSA coated with epoxy and the inorganic copolymer coating showed the same increasing tendency, but the increase started after approximately 18 days of exposure. The corresponding exposure time before the increase started for the 16 days exposure was approximately 2 days for the TSA coated with epoxy, and 7 days the inorganic copolymer coating.
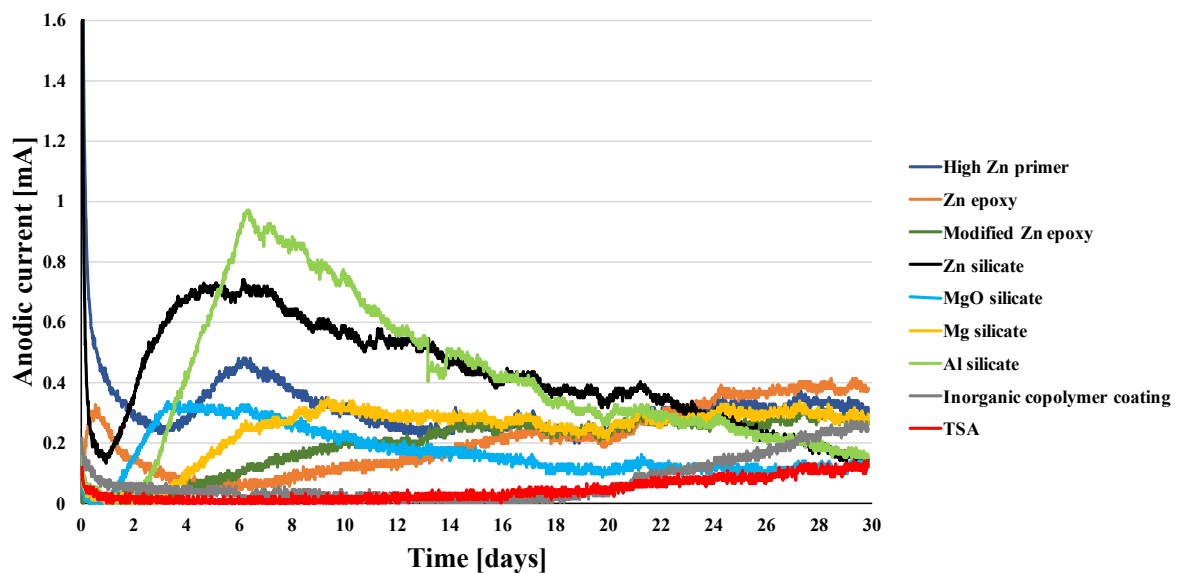

Figure F.21: Anodic current for the repair coatings for test setup 2 run for 30 days with anodic current (y-axis) plotted against time (x-axis).
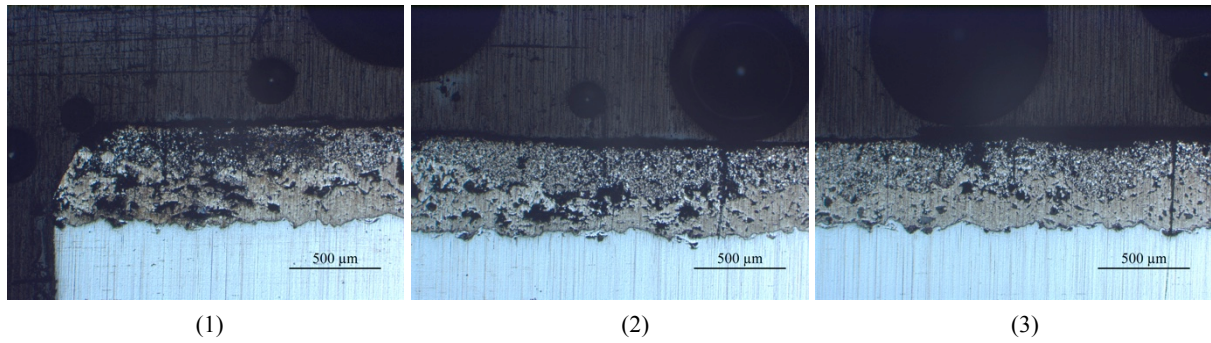
High Zn primer

(1)	(2)	(3)

Figure F.22: Light microscope images of the high Zn primer at the crevice opening (1) and further into the crevice (3). Most severe TSA corrosion was seen at the crevice opening, in addition to some sporadic TSA corrosion further into the crevice. Most corroded zinc particles were also seen at the crevice opening.
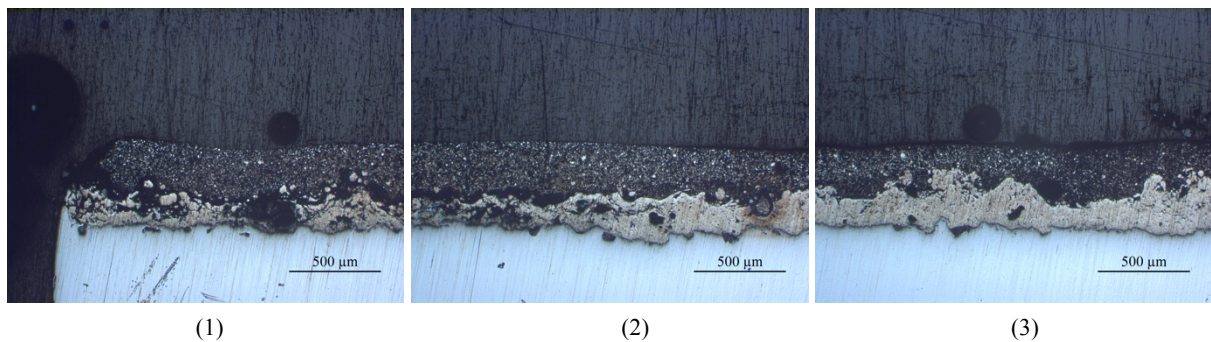
Zn epoxy

(1)	(2)	(3)

Figure F.23: Light microscope images of the Zn epoxy at the crevice opening (1) and further into the crevice (3). TSA corrosion was seen at the crevice opening, in addition to sporadic further into the crevice. A corroded field between the two coating layers can also be seen.

Modified Zn epoxy

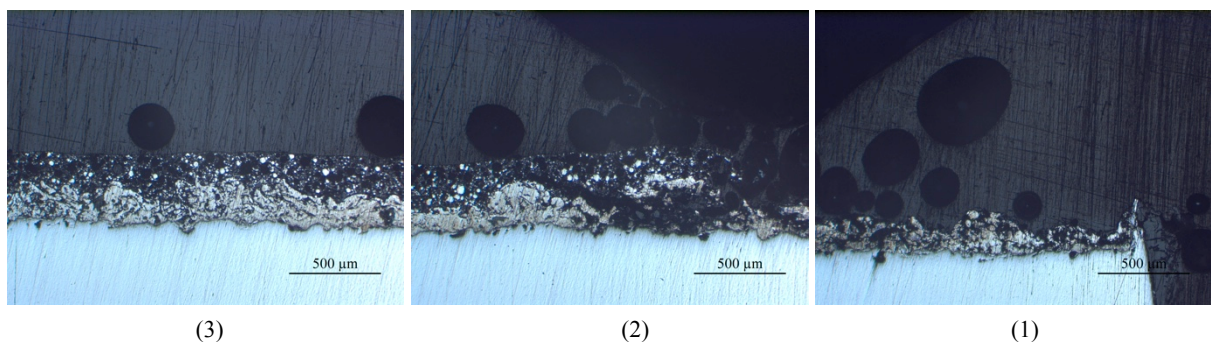|		
(3)	(2)	(1)

Figure F.24: Light microscope images of the modified Zn epoxy at the crevice opening (1) and further into the crevice (3). The modified Zn epoxy was totally corroded or flaked off approximately 2.5 mm into the crevice. General TSA corrosion was seen in the entire crevice.
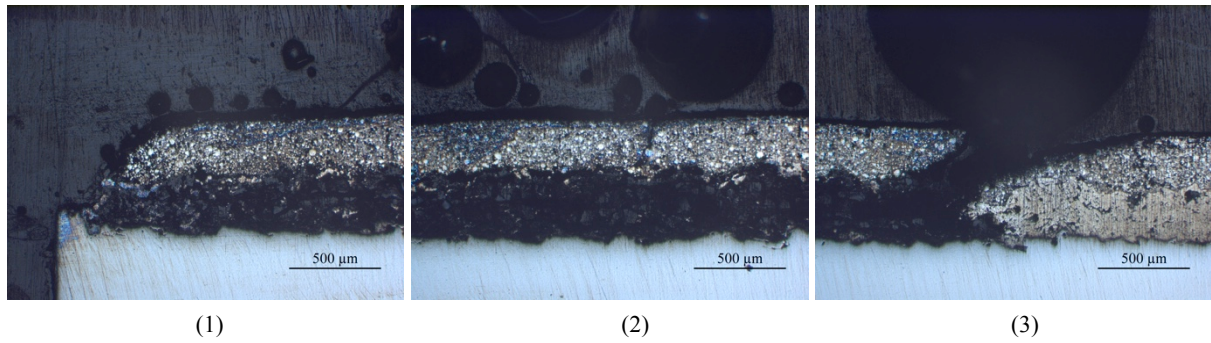
Zn silicate

(1)　　　　　　　　　　　(2)　　　　　　　　　　　(3)

Figure F.25: Light microscope images of the Zn silicate at the crevice opening (1) and further into the crevice (3). Continuous TSA corrosion was seen approximately 5.4 mm into the crevice. A crack in the repair coating was seen approximately 5.1 mm into the crevice. However, the amount of intact zinc particles appeared high.

MgO silicate

(3)　　　　　　　　　　　(2)　　　　　　　　　　　(1)

Figure F.26: Light microscope images of the MgO silicate at the crevice opening (1) and further into the crevice (3). Continuous TSA corrosion was seen approximately 2.9 mm into the crevice. Complete reduction of the MgO silicate was also seen for the same distance.

Mg silicate

(1)　　　　　　　　　　　(2)　　　　　　　　　　　(3)

(4)　　　　　　　　　　　(5)　　　　　　　　　　　(6)

Figure F.27: Light microscope images of the Mg silicate at the crevice opening (1) and further into the crevice (6). Severe corrosion of both the TSA and Mg silicate was seen, with continuous corrosion of the TSA approximately 10.4 mm into the crevice.

Al silicate

(1)　　　　　　　　　　　　　　(2)　　　　　　　　　　　　　　(3)
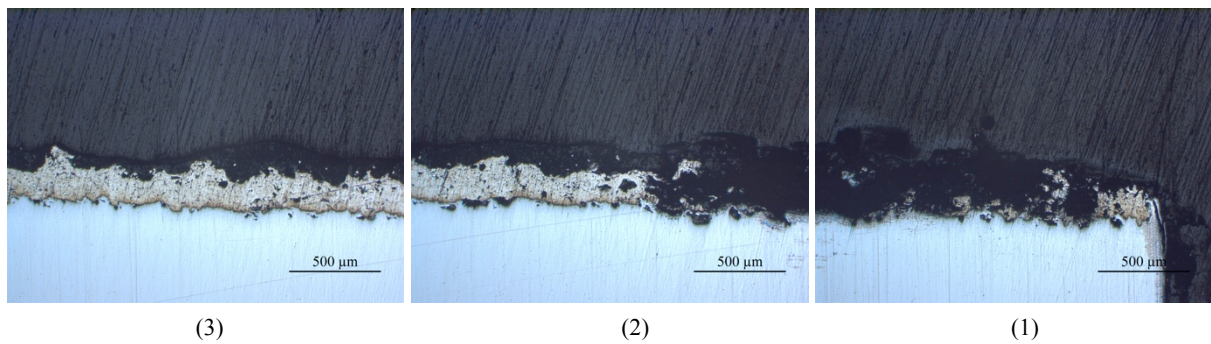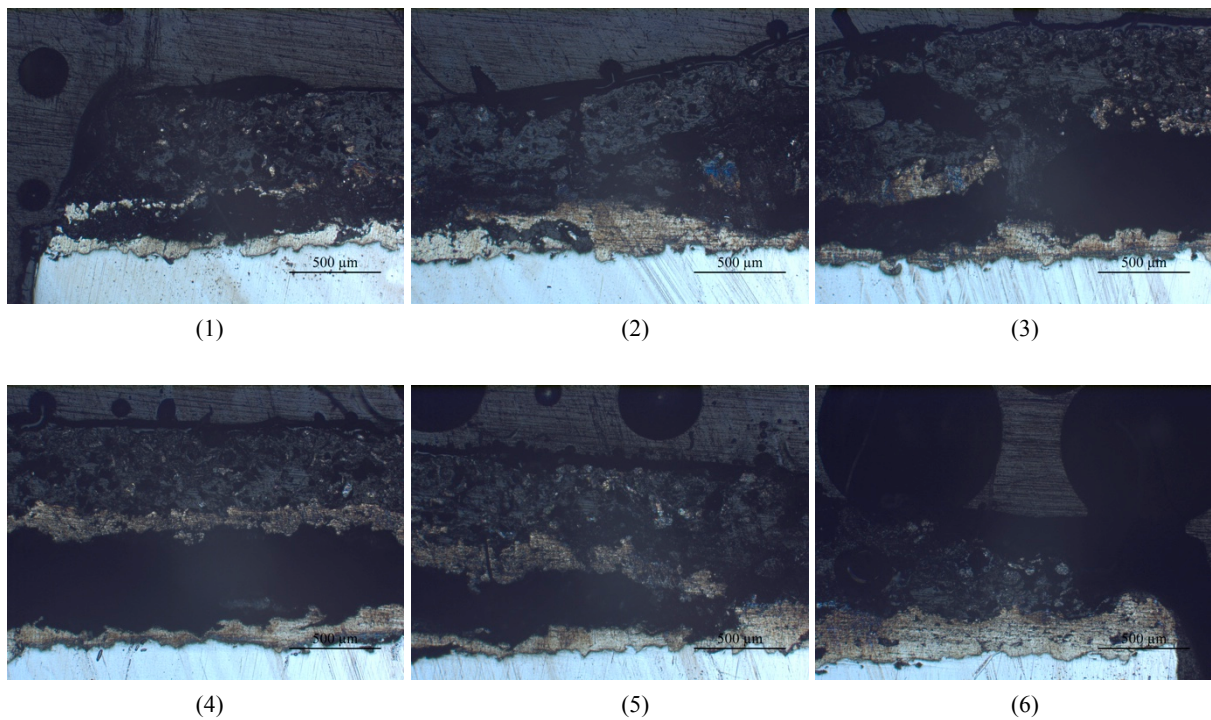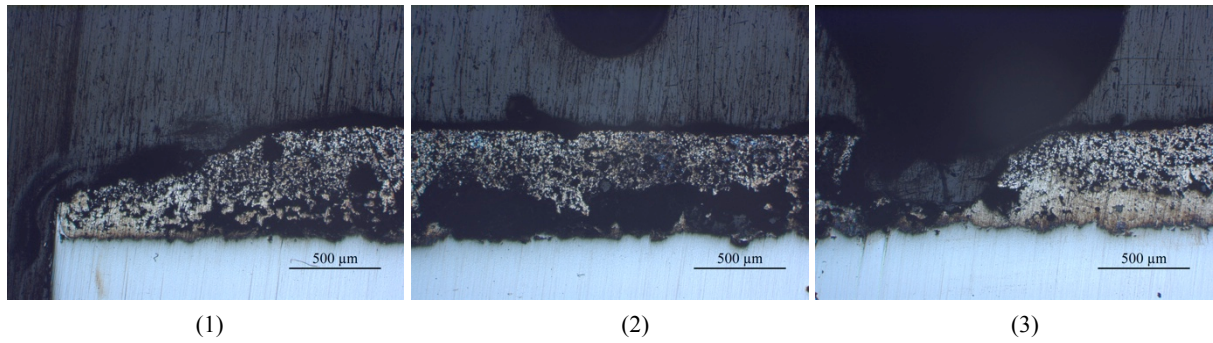
Figure F.28: Light microscope images of the Al silicate at the crevice opening (1) and further into the crevice (3). Continuous TSA corrosion was seen approximately from 0.7 mm to 5.2 mm into the crevice. Some TSA corrosion was also seen at the crevice opening, but not so severe. The amount of intact aluminium particles appeared high.

Inorganic copolymer coating

(3)　　　　　　　　　　　　　　(2)　　　　　　　　　　　　　　(1)

(5)　　　　　　　　　　　　　　(4)
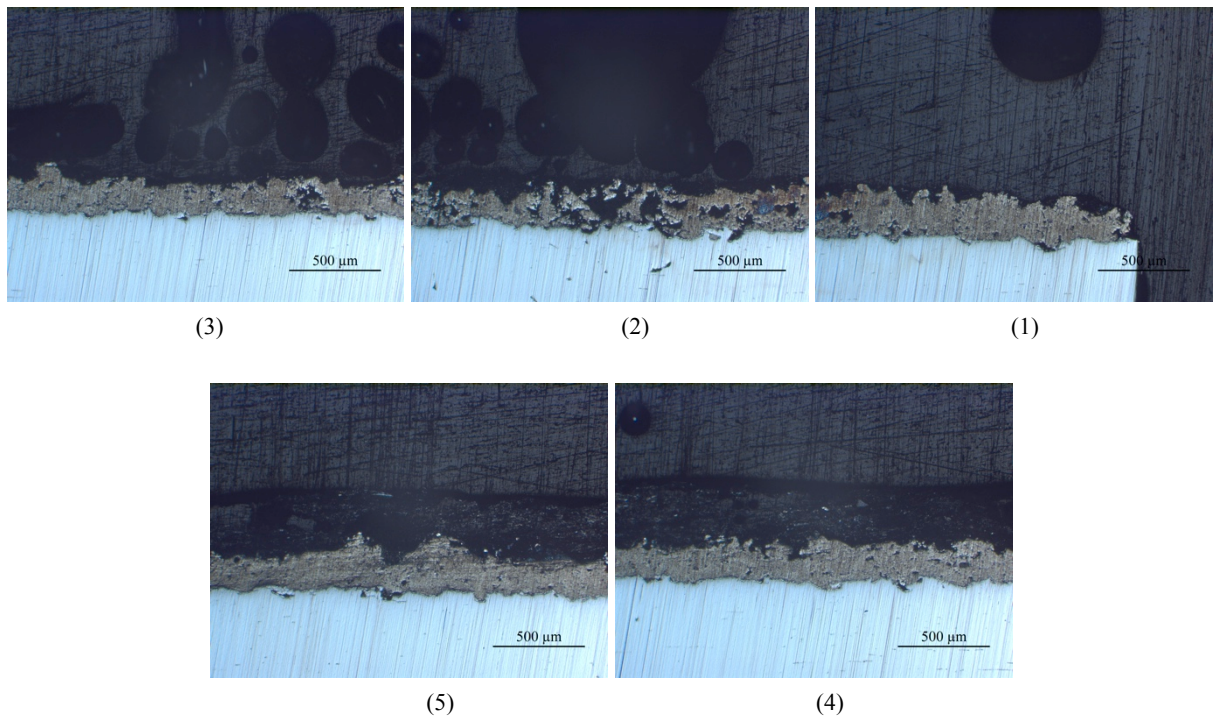
Figure F.29: Light microscope images of the inorganic copolymer coating at the crevice opening (1) and further into the crevice (5). The inorganic copolymer coating was almost completely reduced approximately 6.1 mm into the crevice. A thin remaining layer can be seen. Some sporadic TSA corrosion can be seen a distance into the crevice.

TSA coated with epoxy

(1)　　　　　　　　　　　　　　(2)　　　　　　　　　　　　　　(3)
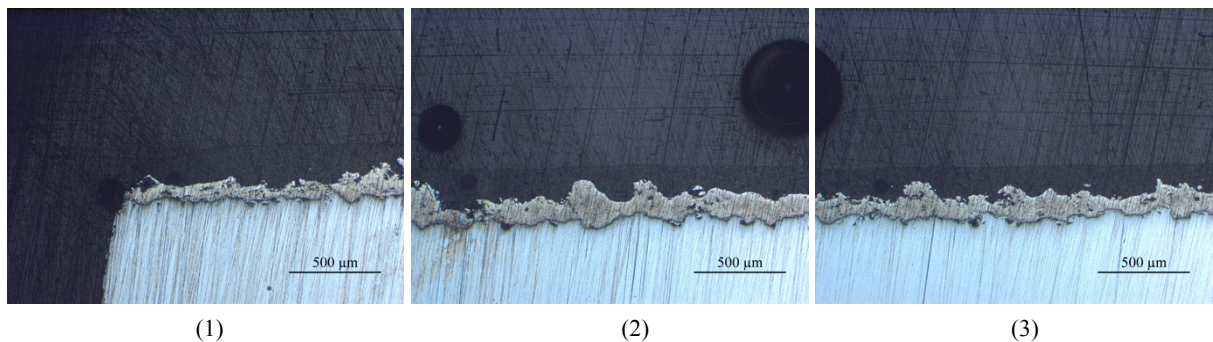
Figure F.30: Light microscope images of the TSA coated with epoxy at the crevice opening (1) and further into the crevice (3). Some TSA corrosion at the crevice opening can be seen. Further into the crevice, the TSA appeared unaffected.

Appendix G Risk Assessment

NTNU / HMS

Kartlegging av risikofylt aktivitet

	Utarbeidet av	Nummer	Dato
	HMS-avd.	HMSRV2601	22.03.2011
	Godkjent av		Erstatter
	Rektor		01.12.2006

Dato: 11.01.2016

Enhet: Institutt for produktutvikling og materialer

Linjeleder: Torgeir Welo

Deltakere ved kartleggingen (m/ funksjon): student og veileder
Kort beskrivelse av hovedaktivitet/hovedprosess: Masteroppgave Heidi Askestad. Reparasjonsbelegg for termisk sprøyta aluminium.

Er oppgaven rent teoretisk? (JA/NEI): Nei

Signaturer: Ansvarlig veileder: _(signature)_ Student: Heidi Askestad

ID nr.	Aktivitet/prosess	Ansvarlig	Eksisterende dokumentasjon	Eksisterende sikringstiltak	Lov, forskrift o.l.	Kommentar
1	Male stålprøver belagt med TSA med ulike uorganiske, organiske og polymer belegg.	Heidi Askestad	Sikkerhetsdatablad, apparaturkort	Vernebriller, labfrakk, hansker, avtrekksskap, førstehjelp- og brannslukningsutstyr	Arbeidsmiljøloven, Kjemikalieforskriften, Lab og verkstedshåndboken NTNU	
2	Blande aluminium- og magnesium pulver med bindemiddel i luft.	Heidi Askestad	Sikkerhetsdatablad, apparaturkort	Vernebriller, labfrakk, hansker, avtrekksskap, førstehjelp- og brannslukningsutstyr	Arbeidsmiljøloven, Kjemikalieforskriften, Lab og verkstedshåndboken NTNU	
3	Eksponere prøver i salttåke-kammer.	Heidi Askestad	Apparaturkort, brukermanual	Vernebriller, hansker, førstehjelp- og brannslukningsutstyr	Arbeidsmiljøloven, Lab og verkstedshåndboken NTNU	
4	Eksponere prøver i UV-kammer.	Heidi Askestad	Apparaturkort, brukermanual	Vernebriller, hansker, førstehjelp- og brannslukningsutstyr	Arbeidsmiljøloven, Lab og verkstedshåndboken NTNU	
5	Eksponere prøver elektrolytt, saltvann.	Heidi Askestad	Sikkerhetsdatablad, apparaturkort	Vernebriller, hansker, førstehjelp- og brannslukningsutstyr	Arbeidsmiljøloven, Lab og verkstedshåndboken NTNU	
6	Støpe inn prøver i epoxy.	Heidi Askestad	Sikkerhetsdatablad, apparaturkort	Vernebriller, førstehjelp- og brannslukningsutstyr	Arbeidsmiljøloven, Kjemikalieforskriften, Lab og verkstedshåndboken NTNU	
7	Pusse og polere prøver.	Heidi Askestad	Sikkerhetsdatablad, apparaturkort	Briller, førstehjelp- og brannslukningsutstyr	Arbeidsmiljøloven, Lab og verkstedshåndboken NTNU	

NTNU		Kartlegging av risikofylt aktivitet			Utarbeidet av	Nummer	Dato	
⬛					HMS-avd.	HMSRV2601	22.03.2011	
HMS					Godkjent av		Erstatter	
					Rektor		01.12.2006	
8		Ta bilder i lysmikroskop.	Heidi Askestad	Sikkerhetsdatablad, apparaturkort		Arbeidsmiljøloven, Lab og verkstedshåndboken NTNU		
9		Ta bilder i SEM.	Heidi Askestad	Sikkerhetsdatablad, apparaturkort		Arbeidsmiljøloven, Lab og verkstedshåndboken NTNU		

Risikovurdering

NTNU — HMS

	Utarbeidet av	Nummer	Dato
	HMS-avd.	HMSRV2601	22.03.2011
	Godkjent av		Erstatter
	Rektor		01.12.2006

Dato: 11.01.2016

Enhet: Institutt for produktutvikling og materialer

Linjeleder: Torgeir Welo

Deltakere ved kartleggingen (m/ funksjon): student

Risikovurderingen gjelder hovedaktivitet: Masteroppgave Heidi Askestad. Reparasjonsbelegg for termisk sprøyta aluminium.

Signaturer: Ansvarlig veileder: _____   Student: Heidi Askestad

ID nr.	Aktivitet fra kartleggings-skjemaet	Mulig uønsket hendelse/ belastning	Vurdering av sannsynlighet (1-5)	Vurdering av konsekvens:				Risikoverdi (menneske)	Kommentarer/status Forslag til tiltak
				Menneske (A-E)	Ytre miljø (A-E)	Øk/ materiell (A-E)	Om- dømme (A-E)		
1a	Male stålprøver belagt med TSA med ulike uorganiske, organiske og polymer.	Puste inn kjemikaler.	2	B	B	A	B	B2	Bruke avtrekksskap.
1b		Søle maling på klær/hud/omgivelser.	2	B	B	A	A	B2	Bruke verneutstyr.
2	Blande aluminium- og magnesium pulver med bindemiddel.	Brann eller eksplosjonsfare ved blanding.	2	C	D	C	C	C2	Blande små mengder i avtrekksskap.
3	Eksponere prøver i salttåke-kammer.	Utløse brannalarm.	1	A	A	A	A	A1	Vente med åpning av kammer til damp har sunket til bunn.
4	Eksponere prøver i UV-kammer.	Eksponeres for UV-lys.	1	B	A	A	B	B1	Ikke åpne kammeret når test kjøres.
5	Eksponere prøver i elektrolytt, saltvann.	Søle elektrolytt.	2	B	B	A	B	B2	
6	Støpe inn prøver i epoxy.	Puste inn kjemikaler.	1	A	A	A	A	A1	Bruke avtrekksskap.
7	Pusse og polere prøver.	Skade fingre.	1	B	A	A	A	A1	

NTNU		Utarbeidet av	Nummer	Dato
		HMS-avd.	HMSRV2601	22.03.2011
HMS		Godkjent av		Erstatter
		Rektor		01.12.2006

Risikovurdering

8	Ta bilder i lysmikroskop.	Ødelegge utstyr.	1	A	A	D	A	A1
9	Ta bilder i SEM.	Ødelegge utstyr.	1	A	A	D	A	A1

Sannsynlighet vurderes etter følgende kriterier:

Svært liten 1	Liten 2	Middels 3	Stor 4	Svært stor 5
1 gang pr 50 år eller sjeldnere	1 gang pr 10 år eller sjeldnere	1 gang pr år eller sjeldnere	1 gang pr måned eller sjeldnere	Skjer ukentlig

Konsekvens vurderes etter følgende kriterier:

Gradering	Menneske	Ytre miljø Vann, jord og luft	Øk/materiell	Omdømme
E Svært Alvorlig	Død	Svært langvarig og ikke reversibel skade	Drifts- eller aktivitetsstans >1 år.	Troverdighet og respekt betydelig og varig svekket
D Alvorlig	Alvorlig personskade. Mulig uførhet.	Langvarig skade. Lang restitusjonstid	Driftsstans > ½ år Aktivitetsstans i opp til 1 år	Troverdighet og respekt betydelig svekket
C Moderat	Alvorlig personskade.	Mindre skade og lang restitusjonstid	Drifts- eller aktivitetsstans < 1 mnd	Troverdighet og respekt svekket
B Liten	Skade som krever medisinsk behandling	Mindre skade og kort restitusjonstid	Drifts- eller aktivitetsstans < 1uke	Negativ påvirkning på troverdighet og respekt
A Svært liten	Skade som krever førstehjelp	Ubetydelig skade og kort restitusjonstid	Drifts- eller aktivitetsstans < 1dag	Liten påvirkning på troverdighet og respekt

Risikoverdi = Sannsynlighet x Konsekvens
Beregn risikoverdi for Menneske. Enheten vurderer selv om de i tillegg vil beregne risikoverdi for Ytre miljø, Økonomi/materiell og Omdømme. I så fall beregnes disse hver for seg.

Til kolonnen "Kommentarer/status, forslag til forebyggende og korrigerende tiltak":
Tiltak kan påvirke både sannsynlighet og konsekvens. Prioriter tiltak som kan forhindre at hendelsen inntreffer, dvs. sannsynlighetsreduserende tiltak foran skjerpet beredskap, dvs. konsekvensreduserende tiltak.

NTNU	Risikomatrise	utarbeidet av	Nummer	Dato
HMS		HMS-avd.	HMSRV2604	08.03.2010
		godkjent av	Erstatter	
		Rektor		09.02.2010

MATRISE FOR RISIKOVURDERINGER ved NTNU

KONSEKVENS		Svært liten	Liten	Middels	Stor	Svært stor
Svært alvorlig	E	E1	E2	E3	E4	E5
Alvorlig	D	D1	D2	D3	D4	D5
Moderat	C	C1	C2	C3	C4	C5
Liten	B	B1	B2	B3	B4	B5
Svært liten	A	A1	A2	A3	A4	A5
		Svært liten	Liten	Middels	Stor	Svært stor
				SANNSYNLIGHET		

Prinsipp over akseptkriterium. Forklaring av fargene som er brukt i risikomatrisen.

Farge		Beskrivelse
Rød		Uakseptabel risiko. Tiltak skal gjennomføres for å redusere risikoen.
Gul		Vurderingsområde. Tiltak skal vurderes.
Grønn		Akseptabel risiko. Tiltak kan vurderes ut fra andre hensyn.